Path integral techniques and Gröbner basis approaches for stochastic response analysis and optimization of diverse nonlinear dynamic systems

Ioannis Petromichelakis

Submitted in partial fulfillment of the
requirements for the degree of
Doctor of Philosophy
under the Executive Committee
of the Graduate School of Arts and Sciences

COLUMBIA UNIVERSITY

2020

Abstract

Path integral techniques and Gröbner basis approaches for stochastic response analysis and optimization of diverse nonlinear dynamic systems

Ioannis Petromichelakis

This thesis focuses primarily on generalizations and enhancements of the Wiener path integral (WPI) technique for stochastic response analysis and optimization of diverse nonlinear dynamic systems of engineering interest. Concisely, the WPI technique, which has proven to be a potent mathematical tool in theoretical physics, has been recently extended to address problems in stochastic engineering dynamics. Herein, the WPI technique has been significantly enhanced in terms of computational efficiency and versatility; these results are presented in Chapters 2-5.

Specifically, in Chapter 2 a brief introduction to the standard WPI solution approach is outlined. In Chapter 3, a novel methodology is presented, which utilizes theoretical results from calculus of variations to extend the WPI for determining marginalized response PDFs of n-degree-of-freedom (n-DOF) nonlinear systems. The associated computational cost relates to the dimension of the PDF and is essentially independent from the dimension n of the system. In several commonly encountered cases, the aforementioned methodology improves the computational efficiency of the WPI by orders of magnitude, and exhibits a significant advantage over the commonly utilized Monte-Carlo-simulation (MCS). Moreover, in Chapter 4, an extension of the WPI technique is presented for addressing the challenge of determining the stochastic response of nonlinear dynamical systems under the presence of singularities in

the diffusion matrix. The key idea behind this approach is to partition the original system into an underdetermined system of SDEs corresponding to a nonsingular diffusion matrix and an underdetermined system of homogeneous differential equations; the latter is treated as a dynamic constraint that allows for employing constrained variational/optimization solution methods. In Chapter 5, this approach is applied for the stochastic response analysis and optimization of electromechanical vibratory energy harvesters.

Next, in Chapter 6, a technique from computational algebraic geometry has been developed, which is based on the concept of Gröbner basis and is capable of determining the entire solution set of systems of polynomial equations. This technique has been utilized to address diverse challenging problems in engineering mechanics. First, after formulating the WPI as a minimization problem, it is shown in Chapter 7 that the corresponding objective function is convex, and thus, convergence of numerical schemes to the global optimum is guaranteed. Second, in Chapter 8, the computational algebraic geometry technique has been applied to the challenging problem of determining nonlinear normal modes (NNMs) corresponding to multi-degree-of-freedom dynamical systems as defined in [1], and has been shown to yield improvements in accuracy compared to the standard treatment in the literature.

Next, a list of the author's journal publications related to this thesis is provided.

- Petromichelakis, I., Psaros, A.F. and Kougioumtzoglou, I.A., "Stochastic response determination and optimization of a class of nonlinear electromechanical energy harvesters: A Wiener path integral approach", *Probabilistic Engineering Mechanics*, vol. 53, pp. 116–125, 2018

- Psaros, A.F., Kougioumtzoglou, I.A. and Petromichelakis, I., "Sparse representations and compressive sampling for enhancing the computational efficiency of the Wiener path integral technique", *Mechanical Systems and Signal Processing*, vol. 111, pp. 87–101, 2018

- Psaros, A.F., Petromichelakis, I. and Kougioumtzoglou, I.A., "Wiener path integrals and multi-dimensional global bases for non-stationary stochastic response determination of structural systems", *Mechanical Systems and Signal Processing*, vol. 128, pp. 551–571, 2019

- Petromichelakis, I., Psaros, A.F. and Kougioumtzoglou, I.A., "Stochastic response determination of nonlinear structural systems with singular diffusion matrices: A Wiener

path integral variational formulation with constraints", *Probabilistic Engineering Mechanics*, vol. 60, p. 103044, 2020

- Kougioumtzoglou, I.A., Petromichelakis, I. and Psaros, A.F., "Sparse representations and compressive sampling approaches in engineering mechanics: A review of theoretical concepts and diverse applications", *Probabilistic Engineering Mechanics*, vol. 61, p. 103082, 2020

- Petromichelakis, I., Psaros, A.F. and Kougioumtzoglou, I.A., "Stochastic response analysis and reliability-based design optimization of nonlinear electromechanical energy harvesters with fractional derivative elements", accepted to *ASCE-ASME Journal of Risk and Uncertainty in Engineering Systems*, 2020

- Petromichelakis, I. and Kougioumtzoglou, I.A., "Addressing the curse of dimensionality in stochastic dynamics: A Wiener path integral variational formulation with free boundaries", (submitted for publication), 2020

- Petromichelakis, I., Bosse, R.M., Kougioumtzoglou, I.A. and Beck, A., "Wiener path integral most probable path determination: A computational algebraic geometry solution treatment", (submitted for publication), 2020

- Petromichelakis, I. and Kougioumtzoglou, I.A., "Normal mode motions of nonlinear systems via a center manifold technique and a Gröbner basis algebraic solution", (submitted for publication), 2020

Table of Contents

List of Tables

List of Figures

Acknowledgements

I would like to express my sincere gratitude to my advisor Prof. Ioannis Kougioumtzoglou for the continuous support of my Ph.D study and related research, for his patience, motivation, and immense knowledge. His guidance and discreet supervision had a tremendous impact in research and writing of this thesis. I could not have imagined having a better advisor and mentor for my Ph.D study.

Besides my advisor, I feel the need to acknowledge all my previous teachers, advisors and mentors for the wealth of knowledge they imparted to me and for their trustfulness; most notably Manolis Maragakis, Manolis Papadrakakis, Wolfgang Graf and Chrysoula Tsogka. Moreover, this thesis has only benefited by the fruitful discussions with my colleagues Savvas Saloustros, Apostolos Psaros, Marcello Morgantini, James McLean, Eleni Chourdaki, Giannis Karamanolakis, Manolis Vlatakis, Kostas Tsampourakis, Vasilis Efthymiou and Kostas Petrakis.

Last but not least, I express my deepest gratitude to my parents Nikos and Anna, my brother Stavros and all my friends for their support, devotion and unconditional love all these years.

I dedicate this thesis to Theano,

my partner in life whom I had the luck to meet during the course of this Ph.D.

and has been a source of inspiration and constant support.

Chapter 1: Introduction

1.1 Wiener path integral (WPI) technique

Accurate response analysis of engineering dynamical systems necessitates an increasingly sophisticated modeling of the system behavior and of the associated excitations. This includes consideration of strong nonlinearities, complex hysteresis, stochastic loads, as well as a relatively high dimensionality of the system response vector. Despite their versatility and implementation simplicity, the performance of purely numerical solution techniques, such as various Monte Carlo simulation (MCS) schemes (e.g., [2, 3, 4, 5, 6, 7]), for determining the system stochastic response is often hindered by the related excessive computational cost, and thus, there is merit in developing alternative efficient semi-analytical solution techniques. In this regard, indicative techniques developed over the past few decades include statistical linearization, stochastic averaging, perturbation approaches, discrete Chapman-Kolmogorov equation schemes, Fokker-Planck equation solution techniques, probability density evolution methods, and polynomial chaos expansions. The interested reader is directed to various standard books in the field for a detailed presentation (e.g., [8, 9, 10, 11, 12, 13]).

Recently, a novel semi-analytical technique based on the concept of Wiener path integral (WPI) (e.g., [14, 15]) has been developed in the field of stochastic engineering dynamics for determining the stochastic response of diverse nonlinear structural and mechanical systems (e.g., [16, 17]). In fact, the technique, which relies on functional integration concepts and on calculus of variations tools, exhibits both computational efficiency and satisfactory accuracy in evaluating the system joint response probability density function (PDF) (e.g., [18, 19, 20, 21]). Further, the WPI technique exhibits versatility in addressing diverse system behaviors, including hysteresis and fractional derivative modeling (e.g., [22, 23]), and in accounting for

various rather sophisticated descriptions of stochastic excitations [24].

An integral part of the standard implementation of the WPI technique relates to a variational treatment for deriving a functional minimization problem, which may be solved by either resorting to the corresponding Euler–Lagrange (E-L) equations, or by directly formulating an ordinary optimization problem in accordance with the Rayleigh–Ritz solution technique [22]. Either of these approaches yields the most probable path, which is used for evaluating a specific point of the joint response PDF (e.g., [17]). The fact that the Rayleigh–Ritz solution approach leads to an ordinary optimization problem, allows for a rigorous convergence analysis of the corresponding numerical scheme. In this regard, a Newton's numerical optimization scheme is developed for determining the most probable path. The rationale relates to the fact that, for the special case of linear systems, the objective function is not only convex, but also quadratic; and thus, a Newton's scheme appears to be an ideal choice as it converges in only one iteration to the unique global extremum (e.g., [25]). This convergence behavior indicates that a Newton's scheme can be a suitable choice also for nonlinear systems, since their response behavior can be construed as a perturbation (not necessarily small) from the linear regime. Further, certain convergence properties of the scheme are derived and discussed. A general overview of the fundamental aspects of the WPI technique is provided in Chapter 2 of this thesis.

1.1.1 Improving WPI in terms of computational efficiency

Ever-increasing computational capabilities, novel signal processing techniques, advanced experimental setups, as well as progress in emerging and transformative technologies (e.g., nano-mechanics) have contributed to a highly sophisticated mathematical modeling of the governing equations of diverse dynamical systems. In general, the governing dynamics is modeled as a high-dimensional system of coupled nonlinear (stochastic) differential equations. In many cases, solving even the deterministic version of such equations is an open issue and an active research topic. Clearly, addressing the stochastic counterparts of these equations

becomes significantly more challenging, since the stochastic dimensions of the problem need to be considered in addition to the system deterministic/physical coordinates; thus, the overall dimensionality and computational complexity of the problem increase (e.g., [13]).

To address the above-described "curse-of-dimensionality", as is typically referred to in the relevant literature, researchers have developed diverse techniques for solving high-dimensional stochastic equations in a computationally efficient manner. Indicatively, these range from "smart" Monte Carlo simulation (MCS) schemes (e.g., [26, 7]) to various approximate dimension/order reduction approaches (e.g., [13]). Nevertheless, in most cases, these methodologies become eventually computationally prohibitive with an increasing number of problem dimensions.

Further, it can be argued that a complete stochastic characterization of the dynamical system response (i.e., determination of the joint response probability density function (PDF)) is not required for the vast majority of practical problems. Instead, determining a relatively small number of marginal PDFs, or low-dimensional joint PDFs, is often adequate in practice. In this regard, an interesting class of solution techniques focus on developing transformed governing stochastic equations involving only a subset of marginalized joint PDFs. The rationale relates to decreasing the dimensionality of the original problem and to determining directly the stochastic response of specific degrees-of-freedom (DOFs) or intrinsic coordinates of interest. Indicatively, appropriate multi-dimensional integration was applied in [27] for deriving PDF evolution equations corresponding to specific quantities of interest. Moreover, high-dimensional Fokker-Planck (F-P) equations were solved in [28] based on a block decomposition of the high-dimensional unobserved subset of variables and of the remaining low-dimensional observed variables. In a relatively similar context, a stochastic collocation scheme was developed in [29] capable of treating high-dimensional stochastic differential equations (SDEs) by constructing a sparse grid of collocation points, which is only weakly dependent on the dimensionality of the state space (see also [30]). Also, it is worth mentioning current research efforts based on deep learning tools for facilitating the

solution of complex SDEs (e.g., [31]).

Although the WPI technique exhibits a relatively high degree of accuracy, its standard numerical implementation leads eventually to prohibitive computational cost with an increasing number of stochastic dimensions. This is due to the fact that the complete joint response PDF is determined by resorting to a point-wise computation on a multi-dimensional lattice. Clearly, this hinders the scalability of the technique in addressing multi-DOF systems described by more than a few DOFs. Although this limitation has been partly addressed in [19, 24] by employing multi-dimensional function approximation techniques in conjunction with compressive sampling concepts and tools for reducing the total number of grid-point calculations, the requirement for determining the complete joint response PDF has not been circumvented to-date. Thus, the overall computational cost still grows rapidly with an increasing number of DOFs.

In Chapter 3 of this thesis, the curse of dimensionality in stochastic dynamics is addressed by marginalizing the joint response PDF based on a WPI variational formulation with free boundaries. In this regard, the associated computational cost becomes independent of the number of DOFs; and thus, high-dimensional systems can be readily treated by the WPI technique. Two indicative numerical examples are considered for highlighting the capabilities of the technique. The first example relates to marine engineering and pertains to a structure exposed to nonlinear flow-induced forces and subjected to non-white stochastic excitation. The second example relates to nano-engineering and pertains to a 100-DOF stochastically excited nonlinear dynamical system modeling the behavior of large arrays of coupled nano-mechanical oscillators. Comparisons with pertinent MCS data demonstrate the computational efficiency and accuracy of the developed technique.

1.1.2 Improving WPI in terms of versatility

The applicability of the WPI technique has so far been restricted to systems with non-singular diffusion matrices. In fact, the general formulation of the technique involving the

inversion of the governing equation diffusion matrix does not allow for a straightforward extension to cases pertaining to singular diffusion matrices, and thus, special mathematical treatments are required (e.g., [32, 33, 34]). Indicative examples, where such special treatments can be rather trivial, include casting the higher-order (e.g., second-order) governing equation into a lower-order (e.g., first-order) form by introducing additional state variables, as well as modeling non-white excitations via filter equations (e.g., [20, 35, 36]). In such cases, the limitation of singular diffusion matrices can be readily bypassed (e.g., [37]) by enforcing compatibility conditions of a rather simple (almost trivial) form between the auxiliary variables and the time-derivatives of the original variables. However, this is not always the case as these auxiliary equations are more than often of a complex form. Examples include (but are not limited to) dynamical systems with only some of their DOFs forced, hysteretic models (e.g., Bouc-Wen [38]) with nonlinear auxiliary differential equations, and diverse energy harvesting systems such as various electromechanical harvesters (e.g., [18]) and wave energy converters (e.g., [39]).

In Chapter 4 of this thesis, the WPI solution technique is generalized to cope with a broad class of systems with singular diffusion matrices. In this regard, the governing equations of motion are represented herein as a set of underdetermined stochastic differential equations (SDEs) coupled with a set of deterministic ordinary differential equations (ODEs). The latter, which can be of arbitrary (nonlinear) form, are construed as constraints on the motion of the system driven by the stochastic excitation (e.g., [40, 41, 42]). This yields a constrained variational problem to be solved for the most probable path, and thus, the system joint response PDF is determined. Several numerical examples pertaining to both linear and nonlinear constraint equations are considered, including MDOF systems with only some of their DOFs stochastically excited, a linear oscillator under Kanai-Tajimi earthquake excitation, as well as a nonlinear oscillator exhibiting hysteresis following the Bouc-Wen formalism. Direct comparisons with MCS data demonstrate a relatively high degree of accuracy.

1.1.3 Utilizing WPI for the design of energy harvesting devices

A large class of energy harvesters exploit the ability of active materials (e.g. piezoelectric) and electromechanical coupling mechanisms to generate an electric potential in response to external excitations. Utilizing an appropriate circuit, the electric potential is converted into current, and thus, mechanical energy is transformed into electrical. Following early efforts referring to linear system modeling (e.g., [43, 44, 45]), researchers intentionally considered nonlinear designs (e.g., via appropriate placement of magnets) for increasing the coupling range between the excitation and the system, and therefore, for enhancing the efficiency and energy output of the harvester (e.g., [46, 47]).

Further, many energy harvesters operate in tandem with structures and civil infrastructure systems, which are subjected to environmental excitations that have random and even time-varying characteristics. Thus, researchers have recently realized the need for modeling the excitations as stochastic processes [48, 49, 50, 51, 52]. Moreover, it has been shown that experimentally collected impedance data related to various energy storage systems can be best represented by fractional derivative modeling (e.g., [53, 54]). In this regard, there have been efforts to propose enhanced versions of the energy harvester coupled electromechanical equations by incorporating fractional derivative elements (e.g., [55, 56]).

Regarding design and optimization of energy harvesters for maximizing energy output, this has been done primarily by considering deterministic harmonic excitations (e.g., [57]), whereas the few papers referring to stochastic excitations employ almost exclusively the maximization of mean harvested power as the optimization criterion [58, 59, 60]. However, as also highlighted in [61, 18], it is clear that consideration of additional restrictions and constraints related to low probability events is necessary for avoiding, for instance, equipment failures. Such constraints may relate to the probability that the voltage and/or the displacement stay within prescribed limits, while their inclusion in the energy harvester optimization problem can lead, potentially, to a more robust and efficient design than what is currently the norm; see also [18] for a more detailed discussion. Thus, advanced stochas-

tic dynamics techniques are required, capable of determining the joint response probability density function (PDF) to be used in the constrained optimization problem of such energy harvesting systems. Obviously, utilization of approximate techniques, such as the widely employed standard statistical linearization [60, 62, 63], which yield only first- and second-order response statistics (i.e., mean and standard deviation) is inadequate for optimization subject to low probability constraints.

In Chapter 5 of this thesis, a methodology based on the Wiener path integral (WPI) technique (e.g., [16, 17, 21, 64, 23]) is developed for stochastic response analysis and optimization of a class of energy harvesters exhibiting asymmetric nonlinearities and endowed with fractional derivative elements. Specifically, the WPI technique is appropriately adapted herein to be used in conjunction with a constrained optimization algorithm for determining efficiently the optimal parameters of the energy harvester. This analysis can be construed as an extension of the work in [18] to account for fractional derivative terms in the governing equations. Further, in comparison to [18], the overall complexity of the constrained optimization problem is increased not only because of the more sophisticated modeling based on fractional derivatives, but also due to considering an augmented higher dimensional vector of optimization variables. Moreover, regarding the reliability-based probabilistic constraint, which is considered in the optimization problem, a rather pragmatic definition is proposed herein for cases referring to space limitations. Several numerical examples are included, while comparisons with pertinent Monte Carlo simulation (MCS) data demonstrate the reliability and robustness of the methodology.

1.2 Applications of computational algebraic geometry in engineering mechanics

1.2.1 Computational algebraic geometry and Gröbner bases

Computational methods that exploit results from algebraic geometry have flourished in recent years and provide powerful tools for the analysis of mathematical problems via computational algebra frameworks. Two prominent results in this direction are Hilbert's

basis theorem and Hilbert's Nullstellensatz, which form the basis of the relationship between algebraic geometry and commutative algebra, and have been exploited in [65, 66, 67, 68] to lay the foundations of computational algebraic geometry. These contributions aided the development of several computer algebra systems such as Mathematica, Macaulay2, Maple, MuPAD, etc., which have significantly influenced a wide range of scientific research fields. However, the great majority of researchers, utilize these tools in a "black box" manner, which prevents possible adaptations of the aformentioned techniques to the unique characteristics of a specific problem of interest.

In Chapter 6 of this thesis, a computational algebraic geometry technique is described which is based on the concept of a Gröbner basis and is capable of obtaining all solutions of an algebraic system of polynomial equations. This is achieved by exploiting the remainders of the division between the system of polynomial equations by the Gröbner basis associated with this system, and constructing multiplication matrices for each monomial in the system. Next, the solutions of the polynomial system are obtained as the real eigenvalues of these matrices. Therefore, this approach is exact, except the final step, i.e., the calculation of the eigenvalues, which is performed numerically. The interested reader is directed to the books [69, 70, 71, 72, 73]) for further detailed information. In general, the Gröbner basis, which was introduced relatively recently, appears very promising for the theoretical study of a wide range of problems in engineering mechanics, e.g., the existence of solutions in the statistical linearization and in general any problem that requires exact solutions of polynomial systems of equations.

1.2.2 Demonstrating convexity of the WPI most probable path optimization problem

Clearly, a wide range of numerical optimization schemes can be employed for determining the WPI most probable path (e.g., [25, 22]) via the Rayleigh–Ritz solution technique. However, there is generally no guarantee that the selected optimization algorithm converges to the global minimum (instead of a local minimum). Of course, it can be argued that the

relatively high accuracy degree exhibited by the WPI technique, based on comparisons with pertinent MCS data in a plethora of numerical examples (e.g., [18, 22]), can be construed as an indication of determining successfully the optimal most probable path. Nevertheless, it becomes clear that there is a need for pursuing the challenging task of proving the existence of a unique global minimum and/or the convexity of the objective function corresponding to an arbitrary nonlinear system under consideration.

In Chapter 7 of this thesis, demonstration of the potential convexity (and thus, the existence of a global extremum) of the objective function to be minimized is addressed by resorting to the computational algebraic geometry concepts and tools such as Gröbner bases, presented in Chapter 6. Various numerical examples pertaining to diverse nonlinear oscillators are considered, where it is proved that the associated objective functions are convex, and that the proposed Newton's scheme converges to the globally optimum most probable path. Comparisons with MCS-based estimates are included as well for demonstrating the reliability of the WPI technique.

1.2.3 Nonlinear normal modes (NNMs)

Effective analysis and design of complex multi-degree-of-freedom (MDOF) dynamical systems encountered in structural/mechanical applications requires a thorough understanding of their vibratory response characteristics. Linear normal modes (LNMs) is a central concept in linear vibration theory, because they are characterized by a fundamental physical interpretation and exhibit interesting mathematical properties. Specifically, LNM can be employed to decouple the equations of motion into a set of linear equations that are independent of each other. Moreover, normal motions are characterized by invariance, i.e., if a motion is initiated on a specific LNM, the rest of the LNMs remain quiescent. Further, the principle of superposition is applicable which means that any general motion of the system (free or forced) can be expressed as a linear combination of individual LNM motions. These facts, have rendered the concept of LNMs extremely popular among researchers and practitioners

in the diverse areas related to engineering dynamics.

In several situations however, the amplitude of vibration might extend beyond the approximately linear regime. Moreover, a plethora of dynamical systems exhibit inherently nonlinear behavior even in the vicinity of the equilibrium points. Under these circumstances, nonlinear equations of motion are required to capture the system dynamics accurately, whereas any attempt to apply traditional linear analysis would lead to large errors and suboptimal designs. In this regard, research in nonlinear vibrations has focused on systems with few degrees of freedom, e.g., lumped-mass models and models obtained via a Galerkin discretization of the governing partial differential equations. These low-order models are useful in describing the general behavior of nonlinear dynamical systems, but they lack of rigorous analytical and broadly applicable tools for extracting the fundamental characteristics of the associated nonlinear motions.

In this context, the concept of nonlinear normal modes (NNMs) has been proposed, as a generalization of its linear counterpart. NNMs, which offer a solid theoretical tool for the study of the complex dynamical phenomena associated to nonlinear systems, were pioneered by Rosenberg [74, 75, 76], where attention was directed toward conservative systems with symmetric nonlinearities. Further studies include [77, 78], whereas NNMs were extended to a wide class of non-conservative systems by Shaw and Pierre [79, 1, 80, 81] and Vakakis [82, 83]. Ever since, nonlinear modal analysis has been employed in various applications in structural mechanics [84, 85], mechanical vibrations [86, 87, 88, 89], dynamic testing [90, 91] and system identification [92]. For further information the interested reader is directed to the books [93, 94] and review papers [95, 96].

Obtaining the NNMs of a nonlinear system is typically reduced to determining all solutions of a nonlinear algebraic system of equations, which often takes the form of a polynomial system of equations. Even though numerical methods for the continuation of periodic solutions (e.g., [97]) have been shown to be relatively efficient and accurate in practice, they do not provide guarantees that the algorithm converges to the desired solution. On the con-

trary, under the assumption that the nonlinear system of algebraic equations is of polynomial form, recent advances in computational algebraic geometry [73] in conjunction with the ever increasing computational power of modern computers, may be employed to determine the NNMs in an exact manner. In this regard, in Chapter 8 of the thesis, the formulation of [1] is adopted and described in Sec. 8.1. Next, all solutions of the corresponding polynomial system of equations are obtained via the computational algebraic geometry technique based on the concept of Gröbner bases, which is presented in Chapter 6. Finally, several examples are presented in Sec. 8.2, where the order of the polynomial expansions of [1] is increased for improved accuracy and the technique is applied to a 3-DOF system, demonstrating its potential applicability to relatively high dimentional problems. Moreover, strong indications have been identified that the form of the corresponding Gröbner basis could provide significant insight about the nonlinear system under study, including information about the coupling between nonlinear normal modes and the complexity of the corresponding computation.

Part I

Wiener path integral technique

Chapter 2: Wiener path integral formalism

2.1 Theoretical aspects

2.1.1 Preliminaries

This section serves as a brief overview of several aspects of the theory of SDEs and the associated Chapman-Kolmogorov (C-K) and Fokker-Plank (F-P) equations. In this regard, consider a multi-dimensional first-order SDE of the general form

$$\dot{\boldsymbol{\alpha}} = \mathbf{A}(\boldsymbol{\alpha}, t) + \mathbf{B}(\boldsymbol{\alpha}, t)\boldsymbol{\eta}(t) \tag{2.1}$$

where the dot above a variable denotes differentiation with respect to time t and $\boldsymbol{\eta}(t)$ is a zero-mean and delta-correlated process of intensity one; i.e., $\mathbb{E}[\boldsymbol{\eta}(t)] = \mathbf{0}$ and $\mathbb{E}[\boldsymbol{\eta}(t)\boldsymbol{\eta}^{\mathrm{T}}(t+\tau)] = \mathbf{I}\delta(\tau)$ where $\mathbf{I}$ is the identity matrix, and $\delta(t)$ is the Dirac delta function. Certain existence and uniqueness conditions related to Eq. (2.1) dictate that the solution $\boldsymbol{\alpha} = [\alpha_j]_{n\times 1}$ is a Markov stochastic vector process [98, 99], for which the C-K equation (e.g., [100])

$$p(\boldsymbol{\alpha}_{i+1}, t_{i+1}|\boldsymbol{\alpha}_{i-1}, t_{i-1}) = \int_{-\infty}^{\infty} p(\boldsymbol{\alpha}_{i+1}, t_{i+1}|\boldsymbol{\alpha}_i, t_i)p(\boldsymbol{\alpha}_i, t_i|\boldsymbol{\alpha}_{i-1}, t_{i-1})\mathrm{d}\boldsymbol{\alpha}_i \tag{2.2}$$

is satisfied for any $t_{i-1} < t_i < t_{i+1}$. In Eq. (2.2), $\boldsymbol{\alpha}_i = \boldsymbol{\alpha}(t_i)$ and $p(\boldsymbol{\alpha}_{i+1}, t_{i+1}|\boldsymbol{\alpha}_{i-1}, t_{i-1})$ denotes the transition PDF of the process $\boldsymbol{\alpha}(t)$. Next, if $\mathbf{A}$ and $\mathbf{B}$ are continuous functions of t, then $\boldsymbol{\alpha}$ is a diffusion process [98] and the following conditions hold true for any $\varepsilon > 0$ (e.g., [99,

101]), i.e.,

$$i) \quad \lim_{\Delta t \to 0} \int\limits_{|\boldsymbol{\alpha}_{i+1}-\boldsymbol{\alpha}_i|<\varepsilon} p(\boldsymbol{\alpha}_{i+1}, t_{i+1}|\boldsymbol{\alpha}_i, t_i)\mathrm{d}\boldsymbol{\alpha}_{i+1} = 0 \tag{2.3}$$

$$ii) \quad \lim_{\Delta t \to 0} \int\limits_{|\boldsymbol{\alpha}_{i+1}-\boldsymbol{\alpha}_i|<\varepsilon} (\boldsymbol{\alpha}_{i+1}-\boldsymbol{\alpha}_i) p(\boldsymbol{\alpha}_{i+1}, t_{i+1}|\boldsymbol{\alpha}_i, t_i)\mathrm{d}\boldsymbol{\alpha}_{i+1} = \mathbf{A}(\boldsymbol{\alpha}_i, t_i) \tag{2.4}$$

$$iii) \quad \lim_{\Delta t \to 0} \int\limits_{|\boldsymbol{\alpha}_{i+1}-\boldsymbol{\alpha}_i|<\varepsilon} (\boldsymbol{\alpha}_{i+1}-\boldsymbol{\alpha}_i)(\boldsymbol{\alpha}_{i+1}-\boldsymbol{\alpha}_i)^{\mathrm{T}} p(\boldsymbol{\alpha}_{i+1}, t_{i+1}|\boldsymbol{\alpha}_i, t_i)\mathrm{d}\boldsymbol{\alpha}_{i+1} = \mathbf{B}(\boldsymbol{\alpha}_i, t_i)\mathbf{B}^{\mathrm{T}}(\boldsymbol{\alpha}_i, t_i) \tag{2.5}$$

where $\Delta t = t_{i+1} - t_i$. Further, employing the C-K Eq. (2.2) leads to the F-P Eq. (2.6) for the transition PDF $p = p(\boldsymbol{\alpha}_{i+1}, t_{i+1}|\boldsymbol{\alpha}_i, t_i)$, i.e.,

$$\frac{\partial p}{\partial t} = -\sum_j \frac{\partial}{\partial \alpha_j}\left(A_j(\boldsymbol{\alpha}, t)p\right) + \frac{1}{2}\sum_{j,k} \frac{\partial^2}{\partial \alpha_j \partial \alpha_k}\left(\tilde{B}_{jk}(\boldsymbol{\alpha}, t)p\right) \tag{2.6}$$

where $\mathbf{A}(\boldsymbol{\alpha}, t) = [A_j(\boldsymbol{\alpha}, t)]_{n\times 1}$ is the drift vector, and $\tilde{\mathbf{B}}(\boldsymbol{\alpha}, t) = [\tilde{B}_{jk}(\boldsymbol{\alpha}, t)]_{n\times n} := \mathbf{B}(\boldsymbol{\alpha}, t)\mathbf{B}^{\mathrm{T}}(\boldsymbol{\alpha}, t)$ denotes the diffusion matrix (e.g., [98, 99, 102]), which is symmetric and positive semidefinite.

2.1.2 Wiener path integral and Lagrangian function

In this section, basic WPI formalism aspects are presented for completeness. The interested reader is directed to [103, 15, 104, 105, 106] for more details. In the limit $\Delta t \to 0$, and assuming a non-singular diffusion matrix $\tilde{\mathbf{B}}$, the transition PDF associated with a diffusion process $\boldsymbol{\alpha}(t)$ has been shown to admit a Gaussian distribution (e.g., [102]) of the form

$$p(\boldsymbol{\alpha}_{i+1}, t_{i+1}|\boldsymbol{\alpha}_i, t_i) = \left[\sqrt{(2\pi\Delta t)^n \det\left[\tilde{\mathbf{B}}(\boldsymbol{\alpha}_i, t_i)\right]}\right]^{-1} \times \ldots$$
$$\exp\left(-\frac{1}{2}\frac{\left[\boldsymbol{\alpha}_{i+1} - \boldsymbol{\alpha}_i - \Delta t\mathbf{A}(\boldsymbol{\alpha}_i, t_i)\right]^{\mathrm{T}}\left[\tilde{\mathbf{B}}(\boldsymbol{\alpha}_i, t_i)\right]^{-1}\left[\boldsymbol{\alpha}_{i+1} - \boldsymbol{\alpha}_i - \Delta t\mathbf{A}(\boldsymbol{\alpha}_i, t_i)\right]}{\Delta t}\right) \tag{2.7}$$

In passing, it is noted that the choice of Eq. (2.7) is not restrictive, and alternative non-Gaussian distributions can also be employed (e.g., [107, 108]). Next, the probability that $\boldsymbol{\alpha}(t)$ follows a specific path $\bar{\boldsymbol{\alpha}}(t)$ can be expressed as the limiting case of the probability of the compound event

$$P[\bar{\boldsymbol{\alpha}}(t)] = \lim_{\substack{\Delta t\to 0\\ N\to\infty}} P\left[\bigcap_{i=1}^{N}\left\{\boldsymbol{\alpha}_i \in \left[\bar{\boldsymbol{\alpha}}_i, \bar{\boldsymbol{\alpha}}_i + [\mathrm{d}\alpha_{ji}]_{n\times 1}\right]\right\}\right] \tag{2.8}$$

In Eq. (2.8), the time is discretized into N time points (slices) Δt apart, while $\mathrm{d}\alpha_{ji}$ denotes the infinitesimal element along dimension j at time t_i. Loosely speaking, Eq. (2.8) represents the probability of the process to propagate through the infinitesimally thin tube surrounding $\bar{\boldsymbol{\alpha}}(t)$. In the following, considering deterministic initial conditions, and employing Eq. (2.7) and the Markovian property of $\boldsymbol{\alpha}(t)$, Eq. (2.8) becomes

$$\begin{aligned}
P[\bar{\boldsymbol{\alpha}}(t)] &= \lim_{\substack{\Delta t\to 0\\ N\to\infty}} \left\{\prod_{i=1}^{N} p(\bar{\boldsymbol{\alpha}}_{i+1}, t_{i+1}|\bar{\boldsymbol{\alpha}}_i, t_i)\prod_{j=1}^{n}\mathrm{d}\alpha_{ji}\right\}\\
&= \lim_{\substack{\Delta t\to 0\\ N\to\infty}} \left\{\left[\prod_{i=1}^{N}\left(\left[\sqrt{(2\pi\Delta t)^n \det\left[\tilde{\mathbf{B}}(\bar{\boldsymbol{\alpha}}_i, t_i)\right]}\right]^{-1}\prod_{j=1}^{n}\mathrm{d}\alpha_{ji}\right)\right]\times\ldots\right.\\
&\left.\exp\left(-\frac{1}{2}\sum_{i=1}^{N}\frac{\left[\bar{\boldsymbol{\alpha}}_{i+1}-\bar{\boldsymbol{\alpha}}_i-\Delta t\mathbf{A}(\bar{\boldsymbol{\alpha}}_i,t_i)\right]^{\mathrm{T}}\left[\tilde{\mathbf{B}}(\bar{\boldsymbol{\alpha}}_i,t_i)\right]^{-1}\left[\bar{\boldsymbol{\alpha}}_{i+1}-\bar{\boldsymbol{\alpha}}_i-\Delta t\mathbf{A}(\bar{\boldsymbol{\alpha}}_i,t_i)\right]}{\Delta t}\right)\right\}\\
&= \exp\left(-\int_{t_0}^{t_f}\mathcal{L}(\bar{\boldsymbol{a}},\dot{\bar{\boldsymbol{a}}})\mathrm{d}t\right)\prod_{t=t_0}^{t_f}\mathrm{d}\boldsymbol{a}(t)
\end{aligned} \tag{2.9}$$

where

$$\mathcal{L}(\boldsymbol{\alpha},\dot{\boldsymbol{\alpha}}) = \frac{1}{2}\left[\dot{\boldsymbol{\alpha}}-\mathbf{A}(\boldsymbol{\alpha},t)\right]^{\mathrm{T}}\left[\tilde{\mathbf{B}}(\boldsymbol{\alpha},t)\right]^{-1}\left[\dot{\boldsymbol{\alpha}}-\mathbf{A}(\boldsymbol{\alpha},t)\right] \tag{2.10}$$

denotes the Lagrangian of the system and $\prod_{t=t_0}^{t_f}\mathrm{d}\boldsymbol{a}(t)$ is a functional measure given by

$$\prod_{t=t_0}^{t_f}\mathrm{d}\boldsymbol{a}(t) = \prod_{j=1}^{n}\prod_{t=t_0}^{t_f}\frac{\mathrm{d}a_j(t)}{\sqrt{2\pi\left(\det\left[\tilde{\mathbf{B}}(\bar{\boldsymbol{a}},t)\right]\right)^{\frac{1}{n}}\mathrm{d}t}} \tag{2.11}$$

The interested reader is also directed to [22, 20] for more details. Further, the total probability that the process $\boldsymbol{a}$ starts from $\boldsymbol{a}_0$ at time t_0 and ends up at $\boldsymbol{a}_f$ at t_f takes the form of a functional integral, which "sums up" the probabilities associated with each and every path that $\boldsymbol{a}$ can possibly follow (e.g., [15]). In this regard, denoting by $C\{\boldsymbol{a}_0, t_0; \boldsymbol{a}_f, t_f\}$ the set of all paths with initial state $\boldsymbol{a}_0$ at time t_0 and final state $\boldsymbol{a}_f$ at time t_f, the transition PDF is expressed as a functional integral (or Wiener path integral) in the form

$$p(\boldsymbol{a}_f, t_f|\boldsymbol{a}_0, t_0) = \int\limits_{C\{\boldsymbol{a}_0,t_0;\boldsymbol{a}_f,t_f\}} \exp\left(-\int_{t_0}^{t_f} \mathcal{L}\left(\boldsymbol{a}, \dot{\boldsymbol{a}}\right) \mathrm{d}t\right) \prod_{t=t_0}^{t_f} \mathrm{d}\boldsymbol{a}(t) \tag{2.12}$$

2.1.3 Most probable path approximation

Considering the significant challenges related to evaluating (2.12) analytically or numerically, researchers have ordinarily resorted to the following approximate technique, also referred to in the path integral literature as semi-classical approximation (e.g., [15]). Specifically, note that the largest contribution to the functional integral of (2.12) comes from the trajectory $\bar{\boldsymbol{a}}(t)$ for which the integral in the exponential (also known as stochastic action) becomes as small as possible (e.g., [15]). This leads to the variational problem

$$\text{minimize} \quad \int_{t_0}^{t_f} \mathcal{L}\left(\boldsymbol{a}, \dot{\boldsymbol{a}}\right) \mathrm{d}t \tag{2.13}$$

The trajectory $\bar{\boldsymbol{a}}(t)$ satisfying (2.13) is also known as the "most probable path" and can be used in conjunction with (2.12) for determining approximately a specific point of the system response transition PDF, i.e.,

$$p(\boldsymbol{a}_f, t_f|\boldsymbol{a}_0, t_0) \approx C \ \exp\left(-\int_{t_0}^{t_f} \mathcal{L}\left(\bar{\boldsymbol{a}}, \dot{\bar{\boldsymbol{a}}}\right) \mathrm{d}t\right) \tag{2.14}$$

where C is a normalization constant. Clearly, the most probable path $\bar{\boldsymbol{a}}(t)$ is the extremal that minimizes the functional in (2.13). According to the fundamental theorem of calculus of variations [109], $\bar{\boldsymbol{a}}(t)$ can be evaluated by employing the necessary condition that the first variation of the functional vanishes. Considering fixed initial and final conditions at t_0 and t_f, respectively, this condition leads to a multivariate boundary value problem (BVP) of the form

$$\mathcal{L}_{a_j} - \frac{\mathrm{d}}{\mathrm{d}t}\mathcal{L}_{\dot{a}_j} = 0 \qquad j = 1, ..., n \tag{2.15}$$

$$a_j(t_0) = a_{j,0}, \quad a_j(t_f) = a_{j,f} \qquad j = 1, ..., n \tag{2.16}$$

where $\mathcal{L}_{a_j}$ and $\mathcal{L}_{\dot{a}_j}$ denote the derivatives of the Lagrangian with respect to a_j and $\dot{a}_j$, respectively. (2.15) represents the Euler–Lagrange (E-L) equations and (2.16) relates to the fixed boundary conditions.

2.2 WPI formulation for second order SDEs

In this section, the formulation delineated in Sections 2.1.2 and 2.1.3 is adapted to account for systems whose dynamics is governed by second-order SDEs; see also [17, 20] for more details. Such cases include structural and/or mechanical dynamical systems with inertia terms in the respective equations of motion, which are generally modeled as a set of n coupled nonlinear second-order SDEs of the form

$$\mathbf{M}\ddot{\boldsymbol{x}} + \boldsymbol{g}(\boldsymbol{x}, \dot{\boldsymbol{x}}, t) = \boldsymbol{w}(t) \tag{2.17}$$

In Eq. (2.17), $\boldsymbol{x} = [x_j(t)]_{n\times 1}$ is the system response displacement vector; $\mathbf{M}$ represents the $n \times n$ mass matrix; $\boldsymbol{g} = [g_j(\boldsymbol{x}, \dot{\boldsymbol{x}}, t)]_{n\times 1}$ is an arbitrary nonlinear vector-valued function, which can account also for hysteretic response behaviors; and $\boldsymbol{w}$ is a white noise stochastic excitation vector process with $\mathbb{E}[\boldsymbol{w}(t)] = \mathbf{0}$ and $\mathbb{E}[\boldsymbol{w}(t)\boldsymbol{w}^{\mathrm{T}}(t-\tau)] = \mathbf{D}\delta(\tau)$, where $\mathbf{D} \in \mathbb{R}^{n\times n}$ is a deterministic coefficient matrix.

Next, introducing a new variable $\boldsymbol{v} = \dot{\boldsymbol{x}}$, Eq. (2.17) can be cast, equivalently, into the

form of Eq. (2.1) with

$$\boldsymbol{\alpha} = \begin{bmatrix} \boldsymbol{x} \\ \boldsymbol{v} \end{bmatrix}, \quad \boldsymbol{A}(\boldsymbol{\alpha}, t) = \begin{bmatrix} \boldsymbol{v} \\ -\mathbf{M}^{-1}\boldsymbol{g}(\boldsymbol{x}, \boldsymbol{v}, t) \end{bmatrix} \quad \text{and} \quad \mathbf{B}(\boldsymbol{\alpha}, t) = \mathbf{B} = \begin{bmatrix} \mathbf{0} & \mathbf{0} \\ \mathbf{0} & \mathbf{M}^{-1}\sqrt{\mathbf{D}} \end{bmatrix} \tag{2.18}$$

where the square root of matrix $\mathbf{D}$ is given by $\sqrt{\mathbf{D}}\sqrt{\mathbf{D}}^{\mathrm{T}} = \mathbf{D}$. Clearly, the diffusion matrix $\tilde{\mathbf{B}} = \mathbf{B}\mathbf{B}^{\mathrm{T}}$ is singular (see Eq. (2.18)), and thus, the expression in Eq. (2.10) cannot be evaluated in a straightforward manner. Nevertheless, this limitation due to the singularity of $\tilde{\mathbf{B}}$ can be addressed by introducing delta-functionals to enforce the compatibility equation $\dot{\boldsymbol{x}} = \boldsymbol{v}$ (e.g., [15, 104, 20]). In particular, defining $\boldsymbol{S}(\boldsymbol{x}, \boldsymbol{v}, \dot{\boldsymbol{v}}) = \dot{\boldsymbol{v}} + \mathbf{M}^{-1}\boldsymbol{g}(\boldsymbol{x}, \boldsymbol{v}, t)$ the transition PDF of $\boldsymbol{\alpha}$ given by Eq. (2.12) becomes

$$\begin{aligned} p(\boldsymbol{\alpha}_f, t_f | \boldsymbol{\alpha}_0, t_0) = \int\limits_{C\{\boldsymbol{x}_0, \boldsymbol{v}_0, t_0; \boldsymbol{x}_f, \boldsymbol{v}_f, t_f\}} \exp\left(-\int\limits_{t_0}^{t_f} \frac{1}{2} \left[\mathbf{M}\boldsymbol{S}(\boldsymbol{x}, \boldsymbol{v}, \dot{\boldsymbol{v}})\right]^{\mathrm{T}} \mathbf{D}^{-1} \left[\mathbf{M}\boldsymbol{S}(\boldsymbol{x}, \boldsymbol{v}, \dot{\boldsymbol{v}})\right] \mathrm{d}t \right) \times \ldots \\ \delta\left[\dot{\boldsymbol{x}} - \boldsymbol{v}\right] \prod_{t=t_0}^{t_f} \mathrm{d}\boldsymbol{x}(t) \prod_{t=t_0}^{t_f} \mathrm{d}\boldsymbol{v}(t) \end{aligned} \tag{2.19}$$

For the derivation of Eq. (2.19), the relationship $\left(\mathbf{M}^{-1}\mathbf{D}\mathbf{M}^{-\mathrm{T}}\right)^{-1} = \mathbf{M}^{\mathrm{T}}\mathbf{D}^{-1}\mathbf{M}$ for an arbitrary non-singular square matrix $\mathbf{D}$ has been taken into account. Following integration over all paths $\boldsymbol{v}(t)$, and adopting for convenience in the ensuing analysis the notation $\boldsymbol{g}(\boldsymbol{x}, \dot{\boldsymbol{x}}, t) = \boldsymbol{g}(\boldsymbol{x}, \dot{\boldsymbol{x}})$, Eq. (2.19) becomes

$$p(\boldsymbol{x}_f, \dot{\boldsymbol{x}}_f, t_f | \boldsymbol{x}_0, \dot{\boldsymbol{x}}_0, t_0) = \int\limits_{C\{\boldsymbol{x}_0, \dot{\boldsymbol{x}}_0, t_0; \boldsymbol{x}_f, \dot{\boldsymbol{x}}_f, t_f\}} \exp\left(-\int\limits_{t_0}^{t_f} \mathcal{L}(\boldsymbol{x}, \dot{\boldsymbol{x}}, \ddot{\boldsymbol{x}}) \mathrm{d}t \right) \prod_{t=t_0}^{t_f} \mathrm{d}\boldsymbol{x}(t) \tag{2.20}$$

where

$$\mathcal{L}(\boldsymbol{x}, \dot{\boldsymbol{x}}, \ddot{\boldsymbol{x}}) = \frac{1}{2} \left[\mathbf{M}\ddot{\boldsymbol{x}} + \boldsymbol{g}(\boldsymbol{x}, \dot{\boldsymbol{x}})\right]^{\mathrm{T}} \mathbf{D}^{-1} \left[\mathbf{M}\ddot{\boldsymbol{x}} + \boldsymbol{g}(\boldsymbol{x}, \dot{\boldsymbol{x}})\right] \tag{2.21}$$

Note that the form of Eqs. (2.19)-(2.21) can accommodate also cases of singular mass matrices

M. This may be the case, for instance, when considering hysteresis models (e.g., Bouc-Wen) that employ auxiliary additional state variables governed by first-order only equations (e.g., [10]). These first-order equations can be directly cast into the form of Eq. (2.1), whereas inversion pertains to the non-singular part of M only; see also Sec. 4.3.2.

Further, it is readily seen that the singularity of the diffusion matrix $\tilde{\mathbf{B}}$, encountered due to the state-variable reformulation of the second-order Eq. (2.17) into the first-order Eq. (2.18), has been addressed in a rather direct and straightforward manner by the introduction of the delta-functional. Specifically, owning to the simple form of the compatibility equation $\dot{\boldsymbol{x}} = \boldsymbol{v}$ between the original variable and the state variable, functional integration over the state variable $\boldsymbol{v}$ is performed in a direct (and rather trivial) manner. However, singular diffusion matrices $\tilde{\mathbf{B}}$ due to reasons other than state-variable reformulation (e.g., cases of systems with only some of their DOFs excited, hysteresis modeling via additional auxiliary state equations, energy harvesters with coupled electro-mechanical equations, etc.) are not amenable, in general, to a similar trivial treatment. This is due to the significantly more complex form of the corresponding (compatibility) equations related to the singularities, and thus, a direct functional integration is not possible. To address this challenge, the WPI-based solution technique is generalized and extended in Chapter 4 by relying on a constrained variational formulation that can account for arbitrary forms of (compatibility) equations related to singular diffusion matrices.

2.2.1 Most probable path and Euler–Lagrange equations

Next, the most probable path approximation presented in Sec. 2.1.3 is extended to second-order systems for approximating the WPI in Eq. (2.20). Specifically, the largest contribution to the functional integral of Eq. (2.20) comes from the trajectory $\bar{\boldsymbol{x}}(t)$ for which the integral in the exponential, also known as stochastic action, is minimized (e.g., [15]). According to calculus of variations (e.g., [110, 111]) this trajectory $\bar{\boldsymbol{x}}(t)$ with fixed endpoints satisfies the

extremality condition

$$\delta \int_{t_0}^{t_f} \mathcal{L}(\boldsymbol{x}, \dot{\boldsymbol{x}}, \ddot{\boldsymbol{x}}) \mathrm{d}t = 0 \tag{2.22}$$

which leads to the Euler–Lagrange (E-L) equations

$$\mathcal{L}_{x_j} - \frac{\mathrm{d}}{\mathrm{d}t}\mathcal{L}_{\dot{x}_j} + \frac{\mathrm{d}^2}{\mathrm{d}t^2}\mathcal{L}_{\ddot{x}_j} = 0, \quad j = 1, ..., n \tag{2.23}$$

with the set of boundary conditions

$$\begin{aligned} &x_j(t_0) = x_{j,0} \quad \dot{x}_j(t_0) = \dot{x}_{j,0} \\ &x_j(t_f) = x_{j,f} \quad \dot{x}_j(t_f) = \dot{x}_{j,f} \end{aligned} \qquad j = 1, ..., n \tag{2.24}$$

Next, solving Eqs. (2.23)-(2.24) yields the n-dimensional most probable path, $\bar{\boldsymbol{x}}(t)$, and thus, a single point of the system response transition PDF is determined as [17]

$$p(\boldsymbol{x}_f, \dot{\boldsymbol{x}}_f, t_f | \boldsymbol{x}_0, \dot{\boldsymbol{x}}_0, t_0) \approx C \ \exp\left(- \int_{t_0}^{t_f} \mathcal{L}(\bar{\boldsymbol{x}}, \dot{\bar{\boldsymbol{x}}}, \ddot{\bar{\boldsymbol{x}}}) \mathrm{d}t \right) \tag{2.25}$$

where C is a normalization constant. It can be readily seen by comparing Eqs. (2.20) and (2.25) that in the approximation of Eq. (2.25) only one trajectory, i.e., the most probable path $\bar{\boldsymbol{x}}(t)$, is considered in evaluating the path integral of Eq. (2.20). Regarding the degree of approximation associated with Eq. (2.25), direct comparisons of Eq. (2.25) with pertinent MCS data related to various engineering dynamical systems have demonstrated satisfactory accuracy (e.g., [20, 23, 21, 19, 18, 24]).

2.3 WPI solution treatment

The determination of the most probable path is achieved by either solving the BVP defined by the Euler–Lagrange equations (2.23) and (2.24) numerically, or by employing the Rayleigh–Rirtz direct solution technique. The system response PDF can be subsequently

evaluated via Eq. (2.25).

2.3.1 Numerical solution of the Euler–Lagrange equations

The solution of the Euler–Lagrange equations (2.23) and (2.24) can be accomplished by employing numerical methods for BVPs (see e.g., [112]). Such methods include different finite differences schemes [113], collocation methods [114] and the shooting method [115], which provide relatively stable and robust numerical schemes that are readily available in various open source and commercial software packages; see, for instance, [116] for the Matlab built in function bvp4c.

2.3.2 Rayleigh–Ritz solution technique for the most probable path

In general, Eqs. (2.23)-(2.24) cannot be solved analytically for the most probable path. Therefore, resorting to numerical solution schemes for boundary value problems (BVPs) is often necessary. Indicatively, since $\bar{\boldsymbol{x}}$ is the solution of the variational problem

$$\text{minimize} \quad \mathcal{J}(\boldsymbol{x}, \dot{\boldsymbol{x}}, \ddot{\boldsymbol{x}}) = \int_{t_0}^{t_f} \mathcal{L}(\boldsymbol{x}, \dot{\boldsymbol{x}}, \ddot{\boldsymbol{x}}) \mathrm{d}t \tag{2.26}$$

or, in other words, an extremum for the functional $\mathcal{J}$, a direct functional minimization formulation can be employed in conjunction with a standard Rayleigh–Ritz solution technique (see [64, 23, 117]). In this regard, $\boldsymbol{x}(t)$ is approximated by

$$\hat{\boldsymbol{x}}(t) = \boldsymbol{\psi}(t) + \mathbf{Z}\boldsymbol{h}(t) \approx \boldsymbol{x}(t) \tag{2.27}$$

The function $\boldsymbol{\psi}(t)$ is chosen so that it satisfies the boundary conditions, while the trial functions $\boldsymbol{h}(t) = [h_l(t)]_{L\times 1}$ should vanish at the boundaries, i.e., $\boldsymbol{h}(t_0) = \boldsymbol{h}(t_f) = \mathbf{0}$; $\mathbf{Z} \in \mathbb{R}^{n\times L}$ is a coefficient matrix and L is the chosen number of trial functions considered. Utilizing a

vectorized form of $\mathbf{Z}$, Eq. (2.27) is cast, equivalently, as

$$\hat{\boldsymbol{x}}(t) = \boldsymbol{\psi}(t) + \mathbf{H}(t)\boldsymbol{z} \tag{2.28}$$

with

$$\boldsymbol{z} = \begin{bmatrix} Z_1^{\mathrm{T}} \\ Z_2^{\mathrm{T}} \\ \vdots \\ Z_L^{\mathrm{T}} \end{bmatrix} \in \mathbb{R}^{nL} \quad \text{and} \quad \mathbf{H}(t) = \begin{bmatrix} \boldsymbol{h}^{\mathrm{T}}(t) & \mathbf{0} & \dots & \mathbf{0} \\ \mathbf{0} & \boldsymbol{h}^{\mathrm{T}}(t) & \dots & \mathbf{0} \\ \vdots & \vdots & \ddots & \vdots \\ \mathbf{0} & \mathbf{0} & \dots & \boldsymbol{h}^{\mathrm{T}}(t) \end{bmatrix} \tag{2.29}$$

where Z_l denotes the l^{th} row of matrix $\mathbf{Z}$ and $\mathbf{H}(t)$ is an $n \times nL$ time-dependent matrix. Clearly, there is a wide range of choices for functions $\boldsymbol{\psi}$ and $\boldsymbol{h}$. In the ensuing analysis, the Hermite interpolating polynomials

$$\psi_j(t) = \sum_{k=0}^{3} a_{j,k} t^k \tag{2.30}$$

are adopted, i.e., $\boldsymbol{\psi}(t) = [\psi_j(t)]_{n\times 1}$, where the $n\times 4$ coefficients $a_{j,k}$ are determined by the $n\times 4$ boundary conditions in Eq. (2.24). For the trial functions, the shifted Legendre polynomials given by the recursive formula

$$\ell_{q+1}(t) = \frac{2q+1}{q+1}\left(\frac{2t - t_0 - t_f}{t_f - t_0}\right)\ell_q(t) - \frac{q}{q+1}\ell_{q-1}(t), \quad q = 1, ..., L-1 \tag{2.31}$$

are employed, which are orthogonal in the interval $[t_0, t_f]$, with $\ell_0(t) = 1$; and $\ell_1(t) = (2t - t_0 - t_f)/(t_f - t_0)$. The trial functions take the form

$$h_l(t) = (t - t_0)^2(t - t_f)^2\ell_l(t) \tag{2.32}$$

where the factor $(t - t_0)^2(t - t_f)^2$ multiplies the l^{th}-order Legendre polynomial $\ell_l(t)$ to yield the l^{th} trial function $h_l(t)$. Note that $h_l(t)$ is a polynomial of order $l + 4$ and vanishes at the

boundaries. Clearly, each component $\hat{x}_j(t)$ of $\hat{\boldsymbol{x}}(t)$ in Eq. (2.27) is a polynomial of order up to $L+4$ in t .

A practical advantage of the Rayleigh–Ritz solution technique is that the variational problem (functional minimization) of Eq. (2.26) degenerates to an ordinary minimization problem of a function that depends on a finite number of variables [111]. Specifically, the functional $\mathcal{J}$, dependent on the n functions $\boldsymbol{x}(t)$ (and their time derivatives), is cast in the form

$$J(\boldsymbol{z}) := \mathcal{J}(\hat{\boldsymbol{x}}, \dot{\hat{\boldsymbol{x}}}, \ddot{\hat{\boldsymbol{x}}}) \tag{2.33}$$

which depends on a finite number of nL coefficients $\boldsymbol{z}$. The corresponding optimization problem takes the form

$$\min_{\boldsymbol{z}} J(\boldsymbol{z}) \tag{2.34}$$

Further, the extremality condition in Eq. (2.22) is replaced by the first-oder optimality condition

$$\nabla J(\boldsymbol{z}) = \mathbf{0} \tag{2.35}$$

which represents essentially a set of nL nonlinear algebraic equations that need to be solved numerically. Once the solution $\boldsymbol{z}^*$ of the optimization problem in Eq. (2.34) is obtained, the most probable path $\bar{\boldsymbol{x}}$ is determined via Eq. (2.28). Obviously, there is a wide range of standard numerical optimization schemes to be employed for obtaining the solution $\boldsymbol{z}^*$. Indicatively, these range from gradient based techniques (e.g., [25]) to rather heuristic global optimization methods (e.g., [118, 119]).

Linear oscillator: A closed-form exact solution case

It has been shown recently in [120] that, for the special case of linear systems under Gaussian white noise, the WPI most probable path approach summarized in Sec. 2.2 is amenable to analytical treatment. In fact, the E-L Eqs. (2.23)-(2.24) become linear and

can be solved analytically for the most probable path, which is substituted into Eq. (2.25) yielding a closed-form expression for the joint response transition PDF. Most importantly, it has been shown in [120] that the expression of Eq. (2.25) corresponding to linear systems is exact, and involves no approximations.

Nevertheless, despite the available exact analytical solution for the joint response PDF derived in [120], the Rayleigh-Ritz numerical solution approach is also considered in detail in the following for the case of linear systems. This is done intentionally as it provides the motivation and elucidates the rationale for developing a Newton's numerical optimization scheme in Sec. 2.3.2. Specifically, consider a linear system whose dynamics is described by Eq.(2.17) with

$$\boldsymbol{g}(\boldsymbol{x},\dot{\boldsymbol{x}},t) = \boldsymbol{g}_{lin}(\boldsymbol{x},\dot{\boldsymbol{x}}) := \mathbf{C}\dot{\boldsymbol{x}} + \mathbf{K}\boldsymbol{x} \tag{2.36}$$

where $\mathbf{C}$ and $\mathbf{K}$ denote the system damping and stiffness matrices, respectively. In this regard, the left hand-side of Eq. (2.17) can be represented by the linear differential operator $\mathbf{G}[\cdot]$ defined as

$$\mathbf{G} = \mathbf{M}\frac{\partial^2}{\partial t^2} + \mathbf{C}\frac{\partial}{\partial t} + \mathbf{K} \tag{2.37}$$

Next, for simplicity and without loss of generality, consider $\mathbf{D} = 2\pi S_0\mathbf{I}$, where $\mathbf{I}$ denotes the identity matrix. Substituting the expansion of Eq. (2.28) into the Lagrangian of Eq. (2.21), and taking into account Eq. (2.37), yields

$$\mathcal{L}(\boldsymbol{x},\dot{\boldsymbol{x}},\ddot{\boldsymbol{x}}) \approx L(\boldsymbol{z},t) = \frac{1}{2}\frac{1}{2\pi S_0}\Big[\mathbf{G}[\boldsymbol{\psi}] + \mathbf{G}[\mathbf{H}]\boldsymbol{z}\Big]^{\mathrm{T}}\Big[\mathbf{G}[\boldsymbol{\psi}] + \mathbf{G}[\mathbf{H}]\boldsymbol{z}\Big] \tag{2.38}$$

Further, expanding Eq. (2.38) and substituting into Eq. (2.33), the objective function takes the form

$$J(\boldsymbol{z}) = J_{lin}(\boldsymbol{z}) := \frac{1}{2\pi S_0}\left[\frac{1}{2}\boldsymbol{z}^{\mathrm{T}}\mathbf{Q}\boldsymbol{z} + \mathbf{b}^{\mathrm{T}}\boldsymbol{z}\right] + c \tag{2.39}$$

where the symmetric matrix $\mathbf{Q} \in \mathbb{R}^{nL \times nL}$ is given by

$$[\mathbf{Q}]_{kl} = \int_{t_0}^{t_f} \sum_{j=1}^{n} \Big[\mathbf{G}[\mathbf{H}]\Big]_{kj} \Big[\mathbf{G}[\mathbf{H}]\Big]_{jl} \mathrm{d}t, \quad k, l = 1, .., nL \tag{2.40}$$

the vector $\mathbf{b} \in \mathbb{R}^{nL}$ is determined as

$$[\mathbf{b}]_{l} = \int_{t_0}^{t_f} \sum_{j=1}^{n} \Big[\mathbf{G}[\psi]\Big]_{j} \Big[\mathbf{G}[\mathbf{H}]\Big]_{jl} \mathrm{d}t, \quad l = 1, .., nL \tag{2.41}$$

and the constant term c (i.e., independent of $\boldsymbol{z}$) is equal to

$$c = \frac{1}{2} \frac{1}{2\pi S_0} \int_{t_0}^{t_f} \mathbf{G}[\psi]^T \mathbf{G}[\psi] \mathrm{d}t \tag{2.42}$$

Clearly, for the optimization problem of Eq. (2.34) the multiplicative factor $\frac{1}{2\pi S_0}$ and the constant term c in the definition of the objective function of Eq. (2.39) do not affect the solution $\boldsymbol{z}^*$. Thus, Eq. (2.34) becomes, equivalently,

$$\min_{\boldsymbol{z}} \ \frac{1}{2} \boldsymbol{z}^{\mathrm{T}} \mathbf{Q} \boldsymbol{z} + \mathbf{b}^{\mathrm{T}} \boldsymbol{z} \tag{2.43}$$

Note that the objective function of Eq. (2.39) (or, alternatively, Eq. (2.43)) is not only quadratic, but also convex for positive definite symmetric matrices $\mathbf{Q}$ and its unique global minimizer is given by

$$\boldsymbol{z}^* = -\mathbf{Q}^{-1} \mathbf{b}. \tag{2.44}$$

Substituting this result into Eq. (2.28) yields a closed-form expression for the most probable path, i.e.,

$$\hat{\boldsymbol{x}}(t) = \boldsymbol{\psi}(t) - \mathbf{H}(t) \mathbf{Q}^{-1} \mathbf{b} \tag{2.45}$$

Further, it is worth pointing out that the time-dependent matrix $\mathbf{Q}$ is a function only of the initial and final time points (t_0 and t_f), and is independent of the boundary values

$\boldsymbol{x}(t_0), \dot{\boldsymbol{x}}(t_0), \boldsymbol{x}(t_f)$ and $\dot{\boldsymbol{x}}(t_f)$; the latter are involved only in the evaluation of vector $\mathbf{b}$ through the Hermite polynomials $\boldsymbol{\psi}$ (see Eq.(2.41)). The interested reader is also directed to B, where, for tutorial effectiveness, the positive definiteness of matrix $\mathbf{Q}$ is demonstrated for the case of a single-degree-of-freedom (SDOF) linear oscillator.

Finally, it has been shown in this section that a Rayleigh-Ritz numerical solution treatment for determining the most probable path yields an objective function to be minimized, which is both quadratic and convex for linear systems. Obviously, for such cases a Newton's optimization scheme for determining the most probable path converges to the global extremum in only one iteration [25]. Thus, taking into account that nonlinear response behaviors can be construed generally as perturbations (not necessarily small) from the linear regime, it can be argued that a Newton's optimization scheme (such as the one developed in the following section) serves as a natural choice for addressing general cases involving arbitrary nonlinearities.

A Newton's numerical scheme formulation

In this section, a Newton's iterative algorithm is developed for solving the optimization problem in Eq. (2.34) corresponding to an arbitrary nonlinear oscillator. In this regard, as highlighted in Sec. 2.3.2, the rationale for developing a Newton's scheme relates to the form of the objective function of Eq. (2.39) referring to linear systems, which is both convex and quadratic; and thus, a Newton's scheme appears to be an ideal choice as it converges in only one iteration to the unique global extremum [25]. This convergence behavior suggests that a Newton's scheme can be a suitable choice also for nonlinear systems following Eq. (2.17) with

$$\mathbf{g}(\boldsymbol{x}, \dot{\boldsymbol{x}}, t) = \mathbf{g}_{lin}(\boldsymbol{x}, \dot{\boldsymbol{x}}) + \varepsilon\, \mathbf{g}_{nl}(\boldsymbol{x}, \dot{\boldsymbol{x}}) \tag{2.46}$$

where $\varepsilon > 0$ is a parameter indicating the intensity of the nonlinearity degree and $\mathbf{g}_{nl}(\boldsymbol{x}, \dot{\boldsymbol{x}})$ is an arbitrary nonlinear function. Obviously, in the limiting case, as $\varepsilon \to 0$ the nonlinear function $\mathbf{g}(\boldsymbol{x}, \dot{\boldsymbol{x}}, t)$ becomes linear, i.e., $\mathbf{g} \to \mathbf{g}_{lin}$ (see also Eq. (2.36)), and the objective

function in Eq. (2.34) approaches the quadratic form of Eq. (2.39), i.e., $J(\boldsymbol{z}) \rightarrow J_{lin}(\boldsymbol{z})$. This asymptotic behavior of $J(\boldsymbol{z})$ suggests that a suitable optimization scheme relates to starting from an initial point $\boldsymbol{z}^{(0)}$ and to successively minimizing a quadratic function J_q^k, which approximates J locally at $\boldsymbol{z}^{(k)}$, i.e.,

$$J_q^k(\boldsymbol{z}) = J(\boldsymbol{z}^{(k)}) + \nabla J(\boldsymbol{z}^{(k)})(\boldsymbol{z} - \boldsymbol{z}^{(k)}) + \frac{1}{2}(\boldsymbol{z} - \boldsymbol{z}^{(k)})^T \nabla^2 J(\boldsymbol{z}^{(k)})(\boldsymbol{z} - \boldsymbol{z}^{(k)}) \tag{2.47}$$

In Eq. (2.47), ∇J and $\nabla^2 J$ denote the gradient vector and the Hessian matrix of J, respectively. The next point $\boldsymbol{z}^{(k+1)}$ of the iterative scheme is obtained by minimizing $J_q^k(\boldsymbol{z})$ and setting $\nabla J = \mathbf{0}$. This yields

$$\boldsymbol{z}^{(k+1)} = \boldsymbol{z}^{(k)} - [\nabla^2 J(\boldsymbol{z}^{(k)})]^{-1} \nabla J(\boldsymbol{z}^{(k)}) \tag{2.48}$$

which is the update formula of the standard Newton's iterative optimization scheme (e.g., [25]).

It is worth noting that for the case of linear oscillators, i.e., $\varepsilon = 0$, and considering Eq. (2.39), the Hessian matrix becomes $\nabla^2 J = \mathbf{Q}$, which is constant with respect to $\boldsymbol{z}$. Thus, the update formula in Eq. (2.48) becomes

$$\boldsymbol{z}^{(k+1)} = \boldsymbol{z}^{(k)} - \mathbf{Q}^{-1}[\mathbf{Q}\boldsymbol{z}^{(k)} + \mathbf{b}]^{-1} = -\mathbf{Q}^{-1}\mathbf{b} \tag{2.49}$$

which is equal to the closed-form solution derived in Eq. (2.44). In other words, as anticipated for linear systems, the Newton's optimization scheme converges to the exact solution in only one iteration for any arbitrarily selected starting point $\boldsymbol{z}^{(0)}$. Further, the optimal (for linear systems) point $\boldsymbol{z}^* = -\mathbf{Q}^{-1}\mathbf{b}$ is expected to be a reasonable choice to be used as a starting point in the optimization scheme for the general case of nonlinear systems.

Next, certain convergence analysis aspects are elucidated pertaining to the herein proposed Newton's scheme in conjunction with the general class of dynamical systems governed

by Eqs. (2.17) and (2.46).

Specifically, as shown in [25], provided that the Hessian matrix $\nabla^2 J$ is Lipschitz continuous in the neighborhood of the solution $\boldsymbol{z}^*$ and that the initial point $\boldsymbol{z}^{(0)}$ is sufficiently close to $\boldsymbol{z}^*$, the Newton's iterative scheme given by Eq. (2.48) converges to $\boldsymbol{z}^*$ at a quadratic rate, i.e.,

$$\|\boldsymbol{z}^{(k+1)} - \boldsymbol{z}^*\| \leq L \, \|[\nabla^2 J(\boldsymbol{z}^*)]^{-1}\| \, \|\boldsymbol{z}^{(k)} - \boldsymbol{z}^*\|^2 \tag{2.50}$$

where L is the Lipschitz constant of $\nabla^2 J(\boldsymbol{z})$ for $\boldsymbol{z}$ near $\boldsymbol{z}^*$, i.e., L is a positive real constant defined as

$$\frac{\left\|\nabla^2 J(\boldsymbol{z}_2) - \nabla^2 J(\boldsymbol{z}_1)\right\|}{\|\boldsymbol{z}_2 - \boldsymbol{z}_1\|} \leq L \tag{2.51}$$

for all $\boldsymbol{z}_1$ and $\boldsymbol{z}_2$ in a neighborhood of $\boldsymbol{z}^*$.

Next, substituting Eq. (2.46) into Eq. (2.21), and considering Eq. (2.39), the gradient vector of $J(\boldsymbol{z})$ becomes

$$\nabla J(\boldsymbol{z}) = \mathbf{Q}\boldsymbol{z} + \boldsymbol{b} + \varepsilon \nabla g_1(\boldsymbol{z}) + \frac{\varepsilon}{2} \nabla g_2(\boldsymbol{z}) \tag{2.52}$$

and the Hessian matrix of $J(\boldsymbol{z})$ takes the form

$$\nabla^2 J(\boldsymbol{z}) = \mathbf{Q} + \varepsilon \nabla^2 g_1(\boldsymbol{z}) + \frac{\varepsilon^2}{2} \nabla^2 g_2(\boldsymbol{z}) \tag{2.53}$$

where

$$g_1(\boldsymbol{z}) = \int_{t_0}^{t_f} \left[\mathbf{M}\ddot{\hat{\boldsymbol{x}}} + \mathbf{C}\dot{\hat{\boldsymbol{x}}} + \mathbf{K}\hat{\boldsymbol{x}}\right]^{\mathrm{T}} \mathbf{g}_{nl}(\hat{\boldsymbol{x}}, \dot{\hat{\boldsymbol{x}}}) \mathrm{d}t \tag{2.54}$$

and

$$g_2(\boldsymbol{z}) = \int_{t_0}^{t_f} \mathbf{g}_{nl}(\hat{\boldsymbol{x}}, \dot{\hat{\boldsymbol{x}}})^{\mathrm{T}} \mathbf{g}_{nl}(\hat{\boldsymbol{x}}, \dot{\hat{\boldsymbol{x}}}) \mathrm{d}t \tag{2.55}$$

Further, substituting Eq. (2.53) into Eq. (2.50) leads to

$$\|\boldsymbol{z}^{(k+1)} - \boldsymbol{z}^*\| \leq L \, \|[\mathbf{Q} + \varepsilon \nabla^2 g_1(\boldsymbol{z}^*) + \frac{\varepsilon^2}{2} \nabla^2 g_2(\boldsymbol{z}^*)]^{-1}\| \, \|\boldsymbol{z}^{(k)} - \boldsymbol{z}^*\|^2 \tag{2.56}$$

Moreover, substituting Eq. (2.53) into Eq. (2.51) yields

$$\frac{\left\|\varepsilon\nabla^2 g_1(\boldsymbol{z}_2) + \frac{\varepsilon^2}{2}\nabla^2 g_2(\boldsymbol{z}_2) - \varepsilon\nabla^2 g_1(\boldsymbol{z}_1) - \frac{\varepsilon^2}{2}\nabla^2 g_2(\boldsymbol{z}_1)\right\|}{\|\boldsymbol{z}_2 - \boldsymbol{z}_1\|} \leq L \tag{2.57}$$

Next, applying the triangle inequality to the left hand-side of Eq. (2.57) leads to

$$\begin{aligned} &\frac{\left\|\varepsilon\nabla^2 g_1(\boldsymbol{z}_2) + \frac{\varepsilon^2}{2}\nabla^2 g_2(\boldsymbol{z}_2) - \varepsilon\nabla^2 g_1(\boldsymbol{z}_1) - \frac{\varepsilon^2}{2}\nabla^2 g_2(\boldsymbol{z}_1)\right\|}{\|\boldsymbol{z}_2 - \boldsymbol{z}_1\|} \leq \\ &\varepsilon\frac{\left\|\nabla^2 g_1(\boldsymbol{z}_2) - \nabla^2 g_1(\boldsymbol{z}_1)\right\|}{\|\boldsymbol{z}_2 - \boldsymbol{z}_1\|} + \frac{\varepsilon^2}{2}\frac{\left\|\nabla^2 g_2(\boldsymbol{z}_2) - \nabla^2 g_2(\boldsymbol{z}_1)\right\|}{\|\boldsymbol{z}_2 - \boldsymbol{z}_1\|} \leq \varepsilon L_1 + \frac{\varepsilon^2}{2}L_2 \end{aligned} \tag{2.58}$$

where L_1 and L_2 represent Lipschitz constants of $\nabla^2 g_1(\boldsymbol{z})$ and $\nabla^2 g_2(\boldsymbol{z})$, respectively, and are independent of ε. Further, considering Eqs. (2.57) and (2.58), it is readily seen that the term $\varepsilon L_1 + \frac{\varepsilon^2}{2}L_2$ represents a Lipschitz constant of $\nabla^2 J(\boldsymbol{z})$ for $\boldsymbol{z}$ in the neighborhood of $\boldsymbol{z}^*$, which decreases with decreasing ϵ. Also, as $\varepsilon \to 0$ the term $\|[\mathbf{Q} + \varepsilon\nabla^2 g_1(\boldsymbol{z}^*) + \frac{\varepsilon^2}{2}\nabla^2 g_2(\boldsymbol{z}^*)]^{-1}\|$ in Eq. (2.56) approaches the constant positive term $\left\|\boldsymbol{Q}^{-1}\right\|$ (see also B for the positive definiteness of $\boldsymbol{Q}$). Thus, as anticipated, the convergence rate shown in Eq. (2.56) is increasing for decreasing nonlinearity degree.

Chapter 3: Efficient marginalization with free boundaries

3.1 Marginalized Wiener path integral representation

It becomes clear that a brute-force determination of the n-dimensional response transition PDF via (2.14) requires point-wise calculations on a n-dimensional lattice. This leads to an exponential growth of the computational cost as a function of the number n of DOFs. In other words, discretizing each dimension of vector $\boldsymbol{a}$ into N points, N^n BVPs of the form of (2.15)-(2.16) need to be solved numerically for evaluating the joint response PDF via (2.14).

To circumvent this limitation, a technique is developed in this paper, capable of determining marginalized joint response PDFs, i.e., PDFs that involve only a subset of the components of vector $\boldsymbol{a}$. In the ensuing analysis, a marginalized transition PDF is denoted as $p(\boldsymbol{u}, t_f|\boldsymbol{a}_0, t_0)$, where $\boldsymbol{u} = \{a_{j,f}|j \in U\}$ and U is an arbitrary subset $U \subseteq \{1, ..., n\}$ with cardinality $p = |U|$. Assuming fixed initial conditions at t_0, the herein developed technique is capable of determining any p-dimensional (marginalized) joint response transition PDF $p(\boldsymbol{u}) = p(\boldsymbol{u}, t_f|\boldsymbol{a}_0, t_0)$ directly, i.e., at a computational cost that is exponentially related to the dimension p of the target PDF only, and is essentially independent of the dimension n of the original system.

In this regard, the corresponding path integral representation of the transition PDF takes the form

$$p(\boldsymbol{u}, t_0|\boldsymbol{a}_0, t_0) = \int\limits_{C\{\boldsymbol{a}_0, t_0; \boldsymbol{u}, t_f\}} \exp\left(-\int\limits_{t_0}^{t_f} \mathcal{L}\left(\boldsymbol{a}, \dot{\boldsymbol{a}}\right) \mathrm{d}t\right) \prod_{t=t_0}^{t_f} \mathrm{d}\boldsymbol{a}(t) \tag{3.1}$$

where $C\{\boldsymbol{a}_0, t_0; \boldsymbol{u}, t_f\}$ denotes the space of all possible paths with initial state $(\boldsymbol{a}_0, t_0)$ and final state $\left(\boldsymbol{u}, t_f\right)$. Note that the coordinates $a_{j,f}$ with $j \notin U$ are considered free.

3.1.1 Most probable path with free boundaries

Clearly, the most probable path, denoted as $\tilde{\boldsymbol{a}}(t)$ in the case of free endpoint boundaries, depends on the choice of set U, since this set determines which coordinates of $\tilde{\boldsymbol{a}}$ are fixed at the endpoint ($t = t_f$). Specifically, accounting for the free endpoint boundaries in the minimization of the functional in (2.13) leads to a BVP with the E-L equations of (2.15), but with the modified boundary conditions

$$a_j(t_0) = a_{j,0} \tag{3.2a}$$

$$\left.\begin{cases} a_j(t_f) = a_{j,f} & \text{if} \quad j \in U \\ \left[\mathcal{L}_{\dot{a}_j}\right]_{t=t_f} = 0 & \text{otherwise} \end{cases}\right\} \; j = 1, ..., n \tag{3.2b}$$

(3.2a) represents the fixed initial conditions, whereas (3.2b) assigns a fixed endpoint condition to the components a_j of $\boldsymbol{a}$ with $j \in U$ and a free endpoint condition to the components a_j with $j \notin U$. The form of the free endpoint conditions in (3.2b) is the outcome of the first-order extremality condition with free endpoint boundaries (see Appendix A for the complete derivation).

In this regard, a specific point of the marginalized system response transition PDF can be determined as

$$p(\boldsymbol{u}, t_f | \boldsymbol{a}_0, t_0) \approx C \; \exp\left(-\int_{t_0}^{t_f} \mathcal{L}\left(\tilde{\boldsymbol{a}}, \dot{\tilde{\boldsymbol{a}}}\right) \mathrm{d}t\right) \tag{3.3}$$

where $\boldsymbol{C}$ is a normalization constant. Indicative examples of sample paths and most probable paths corresponding both to (2.16) and (3.2) are shown in figure 3.1 for comparison.

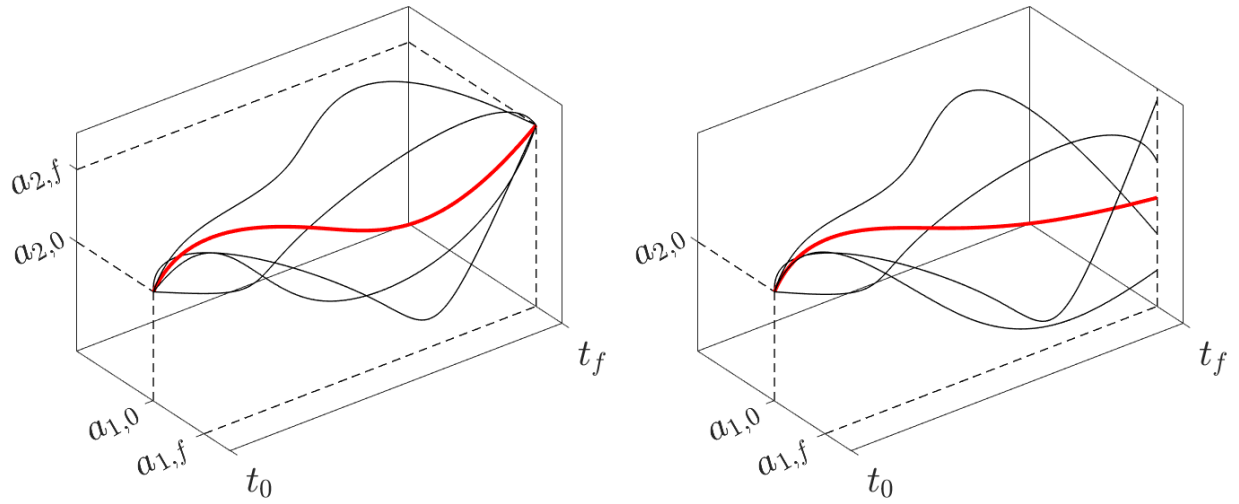

Figure 3.1: Indicative examples of sample paths (thin lines) and most probable path (thick line). **Left**: fixed endpoint boundaries $a_{1,f}$ and $a_{2,f}$. **Right**: fixed endpoint boundary $a_{1,f}$ and free endpoint boundary $a_{2,f}$.

3.2 Generalization to higher-order SDEs

In this section, a generalization of the herein developed technique is presented, which accounts for higher-order systems of the form

$$\boldsymbol{x}^{(m)} = \boldsymbol{P}\left(\boldsymbol{x}, ..., \boldsymbol{x}^{(m-1)}, t\right) + \boldsymbol{Q}\left(\boldsymbol{x}, ..., \boldsymbol{x}^{(m-1)}, t\right)\boldsymbol{\eta}(t) \tag{3.4}$$

where $\boldsymbol{x}$ is a n-dimensional stochastic vector process, i.e., $\boldsymbol{x}(t) = [x_j(t)]_{n\times 1}$ and $\boldsymbol{x}^{(m)}$ denotes the m-th-order derivative with respect to time t. Casting (3.4) into the form of (2.1), by setting $\boldsymbol{a} = [\boldsymbol{x}, ..., \boldsymbol{x}^{(m-1)}]^{\mathrm{T}}$, leads to a first-order system of nm SDEs characterized by a singular diffusion matrix $\tilde{\boldsymbol{B}}$. Thus, the Lagrangian in (2.10) cannot be used in a straightforward manner. However, it was shown in [20] that this type of diffusion matrix singularity can be treated effectively by introducing delta functionals (i.e., the functional counterpart of the Dirac delta) into the path integral expression for enforcing the constraints $\dot{\boldsymbol{a}} = [\dot{\boldsymbol{x}}, ..., \boldsymbol{x}^{(m)}]^{\mathrm{T}}$ similarly to Sec. 2.2. In this manner, functional integration of these delta functionals eliminates the variables corresponding to the singular part of $\tilde{\boldsymbol{B}}$. Ultimately, the path integral expression takes the form of (2.12) in conjunction, however, with a properly defined La-

grangian shown in (3.5), i.e.,

$$\mathcal{L}\left(\boldsymbol{x}, ..., \boldsymbol{x}^{(m)}\right) = \frac{1}{2}\left[\boldsymbol{x}^{(m)} - \boldsymbol{P}\left(\boldsymbol{x}, ..., \boldsymbol{x}^{(m-1)}, t\right)\right]^{\mathrm{T}}\left[\tilde{\mathbf{Q}}\left(\boldsymbol{x}, ..., \boldsymbol{x}^{(m-1)}, t\right)\right]^{-1}\left[\boldsymbol{x}^{(m)} - \boldsymbol{P}\left(\boldsymbol{x}, ..., \boldsymbol{x}^{(m-1)}, t\right)\right] \tag{3.5}$$

where

$$\tilde{\mathbf{Q}}\left(\boldsymbol{x}, ..., \boldsymbol{x}^{(m-1)}, t\right) = \mathbf{Q}\left(\boldsymbol{x}, ..., \boldsymbol{x}^{(m-1)}, t\right)\mathbf{Q}^{\mathrm{T}}\left(\boldsymbol{x}, ..., \boldsymbol{x}^{(m-1)}, t\right) \tag{3.6}$$

(see also [20]).

3.2.1 Most probable path with free boundaries for higher-order SDEs

In a similar manner as in the first-order system of (2.1), the most probable path is determined as the trajectory that minimizes the functional $\int_{t_0}^{t_f}\mathcal{L}\left(\boldsymbol{x}, ..., \boldsymbol{x}^{(m)}\right)\mathrm{d}t$ (see (2.13)). Assuming fixed initial and endpoint boundaries, the most probable path $\bar{\boldsymbol{x}}(t)$ can be evaluated by solving the E-L equations

$$\sum_{k=0}^{m}(-1)^k\frac{\mathrm{d}^k}{\mathrm{d}t^k}\mathcal{L}_{x_j^{(k)}} = 0 \quad \text{for all} \quad j = 1, ..., n \tag{3.7}$$

together with the fixed boundary conditions. A specific point of the complete joint response transition PDF $p(\boldsymbol{x}_f, ..., \boldsymbol{x}_f^{(m-1)}, t_f|\boldsymbol{x}_0, ..., \boldsymbol{x}_0^{(m-1)}, t_0)$ can be obtained by utilizing an expression similar to (2.14). On the other hand, a marginalized response transition PDF $p(\boldsymbol{u}, t_f|\boldsymbol{x}_0, ..., \boldsymbol{x}_0^{(m-1)}, t_0)$ can be determined by utilizing an expression of the form of (3.3). In this case, $\boldsymbol{u}$ denotes the p-dimensional vector that contains a prespecified number of endpoint coordinates, i.e., $1 \leq p \leq nm$ and $\boldsymbol{u} = \{x_{j,f}^{(k)}|j \in U_k\}$ where U_k is the set that contains the indices of the coordinates of the k-th derivative $\boldsymbol{x}^{(k)}$ that participate in the marginalized PDF. For example, the marginal response PDF of the j-th component of the r-th derivative $x_j^{(r)}$ of $\boldsymbol{x}$ can be computed by setting $U_r = \{j\}$ and $U_k = \varnothing$ for all $k \neq r$. Next, accounting for the free endpoint boundaries in the minimization of the functional $\int_{t_0}^{t_f}\mathcal{L}\left(\boldsymbol{x}, ..., \boldsymbol{x}^{(m)}\right)\mathrm{d}t$

leads to a BVP with the E-L equations of (3.7), but with the modified boundary conditions

$$x_j^{(k)}(t_0) = x_{j,0}^{(k)} \tag{3.8a}$$

$$\begin{cases} x_j^{(k)}(t_f) = x_{j,f}^{(k)} & \text{if} \quad i \in U_k \\ \left[\sum_{l=0}^{m-k-1}(-1)^l \frac{\mathrm{d}^l}{\mathrm{d}t^l}\mathcal{L}_{x_j^{(l+k+1)}}\right]_{t=t_f} = 0 & \text{otherwise} \end{cases} \tag{3.8b}$$

These need to be considered for all $j = 1, ..., n$ and $k = 0, ..., m-1$, yielding a total number of $2mn$ boundary conditions. The solution of this problem provides the most probable path $\tilde{\boldsymbol{x}}(t)$, and a specific point of the marginalized response transition PDF is determined in the form

$$p(\boldsymbol{u}, t_f | \boldsymbol{x}_0, ..., \boldsymbol{x}_0^{(m-1)}, t_0) \approx C \ \exp\left(-\int_{t_0}^{t_f} \mathcal{L}\left(\tilde{\boldsymbol{x}}, ..., \tilde{\boldsymbol{x}}^{(m)}\right) \mathrm{d}t\right) \tag{3.9}$$

3.3 Computational efficiency aspects

In the standard WPI solution technique (e.g., [20]), the complete nm-dimensional joint response PDF corresponding to the system of (3.4) is determined and marginalized by integration in an a posteriori manner. This procedure requires the discretization of the PDF effective domain into N^{nm} points, where N is the number of points along each dimension, and the response PDF at a given time instant t_f is computed pointwise on the corresponding lattice. This leads to an exponential growth of the computational cost as a function of the dimensionality n and the order m of the system, since N^{nm} BVPs with fixed boundaries of the form of (2.15)-(2.16) need to be solved numerically. This limitation of the standard WPI technique has been partly addressed in [19, 24] by employing multi-dimensional function approximation techniques in conjunction with compressive sampling concepts and tools for reducing the total number of required BVPs to be solved. However, notwithstanding the significant reduction of the associated computational cost achieved in [19, 24], the requirement of the technique for determining the complete joint response PDF has not been circumvented

to-date. Clearly, this limits the scalability of the methodology since the number of BVPs to be solved becomes, evenually, prohibitive with increasing number n of DOFs.

In contrast, the technique developed in this paper is capable of determining any marginal p-dimensional response PDF by solving only N^p BVPs with free boundaries of the form of (3.8). This constitutes a reduction of the computational cost by orders of magnitude compared to the standard WPI technique. Notably, even in cases where the objective is to determine all marginal response PDFs of an n-dimensional system of m-th order, the free boundaries WPI solution formalism requires a dramatically smaller number of BVPs to be solved than the fixed boundaries WPI formulation, i.e., $nmN << N^{mn}$. Clearly, in many practical problems where decision-making is based only on a readily identified most critical DOF, the computational efficiency enhancement becomes even more impressive, and the above relationship becomes $N << N^{mn}$. Further, indicative comparisons with a standard MCS-based solution approach can be found in the numerical examples of the following section.

3.4 Numerical examples

In this section, the herein developed technique is utilized for determining marginalized joint response PDFs of various multi-DOF nonlinear dynamical systems, typically encountered in engineering applications. In general, a wide range of systems in stochastic engineering dynamics can be modeled as an n-DOF system of the form

$$\mathbf{M}\ddot{\boldsymbol{x}} + \mathbf{C}\dot{\boldsymbol{x}} + \mathbf{K}\boldsymbol{x} + \boldsymbol{g}\left(\boldsymbol{x}, \dot{\boldsymbol{x}}, t\right) = \boldsymbol{D}\boldsymbol{\eta}(t) \tag{3.10}$$

where $\boldsymbol{x}(t) = [x_j(t)]_{n\times 1}$ is the displacement vector process; $\mathbf{M}$ is a $n\times n$ diagonal mass matrix; $\mathbf{C}$ and $\mathbf{K}$ are the $n\times n$ damping and stiffness matrices, respectively; $\boldsymbol{g}\left(\boldsymbol{x}, \dot{\boldsymbol{x}}, t\right) = [g_j\left(\boldsymbol{x}, \dot{\boldsymbol{x}}, t\right)]_{n\times 1}$ denotes an arbitrary nonlinear vector-valued function and $\mathbf{D}$ is a deterministic nonsingular $n \times n$ matrix.

In the following, two distinct numerical examples are considered for demonstrating the

reliability and computational efficiency of the developed WPI solution technique. Comparisons with pertinent MCS data, generated by utilizing a standard 4th-order Runge-Kutta scheme to numerically integrate the equations of motion, are included as well for assessing the accuracy of the technique.

The first example relates to marine engineering and pertains to a structure exposed to nonlinear flow-induced forces described by the Morison equation [121] and subjected to non-white stochastic excitation. The second example relates to nano-engineering and pertains to a 100-DOF stochastically excited nonlinear system modeling the behavior of large arrays of coupled nanomechanical oscillators (e.g., [122, 123, 124]).

3.4.1 Structural system subject to flow-induced forces

In this example, a single-DOF oscillator under flow-induced forces is considered, typically modeled via the Morison nonlinear equation [121]. Further, the excitation is modeled as a non-white process compatible with the JONSWAP sea wave power spectrum, which is approximated herein by a second-order linear filter; see also [20] and references therein for more details. In this regard, the equations of motion become

$$\mu\ddot{y} + \gamma\dot{y} + \kappa y = w(t) \tag{3.11a}$$

$$\ddot{x} + 2\omega\xi\dot{x} + \omega^2 x + \frac{1}{2}\frac{C_D\rho D}{M_0}|V + \dot{x}|(V + \dot{x}) = y(t) \tag{3.11b}$$

where the parameters values $\mu = 1.8268$, $\gamma = 0.4418$, $\kappa = 3.0213$, $\omega = 1.2566$, $\xi = 0.02$, $C_D = 1$, $\rho D/M_0 = 1.136$ and $V = 0$ are used in the ensuing analysis. Next, following [20], (3.11b) is substituted into (3.11a) yielding a 4th-order nonlinear SDE of the form of (3.4) to be solved by the proposed WPI solution methodology. Clearly, from a practical perspective, the higher-order derivatives $x^{(3)}$ and $\ddot{x}$, appearing in the 4th-order SDE due to the filter (3.11a), do not offer any additional information or insight for analyzing and eventually designing the structural system. Thus, the herein developed marginalized WPI

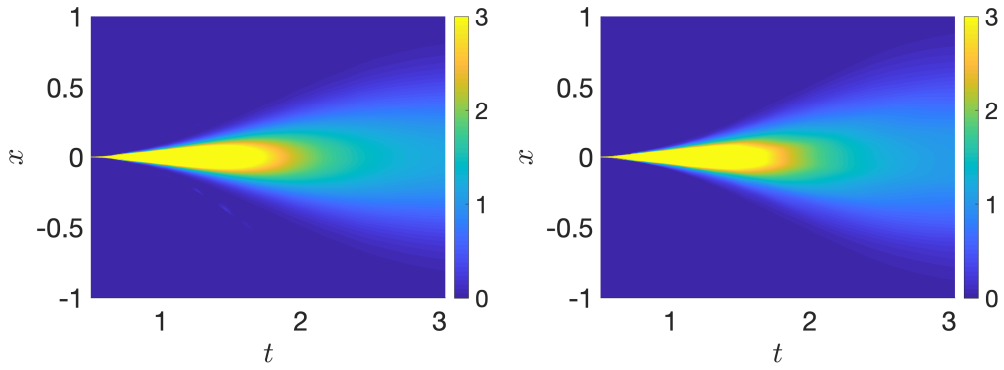

Figure 3.2: Evolution in time of the marginal response displacement PDF $p(x)$ pertaining to the Morison nonlinear system. **Left**: WPI. **Right**: MCS estimates (10,000 realizations).

formulation appears ideal for eliminating variables $x^{(3)}$ and $\ddot{x}$ from the response process vector. Specifically, applying the free boundaries WPI technique, the evolution in time of the marginal response displacement PDF is shown in Fig. 3.2. Comparing with pertinent MCS data demonstrates the accuracy of the developed methodology. It is noted that the evaluation of a marginal PDF at a specific time instant requires the solution of $N = 31$ BVPs, whereas using the standard fixed boundaries WPI requires the solution of $N^4 = 923,521$ BVPs (since marginalization follows after the joint PDF has been obtained first). Also, for this particular example, MCS based on $10,000$ realizations requires approximately 1 hour of computation time, whereas a marginal PDF is determined via the proposed free boundaries WPI technique in approximately 10 seconds on the same computer.

3.4.2 High-dimensional arrays of coupled nonlinear nano-mechanical oscillators

Due to their minuscule size and high sensitivity, micro- and nano-electromechanical systems (MEMS and NEMS) have been proposed recently for applications in signal processing, laser scanning, protein printing and label-free detection of molecules even in low concentrations [124]. In general, MEMS and NEMS can exhibit nonlinear response behavior due to geometrical configurations and various damping mechanisms, are subject to various intrinsic sources of stochastic noise (e.g. adsorption-desorption and thermally induced noises), whereas, to enhance their detection sensitivity, current technology enables the fabrication

of large arrays of nano-oscillators, coupled by electric, magnetic, or elastic forces [123, 124]. In this regard, MEMS and NEMS are typically modeled as stochastically excited high-dimensional nonlinear multi-DOF systems in the form of (3.10) [122, 123]. Note, however, that due to the prohibitively large in many cases number of stochastic dimensions, the analysis of relatively large arrays of MEMS and NEMS has been performed to-date based, primarily, on techniques that are subject to significant simplifications and approximations; see, for instance, [125] where a standard moments equations solution approach was employed, which is capable of providing relatively accurate estimates only for the system response first- and second-order statistics (e.g., mean and standard deviation); see also [10].

Next, the herein developed WPI technique is employed for determining marginalized joint response PDFs of a 100-DOF MEMS modeled according to [123] and following (3.10) with

$$\mathbf{M} = \begin{bmatrix} m_0 & \cdots & 0 \\ \vdots & \ddots & \vdots \\ 0 & \cdots & m_0 \end{bmatrix} \quad \mathbf{C} = \begin{bmatrix} c_0 & \cdots & 0 \\ \vdots & \ddots & \vdots \\ 0 & \cdots & c_0 \end{bmatrix} \quad \mathbf{K} = \begin{bmatrix} k_0 + 2\omega_0 & -\omega_0 & \cdots & 0 \\ -\omega_0 & \ddots & \ddots & \vdots \\ \vdots & \ddots & \ddots & -\omega_0 \\ 0 & \cdots & -\omega_0 & k_0 + 2\omega_0 \end{bmatrix} \tag{3.12}$$

$$\boldsymbol{g}(\boldsymbol{x}, \dot{\boldsymbol{x}}, t) = \left[\epsilon \left(\frac{x_j}{x_j^2 + d_0^2} \right)^{\frac{3}{2}} - A\cos(\omega t) \right]_{100\times 1} \quad \mathbf{D} = \begin{bmatrix} \sqrt{10\pi} & \cdots & 0 \\ \vdots & \ddots & \vdots \\ 0 & \cdots & \sqrt{10\pi} \end{bmatrix}$$

The parameter values are $m_0 = 1$, $c_0 = 1.5$, $k_0 = 120$, $\omega_0 = 70.2\pi$, $\epsilon = 0.1$, $d_0 = 0.1$, $A = 20$ and $\omega = 3\pi$.

In Fig. 3.3 the evolution in time of the marginal response displacement PDF of x_{33} is shown, whereas in Fig. 3.4 the evolution in time of the joint response PDF $p(x_{97}, \dot{x}_{97})$ is plotted. Comparisons with MCS data demonstrate the high accuracy degree exhibited by the technique.

It is worth noting that in this example $N = 31$ BVPs are solved for evaluating a marginal PDF at a specific time instant. Even in the case that knowledge of the marginal response

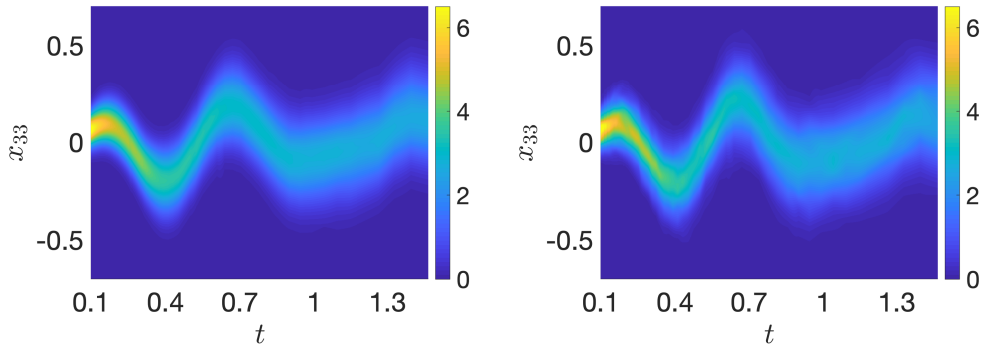

Figure 3.3: Evolution in time of the marginal response displacement PDF of x_{33}. **Left**: WPI. **Right**: MCS estimates (10,000 realizations).

displacement PDFs for all DOFs is required, this translates into solving only $100 \cdot 31 = 3100$ BVPs. In contrast, the standard WPI technique, which unavoidably determines the complete joint response PDF, requires the solution of 31^{200} BVPs, which is clearly a computationally intractable number.

In Fig. 3.5, the accuracy and the efficiency of the proposed technique is compared with pertinent MCS results for a 10-DOF version of the above nanomechanical oscillator at time $t = 0.5s$. Specifically, the horizontal axis shows computational cost represented by actual computation time required based on a MATLAB_R2019a numerical implementation. The vertical axis shows the mean square error (MSE) between the estimated PDF and the target PDF based on MCS with $100,000$ realizations (assumed to be the exact for comparison purposes). The reported MSE corresponds to the average value accounting for all 20 marginal PDFs. In a similar manner, the computation time of the WPI shown on the horizontal axis corresponds to the average over the 20 marginal PDFs (i.e., 10 displacement and 10 velocity PDFs). MCS-based PDF estimates with a varying number of realizations are included as well. As anticipated, these estimates converge to the target PDF with an increasing number of realizations, at the expense of course of increasing computational cost. Regarding the WPI-based PDF estimates, it is seen that the accuracy exhibited by the technique increases as the discretization of the PDF domain becomes finer. In other words, as the number N of BVPs to be solved becomes larger, the associated error becomes smaller. More importantly,

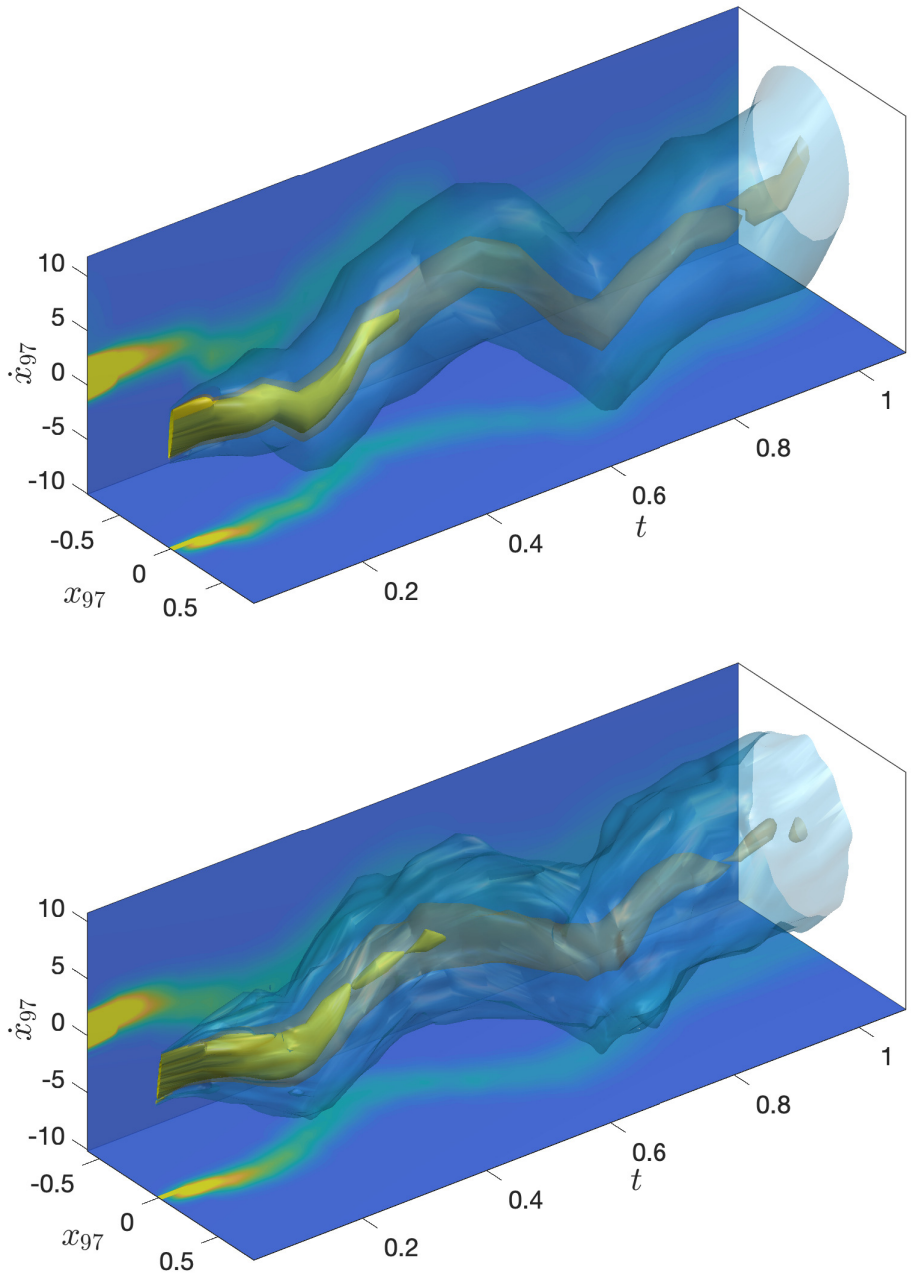

Figure 3.4: Evolution in time of the joint response PDF $p(x_{97}, \dot{x}_{97})$. **Top**: WPI. **Bottom**: MCS estimates (10,000 realizations). The three isosurfaces shown correspond to PDF values of 0.01 (blue), 0.32 (orange) and 0.6 (yellow).

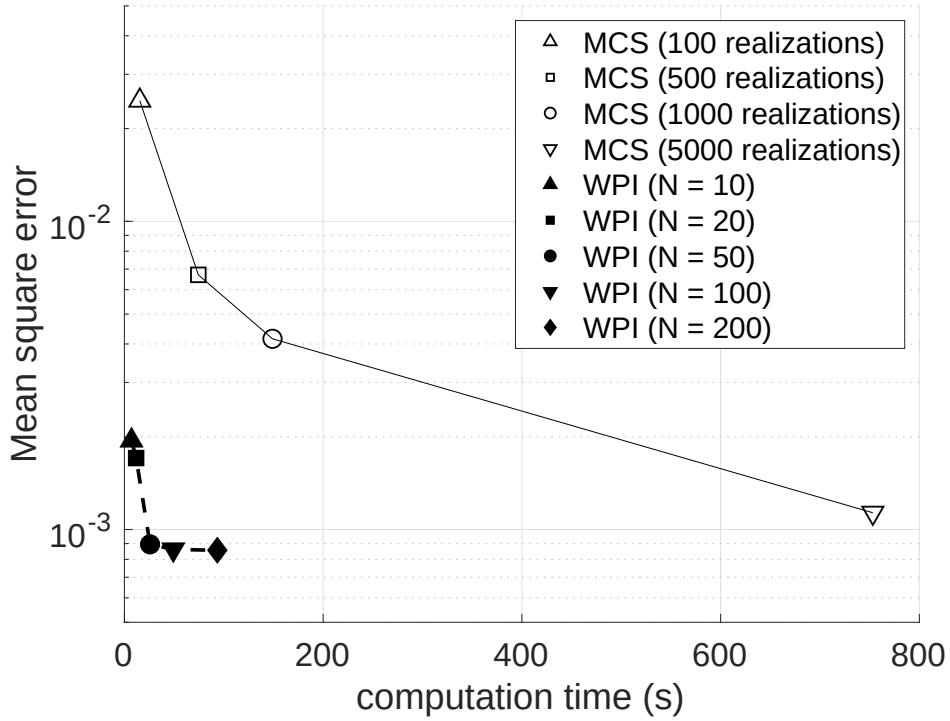

Figure 3.5: Comparisons between MCS and WPI technique in terms of accuracy and efficiency: Mean square error and corresponding computation time for estimating a marginal PDF of a 10-DOF nano-mechanical oscillator.

in all cases, the performance of the WPI technique appears superior to that of the standard MCS. In fact, for approximately the same accuracy degree, it is seen that the WPI associated computation time is several orders of magnitude smaller than that corresponding to MCS.

Chapter 4: Systems with singular diffusion matrices

4.1 WPI formulation accounting for singular diffusion matrices

In this section, the WPI solution technique delineated in Sec. 2.2 is extended to account for a general class of systems with singular diffusion matrices. In this regard, a novel WPI based variational formulation with constraints is developed. Specifically, consider in the following the general class of structural/mechanical systems whose governing equation of motion takes the form

$$\mathbf{M}\ddot{\boldsymbol{x}} + \boldsymbol{g}(\boldsymbol{x}, \dot{\boldsymbol{x}}) = \begin{bmatrix} \boldsymbol{w}(t) \\ \mathbf{0} \end{bmatrix} \tag{4.1}$$

where $\mathbf{M}$ is an $n \times n$, (potentially singular) mass matrix, and $\boldsymbol{g}$ is a nonlinear vector valued function. Indicative examples of engineering systems whose dynamics is described by Eq. (4.1) include, but are not limited to, structures subject to excitations applied to some (and not all) of their DOFs, hysteretic (e.g., Bouc-Wen) systems modeled via additional auxiliary state equations [10], and certain electromechanical energy harvesters [18]. Next, comparing Eqs. (2.17) and (4.1), it can be readily seen that the $\mathbf{D}$ matrix corresponding to the right-hand-side of Eq. (4.1), and defined as

$$\mathbf{D}\delta(\tau) = \mathbb{E}\left[\begin{bmatrix} \boldsymbol{w}(t) \\ \mathbf{0} \end{bmatrix}\begin{bmatrix} \boldsymbol{w}^{\mathrm{T}}(t+\tau) & \mathbf{0} \end{bmatrix}\right] = \begin{bmatrix} \mathbb{E}\left[\boldsymbol{w}(t)\boldsymbol{w}^{\mathrm{T}}(t+\tau)\right] & \mathbf{0} \\ \mathbf{0} & \mathbf{0} \end{bmatrix} = \begin{bmatrix} \mathbf{D}_{rr} & \mathbf{0} \\ \mathbf{0} & \mathbf{0} \end{bmatrix}\delta(\tau) \tag{4.2}$$

is singular, and thus, the Lagrangian of Eq. (2.21) cannot be determined in a straightforward manner. Note that the symbol $\mathbf{D}_{rr}$ is used to denote the non-singular square sub-matrix of $\mathbf{D}$.

In the ensuing analysis, the singularity of $\mathbf{D}$ is addressed by partitioning the system of

Eq. (4.1) into two coupled subsystems: one that contains the equations corresponding to vector $\boldsymbol{w}$ on the right-hand-side of Eq. (4.1) and another referring to the equations that correspond to the zero entries on the right-hand-side of Eq. (4.1); this yields

$$\begin{bmatrix} \mathbf{M}_r\ddot{\boldsymbol{x}} + \boldsymbol{g}_r(\boldsymbol{x}, \dot{\boldsymbol{x}}) \\ \mathbf{M}_s\ddot{\boldsymbol{x}} + \boldsymbol{g}_s(\boldsymbol{x}, \dot{\boldsymbol{x}}) \end{bmatrix} = \begin{bmatrix} \boldsymbol{w}(t) \\ \mathbf{0} \end{bmatrix} \tag{4.3}$$

Note that the upper subsystem, hereinafter referred to as the $r-$system, constitutes an underdetermined system of $n-m$ SDEs and the lower subsystem, hereinafter referred to as the $s-$system, represents an underdetermined system of m homogeneous ODEs. Clearly, matrix $\mathbf{M}_r \in \mathbb{R}^{(n-m)\times n}$ consists of the first $n-m$ rows of matrix $\mathbf{M}$, while $\mathbf{M}_s \in \mathbb{R}^{m\times n}$ consists of the last m rows of $\mathbf{M}$. Further, by recasting Eq. (4.1) into the form of Eq. (4.3), it can be argued that the motion of the dynamical system in Eq. (4.1) is governed by the $r-$system of equations constrained by the $s-$system of equations.

Next, defining $\boldsymbol{x}(t) = [\boldsymbol{x}_r(t) \quad \boldsymbol{x}_s(t)]^{\mathrm{T}}$, $\mathbf{M}_r = [\mathbf{M}_{rr} \quad \mathbf{M}_{rs}]$ and $\mathbf{M}_s = [\mathbf{M}_{sr} \quad \mathbf{M}_{ss}]$, where $\mathbf{M}_{rr}$, $\mathbf{M}_{rs}$, $\mathbf{M}_{sr}$ and $\mathbf{M}_{ss}$ are square matrices, and employing a δ-functional as in Sec. 2.2, the WPI for the system response PDF takes the form

$$\begin{aligned} p(\boldsymbol{\alpha}_f, t_f|\boldsymbol{\alpha}_0, t_0) = \int_{C\{\boldsymbol{\alpha}_f, t_f|\boldsymbol{\alpha}_0, t_0\}} \exp\left(-\int_{t_0}^{t_f} \frac{1}{2}\left[\boldsymbol{S}_r(\boldsymbol{\alpha}, \dot{\boldsymbol{\alpha}})\right]^{\mathrm{T}} \mathbf{D}_{rr}^{-1}\left[\boldsymbol{S}_r(\boldsymbol{\alpha}, \dot{\boldsymbol{\alpha}})\right] \mathrm{d}t\right) \times \ldots \\ \delta\left[\boldsymbol{S}_s(\boldsymbol{\alpha}, \dot{\boldsymbol{\alpha}})\right] \prod_{t=t_0}^{t_f} \mathrm{d}\boldsymbol{x}_r(t) \prod_{t=t_0}^{t_f} \mathrm{d}\boldsymbol{x}_s(t) \end{aligned} \tag{4.4}$$

where $\boldsymbol{\alpha} = [\boldsymbol{x}_r, \boldsymbol{x}_s, \dot{\boldsymbol{x}}_r, \dot{\boldsymbol{x}}_s]^{\mathrm{T}}$, while

$$\boldsymbol{S}_r(\boldsymbol{\alpha}, \dot{\boldsymbol{\alpha}}) = \mathbf{M}_{rr}\ddot{\boldsymbol{x}}_r + \mathbf{M}_{rs}\ddot{\boldsymbol{x}}_s + \boldsymbol{g}_r(\boldsymbol{\alpha}) \tag{4.5}$$

and

$$\boldsymbol{S}_s(\boldsymbol{\alpha}, \dot{\boldsymbol{\alpha}}) = \mathbf{M}_{sr}\ddot{\boldsymbol{x}}_r + \mathbf{M}_{ss}\ddot{\boldsymbol{x}}_s + \boldsymbol{g}_s(\boldsymbol{\alpha}) \tag{4.6}$$

Following a similar procedure as in Sec. 2.2, the aim is to integrate over paths $\boldsymbol{x}_s(t)$ and to obtain a path integral formulation involving $\boldsymbol{x}_r(t)$ only. However, this is not generally possible because the argument of the δ-functional in Eq. (4.4) is not merely a trivial compatibility relationship, as in Sec. 2.2, but a rather complex general function of $\boldsymbol{x}_s$. To address this challenge, the equation $\boldsymbol{S}_s(\boldsymbol{\alpha}, \dot{\boldsymbol{\alpha}}) = \mathbf{0}$ is enforced explicitly and takes the form of a constraint $\boldsymbol{\phi}(\boldsymbol{x}, \dot{\boldsymbol{x}}, \ddot{\boldsymbol{x}}) = \mathbf{0}$ given by

$$\boldsymbol{\phi}(\boldsymbol{x}, \dot{\boldsymbol{x}}, \ddot{\boldsymbol{x}}) = \mathbf{M}_s \ddot{\boldsymbol{x}} + \boldsymbol{g}_s(\boldsymbol{x}, \dot{\boldsymbol{x}}) \tag{4.7}$$

In this regard, the transition PDF can be expressed in the compact form

$$p(\boldsymbol{x}_f, \dot{\boldsymbol{x}}_f, t_f | \boldsymbol{x}_0, \dot{\boldsymbol{x}}_0, t_0) = \int\limits_{C\{\boldsymbol{x}_0, \dot{\boldsymbol{x}}_0, t_0; \boldsymbol{x}_f, \dot{\boldsymbol{x}}_f, t_f | \boldsymbol{\phi}=\mathbf{0}\}} \exp\left(- \int_{t_0}^{t_f} \mathcal{L}_r(\boldsymbol{x}, \dot{\boldsymbol{x}}, \ddot{\boldsymbol{x}}) \mathrm{d}t \right) \prod_{t=t_0}^{t_f} \mathrm{d}\boldsymbol{x}(t) \tag{4.8}$$

where

$$\mathcal{L}_r(\boldsymbol{x}, \dot{\boldsymbol{x}}, \ddot{\boldsymbol{x}}) = \frac{1}{2} [\mathbf{M}_r \ddot{\boldsymbol{x}} + \boldsymbol{g}_r(\boldsymbol{x}, \dot{\boldsymbol{x}})]^T \mathbf{D}_{rr}^{-1} [\mathbf{M}_r \ddot{\boldsymbol{x}} + \boldsymbol{g}_r(\boldsymbol{x}, \dot{\boldsymbol{x}})] \tag{4.9}$$

and $C\{\boldsymbol{x}_0, \dot{\boldsymbol{x}}_0, t_0; \boldsymbol{x}_f, \dot{\boldsymbol{x}}_f, t_f | \boldsymbol{\phi} = \mathbf{0}\}$ denotes the set of all paths, with initial state $(\boldsymbol{x}_0, \dot{\boldsymbol{x}}_0)$ at time t_0 and final state $(\boldsymbol{x}_f, \dot{\boldsymbol{x}}_f)$ at time t_f, which satisfy the constraint $\boldsymbol{\phi}(\boldsymbol{x}, \dot{\boldsymbol{x}}, \ddot{\boldsymbol{x}}) = \mathbf{0}$.

4.2 Constrained variational problem solution treatment

Following the WPI formulation of Sec. 4.1, determining the most probable path is pursued next by seeking for the solutions of the $r-$system that satisfy also the constraints of the $s-$ system. This leads to the formulation of a constrained variational problem for the determination of the most probable path $\bar{\boldsymbol{x}}$, i.e.,

$$\text{minimize} \quad \mathcal{J}_r(\boldsymbol{x}, \dot{\boldsymbol{x}}, \ddot{\boldsymbol{x}}) = \int_{t_0}^{t_f} \mathcal{L}_r(\boldsymbol{x}, \dot{\boldsymbol{x}}, \ddot{\boldsymbol{x}}) \mathrm{d}t \tag{4.10}$$

$$\text{subject to} \quad \boldsymbol{\phi}(\boldsymbol{x}, \dot{\boldsymbol{x}}, \ddot{\boldsymbol{x}}) = \mathbf{0} \tag{4.11}$$

where the Lagrangian $\mathcal{L}_r$ in Eq. (4.10) corresponds to the $r-$system only and is given by Eq. (4.9), and the constraint function $\boldsymbol{\phi}$ is given by Eq. (4.7).

Constrained variational problems of the form of Eqs. (4.10)-(4.11) can be solved by employing the general Lagrange multipliers approach (e.g., [126, 127]). This leads to an unconstrained variational problem by considering the auxiliary Lagrangian $\mathcal{L}^*(\boldsymbol{x}, \dot{\boldsymbol{x}}, \ddot{\boldsymbol{x}}) = \mathcal{L}_r(\boldsymbol{x}, \dot{\boldsymbol{x}}, \ddot{\boldsymbol{x}}) + \boldsymbol{\lambda}(t)\boldsymbol{\phi}(\boldsymbol{x}, \dot{\boldsymbol{x}}, \ddot{\boldsymbol{x}})$. This unconstrained problem yields a system of n Euler–Lagrange equations, similar to the ones in Eq. (2.23)-(2.24), to be solved together with the m constraint functions in Eq. (4.11) for the n unknown functions $\boldsymbol{x}(t)$ and the m unknown Lagrange multiplier functions $\boldsymbol{\lambda}(t)$; see for instance [18]. In practice, however, the reformulation of this complex system of $n+m$ equations into an equivalent first-order system, as dictated by most numerical BVP solvers, requires multiple time differentiations of the constraint functions. As a result, the time derivatives of the constraints are fulfilled, but not the constraints themselves. This is a common limitation in several numerical solution methods for BVPs as highlighted in [128]. Therefore, in the ensuing analysis, attention is directed to a Rayleigh–Ritz solution approach for the determination of the most probable path.

Specifically, following Sec. 2.3.2, the polynomial expansion of Eq. (2.28) is utilized for the response vector $\boldsymbol{x}(t)$. This reduces the functional $\mathcal{J}_r(\boldsymbol{x}, \dot{\boldsymbol{x}}, \ddot{\boldsymbol{x}})$ of Eq. (4.10) to a function

$$J_r(\boldsymbol{z}) := \mathcal{J}_r(\hat{\boldsymbol{x}}, \dot{\hat{\boldsymbol{x}}}, \ddot{\hat{\boldsymbol{x}}}) \tag{4.12}$$

which depends on the vectorized expansion parameters $\boldsymbol{z} \in \mathbb{R}^p$, where $p = nL$. Further, by defining the functions

$$\hat{\boldsymbol{\phi}}(\boldsymbol{z}, t) := \boldsymbol{\phi}(\hat{\boldsymbol{x}}, \dot{\hat{\boldsymbol{x}}}, \ddot{\hat{\boldsymbol{x}}}) \tag{4.13}$$

the constraints in Eq. (4.11) are replaced by $\hat{\boldsymbol{\phi}}(\boldsymbol{z}, t) = \boldsymbol{0}$. The adoption of the Rayleigh–Ritz solution approach simplifies the constrained variational problem in Eq. (4.10)-(4.11) to an

ordinary constrained optimization problem of the form

$$\min_{\boldsymbol{z}\in\mathbb{R}^p} \quad J_r(\boldsymbol{z}) \tag{4.14}$$

$$\text{subject to} \quad \hat{\boldsymbol{\phi}}(\boldsymbol{z},t)=\mathbf{0} \quad \forall\ t\in[t_0,t_f] \tag{4.15}$$

and facilitates further its numerical treatment. Taking into account Eq. (2.28), the solution $\boldsymbol{z}^*$ to the above problem yields the most probable path in the form $\hat{\tilde{\boldsymbol{x}}}(t)=\boldsymbol{\psi}(t)+\mathbf{H}(t)\boldsymbol{z}^*$. Next, a single point of the system response transition PDF can be determined via the semi-classical approximation of Eq. (2.25) as

$$p(\boldsymbol{x}_f,\dot{\boldsymbol{x}}_f,t_f|\boldsymbol{x}_0,\dot{\boldsymbol{x}}_0,t_0)\approx C\ \exp\left(-\int_{t_0}^{t_f}\mathcal{L}_r(\hat{\tilde{\boldsymbol{x}}},\dot{\hat{\tilde{\boldsymbol{x}}}},\ddot{\hat{\tilde{\boldsymbol{x}}}})\mathrm{d}t\right) \tag{4.16}$$

where C is a normalization constant.

4.2.1 Linear constraints

The special case of function $\boldsymbol{g}_s$ in Eq. (4.3) taking the linear form $\boldsymbol{g}_s(\boldsymbol{x},\dot{\boldsymbol{x}})=\mathbf{C}_s\dot{\boldsymbol{x}}+\mathbf{K}_s\boldsymbol{x}$, where $\mathbf{C}_s\in\mathbb{R}^{m\times n}$ and $\mathbf{K}_s\in\mathbb{R}^{m\times n}$, leads to linear constraint functions in Eq. (4.11). This considerable simplification facilitates a computationally efficient numerical treatment of the optimization problem of Eqs. (4.14)-(4.15). In particular, a solution is pursued by restricting the optimization within the space of solutions of Eq. (4.15) via a nullspace approach. Specifically, linearity of the constraint equations ensures that $\hat{\boldsymbol{\phi}}(\boldsymbol{z},t)$ is a vector of m polynomial functions of t, each of degree $L+4$ (see Eqs. (2.27)-(2.29), (4.7) and (4.13)), with coefficients linear in the nL unknown expansion parameters $\boldsymbol{z}$. Setting these polynomial coefficients equal to zero yields a set of $m(L+4)$ linear equations with $p=nL$ unknown variables. Next, these equations are cast as a linear system of the form

$$\mathbf{F}\boldsymbol{z}=\mathbf{d} \tag{4.17}$$

where $\mathbf{F} \in \mathbb{R}^{s\times p}$, $\mathbf{d} \in \mathbb{R}^s$ and $s = m(L+4)$. Of course, for any well-posed constrained optimization problem, the number of independent constraints is smaller than the dimension of $\boldsymbol{z}$. For the herein concerned problem, this yields $m(L+4) < p$, which provides the lower bound $L > \frac{4m}{n-m}$ for the number L of trial functions used in the polynomial expansion. The system in Eq. (4.17) is underdetermined, while $\mathbf{F}$ may not have full row rank, i.e., $r_F \leq s$. It is now possible to restrict minimization of the objective function $J_r = J_r(\boldsymbol{z})$, where $\boldsymbol{z} \in \mathbb{R}^p$, to the set of solutions of Eq. (4.17) that lie on a lower dimensional space of dimension $p - r_F$. To elaborate further, note that the vector space $U \subseteq \mathbb{R}^p$ of solutions of the system $\mathbf{F}\boldsymbol{z} = \mathbf{0}$, can be fully described with the aid of a basis $\mathbf{S} = [\boldsymbol{s}_1 \ \boldsymbol{s}_2 \ \ldots \ \boldsymbol{s}_{p-r_F}]$ for the nullspace of $\mathbf{F}$ [129], where $\mathbf{S} \in \mathbb{R}^{p\times(p-r_F)}$. In this regard, any element $\boldsymbol{z} \in U$ can be represented by an element $\boldsymbol{v} \in V \subseteq \mathbb{R}^{p-r_F}$ as $\boldsymbol{z} = \mathbf{S}\boldsymbol{v}$, and the vector space $U_d \subseteq \mathbb{R}^p$ of solutions of $\mathbf{F}\boldsymbol{z} = \mathbf{d}$ can be obtained as an affine transformation of U [130]. More specifically, the solutions $\boldsymbol{z} \in U_d$ of Eq. (4.17) can be represented as

$$\boldsymbol{z} = \mathbf{S}\boldsymbol{v} + \boldsymbol{z}_p \tag{4.18}$$

where $\boldsymbol{z}_p$ is any particular solution of Eq. (4.17) [129, 130]; see also [131]. This approach enables the corresponding constrained optimization problem

$$\min_{\boldsymbol{z}\in\mathbb{R}^p} J_r(\boldsymbol{z}) \quad \text{subject to} \quad \mathbf{F}\boldsymbol{z} = \mathbf{d} \tag{4.19}$$

of dimension p to be recast into a lower dimensional unconstrained problem of dimension $p - r_F$ as

$$\min_{\boldsymbol{v}\in\mathbb{R}^{p-r_F}} J_r(\mathbf{S}\boldsymbol{v} + \boldsymbol{z}_p) \tag{4.20}$$

Note that the minimizer $\boldsymbol{z}^*$ of Eq. (4.19) can be obtained by the minimizer $\boldsymbol{v}^*$ of Eq. (4.20) using the relationship in Eq. (4.18).

Further, it is worth highlighting the special case of a linear oscillator with non-singular diffusion matrix (unconstrained problem), where the most probable path can be derived

in closed-form. Specifically, the linear oscillator yields a quadratic objective function in Eq. (2.33) that can be written as

$$J(\boldsymbol{z}) = \frac{1}{2}\boldsymbol{z}^{\mathrm{T}}\mathbf{Q}\boldsymbol{z} + \mathbf{b}^{\mathrm{T}}\boldsymbol{z} \tag{4.21}$$

where matrix $\mathbf{Q}$ and vector $\mathbf{b}$ are given in Eqs. (2.40) and (2.41) respectively. Given that $\mathbf{Q}$ is positive definite, $J(\boldsymbol{z})$ has the unique minimizer $\boldsymbol{z}^* = -\mathbf{Q}^{-1}\mathbf{b}$ and the most probable path can be determined in closed-form via Eq. (2.28). This result can be utilized in conjunction with the nullspace approach described earlier in this section, to determine the most probable path of a linear oscillator with singular diffusion matrix in closed-form as well. This is the case where the constraint function is linear ($\boldsymbol{g}_s(\boldsymbol{x}, \dot{\boldsymbol{x}}) = \mathbf{C}_s\dot{\boldsymbol{x}} + \mathbf{K}_s\boldsymbol{x}$) and function $\boldsymbol{g}_r$ in Eq. (4.3) is also linear, i.e., $\boldsymbol{g}_r(\boldsymbol{x}, \dot{\boldsymbol{x}}) = \mathbf{C}_r\dot{\boldsymbol{x}} + \mathbf{K}_r\boldsymbol{x}$, where $\mathbf{C}_r \in \mathbb{R}^{(n-m)\times n}$ and $\mathbf{K}_r \in \mathbb{R}^{(n-m)\times n}$, while the optimization problem of Eq. (4.20) takes the form

$$\min_{\boldsymbol{v}\in\mathbb{R}^{p-r_F}} \quad \frac{1}{2}[\mathbf{S}\boldsymbol{v} + \boldsymbol{z}_p]^{\mathrm{T}}\mathbf{Q}[\mathbf{S}\boldsymbol{v} + \boldsymbol{z}_p] + \mathbf{b}^{\mathrm{T}}[\mathbf{S}\boldsymbol{v} + \boldsymbol{z}_p] \tag{4.22}$$

Next, solving the problem in Eq. (4.22) with respect to $\boldsymbol{v}$ leads to the unique stationary point

$$\boldsymbol{v}^* = -(\mathbf{S}^{\mathrm{T}}\mathbf{Q}\mathbf{S})^{-1}[\boldsymbol{z}_p^{\mathrm{T}}\mathbf{Q}\mathbf{S} + \mathbf{b}^{\mathrm{T}}\mathbf{S}] \tag{4.23}$$

which, in conjunction with Eqs. (2.28) and (4.18), yields the following closed-form expression for the most probable path, i.e.,

$$\hat{\boldsymbol{x}}(t) = \boldsymbol{\psi}(t) + \mathbf{H}(t)\left[\mathbf{S}(\mathbf{S}^{\mathrm{T}}\mathbf{Q}\mathbf{S})^{-1}[\boldsymbol{z}_p^{\mathrm{T}}\mathbf{Q}\mathbf{S} + \mathbf{b}^{\mathrm{T}}\mathbf{S}] - \boldsymbol{z}_p\right] \tag{4.24}$$

4.2.2 Nonlinear constraints

In the more general case of arbitrary nonlinear constraints, it is possible to formulate an optimization problem with nonlinear equality constraints to be solved by an appropriate

numerical technique, such as a Newton scheme in conjunction with a Lagrange multiplier approach for the enforcement of constraints. Specifically, a necessary and sufficient condition for Eq. (4.15) to hold is

$$\boldsymbol{\xi}(\boldsymbol{z}) := \sqrt{\int_{t_0}^{t_f} \hat{\boldsymbol{\phi}}^2(\boldsymbol{z}, t)\mathrm{d}t} = \mathbf{0} \tag{4.25}$$

where integration and square root are performed element-wise, and thus, the corresponding optimization problem can be formulated as

$$\min_{\boldsymbol{z}\in\mathbb{R}^p} J_r(\boldsymbol{z}) \quad \text{subject to} \quad \boldsymbol{\xi}(\boldsymbol{z}) = \mathbf{0} \tag{4.26}$$

Next, two typically utilized methods for the solution of nonlinear optimization problems with equality constraints of the form of Eq. (4.26) are presented.

Sequential Quadratic Programming (SQP)

The optimization problem with equality constraints in Eq. (4.26) can be solved by using a Lagrange multiplier approach and by employing the corresponding Karush-Kuhn-Tucker (KKT) conditions [25]. To this aim, the Lagrangian function L_M is defined as

$$L_M(\boldsymbol{z}, \boldsymbol{\lambda}) = J_r(\boldsymbol{z}) - \boldsymbol{\lambda}^{\mathrm{T}}\boldsymbol{\xi}(\boldsymbol{z}) \tag{4.27}$$

where $\boldsymbol{\lambda} \in \mathbb{R}^m$ is a vector of Lagrange multipliers, and the Jacobian of the constraints is denoted as

$$A(\boldsymbol{z})^{\mathrm{T}} = [\nabla\xi_1(\boldsymbol{z}), \nabla\xi_2(\boldsymbol{z}), ..., \nabla\xi_m(\boldsymbol{z})] \tag{4.28}$$

The first-order KKT conditions for the optimization problem with equality constraints in Eq. (4.26) take the form of an $n+m$ system of equations with $n+m$ unknowns $\boldsymbol{z}$ and $\boldsymbol{\lambda}$ as

$$F(\boldsymbol{z},\boldsymbol{\lambda}) = \begin{bmatrix} \nabla J_r(\boldsymbol{z}) - A(\boldsymbol{z})^{\mathrm{T}}\boldsymbol{\lambda} \\ \boldsymbol{\xi}(\boldsymbol{z}) \end{bmatrix} = \mathbf{0} \tag{4.29}$$

while the Jacobian of Eq. (4.29) becomes

$$F'(\boldsymbol{z},\boldsymbol{\lambda}) = \begin{bmatrix} \nabla^2_{\boldsymbol{zz}} L_M(\boldsymbol{z},\boldsymbol{\lambda}) & -A(\boldsymbol{z})^{\mathrm{T}} \\ A(\boldsymbol{z}) & 0 \end{bmatrix} \tag{4.30}$$

Next, a Newton scheme is utilized for the solution of the KKT system in Eq. (4.29). The corresponding Newton step at the k^{th} iteration $(\boldsymbol{z}^k, \boldsymbol{\lambda}^k)$ takes the form

$$\begin{bmatrix} \boldsymbol{z}^{k+1} \\ \boldsymbol{\lambda}^{k+1} \end{bmatrix} = \begin{bmatrix} \boldsymbol{z}^{k} \\ \boldsymbol{\lambda}^{k} \end{bmatrix} + \begin{bmatrix} \boldsymbol{p}^{k} \\ \boldsymbol{p}^{k}_{\lambda} \end{bmatrix} \tag{4.31}$$

where p^k and p^k_λ are obtained by solving the Newton-KKT system

$$\begin{bmatrix} \nabla^2_{\boldsymbol{zz}} L_M(\boldsymbol{z}^k,\boldsymbol{\lambda}^k) & -A(\boldsymbol{z}^k)^{\mathrm{T}} \\ A(\boldsymbol{z}^k) & 0 \end{bmatrix} \begin{bmatrix} \boldsymbol{p}^{k} \\ \boldsymbol{p}^{k}_{\lambda} \end{bmatrix} = \begin{bmatrix} -\nabla J_r(\boldsymbol{z}^k) + A(\boldsymbol{z}^k)^{\mathrm{T}}\boldsymbol{\lambda}^k \\ -\boldsymbol{\xi}(\boldsymbol{z}^k) \end{bmatrix} \tag{4.32}$$

Solving the system in Eq. (4.32) and utilizing Eqs. (4.29) and (4.31), the update formulae for $\boldsymbol{\lambda}^{k+1}$ and $\boldsymbol{z}^{k+1}$ are given by

$$\boldsymbol{\lambda}^{k+1} = \left[A_k B_k^{-1} A_k^{\mathrm{T}}\right]^{-1} \left[-\boldsymbol{\xi}_k + A_k B_k^{-1} G_k\right] \tag{4.33}$$

$$\boldsymbol{p}^k = B_k^{-1}\left(A_k^{\mathrm{T}}\boldsymbol{\lambda}^{k+1} - G_k\right) \tag{4.34}$$

$$\boldsymbol{z}^{k+1} = \boldsymbol{z}^k + \alpha_k \boldsymbol{p}^k \tag{4.35}$$

where $A_k := A(\boldsymbol{z}^k) \in \mathbb{R}^{m\times p}$, $B_k := \nabla^2_{\boldsymbol{zz}} L_M(\boldsymbol{z}^k, \boldsymbol{\lambda}^k) \in \mathbb{R}^{p\times p}$, $\boldsymbol{\xi}_k := \boldsymbol{\xi}(\boldsymbol{z}^k) \in \mathbb{R}^m$ and $G_k := \nabla J_r(\boldsymbol{z}^k) \in \mathbb{R}^p$.

In passing, it is noted that the above proposed Newton solution scheme for the KKT system of Eq. (4.29) can be identified as a Sequential Quadratic Programming (SQP) methodology, which is a broader class of optimization algorithms capable of treating both equality and inequality constraints [25]. Further, in Eq. (4.35), $\boldsymbol{p}^k$ is the step direction and α_k is a step size parameter that is equal to 1 in the standard implementation of the scheme (see Eq. (4.31)). In practice, however, a smaller value is typically chosen for the step size α_k as the iterations approach the local minimum. This yields faster convergence potentially, while the value of α_k at each iteration can be determined by an appropriate line search algorithm. In the following, a line search scheme based on Wolfe conditions and described in [132] is adopted in the numerical examples. Moreover, regarding numerical implementation of the optimization scheme, the standard Broyden-Fletcher-Goldfarb-Shanno (BFGS) formula [133, 134] is employed herein for approximating the inverse of the Hessian matrix $\nabla^2_{\boldsymbol{zz}} L_M$; see also [25] for a broader perspective.

Augmented Lagrangian Method (ALM)

A relatively popular alternative approach for the solution of the constrained optimization problem in Eq. (4.26) is the Augmented Lagrangian Method (ALM) [135, 136, 137]. The ALM approximates the solution by successively minimizing the augmented Lagrangian function

$$L_A(\boldsymbol{z}, \boldsymbol{\lambda}; \mu) = J_r(\boldsymbol{z}) - \sum_{j=1}^{m} \lambda_j \xi_j(\boldsymbol{z}) + \frac{\mu}{2} \sum_{j=1}^{m} \xi_j^2(\boldsymbol{z}) \tag{4.36}$$

for a sequence of penalty factors μ with increasing values. Therefore, a sequence of unconstrained subproblems is formulated, where the solution of the previous problem is used as

the initial guess for the next one, i.e.,

$$\boldsymbol{z}^{k+1} = \underset{\substack{\boldsymbol{z}\in\mathbb{R}^p \\ \boldsymbol{z}_{init}=\boldsymbol{z}^k}}{\arg\min}\, L_A(\boldsymbol{z}, \boldsymbol{\lambda}^k; \mu^k) \tag{4.37}$$

where the Lagrange multiplier vector $\boldsymbol{\lambda} = [\lambda_j]_{m\times 1}$ at each step is given by the explicit estimate

$$\boldsymbol{\lambda}^{k+1} = \boldsymbol{\lambda}^k - \mu^k \boldsymbol{\xi}(\boldsymbol{z}^k) \tag{4.38}$$

and $\boldsymbol{z}_{init}$ denotes the initial guess for the solution of the corresponding optimization problem. The ALM has shown to improve the ill-posedeness of the quadratic penalty method (QPM), as it can approximate the solution of the original problem even with moderate values of the penalty factor μ [25]. Also, the augmented Lagrangian function in Eq. (4.36) can be derived as the dual of the corresponding quadratic penalty function of the QPM, as shown in [138].

4.3 Numerical examples

To assess the reliability of the herein developed technique for determining the response PDF of stochastically excited MDOF systems with singular diffusion matrices, two indicative examples are considered in this section. The first example pertains to a 2-DOF oscillator, where only one DOF is stochastically excited. It is shown that the special case of a linear oscillator under Kanai-Tajimi earthquake excitation, which yields a singular diffusion matrix, can also be cast in that form and treated under the same framework. The second example refers to a single-degree-of-freedom (SDOF) Bouc-Wen hysteretic oscillator, where hysteresis is modeled by introducing an additional auxiliary state equation. The WPI-based system response PDF estimates are compared with pertinent MCS data ($10,000$ realizations) for assessing the accuracy of the herein developed technique. In this regard, a standard fourth-order Runge-Kutta numerical integration scheme is employed for solving the governing equations of motion within the MCS context.

4.3.1 2-DOF oscillator with only one DOF stochastically excited

The following 2-DOF oscillator with only one DOF stochastically excited is considered in the present example. Specifically, the equation of motion takes the form

$$\boldsymbol{M}\ddot{\boldsymbol{x}} + \boldsymbol{C}\dot{\boldsymbol{x}} + \boldsymbol{K}\boldsymbol{x} + \varepsilon \boldsymbol{g}_{nl}(\boldsymbol{x}, \dot{\boldsymbol{x}}) = \begin{bmatrix} w(t) \\ 0 \end{bmatrix} \tag{4.39}$$

where

$$\mathbf{M} = \begin{bmatrix} 1 & 0 \\ 0 & 1 \end{bmatrix}, \quad \mathbf{C} = \begin{bmatrix} 0.2 & -0.1 \\ -0.1 & 0.1 \end{bmatrix}, \quad \mathbf{K} = \begin{bmatrix} 2 & -1 \\ -1 & 1 \end{bmatrix} \tag{4.40}$$

and $S_0 = 0.1$, whereas three different forms are considered next for the nonlinear function $\boldsymbol{g}(\boldsymbol{x}, \dot{\boldsymbol{x}})$.

Linear oscillator with linear constraints

First, a linear version of the 2-DOF oscillator of Eq. (4.39) with $\varepsilon = 0$ is considered. The WPI technique in conjunction with the closed-form expression in Eq. (4.24) for the most probable path is utilized, and the joint response PDF $p(\boldsymbol{x}, \dot{\boldsymbol{x}})$ is calculated for two indicative time instants $t = 2$ s and $t = 8$ s. The corresponding marginal response PDFs are shown in Fig. 4.1 demonstrating a high degree of accuracy based on comparisons with the exact solution obtained by numerically solving the related Lyapunov differential equation for the time-dependent response covariance matrix (see for instance [10]).

Linear oscillator under Kanai-Tajimi earthquake excitation

A widely utilized earthquake excitation model relates to the Kanai-Tajimi power spectrum introduced in [139, 140] and further generalized in [141] and [142]. The rationale behind the Kanai-Tajimi modeling relates to approximating the bedrock acceleration as a white noise process filtered through the soil deposit, which is modeled as a SDOF oscillator,

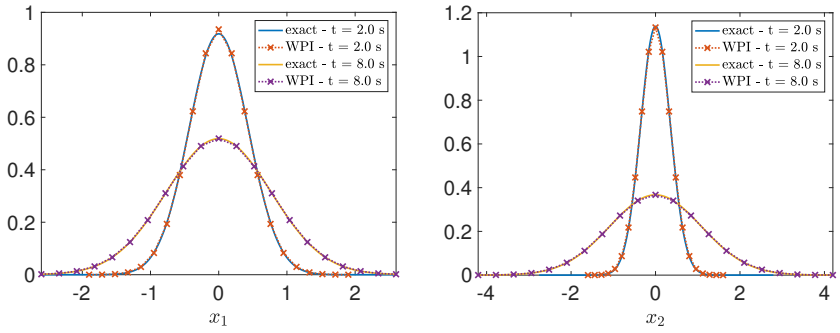

(a) $p(x_1)$ (b) $p(x_2)$

(c) $p(\dot{x}_1)$ (d) $p(\dot{x}_2)$

Figure 4.1: Marginal response PDFs of a stochastically excited 2-DOF linear oscillator with linear constraints; comparisons with exact solutions.

i.e.,

$$\ddot{y} + 2\zeta_g \omega_g \dot{y} + \omega_g^2 y = -w(t) \tag{4.41}$$

where y, $\dot{y}$ and $\ddot{y}$ are the ground displacement, velocity and acceleration, respectively, relative to the bedrock, while $w(t)$ is a white noise process with $\mathbb{E}[w(t)w(t-\tau)] = 2\pi S_0 \delta(\tau)$. In Eq. (4.41), ζ_g is the damping ratio and ω_g is the natural frequency of the ground whose values are taken equal to $\zeta_g = 0.6$ and $\omega_g = 5\pi$ rad/s [142]. The absolute ground acceleration in this case can be expressed as

$$\ddot{x}_g(t) = \ddot{y}(t) + w(t) \tag{4.42}$$

characterized by the Kanai-Tajimi power spectrum

$$S_{\ddot{x}_g}(\omega) = S_0 \frac{\omega_g^4 + 4\zeta_g^2 \omega_g^2 \omega^2}{(\omega_g^2 - \omega^2)^2 + 4\zeta_g^2 \omega_g^2 \omega^2} \tag{4.43}$$

Next, the equation of motion of a linear SDOF oscillator, with mass m_0, damping coefficient c_0 and stiffness k_0, under Kanai-Tajimi earthquake excitation takes the form

$$m_0\ddot{x} + c_0\dot{x} + k_0 x = -m_0\ddot{x}_g(t) \tag{4.44}$$

Further, dividing Eq. (4.44) by m_0 and considering Eqs. (4.41) and (4.42), the overall system can be written in the form

$$\mathbf{M}\ddot{\boldsymbol{z}} + \mathbf{C}\dot{\boldsymbol{z}} + \mathbf{K}\boldsymbol{z} = \begin{bmatrix} -1 \\ -1 \end{bmatrix} w(t) \tag{4.45}$$

where

$$\boldsymbol{z} = \begin{bmatrix} x \\ y \end{bmatrix}, \quad \mathbf{M} = \begin{bmatrix} 1 & 1 \\ 0 & 1 \end{bmatrix}, \quad \mathbf{C} = \begin{bmatrix} c_0/m_0 & 0 \\ 0 & 2\zeta_g\omega_g \end{bmatrix} \quad \text{and} \quad \mathbf{K} = \begin{bmatrix} k_0/m_0 & 0 \\ 0 & \omega_g^2 \end{bmatrix} \tag{4.46}$$

Clearly, the white noise process $w(t)$ in Eq. (4.45) can be equivalently expressed as a sum of two independent white noise processes, i.e., $w(t) = w_1(t) + w_2(t)$. In this regard, Eq. (4.45) becomes

$$\mathbf{M}\ddot{\boldsymbol{z}} + \mathbf{C}\dot{\boldsymbol{z}} + \mathbf{K}\boldsymbol{z} = \begin{bmatrix} -1 & -1 \\ -1 & -1 \end{bmatrix} \begin{bmatrix} w_1(t) \\ w_2(t) \end{bmatrix} \tag{4.47}$$

and hence, Eq. (4.45) takes the form of Eq. (2.17) with $\boldsymbol{w}(t) = [w_1(t), w_2(t)]^{\mathrm{T}}$. It can be readily seen in Eq. (4.47) that the white noise vector process $[w_1(t), w_2(t)]^{\mathrm{T}}$ is multiplied by a rank-one matrix. Thus, matrix $\mathbf{D}$ in Eq. (2.18) is also rank-one (it has the value of 2 in all its entries) which leads to a singular diffusion matrix $\tilde{\mathbf{B}}$. Next, Eq. (4.47) can be multiplied by the non-singular transformation matrix

$$\mathbf{T} = \begin{bmatrix} 1 & 0 \\ -1 & 1 \end{bmatrix} \tag{4.48}$$

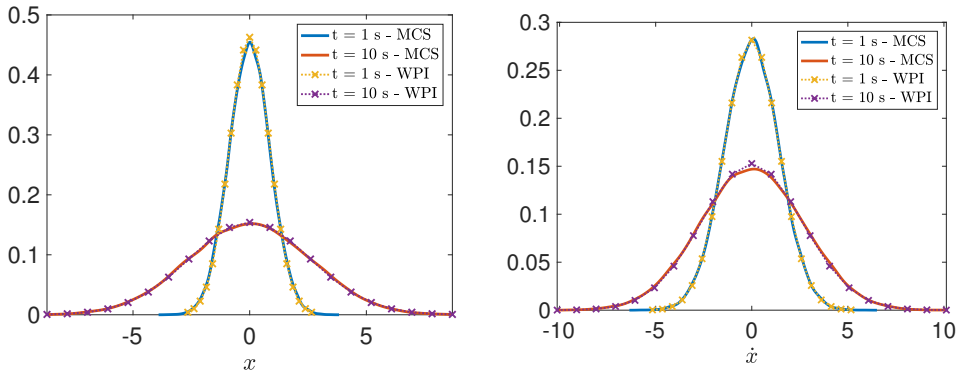

(a) $p(x)$ (b) $p(\dot{x})$

Figure 4.2: Marginal response PDFs of a SDOF linear oscillator under Kanai-Tajimi earthquake excitation; comparisons with MCS data (10,000 realizations).

and written, alternatively, as

$$\mathbf{TM}\ddot{\boldsymbol{z}} + \mathbf{TC}\dot{\boldsymbol{z}} + \mathbf{TK}\boldsymbol{z} = \mathbf{T}\begin{bmatrix} -1 & -1 \\ -1 & -1 \end{bmatrix}\begin{bmatrix} w_1(t) \\ w_2(t) \end{bmatrix} = \begin{bmatrix} -1 & -1 \\ 0 & 0 \end{bmatrix}\begin{bmatrix} w_1(t) \\ w_2(t) \end{bmatrix} = \begin{bmatrix} -w(t) \\ 0 \end{bmatrix} \tag{4.49}$$

Note that Eq. (4.49) has exactly the form of Eq. (4.39) with $\varepsilon = 0$, and thus, can be treated by the herein developed technique. Further, since Eq. (4.49) is linear, the solution approach of Sec. 4.2.1 can be applied, where the most probable path is given by Eq. (4.24) in closed form. The corresponding marginal response PDFs are shown in Fig. 4.2 for an oscillator with parameters $m_0 = 1$, $c_0 = 0.2$, $k_0 = 1$ and $S_0 = 0.5$. Comparisons with MCS data obtained by utilizing the spectral representation method [143] to generate realizations compatible with the Kanai-Tajimi power spectrum of Eq. (4.43) demonstrate a high degree of accuracy.

Nonlinear oscillator with linear constraints

Next, a version of the 2-DOF oscillator of Eq. (4.39) with stiffness and damping nonlinearities in the first equation and linear second equation is considered; thus, yielding linear constraints in the herein developed computational framework. In particular, the nonlinear

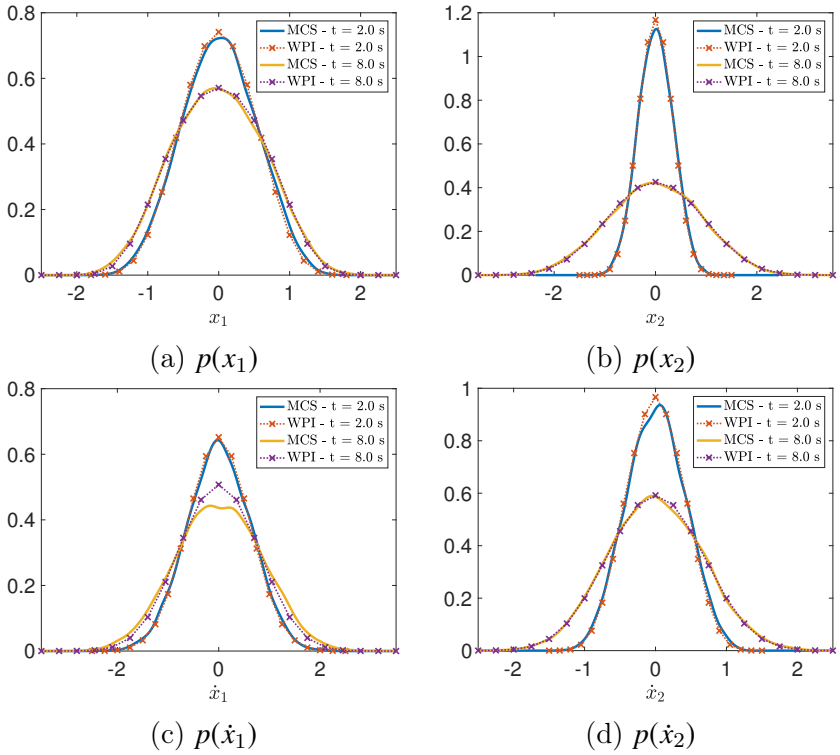

(a) $p(x_1)$ (b) $p(x_2)$

(c) $p(\dot{x}_1)$ (d) $p(\dot{x}_2)$

Figure 4.3: Marginal response PDFs of a stochastically excited 2-DOF nonlinear oscillator with linear constraints; comparisons with MCS data (10,000 realizations).

function $\boldsymbol{g}_{nl}(\boldsymbol{x}, \dot{\boldsymbol{x}})$ takes the form

$$\boldsymbol{g}_{nl}(\boldsymbol{x}, \dot{\boldsymbol{x}}) = \begin{bmatrix} c_{11}\dot{x}_1^3 + k_{11}x_1^3 \\ 0 \end{bmatrix} \tag{4.50}$$

where x_1 is the first component of the response vector $\boldsymbol{x}$, c_{11} and k_{11} are the upper left elements of matrices $\mathbf{C}$ and $\mathbf{K}$, respectively, and the magnitude of the nonlinearity ε is taken equal to 0.5. The WPI technique in conjunction with the methodology described in Sec. 4.2.1 is utilized next, and the joint response PDF $p(\boldsymbol{x}, \dot{\boldsymbol{x}})$ is calculated for two indicative time instants $t = 2$ s and $t = 8$ s. The corresponding marginal response PDFs are presented in Fig. 4.3, and compared with pertinent MCS data (10,000 realizations). The accuracy degree exhibited by the WPI is generally high, whereas slight deviations from the MCS-based estimates, such as in Fig. 4.3c, may be attributed not only to the various approximations involved in the WPI technique (see Sec. 2.2), but also to the specific accuracy characterizing

the MCS-based estimate given the utilized number of realizations.

Nonlinear oscillator with nonlinear constraints

Further, a third version of the 2-DOF oscillator in Eq. (4.39) with stiffness nonlinearities in both equations is considered; thus, yielding nonlinear constraints in the proposed computational framework. In this case, the nonlinear function $\boldsymbol{g}_{nl}(\boldsymbol{x}, \dot{\boldsymbol{x}})$ takes the form

$$\boldsymbol{g}_{nl}(\boldsymbol{x}, \dot{\boldsymbol{x}}) = \begin{bmatrix} k_{11} x_1^3 \\ k_{22} x_2^3 \end{bmatrix} \tag{4.51}$$

where x_1 and x_2 are the first and second components of the response vector $\boldsymbol{x}$, k_{11} and k_{22} are the upper left and lower right elements of matrix $\mathbf{K}$, respectively, and the nonlinearity magnitude $\boldsymbol{\varepsilon}$ is taken equal to 0.5.

The WPI technique in conjunction with the SQP method described in Sec. 4.2.2 is utilized next. In this regard, each point of the joint response PDF $p(\boldsymbol{x}, \dot{\boldsymbol{x}})$ at time $t = 1$ s is obtained by utilizing the SQP algorithm combined with a line search scheme and by employing the BFGS formula, with an initial guess $\boldsymbol{z}_{init} = \mathbf{0}$. Following integration of the joint response PDF, the corresponding marginal PDFs are obtained and presented in Fig. 4.4. Comparisons with pertinent MCS data ($10,000$ realizations) demonstrate a high degree of accuracy. Further, the joint response PDFs $p(x_1, x_2)$, $p(x_1, \dot{x}_1)$ and $p(x_2, \dot{x}_2)$ are also shown in Figures 4.5, 4.6 and 4.7, respectively, for the two time instants $t = 1$ s and $t = 3$ s. In a similar manner as before, satisfactory accuracy is observed based on comparisons with corresponding MCS data.

Next, the WPI technique in conjunction with the ALM method described in Sec. 4.2.2 is utilized. In this context, each point of the joint response PDF $p(\boldsymbol{x}, \dot{\boldsymbol{x}})$ at time $t = 1$ s is obtained by successively minimizing the augmented Lagrangian function of Eq. (4.36), for the sequence of penalty factors with increasing values $\mu = 3^k$ for $k = 0$, 2, 4, 6, 8, 10, 12. Following integration of the joint response PDF, the corresponding marginal PDFs

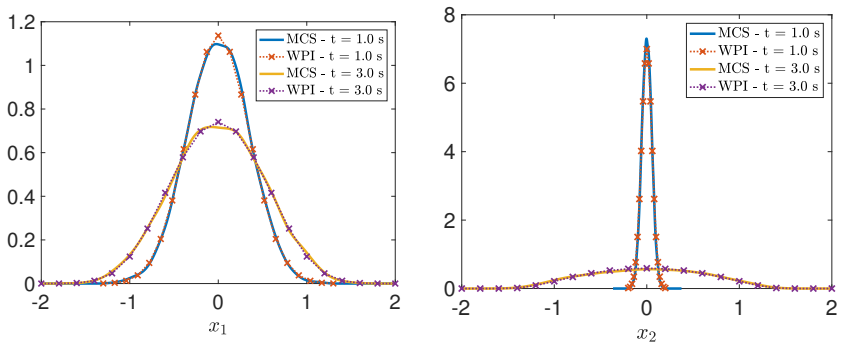

(a) $p(x_1)$ (b) $p(x_2)$

(c) $p(\dot{x}_1)$ (d) $p(\dot{x}_2)$

Figure 4.4: Marginal response PDFs of a stochastically excited 2-DOF nonlinear oscillator with nonlinear constraints at $t = 1$ s and $t = 3$ s; comparisons with MCS data (10,000 realizations).

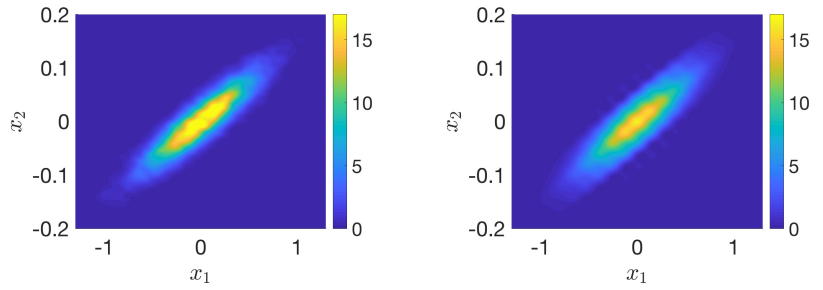

(a) MCS - $t = 1$ s

(b) WPI - $t = 1$ s

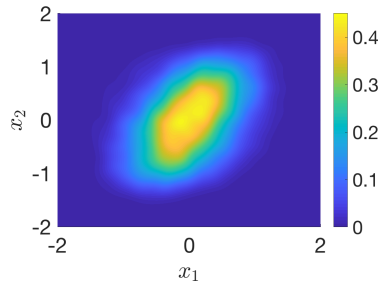

(c) MCS - $t = 3$ s

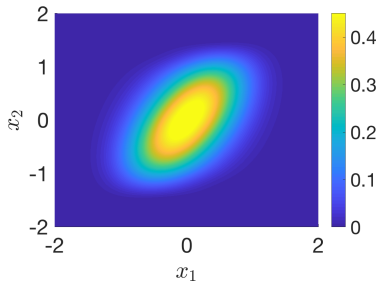

(d) WPI - $t = 3$ s

Figure 4.5: Joint response PDF $p(x_1, x_2)$ of a stochastically excited 2-DOF nonlinear oscillator with nonlinear constraints at $t = 1$ s and $t = 3$ s.

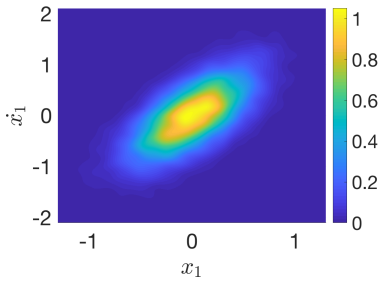

(a) MCS - $t = 1$ s

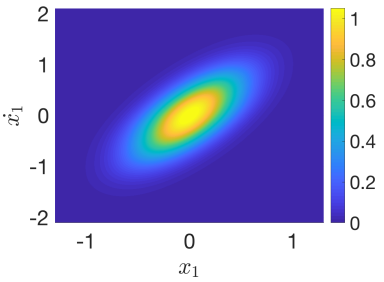

(b) WPI - $t = 1$ s

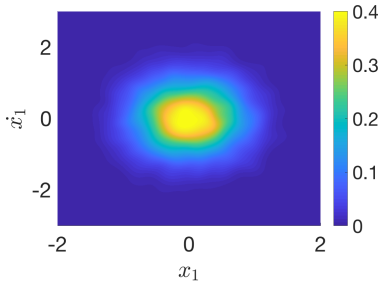

(c) MCS - $t = 3$ s

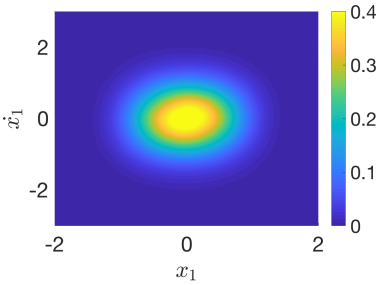

(d) WPI - $t = 3$ s

Figure 4.6: Joint response PDF $p(x_1, \dot{x}_1)$ of a stochastically excited 2-DOF nonlinear oscillator with nonlinear constraints at $t = 1$ s and $t = 3$ s.

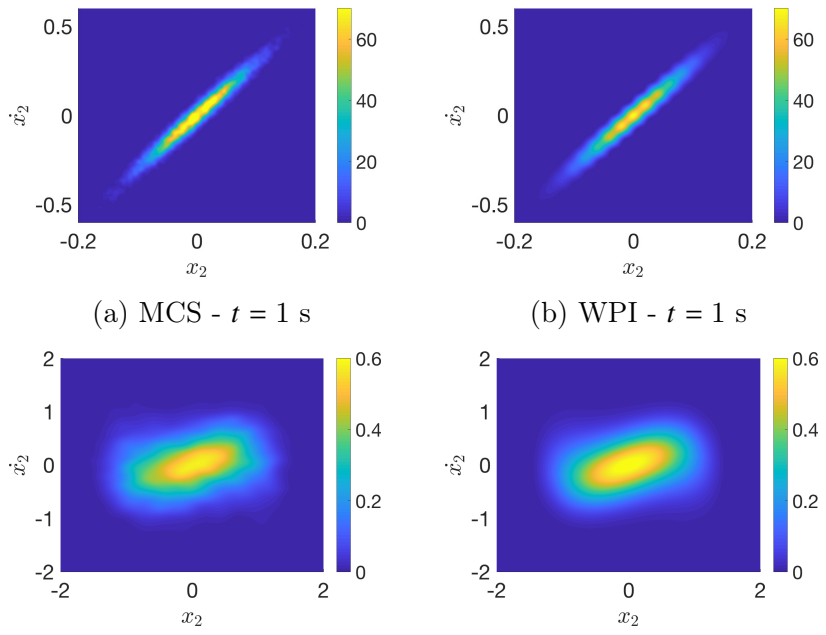

(a) MCS - t = 1 s (b) WPI - t = 1 s

(c) MCS - t = 3 s (d) WPI - t = 3 s

Figure 4.7: Joint response PDF $p(x_2, \dot{x}_2)$ of a stochastically excited 2-DOF nonlinear oscillator with nonlinear constraints at t = 1 s and t = 3 s.

are obtained for three indicative values of μ and presented in Fig. 4.8. A comparison with pertinent MCS results (10, 000 realizations) shows the convergence of the marginal PDFs to the MCS-based estimates for increasing values of μ.

It is seen that both the SQP and the ALM optimization schemes of section 4.2.2, perform satisfactorily in solving the problem of Eq. (4.26) with relatively high accuracy. Nevertheless, there are cases where the SQP algorithm may not converge to the optimum value for various reasons, such as poor choice of the initial guess or non-smooth and numerically ill-behaved governing / constraint equations. In such cases, the ALM or an appropriate combination of the SQP and ALM schemes may yield a more robust and efficient solution approach. An indicative example is considered next.

4.3.2 Bouc-Wen hysteretic oscillator

A SDOF Bouc-Wen nonlinear oscillator, which has been widely utilized in engineering dynamics for modeling systems exhibiting hysteresis, is considered in this numerical exam-

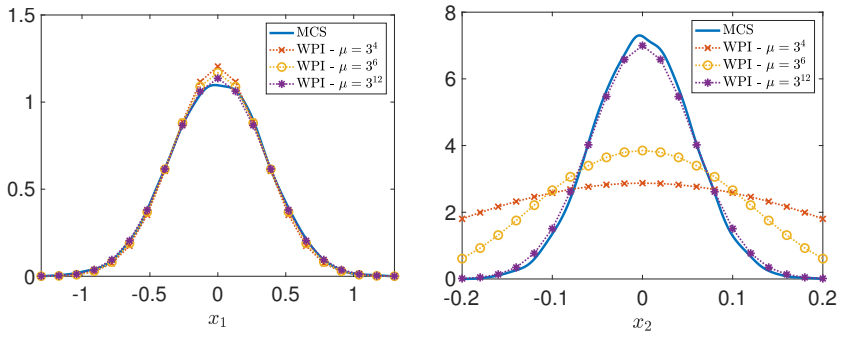

(a) $p(x_1)$ (b) $p(x_2)$

(c) $p(\dot{x}_1)$ (d) $p(\dot{x}_2)$

Figure 4.8: Marginal response PDFs of a stochastically excited 2-DOF nonlinear oscillator with nonlinear constraints at $t = 1$ s for increasing values of the penalty factor μ; comparisons with MCS data $(10,000$ realizations).

ple. The introduction of the smooth and versatile Bouc-Wen hysteretic model [144, 145] was followed by its successful application to various engineering mechanics related fields. Besides its versatility in efficiently capturing a broad range of hysteretic behaviors, corresponding equivalent linear elements can be readily determined in an explicit manner [146]. Specifically, a statistical linearization method (e.g., [10]) was proposed in [147] that involved deriving closed-form expressions for the equivalent linear elements of the Bouc-Wen model. Furthermore, a wavelet-based statistical linearization method was developed in [148] to determine the response evolutionary power spectrum. Indicatively, the Bouc-Wen formalism and its variants have been employed recently for modeling the inelastic behavior of steel beams with hysteretic damping [149], while in [150] a Bouc-Wen model compatible with plasticity postulates has been developed. A detailed presentation of the applications and the extensions of the Bouc-Wen model can be found in [38] and in review papers such as [151] and [152].

The Bouc-Wen oscillator is generally described by the system of coupled differential equations

$$\ddot{x} + 2\zeta_0\omega_0\dot{x} + \alpha\omega_0^2 x + (1-\alpha)\omega_0^2 z = w(t) \tag{4.52}$$

$$\dot{z} + \gamma|\dot{x}|z|z|^{\nu-1} + \beta\dot{x}|z|^{\nu} - A\dot{x} = 0 \tag{4.53}$$

where in Eq. (4.52) α can be viewed as a form of post-yield-to-pre-yield stiffness ratio. In the Bouc-Wen model, the additional auxiliary state z is related to the response x via Eq. (4.53). Various both softening and hardening behaviors can be modeled by appropriately choosing the constant parameters γ, β and A (see e.g., [152]).

Clearly, Eqs. (4.52)-(4.53) can be construed as a coupled system of a SDE (Eq. (4.52)) and a homogeneous ODE (Eq. (4.53)). This can be readily cast in the form of Eq. (4.1), and thus, treated by the herein developed solution technique. In passing, it is worth mentioning that, due to Eq. (4.53) being first-order, the system augmented mass matrix $\mathbf{M}$ in Eq. (2.17) is singular. Nevertheless, this poses no difficulties in applying the solution technique in a rather straightforward manner; see also discussion following Eq. (2.21). Moreover, it is noted that

the Bouc-Wen model in Eqs. (4.52) and (4.53) has some special characteristics that affect the form of the corresponding optimization problem. In particular, Eq. (4.52) is linear, which yields a corresponding objective function of a quadratic form (see Eq. (4.21)). This suggests that the SQP method presented in Sec. 4.2.2 is expected to perform satisfactorily, as it is essentially a quasi-Newton method. However, due to the form of Eq. (4.53) containing multiplicative relations involving absolute value functions, the constraint function takes a relatively complex form that can be locally non-differentiable; thus, leading to a potentially ill-posed optimization problem.

Next, for the parameter values $\zeta_0 = 0.01$, $\omega_0 = 1$, $\alpha = 0.01$, $\gamma = 0.5$, $\nu = 1$, $\beta = 0.5$ and $A = 1$, the joint response PDF $p(x, z, \dot{x})$ is obtained by employing the SQP method of Sec. 4.2.2 with an initial guess $\boldsymbol{z}_{init} = \mathbf{0}$. The corresponding marginal PDFs of the response displacement x and velocity $\dot{x}$ are plotted in Fig. 4.9 (line with x markers) for an indicative time instant $t = 10$ s. Clearly, based on comparisons with pertinent MCS data, this solution approach does not exhibit a satisfactory accuracy degree. As explained earlier, this may be due to a potentially ill-posed optimization problem, or due to the initial guess $\boldsymbol{z}_{init}$ not being sufficiently close to the optimum. In this regard, it can be argued that an ALM solution treatment may be, perhaps, a more appropriate choice. Specifically, for a sequence of penalty factors starting from zero, the initial ALM optimization problem becomes unconstrained and convex (quadratic form); thus, yielding a unique solution. Next, given that the sequence of penalty factors is sufficiently long and densely discretized, the ALM solution approach could potentially converge to the global optimum, at the expense, however, of considerable computational cost due to the large number of optimization subproblems; see Eq. (4.37).

In this regard, an alternative hybrid solution approach is proposed, which attempts to benefit from the advantages of both the ALM and the SQP schemes. Specifically, an ALM run is performed first by using a small number of penalty factors with moderate values and by setting large convergence tolerances to accelerate convergence. Of course, this ALM step is not expected to yield the optimum with high accuracy (see line with o markers in Fig. 4.9).

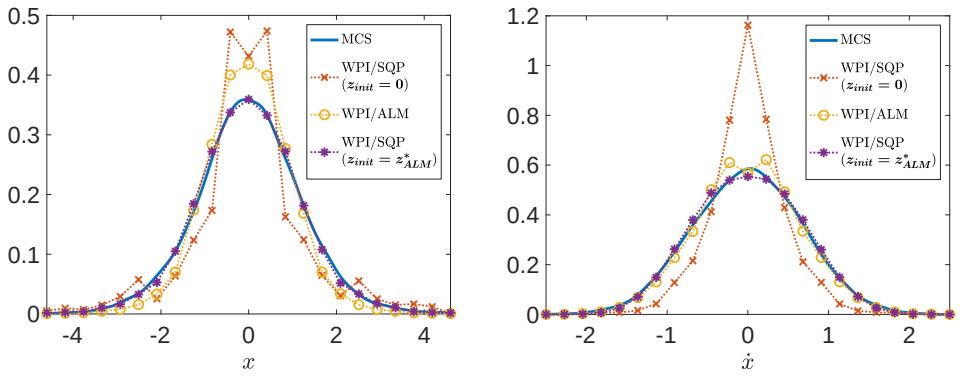

(a) $p(x)$ (b) $p(\dot{x})$

Figure 4.9: Marginal response PDFs of a SDOF Bouc-Wen oscillator at $t = 10$ s by employing various optimization schemes; comparisons with pertinent MCS data (10,000 realizations).

Instead, it is aimed to be used as a reasonable initial guess for the SQP methodology, which can now converge to a solution of relatively high accuracy (see line with * markers in Fig. 4.9) as compared to corresponding MCS data (10,000 realizations). Further, in Fig. 4.10 the marginal PDFs $p(x)$ and $p(\dot{x})$ are plotted for two indicative time instants as obtained by the above proposed hybrid ALM/SQP solution approach. In a similar manner as in Fig. 4.9, comparisons with relevant MCS data ($10,000$ realizations) show a relatively high degree of accuracy exhibited by the WPI technique. Indeed, despite the non-smooth character of the nonlinearities involved in the Bouc-Wen model (e.g., absolute value functions in Eq. (4.53)) that render the problem rather challenging, the herein developed technique has performed satisfactorily in determining the response statistics. The corresponding joint response PDF $p(x, \dot{x})$ is shown in Fig. 4.11.

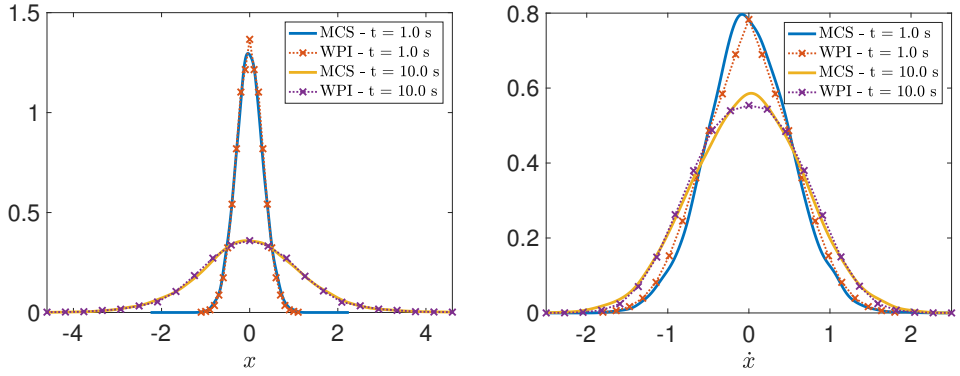

(a) $p(x)$ (b) $p(\dot{x})$

Figure 4.10: Marginal response PDFs of a SDOF Bouc-Wen oscillator determined by the combined ALM/SQP approach at $t = 1$ s and $t = 10$ s.

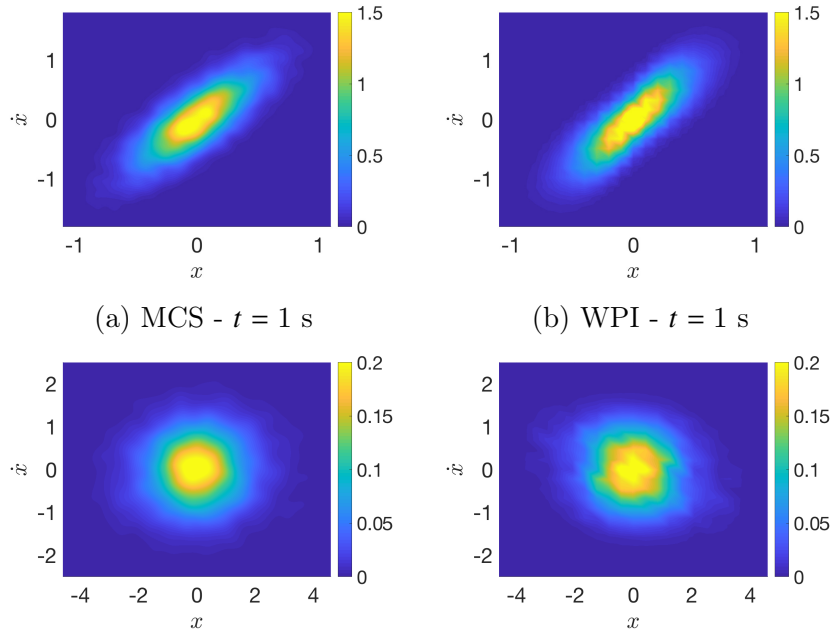

(a) MCS - $t = 1$ s (b) WPI - $t = 1$ s

(c) MCS - $t = 10$ s (d) WPI - $t = 10$ s

Figure 4.11: Joint response PDF $p(x, \dot{x})$ of a SDOF Bouc-Wen oscillator determined by the combined ALM/SQP approach at $t = 1$ s and $t = 10$ s

Chapter 5: Application: Design optimization of electromechanical energy harvesters under random vibration

5.1 Problem formulation

5.1.1 Modeling aspects

One of the most widely studied electromechanical energy harvesters consists of a cantilever beam with piezoelectric patches attached near its clamped ends as shown in Fig. 5.1a. The vibrating beam induces strain to the piezoelectric patches, and thus, electrical voltage is generated and energy is harvested with the aid of an electrical circuit connected to the patches. It has been shown experimentally [153, 50, 154] that intentional incorporation of system nonlinearities, typically realized by appropriate installation of magnets as shown in Fig. 5.1a, can potentially increase the harvested energy. This has been also verified numerically in several studies [155, 156, 47] in conjunction with a Duffing model to describe the mechanical nonlinearities. As discussed in detail in [47], the dynamics of such a system (see Fig. 5.1a) can be approximated by the following general mathematical model of coupled electromechanical equations, expressed in a non-dimensional form as

$$\ddot{x} + 2\zeta\dot{x} + \frac{dU(x)}{dx} + \kappa^2 y = w(t) \tag{5.1a}$$

$$\dot{y} + \alpha y - \dot{x} = 0 \tag{5.1b}$$

where x denotes the response displacement, and y represents the induced voltage in capacitative harvesters or the induced current in inductive ones. Further, ζ is the damping, κ is the coupling coefficient, α (referred to as the electrical constant in the following) is defined as the ratio between the mechanical and electrical time constants of the harvester (see [62]),

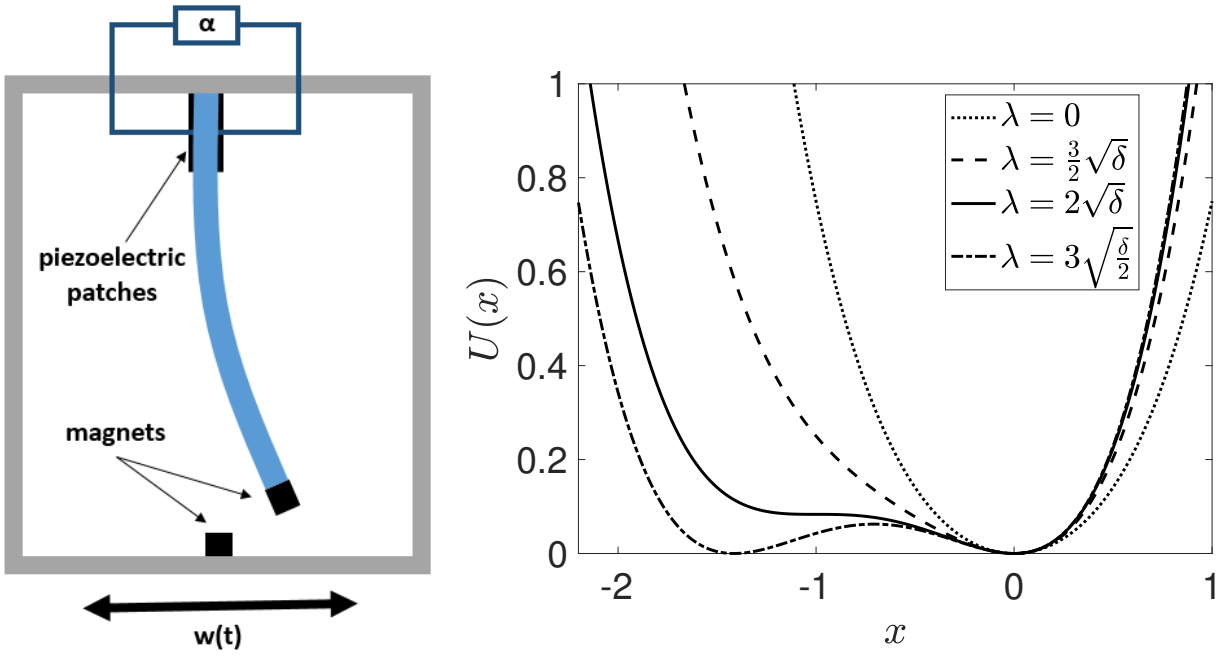

(a) (b)

Figure 5.1: (a) Schematic representation of the electromechanical energy harvesting device. (b) Various shapes of the potential function for $\delta = 1$.

and $U(x)$ denotes the potential function. Its derivative $\frac{dU(x)}{dx}$ represents the restoring force, which is nonlinear in general; see [47] for more details. Also, $w(t)$ represents the external excitation, which is modeled as a Gaussian white noise stochastic process with a constant power spectrum value S_0. Details regarding the non-dimensionalization of the governing equations can be found in [62] and [157].

In modeling the restoring force $\frac{dU(x)}{dx}$, a wide range of nonlinear behaviors can be captured by the 3^{rd} order polynomial

$$\frac{dU(x)}{dx} = x + \lambda x^2 + \delta x^3 \tag{5.2}$$

where λ and δ control the intensity of the quadratic and cubic nonlinear terms, respectively, while the coefficient corresponding to the linear stiffness term equals 1 as a result of the non-dimensionalization [62]. Further, considering the behavior of the potential function $U(x)$ for $\delta \geq 0$ (see Fig. 5.1b), Eq. (5.2) leads to a bistable asymmetric potential for $\lambda > 2\sqrt{\delta}$ (dashed-dotted line), to a monostable asymmetric potential for $0 < \lambda \leq 2\sqrt{\delta}$ (dashed line), and to

a monostable symmetric potential for $\lambda = 0$ (dotted line). As shown in [62], for $\lambda = 0$ and Gaussian white noise excitation, the maximum mean harvested power is achieved for $\delta = 0$, or in other words, the linear system is optimal; see also [158, 156, 159, 160] for a relevant discussion on the optimality of linear systems under certain conditions. Furthermore, it was shown in [63, 157] that utilizing nonlinear oscillators with symmetric bistable potentials, i.e., $\lambda = 0$ and a restoring force of the form $\frac{dU(x)}{dx} = -x + \delta x^3$, can be beneficial for maximizing the mean harvested power. In this regard, a question is posed naturally regarding the performance, in terms of harvesting efficiency, of potential functions with asymmetries, i.e., $\lambda \neq 0$. This was addressed in [161, 62] where the response statistics of monostable harvesters in the regime $0 \leq \lambda \leq 2\sqrt{\delta}$ were determined via statistical linearization. It was shown that the maximum mean harvested power is achieved for some $\delta > 0$ and for the bistability limit $\lambda = 2\sqrt{\delta}$ (solid line in Fig. 5.1b).

Further, it can be argued that models of electric circuits involving fractional derivative terms are, in general, in better agreement with experimental data than their traditionally used integer order counterparts. In fact, it has been shown that experimentally collected impedance data from a variety of energy storage systems (e.g. supercapacitors) can be best represented by fractional order models (e.g. [53, 54]).

Although there have been few recent research efforts to provide an enhanced version of Eq. (5.1) by incorporating fractional derivative terms in the electrical Eq. (5.1a) (e.g.[55, 56]), these have been either limited to considering cases of deterministic excitation only, or restricted to system response analysis without proposing any efficient optimization framework. In this paper, a class of nonlinear electromechanical energy harvesters with fractional order derivatives in the electrical equation and parameter $\lambda \leq 2\sqrt{\delta}$, with $\delta \geq 0$ (i.e., monostable asymmetric system) is considered. These systems are characterized by a single equilibrium position at $(x, y) = (0, 0)$. Following [56] for the fractional derivative modeling of the capaci-

tance, the coupled electromechanical system of equations takes the general form

$$\ddot{x} + 2\zeta\dot{x} + x + \lambda x^2 + \delta x^3 + \kappa^2 y = w(t) \tag{5.3a}$$

$$D^r y + \alpha y - \dot{x} = 0 \tag{5.3b}$$

where D^r is the r-th order fractional derivative operator, defined as

$$D^r[f(t)] = \frac{d^r f}{dt^r} = \frac{1}{\Gamma(1-r)} \int_{t_i}^{t} \frac{\dot{f}(\tau)}{(t-\tau)^r} \mathrm{d}\tau \tag{5.4}$$

Eq. (5.4) represents a Caputo fractional derivative of order $0 < r < 1$ (see also [162] for alternative fractional derivative definitions). Note that in the limit $r \to 1$ Eq. (5.3b) degenerates to Eq. (5.1b). Next, to provide some insight regarding the dynamics of the system of Eq. (5.3), Eq. (5.3a) can be construed as the governing stochastic differential equation (SDE) constrained by the fractional differential equation (FDE) of Eq. (5.3b). The system response vector process $\boldsymbol{q} = [x, \dot{x}, y]^T$ starts from initial conditions, exhibits a transient phase, and eventually reaches stationarity where the maximum response variance is observed. In this regard, the mean harvested power P_h is proportional to the stationary variance of the zero-mean electrical quantity y, and is given by (e.g. [47])

$$P_h = \alpha \mathbb{E}\{y^2\} \tag{5.5}$$

where $\mathbb{E}\{.\}$ represents the expectation operator. It is noted that in comparison with reference [18], not only the complexity of the governing equations (Eq. (5.1)) is increased by considering fractional derivative terms, but also the range of harvester design configurations to be studied herein is extended by allowing $\lambda \leq 2\sqrt{\delta}$ (unlike $\lambda = 2\sqrt{\delta}$ used in [18]).

5.1.2 Optimization aspects

From an optimal design perspective, the objective is typically expressed in the literature as maximizing the mean stationary harvested power P_h for a given excitation intensity S_0. This can be formulated as an optimization problem in the set of parameters $\{\zeta, \delta, \lambda, \kappa, \alpha\} \subseteq \mathbb{R}_+^5$, where $\mathbb{R}_+$ denotes the set of positive real numbers. Nevertheless, the complexity of the problem can be decreased by examining the impact of parameter κ on the system dynamics. Specifically, considering equations (5.1) and (5.5), it is seen that a larger coupling coefficient κ yields a larger variance of the electrical quantity y in a monotonic manner. As a result, κ should take the largest value possible, and thus, can be excluded from the optimization problem. The rest of the parameters affect the output harvested power in a more complex manner (see also [18] for a relevant discussion). Therefore, they need to be included in the optimization. In this regard, for the parameter vector $\boldsymbol{z} = [\alpha, \delta, \zeta, \lambda]$ and for κ and S_0 fixed, the harvester design problem can be formulated as an optimization problem of the form

$$\arg\max_{\boldsymbol{z} \in Z} P_h(\boldsymbol{z}) \tag{5.6}$$

where $Z \subset \mathbb{R}_+^4$ is an effective domain of parameter values.

Nevertheless, additional design criteria need to be considered in practice, which translate into constraints to be enforced. Such constraints can take the general form $P_f(\boldsymbol{z}) < \epsilon$, where the probability of failure P_f refers typically to an "extreme event" characterized by a low probability of occurrence. Indicatively, excessively high voltage levels, or extreme displacement values, may compromise the proper function of the electronic circuits, or may cause mechanical failure to the oscillator, respectively. In such cases, P_f can be defined as the probability that either $|x|$ or $|y|$ exceed some prescribed limit, i.e. $P_f = P(|x| > x_{limit} \text{ or } |y| > y_{limit})$. Taking such an additional design criterion into account, Eq. (5.6) is reformulated as

a reliability-based optimization problem in the form

$$\arg\max_{z \in Z} P_h(z) \quad \text{s.t.} \quad P_f(z) \leq \epsilon \tag{5.7}$$

Note, however, that if failure is defined as $|x| > x_{limit}$, the imposed limits on the displacement x are symmetric with respect to the equilibrium position $x = 0$. Although this may be a reasonable constraint definition for cases referring, for instance, to mechanical failures due to excessive levels of displacement, it is problematic when addressing the challenge of limited available space for the harvester. Specifically, it can be readily seen that since the herein considered harvesting system is asymmetric, employing such a failure definition does not exploit fully the available space; thus, leading potentially to an unnecessarily conservative design. In this regard, a more pragmatic approach regarding the failure criterion for such cases is proposed in the following. This relates to considering a box of specific width L_b, and to defining the probability of failure as the smallest probability of exceeding either end of the box for all possible locations of the harvester within the box. This is represented graphically and explained in Fig. 5.2a, which depicts the stationary marginal PDF of the response displacement x of a typical asymmetric harvester, positioned at two different locations within a box of width L_b. The thin solid curve denotes the PDF of the harvester with equilibrium position at $x = 0$, leading to a probability of failure $P_{f,1}$ (shaded red region). This configuration can be found by utilizing a constraint on the probability of failure of the form $P_f = P(|x| > x_{limit}) < \epsilon$ with $x_{limit} = \frac{L_b}{2}$. Further, the thick solid curve in Fig. 5.2a, represents the PDF of the same harvester, shifted by δx to the right to yield an overall lower probability of failure $P_{f,2} < P_{f,1}$ (shaded blue region). Thus, from a practical perspective, the optimal design of an asymmetric harvester subject to limited available space should, ideally, specify the location of the device (or more specifically, the location of its equilibrium position) within the box, so that the probability of failure is minimized (see Fig. 5.2b). This is typically achieved when P_f is "shared" by both tails in an optimal manner. In other words,

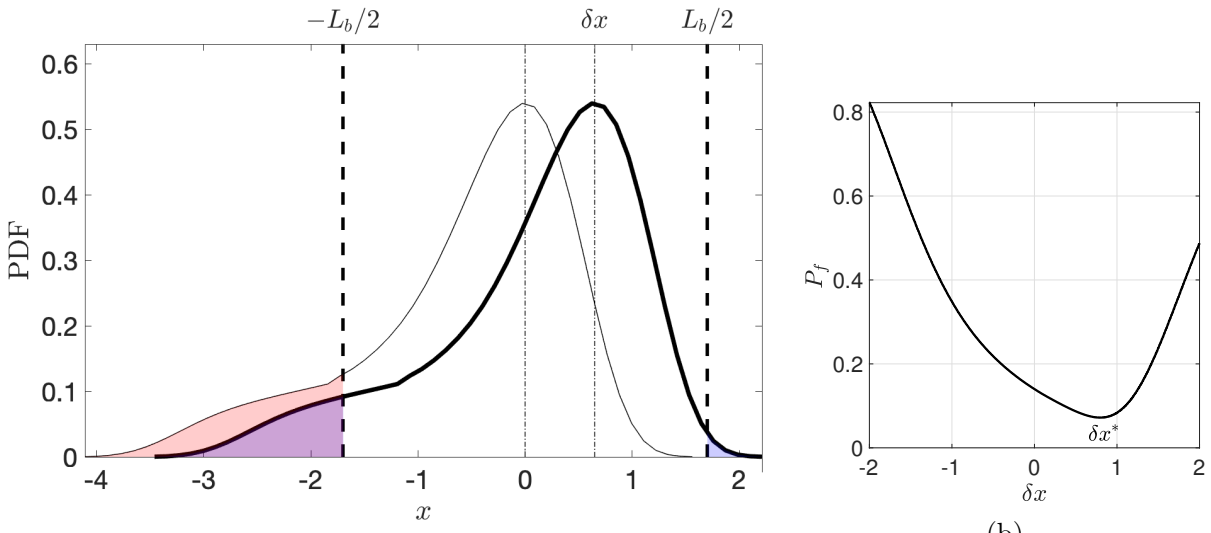

(a) (b)

Figure 5.2: Impact of the harvester location δx within a box of width L_b on the probability of failure P_f. (a) Stationary marginal PDFs of the response displacement x. **Thin solid curve**: $\delta x = 0$ yielding $P_{f,1}$. **Thick solid curve**: $\delta x > 0$ yielding $P_{f,2} < P_{f,1}$. (b) Relationship between δx and P_f, depicting a well defined optimal position.

the harvester should be placed within the box in a manner that exploits fully the available space for a given box width L_b.

In this regard, the location of a harvester's equilibrium position within the box, i.e., the shift parameter δx, needs to be considered as an additional unknown variable to be determined. Thus, the design optimization problem in Eq. (5.7) is adapted by considering the augmented variable vector $\boldsymbol{z}_{aug} = [\boldsymbol{z}, \delta x] = [\alpha, \delta, \zeta, \lambda, \delta x]$ and by defining the probability of failure P_f as

$$P_f(\boldsymbol{z}_{aug}) = 1 - S_{\boldsymbol{z}}(\delta x) \tag{5.8}$$

where

$$S_{\boldsymbol{z}}(u) = \int_{-\infty}^{\infty} \text{rect}\left(\frac{v}{L_b}\right) p_{\boldsymbol{z},s}(v+u)\mathrm{d}v \tag{5.9}$$

represents the survival probability and rect (.) is a rectangular pulse function defined as

$$\text{rect}\,(x) = \begin{cases} 0, & \text{if } |x| > \frac{1}{2} \\ \frac{1}{2}, & \text{if } |x| = \frac{1}{2} \\ 1, & \text{if } |x| < \frac{1}{2} \end{cases} \tag{5.10}$$

Also, Fig. 4.1b shows a typical behavior of Eq. (5.8) with respect to δx.

However, a closer examination of the objective function in Eq. (5.7), reveals that this depends only on $\boldsymbol{z}$, i.e., the variables α, δ, ζ and λ, whereas δx is involved only in the constraint. Moreover, for a given set of values $\boldsymbol{z}$, the optimal location δx^*, i.e., the one corresponding to minimal probability of failure, can be determined simply as

$$\delta x^* = \arg\max_u S_{\boldsymbol{z}}(u) \tag{5.11}$$

From a numerical optimization perspective, this enables the evaluation of the vector $\boldsymbol{z}$ at each iteration step independently of δx, followed by the estimation of the optimal δx^* by solving the rather trivial (1-dimensional) problem of Eq. 5.11. In other words, the optimization problem considers effectively only the four variables of vector $\boldsymbol{z}$ to be optimized simultaneously at each iteration, whereas the optimal location δx^* is provided essentially as a by-product. Thus, the complexity of the optimization problem relates, essentially, to a 4-dimensional problem involving $\boldsymbol{z}$, such as in Eq. (5.7) (as opposed to an augmented 5-dimensional problem involving $\boldsymbol{z}_{aug}$), whereas considering (5.11), Eq. (5.8) is written as

$$P_f(\boldsymbol{z}) = 1 - \max_u S_{\boldsymbol{z}}(u) \tag{5.12}$$

Further, a penalty approach is utilized herein for solving the constrained problem of Eq. (5.7). This yields an unconstrained problem with the modified objective function $P_{h,\epsilon}(\boldsymbol{z}) =$

$\mathbb{1}_\epsilon(\boldsymbol{z})P_h(\boldsymbol{z})$, where $\mathbb{1}_\epsilon$ is an indicator function defined as

$$\mathbb{1}_\epsilon(\boldsymbol{z}) = \begin{cases} 0, & P_f(\boldsymbol{z}) \geq \epsilon \\ 1, & \text{otherwise} \end{cases} \tag{5.13}$$

Considering that information regarding the gradient of the objective function $P_h(\boldsymbol{z})$ related to Eq. (5.7) is not available in general, the extended gradient-free Generalized Pattern Search (GPS) optimization algorithm is utilized next, which requires no assumptions about the differentiability and continuity of the objective function [163, 164, 119].

Obviously, knowledge of the harvester complete response PDF is required to be used in the optimization procedure, and not only of the response mean and variance that are typically determined in the literature. To this aim, the WPI stochastic response determination technique is adapted and applied herein in conjunction with the constrained optimization problem of Eq. (5.7). In comparison with reference [18], a more pragmatic version of the reliability-based constraints referring to space limitations is considered in Eq. (5.12), while the overall complexity of the optimization problem is increased. This is not only because of a more sophisticated modeling of Eq. (5.1) based on fractional derivatives, but also due to considering a higher dimensional vector $\boldsymbol{z}$; that is, five optimization variables (i.e., $[\alpha, \zeta, \lambda, \delta]$ and δx) are considered herein in contrast to the two variables in [18]. Hereinafter, the explicit dependence of a stationary marginal response PDF on $\boldsymbol{z}$ is suppressed for simplicity and $p_{\boldsymbol{z},s}(.)$ is denoted as $p_s(.)$.

5.2 Adaptation of the Wiener path integral technique to address the nonlinear electromechanical harvester with fractional derivative terms

5.2.1 Theoretical aspects

Considering Eq. (5.3), it can be readily seen that a straightforward application of Eq. (2.21) would lead to a singular matrix $\mathbf{D}$. Thus, the methodology presented in Chapter 4 is

required to account for the special form of Eq. (5.3). In this regard, in the ensuing analysis, Eq. (5.3a) is construed as an under-determined SDE with 2 unknown functions ($x(t)$ and $y(t)$), excited by the Gaussian white noise process $w(t)$. Setting $\boldsymbol{q} = [x, y]^T$, the corresponding Lagrangian is expressed as

$$\mathcal{L}(\boldsymbol{q}, \dot{\boldsymbol{q}}, \ddot{\boldsymbol{q}}) = \mathcal{L}(x, y, \dot{x}, \ddot{x}) = \frac{1}{4\pi S_0} \left[\ddot{x} + 2\zeta\dot{x} + x + \lambda x^2 + \delta x^3 + \kappa^2 y\right]^2 \tag{5.14}$$

Next, to account also for the impact of Eq. (5.1b) on the harvester dynamics, Eq. (5.1b) is treated as a dynamic constraint in the form

$$\phi(y, D^r y, \dot{x}) = D^r y + \alpha y - \dot{x} = 0 \tag{5.15}$$

Eq. (5.14) in conjunction with Eq. (5.15) lead to a fractional constrained variational problem of the form

$$\text{minimize} \quad \mathcal{J}(x, y, \dot{x}, \ddot{x}) = \int_{t_i}^{t_f} \mathcal{L}(x, y, \dot{x}, \ddot{x}) \mathrm{d}t \quad \text{subject to} \quad \phi(y, D^r y, \dot{x}) = 0 \tag{5.16}$$

with the boundary conditions

$$\begin{aligned} x(t_i) = x_i, \quad \dot{x}(t_i) = \dot{x}_i, \quad y(t_i) = y_i \\ x(t_f) = x_f, \quad \dot{x}(t_f) = \dot{x}_f, \quad y(t_f) = y_f \end{aligned} \tag{5.17}$$

In the following section, the numerical solution of Eqs. (5.16)-(5.17) is determined by formulating and employing a constrained optimization numerical scheme (e.g. [25]).

5.2.2 Numerical aspects

In this section, a Rayleigh–Ritz direct minimization approach is proposed for solving the constrained variational problem of equations (5.16)-(5.17), and for determining the most

probable path $\bar{\boldsymbol{q}}(t) = [\bar{x}(t), \bar{y}(t)]^T$.

In this regard, the standard Rayleigh–Ritz approach relies on an expansion for $\boldsymbol{q}(t)$ in the form $\boldsymbol{q}(t) \approx \hat{\boldsymbol{q}}(t) = \boldsymbol{\psi}(t) + \mathbf{C}\boldsymbol{h}(t)$, where $\boldsymbol{h}(t) = [h_0(t), ..., h_{L-1}(t)]^T$ is a basis of polynomial functions vanishing at the boundaries, $\boldsymbol{\psi}(t) = [\psi_1(t), ..., \psi_n(t)]^T$ is a vector of n polynomials satisfying the boundary conditions and $\mathbf{C} \in \mathbb{R}^{n \times L}$ is the expansion coefficient matrix, similarly to Sec. 2.3.2. Obviously, since this expansion satisfies the boundary conditions by construction, the functional minimization problem of equations (5.16)-(5.17) can be directly reformulated as an unconstrained optimization problem over the space of the coefficients $\mathbf{C}$. Note, however, that in the herein developed formulation, in addition to the boundary conditions of Eq. (5.17), the dynamic constraint of Eq. (5.15) needs to be accounted for as well. Thus, a standard implementation of the Rayleigh–Ritz approach would lead, unavoidably, to an overall constrained optimization problem (e.g. [18]). In this regard, an alternative formulation of the optimization problem is proposed next, which accounts for the boundary conditions and the dynamic constraint in a more direct and straightforward manner. Specifically, a standard polynomial expansion for $\boldsymbol{q}(t) = [x(t), y(t)]^T$ is adopted, which takes the form

$$\begin{bmatrix} \hat{x}(t) \\ \hat{y}(t) \end{bmatrix} = \mathbf{C}\boldsymbol{g}(t) = \begin{bmatrix} \boldsymbol{c}_x & \boldsymbol{c}_y \end{bmatrix}^T \boldsymbol{g}(t) \tag{5.18}$$

where $\boldsymbol{g}(t) = [g_0(t), ..., g_{L-1}(t)]^T$ is a basis of polynomial functions that are orthogonal in the interval $[t_i, t_f]$. In the ensuing analysis, the shifted Legendre polynomials given by the recursive formula

$$g_{p+1}(t) = \frac{2p+1}{p+1}\left(\frac{2t - t_i - t_f}{t_f - t_i}\right) g_p(t) - \frac{p}{p+1} g_{p-1}(t), \quad p = 1, 2, ... \tag{5.19}$$

are employed, with $g_0(t) = 1$; and $g_1(t) = (2t - t_i - t_f)/(t_f - t_i)$. Next, the first and second derivatives of $x(t)$ are expressed as $\dot{\hat{x}} = \boldsymbol{c}_x \dot{\boldsymbol{g}}$ and $\ddot{\hat{x}} = \boldsymbol{c}_x \ddot{\boldsymbol{g}}$, respectively, and thus, the functional

$\mathcal{J}(x, y, \dot{x}, \ddot{x})$ in Eq. (5.16) is approximated by the function

$$J(\boldsymbol{c}) = \mathcal{J}(\hat{x}, \hat{y}, \dot{\hat{x}}, \ddot{\hat{x}}) \tag{5.20}$$

where $\boldsymbol{c} = \begin{bmatrix} \boldsymbol{c}_x^T & \boldsymbol{c}_y^T \end{bmatrix}^T \in \mathbb{R}^{2L}$ is the vectorized form of $\mathbf{C} \in \mathbb{R}^{2\times L}$. Moreover, the fractional order derivative of $y(t)$ is expressed as

$$D^r \hat{y} = \boldsymbol{c}_y D^r \boldsymbol{g} \tag{5.21}$$

where $D^r \boldsymbol{g} = \{D^r[g_0(t)], ..., D^r[g_{L-1}(t)]\}^T$ is the vector of fractional derivatives of the L polynomial basis functions.

Clearly, compared to the classical Rayleigh–Ritz method, $[\hat{x}(t), \hat{y}(t)]^T$ in the expansion of Eq. (5.18) do not necessarily satisfy the boundary conditions of Eq. (5.17). To address this point, the initial and final boundary conditions of Eq. (5.17) are imposed explicitly as linear constraints of the form

$$\begin{aligned} \boldsymbol{A}_i \boldsymbol{c} &= \mathbf{b}_i \\ \boldsymbol{A}_f \boldsymbol{c} &= \mathbf{b}_f \end{aligned} \tag{5.22}$$

where the matrices $\boldsymbol{A}_i, \boldsymbol{A}_f \in \mathbb{R}^{3\times 2L}$ are given by

$$\boldsymbol{A}_i = \begin{bmatrix} \boldsymbol{g}(t_i)^T & \mathbf{0} \\ \mathbf{0} & \boldsymbol{g}(t_i)^T \\ \dot{\boldsymbol{g}}(t_i)^T & \mathbf{0} \end{bmatrix} \quad \text{and} \quad \boldsymbol{A}_f = \begin{bmatrix} \boldsymbol{g}(t_f)^T & \mathbf{0} \\ \mathbf{0} & \boldsymbol{g}(t_f)^T \\ \dot{\boldsymbol{g}}(t_f)^T & \mathbf{0} \end{bmatrix} \tag{5.23}$$

and the initial and final state vectors $\mathbf{b}_i$ and $\mathbf{b}_f$ take the form

$$\mathbf{b}_i = \begin{bmatrix} x_i \\ y_i \\ \dot{x}_i \end{bmatrix} \quad \text{and} \quad \mathbf{b}_f = \begin{bmatrix} x_f \\ y_f \\ \dot{x}_f \end{bmatrix} \tag{5.24}$$

Moreover, by employing the expansion of Eq. (5.18), the dynamic constraint $\phi(y, D^r y, \dot{x}) = 0$ of Eq. (5.16), which needs to be satisfied for all $t \in [t_i, t_f]$, is approximated by $\hat{\phi}(\boldsymbol{c}, t) = \phi(\hat{y}, D^r \hat{y}, \dot{\hat{x}}) = 0$, and is equivalently expressed as

$$\xi(\boldsymbol{c}) := \int_{t_i}^{t_f} [\hat{\phi}(\boldsymbol{c}, t)]^2 \mathrm{d}t = 0 \tag{5.25}$$

Next, taking into account both the constraint of Eq. (5.22) and the constraint of Eq. (5.25), the constrained variational problem in equations (5.16)-(5.17) is reformulated as a constrained optimization problem in the form

$$\begin{aligned} J^*_{\mathbf{b}_f} &= \min_{\boldsymbol{c} \in \mathbb{R}^{nL}} J(\boldsymbol{c}) \\ \text{subject to} \qquad & \xi(\boldsymbol{c}) = 0 \\ & \begin{bmatrix} \boldsymbol{A}_i \\ \boldsymbol{A}_f \end{bmatrix} \boldsymbol{c} = \begin{bmatrix} \mathbf{b}_i \\ \mathbf{b}_f \end{bmatrix} \end{aligned} \tag{5.26}$$

Further, according to Eq. (2.25) and assuming fixed initial conditions $\mathbf{b}_i$ at t_i (e.g., system initially at rest), a specific point of the response transition PDF corresponding to final state $\mathbf{b}_f$ at t_f is determined as

$$\hat{p}(\mathbf{b}_f, t_f | \mathbf{b}_i, t_i) = C \exp\left(-J^*_{\mathbf{b}_f}\right) \tag{5.27}$$

where C is a normalization constant. Obviously, choosing a sufficiently large final time instant t_f Eq. (5.27) converges to the stationary joint response PDF $p_s(\mathbf{b}_f) = \hat{p}(\mathbf{b}_f, t_f | \mathbf{b}_i, t_i)$. The optimization problem of Eq. (5.26), which has both linear and nonlinear equality constraints, is solved in the following examples by a standard interior point method presented in [165, 166].

5.3 Numerical examples

To demonstrate the reliability of the proposed technique for analyzing and optimizing energy harvesting systems, a mono-stable asymmetric nonlinear harvester ($0 \leq \lambda \leq 2\sqrt{\delta}, \delta \geq 0$) with a fractional derivative term described by Eq. (5.3) is considered in this section. First, to demonstrate the accuracy of the adapted WPI technique described in Sec. 5.2, the stationary marginal response PDFs are determined and compared with pertinent MCS data. Next, optimal energy harvester designs are obtained by employing the aforementioned WPI technique in conjunction with Eq. (5.5) as the objective function of a global optimization algorithm, constrained via a prescribed probability of failure (see Eq. (5.7) and Eq. (5.12)).

5.3.1 Energy harvester stochastic response analysis

The nonlinear energy harvester with mono-stable asymmetric potential (see Eq. (5.3)) and parameters $\zeta = 0.1$, $\kappa = 0.65$, $\alpha = 0.8$, $\delta = 0.2$ and $S_0 = 0.05$ is considered next. The stationary marginal response PDFs $p_s(x)$ and $p_s(y)$ for fractional derivative order $r = 0.75$ and for three (non-dimensional) time instants $t = 1$, $t = 10$ and $t = 20$ are shown in Fig. 5.3 and compared with pertinent MCS data. It is observed that the system has practically reached stationarity for $t = 10$. Clearly, the WPI technique exhibits a high degree of accuracy in determining the stochastic response of the nonlinear harvester, even for the challenging case of the strongly non-Gaussian and asymmetric displacement PDF $p_s(x)$.

Moreover, the stationary marginal response PDFs determined by the WPI technique for fractional derivative order r values 1, 0.75 and 0.5 are shown in Fig. 5.4 and compared with pertinent MCS data. The WPI technique exhibits a high degree of accuracy in determining the response PDFs, for all considered values of the fractional derivative order. Obviously, the impact of the fractional derivative order is larger on the electrical quantity y (as compared to x), since the fractional derivative in Eq. (5.1b) operates directly on y.

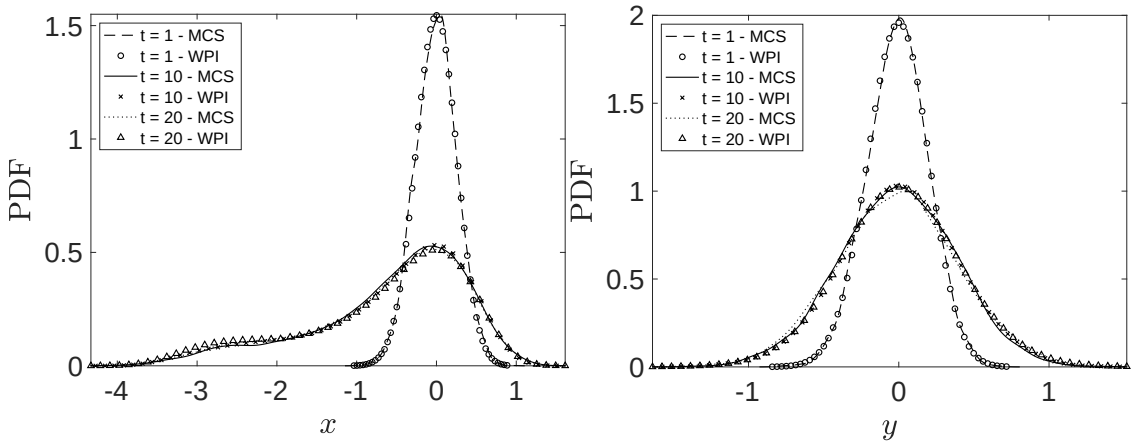

(a) displacement x (b) electrical quantity y

Figure 5.3: Marginal response PDFs of a nonlinear energy harvester with $\zeta = 0.1$, $\kappa = 0.65$, $\alpha = 0.8$, $\delta = 0.2$, $S_0 = 0.05$ and fractional derivative order $r = 0.75$ for three (non dimensional) time instants $t = 1$, $t = 10$ and $t = 20$. Comparison with MCS data (10, 000 realizations).

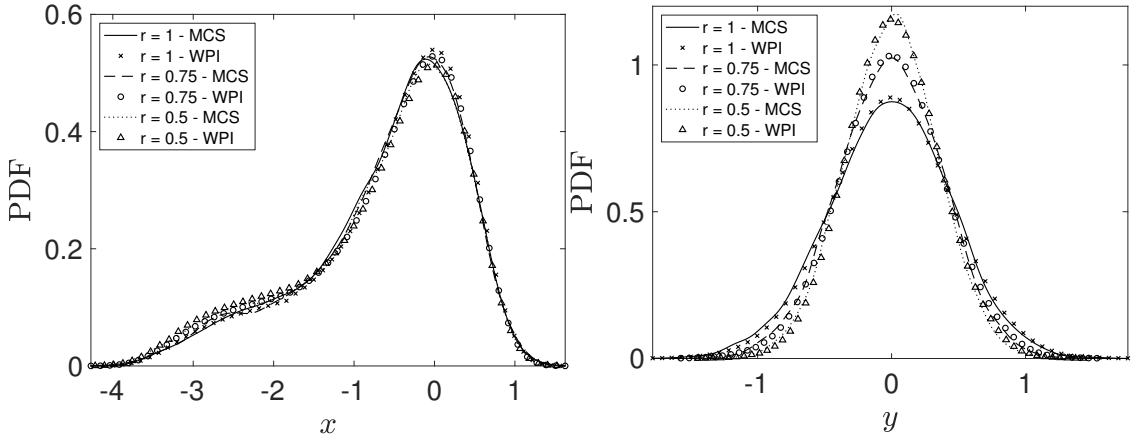

(a) displacement x (b) electrical quantity y

Figure 5.4: Stationary marginal response PDFs of a nonlinear energy harvester with $\zeta = 0.1$, $\kappa = 0.65$, $\alpha = 0.8$, $\delta = 0.2$ and $S_0 = 0.05$ for various values of the fractional derivative order $r = 1$, $r = 0.75$ and $r = 0.5$. Comparison with MCS data (10, 000 realizations).

5.3.2 Energy harvester design optimization

In this section, the results of a 4-parameter (α, δ ζ, λ) and a 2-parameter (α, δ) harvester design optimization problems, both with and without constraints related to probability of failure, are presented and discussed. In both cases, the optimal locations δx^* are provided as well according to the formulation in Sec. 5.1.2.

4-parameter design optimization

The general 4-parameter optimization problem is considered herein with $\boldsymbol{z} = [\alpha, \delta, \zeta, \lambda]^T \in [0.5, 3] \times [0, 5] \times [0.05, 0.2] \times [0, 2\sqrt{\delta}]$ and fractional derivative order $r = 1$. The GPS algorithm [163] is utilized for the solution of the optimization problem of Eq. (5.7) with constrained P_f defined in Eq. (5.12), whereas the unconstrained case is studied as well by setting $L_b \to \infty$.

Since the GPS algorithm is not guaranteed to converge to the global optimum, 5 optimization chains are considered, i.e., 5 independent optimization runs starting from different initial points, to increase the probability of converging to the global optimum. These 5 initial points are chosen based on the rationale described in the following. First, the 4-dimensional input space is discretized into a coarse grid of 961 points and the marginal PDFs of x and y corresponding to each grid point are obtained by utilizing the WPI technique presented in Sec. 5.2.2. Next, the points violating the condition $\lambda \leq 2\sqrt{\delta}$, and/or leading to failure with respect to the specific box size parameter L_b and probability threshold ϵ, are discarded. The 30 feasible points yielding the highest energy output P_h are identified and the one corresponding to the highest overall P_h value is selected as the first initial point. Further, the remaining 4 initial points for each optimization chain are chosen among the rest of the 29 points as the ones exhibiting the largest sum of distances with respect to the other points. Clearly, this procedure selects initial points with the following desirable properties: a) they are feasible; b) they are located in regions corresponding to high energy output; and c) they are reasonably dispersed over these high output regions.

The results of the 5 optimization chains for the unconstrained probability of failure case

($L_b \to \infty$) are plotted in Fig. 5.5 as projections on 2D planes, where the color of the circles varies with the iteration number (starting from dark blue and converging to yellow). This representation provides a crude illustration of the optimization solution path in the 4-dimensional space. It is seen, that the 5 chains converged to different points characterized by different mean harvester power outputs, and that all converged points are located on the bistability limit $\lambda = 2\sqrt{\delta}$. Moreover, the optimal parameter ζ^* reaches its lower bound of 0.05 (see figures 5.5d-5.5f). This is anticipated as a mechanical system with low damping leads to higher amplitude vibrations, and thus, to higher harvested power.

However, in many practical implementations, space limitations dictate constraints on the vibration amplitude, such as the one described by Eqs. (5.7)-(5.12). In this regard, and focusing on the constrained optimization problem of Eqs. (5.7)-(5.12) with $\epsilon = 10^{-3}$, the results of the 5 optimization chains are shown in Fig. 5.6 for two design examples with $L_b = 2.4$ (figures 5.6a,5.6c,5.6e) and $L_b = 3$ (figures 5.6b,5.6d,5.6f). In these examples, some chains converge to designs, which do not correspond to the bistability limit ($\lambda = 2\sqrt{\delta}$). In fact, it can be seen in Fig. 5.6e that for a relatively "tight" box with $L_b = 2.4$, the global optimum found yields a symmetric harvester, i.e., $\lambda \approx 0$. This trend is evident in Tab. 5.1, which summarizes the optimal (among the 5 chains) results, for various examples with increasing L_b, including the unconstrained case ($L_b = \infty$). Indeed, note that for $L_b < 2.9$, the optimal harvester is approximately symmetric ($\lambda \approx 0$), whereas for $L_b \geq 2.9$ the constraint on the probability of failure becomes less severe and asymmetric designs appear to yield higher power output. In fact, these asymmetric designs tend to converge to the bistability limit with $\lambda = 2\sqrt{\delta}$. Moreover, as the available space L_b decreases, the parameter δ^* is increased to provide additional stiffness and restrict the oscillator within the gradually tighter bounds.

2-parameter design optimization

According to the results of the 4-parameter design optimization examples presented in Tab. 5.1, ζ^* always takes its lower bound value, while λ^* converges either to its lower

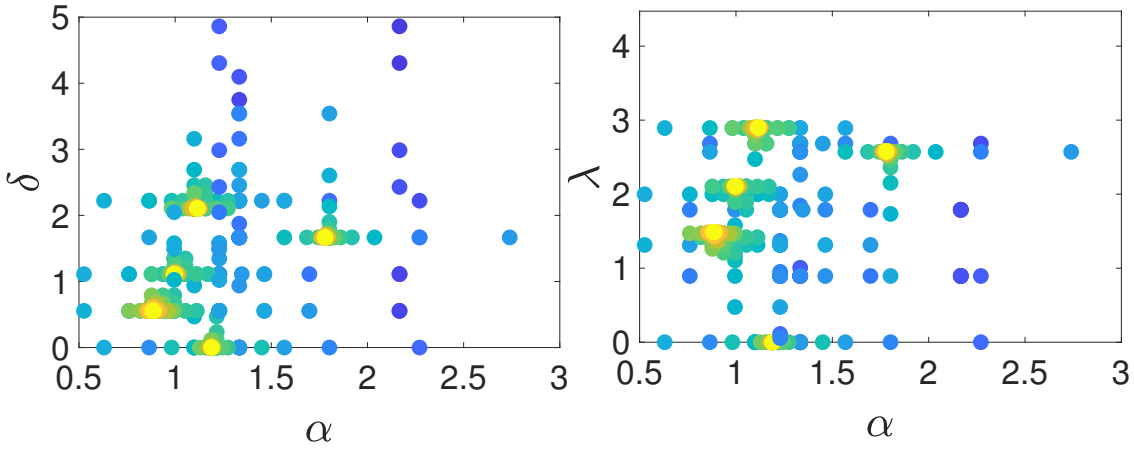

(a) $L_b = \infty$, α-δ plane

(b) $L_b = \infty$, α-λ plane

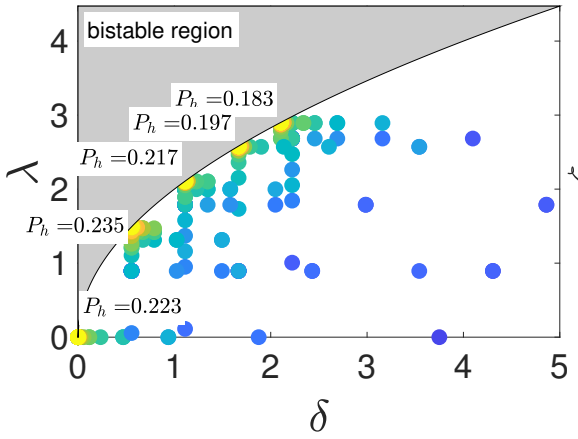

(c) $L_b = \infty$, δ-λ plane

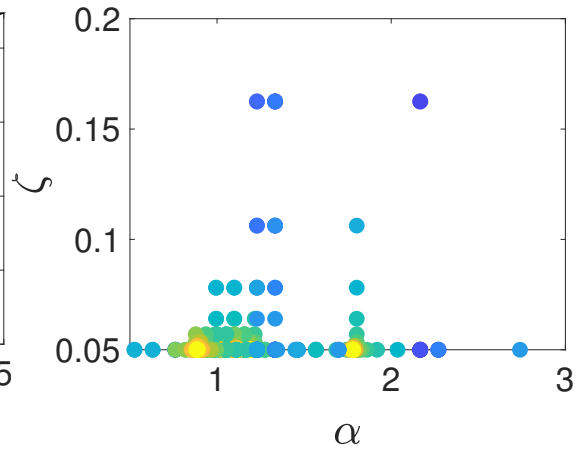

(d) $L_b = \infty$, α-ζ plane

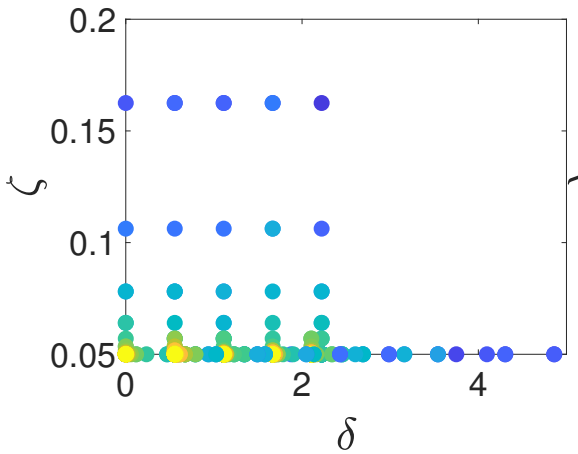

(e) $L_b = \infty$, δ-ζ plane

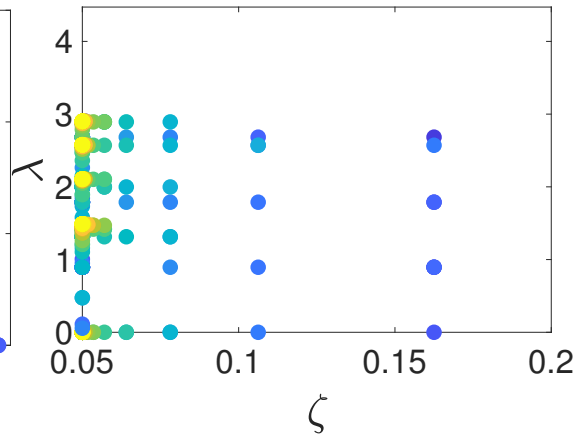

(f) $L_b = \infty$, ζ-λ plane

Figure 5.5: 2D projections of computed points (color varies with iteration count). Optimization by GPS algorithm with $\boldsymbol{z} = [\alpha, \delta, \zeta, \lambda]^T \in [0.5, 3] \times [0, 5] \times [0.05, 0.2] \times [0, 2\sqrt{\delta}]$, $\kappa = 0.65$, $r = 1$ and unconstrained probability of failure ($L_b = \infty$).

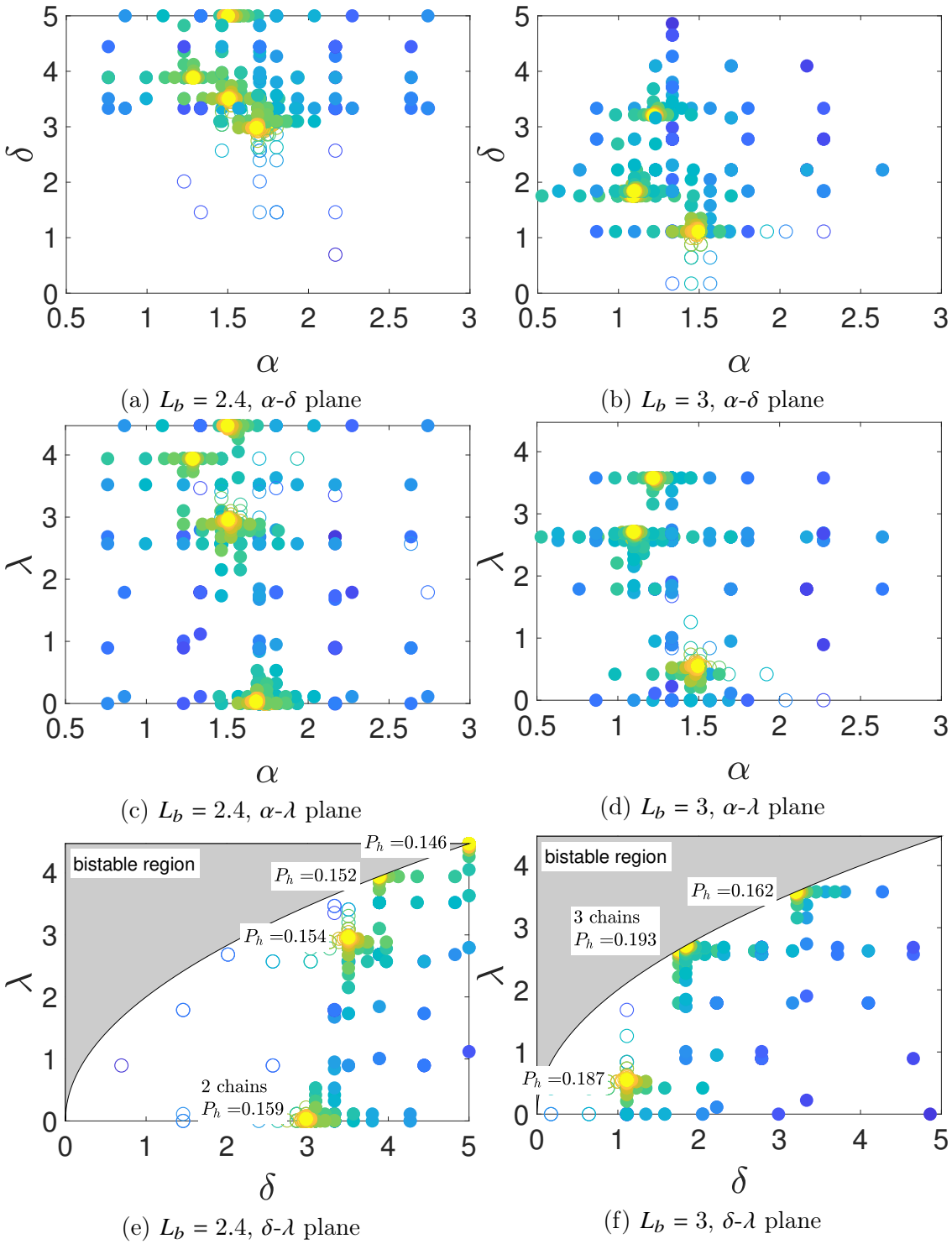

(a) $L_b = 2.4$, α-δ plane

(b) $L_b = 3$, α-δ plane

(c) $L_b = 2.4$, α-λ plane

(d) $L_b = 3$, α-λ plane

(e) $L_b = 2.4$, δ-λ plane

(f) $L_b = 3$, δ-λ plane

Figure 5.6: 2D projections of computed points (color varies with iteration count and unfilled circles correspond to probabilities of failure larger that ϵ). Optimization by GPS algorithm with $\boldsymbol{z} = [\alpha, \delta, \zeta, \lambda]^T \in [0.5, 3] \times [0, 5] \times [0.05, 0.2] \times [0, 2\sqrt{\delta}]$, $\kappa = 0.65$, $r = 1$ and constrained probability of failure with L_b equal to 2.4 (5.6a,5.6c,5.6e) and 3 (5.6b,5.6d,5.6f) and $\epsilon = 10^{-3}$.

Table 5.1: Summary of optimal energy harvester designs for $\boldsymbol{z} = [\alpha, \delta, \zeta, \lambda]^T \in [0.5, 3] \times [0, 5] \times [0.05, 0.2] \times [0, 2\sqrt{\delta}]$, $\kappa = 0.65$, $r = 1$ and different box sizes L_b. Unconstrained ($L_b = \infty$) and constrained probability of failure with $\epsilon = 10^{-3}$.

Box size	Optimal design					Average	Probability of
L_b	α^*	δ^*	ζ^*	λ^*	δx^*	power P_h	failure P_f
2.3	1.761	3.573	0.05	0.000	0.000	0.1514	0.000999
2.4	1.678	2.982	0.05	0.033	0.005	0.1593	0.000997
2.5	1.678	2.510	0.05	0.013	0.002	0.1635	0.000994
2.6	1.640	2.112	0.05	0.003	0.001	0.1701	0.000999
2.7	1.610	1.810	0.05	0.105	0.025	0.1736	0.000936
2.8	1.557	1.503	0.05	0.004	0.001	0.1807	0.000993
2.9	1.115	1.973	0.05	2.809	0.565	0.1864	0.000780
3.0	1.090	1.753	0.05	2.648	0.557	0.1926	0.000727
∞	0.887	0.556	0.05	1.491	-	0.2349	0.000000

allowable value of 0 or to the bistability limit $2\sqrt{\delta}$. Motivated by the above observations, a 2-parameter design optimization is pursued in this section aiming at enhanced computational efficiency and more robust convergence behavior. Specifically, $\boldsymbol{z}$ in Eq. (5.7) becomes $\boldsymbol{z} = [\alpha, \delta]^T \in [0.5, 3] \times [0, 5]$ with $\zeta = 0.05$, $\kappa = 0.65$. Two distinct values of lamda are considered in the examples, i.e., $\lambda = 0$ and $\lambda = 2\sqrt{\delta}$. Notably, employing a similar approach as in Sec. 5.3.2, all 5 optimization chains applied for a given set of fixed parameters converged to the same optimal point. Clearly, this indicates that the 2-parameter optimization exhibits a more robust convergence behavior than its 4-parameter counterpart. For various values of the box size parameter L_b the converged optimal points are presented in Tab. 5.2 for $\lambda = 0$ and in Tab. 5.3 for $\lambda = 2\sqrt{\delta}$. Moreover, Fig. 5.7 depicts the points accessed by the 5 optimization chains for $\lambda = 2\sqrt{\delta}$, and box size parameter L_b equal to 2.4, 3 and ∞.

It is seen in tables 5.2 and 5.3 that, similarly to the 4-parameter optimization of Sec. 5.3.2, for relatively small box sizes L_b the symmetric design ($\lambda = 0$ - Tab. 5.2) outperforms the asymmetric design ($\lambda = 2\sqrt{\delta}$ - Tab. 5.3), whereas as L_b increases, asymmetry leads to higher energy output, even for the unconstrained case ($L_b = \infty$). Further, the theoretically supported fact (e.g. [156, 158, 159, 160]), that the linear design, i.e., $\delta = 0$, is optimal among symmetric ($\lambda = 0$) and unconstrained ($L_b \to \infty$) harvesters, is further corroborated by the

Table 5.2: Summary of optimal energy harvester designs for $\boldsymbol{z} = [\alpha, \delta]^T \in [0.5, 3] \times [0, 5]$, $\lambda = 0$, $\zeta = 0.05$, $\kappa = 0.65$, $r = 1$ and different box sizes L_b. Unconstrained ($L_b = \infty$) and constrained probability of failure with $\epsilon = 10^{-3}$.

Box size	Optimal design			Average	Probability of
L_b	α^*	δ^*	δx^*	power P_h	failure P_f
2.3	1.765	3.574	0.000	0.1516	0.001000
2.4	1.750	3.008	0.000	0.1578	0.000971
2.5	1.672	2.578	0.000	0.1624	0.000879
2.6	1.638	2.130	0.000	0.1680	0.000962
2.7	1.589	1.782	0.000	0.1738	0.000991
2.8	1.560	1.509	0.000	0.1787	0.000982
2.9	1.574	1.289	0.000	0.1837	0.000969
3.0	1.480	1.082	0.000	0.1906	0.000995
∞	1.190	0.000	-	0.2231	0.000000

Table 5.3: Summary of optimal energy harvester designs for $\boldsymbol{z} = [\alpha, \delta]^T \in [0.5, 3] \times [0, 5]$, $\lambda = 2\sqrt{\delta}$, $\zeta = 0.05$, $\kappa = 0.65$, $r = 1$ and different box sizes L_b. Unconstrained ($L_b = \infty$) and constrained probability of failure with $\epsilon = 10^{-3}$.

Box size	Optimal design			Average	Probability of
L_b	α^*	δ^*	δx^*	power P_h	failure P_f
2.3	1.325	4.407	0.442	0.1465	0.000997
2.4	1.284	3.801	0.488	0.1533	0.000999
2.5	1.252	3.259	0.516	0.1607	0.000905
2.6	1.188	2.823	0.537	0.1677	0.000996
2.7	1.195	2.477	0.550	0.1746	0.000989
2.8	1.130	2.178	0.558	0.1817	0.000972
2.9	1.103	1.917	0.559	0.1898	0.000992
3.0	1.086	1.659	0.572	0.1952	0.000963
∞	0.890	0.459	-	0.2373	0.000000

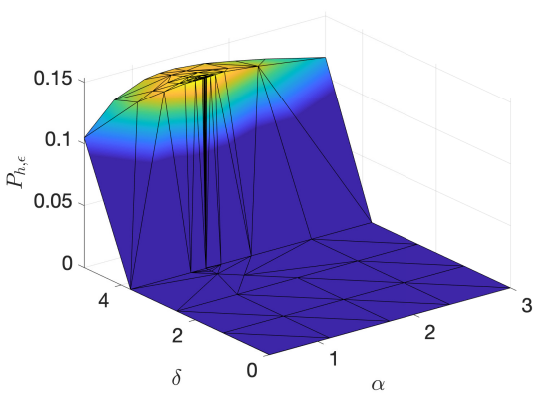

(a) 3D plot - $L_b = 2.4$

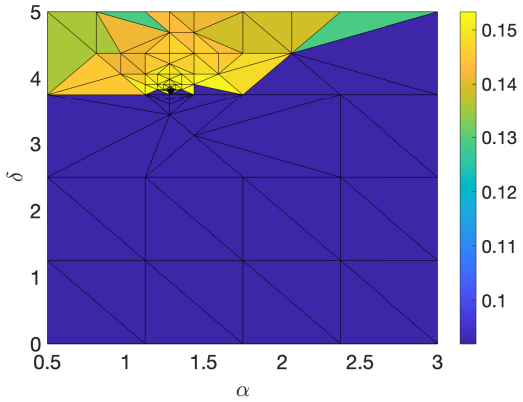

(b) overview plot - $L_b = 2.4$

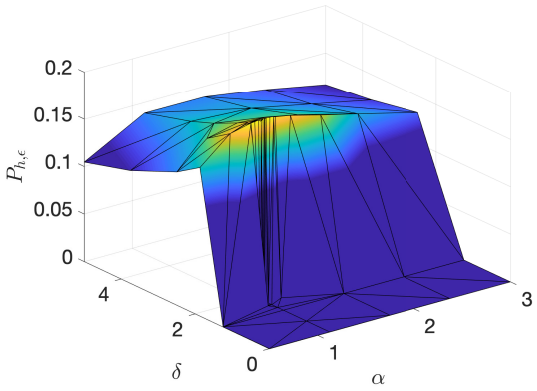

(c) 3D plot - $L_b = 3$

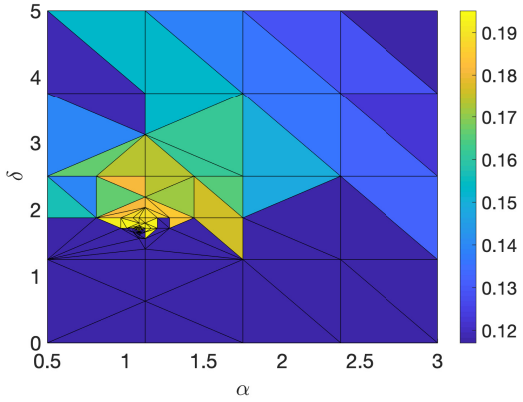

(d) overview plot - $L_b = 3$

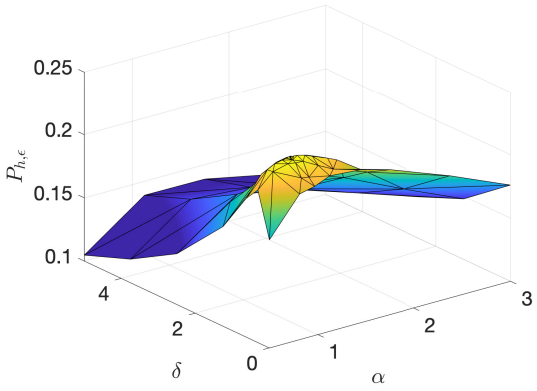

(e) 3D plot - $L_b = \infty$

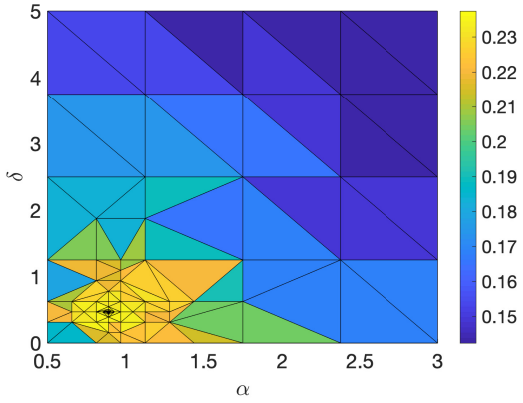

(f) overview plot - $L_b = \infty$

Figure 5.7: Stationary mean harvested power P_h. Optimization by GPS algorithm with $\boldsymbol{z} = [\alpha, \delta]^T \in [0.5, 3] \times [0, 5]$, $\lambda = 2\sqrt{\delta}$, $\zeta = 0.05$, $\kappa = 0.65$, $r = 1$. (a),(c) and (e): 3D surface plots with gradient coloring. (b),(d) and (f): overview plots with flat coloring.

herein analysis; see last row of Tab. 5.2. In contrast, it appears that the introduction of asymmetric nonlinearities, i.e., $\delta > 0$ and $\lambda = 2\sqrt{\delta}$ yields designs that outperform significantly the linear design in terms of energy output; this is also in agreement with conclusions drawn in [161, 62, 18] based on relevant numerical studies. Moreover, considering the shape of the surface plots in Fig. 5.7, and that all 5 chains converged to the same point, indicates the existence of a single (global) optimum for the 2-parameter optimization case.

Next, attention is directed to three indicative optimal harvesters in Tab. 5.3 with L_b values of 2.4, 3 and ∞. The corresponding stationary marginal response PDFs $p_s(x)$ and $p_s(y)$ are obtained by employing the herein adapted WPI technique. These are plotted in Fig. 5.8 and compared with MCS data. Besides the relatively high degree of accuracy exhibited by the WPI technique, it is seen in figures 5.8a and 5.8c that the optimal shape of $p_s(x)$ tends towards a rectangular form. This is anticipated, since this particular shape of $p_s(x)$ leads, in general, to low probability of failure. Also, it corresponds to a relatively higher variance of x, and therefore (see Eq. (5.1a)), to a higher variance of y as well, i.e., higher energy output (see Eq. 5.5).

2-parameter design optimization for various fractional derivative order values

In this subsection, the 2-parameter design optimization problem of Sec. 5.3.2 is considered for harvesters with $\lambda = 2\sqrt{\delta}$ and with two distinct fractional derivative order values, i.e., $r = 0.75$ and $r = 0.50$. The results are summarized in Tab. 5.4 for $r = 0.75$ and in Tab. 5.5 for $r = 0.50$. The conclusions are similar to Sec. 5.3.2 (see Tab. 5.3), while it is evident that the energy output decreases for decreasing fractional derivative order r as shown in Sec. 5.3.1 (see Fig. 5.4b).

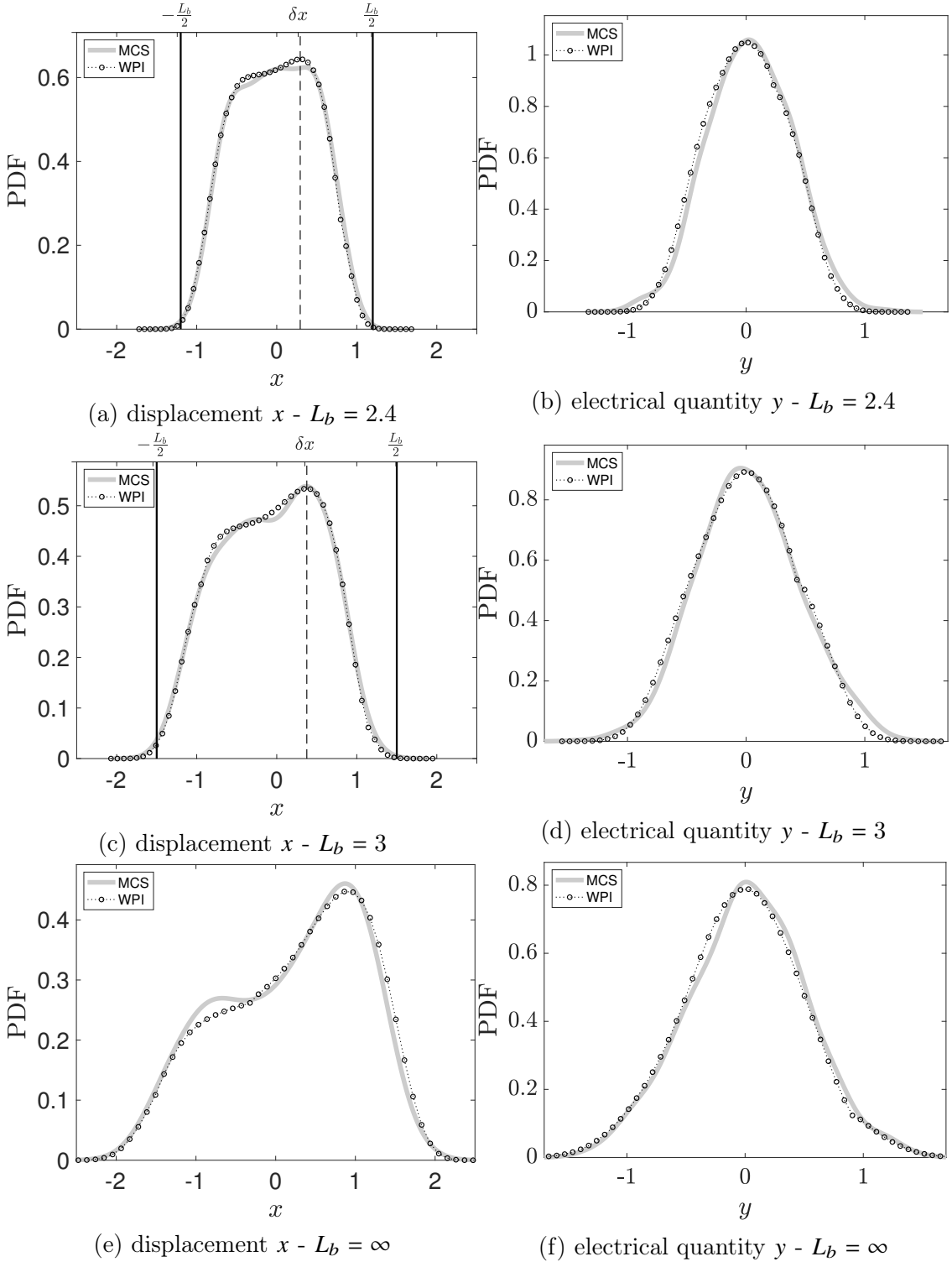

(a) displacement x - $L_b = 2.4$

(b) electrical quantity y - $L_b = 2.4$

(c) displacement x - $L_b = 3$

(d) electrical quantity y - $L_b = 3$

(e) displacement x - $L_b = \infty$

(f) electrical quantity y - $L_b = \infty$

Figure 5.8: Response PDFs of three optimal designs corresponding to box size parameter L_b values of 2.4, 3 and ∞; see second, eighth and ninth rows of Tab. 5.3, respectively, for optimal design parameters (α^*, δ^*), shift parameter δx, mean harvested power P_h and probability of failure P_f.

Table 5.4: Summary of optimal energy harvester designs for $\boldsymbol{z} = [\alpha, \delta]^T \in [0.5, 3] \times [0, 5]$, $\lambda = 2\sqrt{\delta}$, $\zeta = 0.05$, $\kappa = 0.65$, $r = 0.75$ and different box sizes L_b. Unconstrained ($L_b = \infty$) and constrained probability of failure with $\epsilon = 10^{-3}$.

Box size	Optimal design			Average	Probability of
L_b	α^*	δ^*	δx^*	power P_h	failure P_f
2.3	1.408	4.531	0.429	0.1235	0.000917
2.4	1.359	3.906	0.476	0.1280	0.000907
2.5	1.398	3.350	0.509	0.1331	0.000983
2.6	1.555	2.969	0.521	0.1377	0.000941
2.7	1.440	2.617	0.540	0.1419	0.000832
2.8	1.438	2.266	0.552	0.1471	0.000953
2.9	1.379	1.992	0.559	0.1505	0.000881
3.0	1.474	1.783	0.553	0.1593	0.000916
∞	1.047	0.625	-	0.1767	0.000000

Table 5.5: Summary of optimal energy harvester designs for $\boldsymbol{z} = [\alpha, \delta]^T \in [0.5, 3] \times [0, 5]$, $\lambda = 2\sqrt{\delta}$, $\zeta = 0.05$, $\kappa = 0.65$, $r = 0.50$ and different box sizes L_b. Unconstrained ($L_b = \infty$) and constrained probability of failure with $\epsilon = 10^{-3}$.

Box size	Optimal design			Average	Probability of
L_b	α^*	δ^*	δx^*	power P_h	failure P_f
2.3	1.398	4.492	0.433	0.1102	0.000920
2.4	1.438	3.866	0.478	0.1136	0.000975
2.5	1.357	3.330	0.513	0.1177	0.000942
2.6	1.320	2.930	0.533	0.1213	0.000867
2.7	1.276	2.490	0.553	0.1252	0.000989
2.8	1.342	2.224	0.559	0.1288	0.000983
2.9	1.474	2.012	0.556	0.1317	0.000981
3.0	1.408	1.787	0.556	0.1369	0.000901
∞	1.875	1.000	-	0.1569	0.000000

Part II

Computational algebraic geometry and Gröbner bases

Chapter 6: Solution of algebraic polynomial systems of equations with Gröbner bases

In this section, a computational algebraic technique based on Gröbner bases is developed, which is capable of determining the entire set of solutions corresponding to an algebraic system of coupled multivariate polynomial equations of the form

$$\begin{aligned} f_1(z_1,..., z_p) &= 0 \\ &\vdots \\ f_s(z_1,..., z_p) &= 0 \end{aligned} \tag{6.1}$$

Indicatively, the interested reader is also directed to papers [167, 168, 169] and to books [69, 70, 71, 72, 73] for a more detailed presentation of the topic.

6.1 Algebraic geometry: Selected basic elements and concepts

In this section, selected basic elements and concepts of algebraic geometry are presented for completeness, including certain fundamental results to be used in the following.

Definition 6.1.1 (Polynomial Ring) *A polynomial ring over a field $\mathbb{K}$ is defined as the set of all polynomials in p variables with coefficients in $\mathbb{K}$ and is denoted as $\mathbb{K}[z_1, ..., z_p]$.*

Definition 6.1.2 (Affine Variety) *Let $f_1, ..., f_s$ be polynomials in $\mathbb{K}[z_1, ..., z_p]$, then*

$$\boldsymbol{V}(f_1, ..., f_s) = \{(a_1, ..., a_n) \in \mathbb{K}^n \mid f_i(a_1, ..., a_n) = 0 \quad \forall\ i = 1, ..., s\}$$

is the affine variety defined by $f_1, ..., f_s$.

Based on Definition 6.1.2, the entire set of solutions of a polynomial system of the form of Eq. (6.1) constitutes an affine variety. Further, it is noted that an affine variety can be construed as a generalization of the concept of nullspace, referring to linear transformations in vector spaces, to consider polynomial transformations in polynomial rings. Also, a linear subspace is a subset of a vector space with certain properties. A similar concept corresponding to a polynomial ring is referred to as an ideal and is formally defined next.

Definition 6.1.3 (Ideal) *A subset* $I \subseteq \mathbb{K}[z_1, ..., z_p]$ *is an ideal if:*

(i) $0 \in I$

(ii) If $f, g \in I$*, then* $f + g \in I$

(iii) If $f \in I$ *and* $h \in \mathbb{K}[z_1, ..., z_p]$*, then* $hf \in I$

An ideal can be defined by an arbitrary collection of polynomials $F = \{f_1, ..., f_s\}$ in $\mathbb{K}[z_1, ..., z_p]$ as

$$\langle f_1, ..., f_s \rangle = \left\{ \sum_{i=1}^{s} h_i f_i \mid h_1, ..., h_s \in \mathbb{K}[z_1, ..., z_p] \right\} \tag{6.2}$$

and is referred to as the ideal generated by $f_1, ..., f_s$. It is seen that $F = \{f_1, ..., f_s\}$ forms a basis for the ideal $\langle f_1, ..., f_s \rangle$ in the sense that every element in $\langle f_1, ..., f_s \rangle$ can be constructed as a combination of elements in F with elements in $\mathbb{K}[z_1, ..., z_p]$. In fact, according to a fundamental result in algebraic geometry, known as Hilbert's Basis Theorem, every ideal $I \subseteq \mathbb{K}[z_1, ..., z_p]$ has a finite generating set, i.e., $I = \langle g_1, ..., g_t \rangle$ for some $g_1, ..., g_t \in I$. The interested reader is directed to [72] for a detailed proof.

Further, consider the ideal $\boldsymbol{I}(V)$ related to the affine variety $V \in \mathbb{K}^p$ defined as

$$\boldsymbol{I}(V) = \{f \in \mathbb{K}[z_1, ..., z_p] \mid f(\alpha) = 0 \ \forall \ a \in V\} \tag{6.3}$$

In Eq. (6.3), $\boldsymbol{I}(V)$ represents the ideal containing all polynomials that vanish on V. In other words, V is the set of common solutions of all (infinite in number) polynomials in $\boldsymbol{I}(V)$ (e.g.,

[72]). Note that Eq. (6.3) can be construed as a mapping from a finite set of vectors V to an infinite set of polynomials $\boldsymbol{I}(V)$. In this regard, it is also possible to define a mapping in the form

$$\boldsymbol{V}(I) = \{(\alpha_1, ..., \alpha_n) \in \mathbb{K}^n \mid f(\alpha_1, ..., \alpha_n) = 0 \ \forall \ f \in I\} \tag{6.4}$$

Hilbert's Basis Theorem can be used to prove that $\boldsymbol{V}(I)$ in Eq. (6.4) is an affine variety (see [72]). In particular, if $I = \langle f_1, ..., f_s \rangle$, then

$$\boldsymbol{V}(I) = \boldsymbol{V}(f_1, ..., f_s) \tag{6.5}$$

It can be readily seen in Eq. (6.5) that although a nonzero ideal I always contains an infinite number of polynomials, the set $\boldsymbol{V}(I)$ can be defined based on a finite set of polynomial equations. Also, Eq. (6.5) demonstrates that the common solutions of all the polynomials in an ideal coincide with the common solutions of its generating polynomials.

Next, Theorem 1 is presented, which relates to the celebrated Hilbert's Nullstellensatz (e.g., [72]). The interested reader is directed to [72] for a detailed proof.

Theorem 1 (Weak Nullstellensatz) *Let $\mathbb{K}$ be an algebraically closed field and $I \subseteq \mathbb{K}[z_1, ..., z_p]$ be an ideal satisfying $\boldsymbol{V}(I) = \varnothing$. Then $I = \mathbb{K}[z_1, ..., z_p]$.*

Theorem 1 shows that the system of polynomial equations in Eq. (6.1) may not have a solution only under the condition that the ideal it generates is equal to the associated polynomial ring, i.e., $I = \langle f_1, ..., f_s \rangle = \mathbb{K}[z_1, ..., z_p]$. However, $\mathbb{K}[z_1, ..., z_p]$ is generated by 1, since $\langle 1 \rangle = \mathbb{K}[z_1, ..., z_p]$, and thus, Eq. (6.5) shows that the only system of polynomial equations without a solution is the system $1 = 0$. This can only hold true under the condition that the field $\mathbb{K}$ is algebraically closed (e.g., [72]). Taking into account that the algebraic closure of $\mathbb{R}$ is $\mathbb{C}$, the weak Nullstellensatz can be construed as a generalization of the Fundamental Theorem of Algebra, which states that any non-constant polynomial in one variable with coefficients in $\mathbb{C}$ has at least one root in $\mathbb{C}$. Accordingly, any system of non-constant polynomial

equations with coefficients in $\mathbb{C}$ has at least one solution in $\mathbb{C}$. The following section pertains to techniques relying on the aforementioned algebraic geometry results for determining the entire set of solutions (assumed to be of a finite number).

6.2 Computational algebraic geometry: Selected basic elements and concepts

In this section, fundamental results related to computer implementations of algebraic geometry concepts are presented for determining the entire set of solutions of Eq. (6.1) in an algebraic symbolic manner.

First, defining a precise monomial order denoted by $>$ is a prerequisite for the ensuing analysis. Indicative standard monomial orders include the lexicographical order (*lex*), the graded lexicographical order (*grlex*) and the reverse graded lexicographical order (*grevlex*). Following the selection of an order $>$, $LT(f)$ is defined as the leading term of a polynomial $f \in \mathbb{K}[z_1, ..., z_p]$ with respect to the order $>$. Similarly, $LM(f)$ denotes the leading monomial of f, i.e., the monomial of $LT(f)$. Moreover, for an ideal $I \subseteq \mathbb{K}[z_1, ..., z_p]$, $LT(I)$ denotes the ideal generated by the leading terms of every element in I, i.e., $LT(I) = \langle LT(f) | f \in I \rangle$. Also, for an ideal $I = \langle f_1, ..., f_s \rangle$, the following property is satisfied; that is,

$$\langle LT(f_i), ..., LT(f_s) \rangle \subseteq \langle LT(I) \rangle \tag{6.6}$$

Moreover, the degree of a polynomial, denoted as $\deg(f)$, is defined as the maximum among the sums of powers of all monomials in f and is independent of the monomial order.

Next, a division algorithm is presented, which can be construed as a multivariate generalization of the Euclidean division of univariate polynomials (e.g., [73]).

Definition 6.2.1 (Division Algorithm) *Let $>$ be a monomial order and $F = \{f_1, ..., f_s\}$ be an ordered s-tuple of polynomials in $\mathbb{K}[z_1, ..., z_p]$. Then, every $f \in \mathbb{K}[z_1, ..., z_p]$ can be written as*

$$f = q_1 f_1 + ... + q_s f_s + r$$

where $q_i, r \in \mathbb{K}[z_1, ..., z_p]$*, and either* $r = 0$*, or* r *is a linear combination of monomials, none of which is divisible by any of* $LT(f_1), ..., LT(f_s)$*.*

It is noted that not only different monomial orders, but also different arrangements of the f_i's lead, in general, to different q_i's and r. Nevertheless, in the latter case, it is possible to use the Division Algorithm for dividing polynomials $f \in \mathbb{K}[z_1, ..., z_p]$ by s-tuples of polynomials $F = \{f_1, ..., f_s\}$, yielding unique remainders r, unaffected by the arrangement of the f_i's in F. This leads to the concept of a Gröbner basis.

Definition 6.2.2 (Gröbner basis) *Define a monomial order* $>$ *on* $\mathbb{K}[z_1, ..., z_p]$ *and let* $I \subset \mathbb{K}[z_1, ..., z_p]$ *be an ideal. Next, two equivalent definitions for a Gröbner basis are presented (see also [72]).*

1. *A finite subset* $G = \{g_1, ..., g_t\}$ *of* I *is a Gröbner basis if*

$$\langle LT(g_1), ..., LT(g_t)\rangle = \langle LT(I)\rangle$$

2. *A Gröbner basis for* I *(w.r.t.* $>$*) is a finite collection of polynomials* $G = \{g_1, ..., g_t\} \subset I$ *with the property that for every* $f \in I$*,* $LT(f)$ *is divisible by* $LT(g_i)$ *for some* i*.*

The construction of a Gröbner basis G for the ideal $I = \langle f_1, ..., f_s\rangle$, provided an arbitrary generating set $\{f_1, ..., f_s\}$, can be achieved by Buchberger's algorithm (e.g., [65, 66, 73]), and in this case the property $I = \langle f_1, ..., f_s\rangle = \langle g_1, ..., g_t\rangle$ holds. It is noted that a Gröbner basis $G = \{g_1, ..., g_t\}$ of $I \in \mathbb{K}[z_1, ..., z_p]$ is not unique for a given monomial order $>$. Also, division of any $f \in \mathbb{K}[z_1, ..., z_p]$ by G using the Division Algorithm, yields a representation in the form

$$f = q_1 g_1 + ... + q_t g_t + \bar{f}^G \tag{6.7}$$

In the above representation, although the q_i's are non-unique elements of I, (i.e., they depend on the arrangement of the g_i's in G), the remainder $\bar{f}^G$ is unique for a given $>$. Further, $\bar{f}^G$ is not divisible by any $LT(g_i)$, and thus, it is not divisible by any element in $LT(I)$. In this

regard, $\bar{f}^G$, represents a uniquely determined normal form for modulo I, and is given as a linear combination of the monomials $x^a \notin \langle LT(I) \rangle$, where $x^a = z_1^{a_1} z_2^{a_2} ... z_n^{a_n}$ for some n-tuple $a = (a_1, ..., a_n)$ of non-negative integers. Furthermore, the remainders $\bar{f}^G$ and $\bar{g}^G$ generated by the divisions of polynomials $f, g \in I \subset \mathbb{K}[z_1, ..., z_p]$ by a Gröbner basis, respectively, exhibit the following properties (e.g., [73]), i.e.,

$$f \in I \Leftrightarrow \bar{f}^G = 0 \tag{6.8}$$

$$\bar{f}^G = \bar{g}^G \Leftrightarrow f - g \in I \tag{6.9}$$

$$\bar{f}^G + \bar{g}^G = \overline{f + g}^G \tag{6.10}$$

$$\overline{\bar{f}^G \cdot \bar{g}^G}^G = \overline{f \cdot g}^G \tag{6.11}$$

Next, the uniqueness of the remainder $\bar{f}^G$ determined by division of a polynomial $f \in \mathbb{K}[z_1, ..., z_p]$ by a Gröbner basis G of $I \subset \mathbb{K}[z_1, ..., z_p]$ enables the definition of the coset $[f]$.

Definition 6.2.3 (Coset) *Given $f \in \mathbb{K}[z_1, ..., z_p]$, the coset $[f]$ is defined as the set*

$$[f] = f + I = \{f + h \mid h \in I\}$$

In essence, the coset $[f]$ groups together all polynomials in $\mathbb{K}[z_1, ..., z_p]$ that yield the same remainder when divided by G. Hence, this implies a one-to-one correspondence between remainders and cosets ($\bar{f}^G \leftrightarrow [f]$), and thus, $\bar{f}^G$ can be construed as a representative of its coset $[f]$. Next, the quotient ring $\mathbb{K}[z_1, ..., z_p]/I$ is defined formally, which represents the set of all cosets of polynomials in $\mathbb{K}[z_1, ..., z_p]$ with respect to an ideal $I \in \mathbb{K}[z_1, ..., z_p]$.

Definition 6.2.4 (Quotient Ring) *The quotient ring $\mathbb{K}[z_1, ..., z_p]/I$ is defined as the set*

$$\mathbb{K}[z_1, ..., z_p]/I = \{[f] \mid f \in \mathbb{K}[z_1, ..., z_p]\}$$

According to [73], equations (6.10) and (6.11) for the remainder apply also on $\mathbb{K}[z_1, ..., z_p]/I$,

i.e., $\bar{f}^G + \bar{g}^G \leftrightarrow [f]+[g]$ and $\overline{\bar{f}^G \cdot \bar{g}^G}^G \leftrightarrow [f]\cdot[g]$. In this regard, the quotient ring $\mathbb{K}[z_1, ..., z_p]/I$ constitutes also an algebra, which is denoted by A in the ensuing analysis.

It is important to note that the remainders $\bar{f}^G$ are linear combinations of the monomials

$$B = \{x^a \mid x^a \notin LT(I)\} \tag{6.12}$$

which form a basis of A (also known as the basis of standard monomials in the literature). The role of algebra A in obtaining the entire set of solutions of Eq. (6.1) is catalytic. However, an important requirement relates to A being finite-dimensional, which is ensured by the following theorem; see also [73] for a detailed proof.

Theorem 2 (Finiteness Theorem) *Let $I \subseteq \mathbb{K}[z_1, ..., z_p]$ be an ideal. Then, the algebra*

$$A = \mathbb{K}[z_1, ..., z_p]/I$$

is finite-dimensional, if and only if, the variety $\boldsymbol{V}(I) \subset \mathbb{K}^n$ is a finite set.

Next, considering $\mathbb{K} = \mathbb{C}$, $f \in \mathbb{C}[z_1, ..., z_p]$ and $I \subset \mathbb{C}[z_1, ..., z_p]$, the multiplication defined in Eq. (6.11) can be used to define a linear map m_f from the algebra $A = \mathbb{C}[z_1, ..., z_p]/I$ to itself. Specifically, for $[g] \in A$, $m_f : A \to A$ is defined as

$$m_f([g]) = [f] \cdot [g] = [f \cdot g] \in A \tag{6.13}$$

Relying on the vector space structure of the algebra A, it can be shown that m_f is, indeed, a linear map [73]. Further, assuming that the system of polynomial equations in Eq. (6.1) has a finite number of solutions, Theorem 2 implies that A is a finite-dimensional algebra. This fact, enables the representation of the linear map m_f by a matrix $\boldsymbol{M}_f$ associated with a basis of A. This is precisely the basis $\boldsymbol{B}$ of standard monomials defined in Eq. (6.12). More importantly, Theorem 3 shows that the multiplication matrix $\boldsymbol{M}_f$ can be utilized to evaluate

f on $\boldsymbol{V}(I)$; see [73] for a detailed proof.

Theorem 3 *Let $I \subset \mathbb{C}[z_1, ..., z_p]$ be a zero-dimensional ideal and $A = \mathbb{C}[z_1, ..., z_p]/I$. Further, let $f \in \mathbb{C}[z_1, ..., z_p]$ with $\boldsymbol{M}_f$ being the multiplication matrix corresponding to the linear map $m_f : A \rightarrow A$ defined in Eq.* (6.13)*. Then, the eigenvalues of $\boldsymbol{M}_f$ are equal to the values of f on $\boldsymbol{V}(I)$.*

In other words, according to Theorem 3, if the system in Eq. (6.1) has a finite number of μ solutions (i.e., $\boldsymbol{V}(I)$ is a finite set of size μ), substituting these solutions into any polynomial $f \in \mathbb{C}[z_1, ..., z_p]$ yields μ values that are equal to the eigenvalues of $\boldsymbol{M}_f$. In passing, it is worth noting that the (Strong) Nullstellensatz, which is a consequence of Hilbert's original result and is used in the proof of Theorem 3, is of paramount importance to efforts attempting to associate ideals $\boldsymbol{I}$ with the corresponding varieties $\boldsymbol{V}(I)$. In this regard, it can be argued that it provides the tools for establishing a "dictionary" between geometry and algebra [73].

It is important to note that matrix $\boldsymbol{M}_f$ can only be defined if the standard basis $\boldsymbol{B}$ of Eq. (6.12) is finite. This is true if the variety $\boldsymbol{V}(f_1, ..., f_s)$ is a finite set, i.e., the system of polynomial equations in Eq. (6.1) has a finite number of μ solutions in $\mathbb{C}$. Thus, it becomes clear that the total number μ of (complex) solutions of the system in Eq. (6.1) is equal to the number of monomials in the standard basis $\boldsymbol{B}$, i.e., $\mu = \text{length}(\boldsymbol{B})$. If f is a dense polynomial of even degree $2d$, then it follows from Bézout's Theorem that $\mu = (2d-1)^n$ [169].

6.3 Algorithmic aspects and mechanization of the technique

The steps for determining the multiplication matrix $\boldsymbol{M}_f$ of an arbitrary $f \in \mathbb{K}[z_1, ..., z_p]$ corresponding to the system of polynomials in Eq. (6.1) are presented in Algorithm 1, which is based on the following three main subroutines:

- `Groebner`$(f_1, ..., f_s)$: This subroutine computes a Gröbner basis $G = \{g_1, ..., g_t\}$ of the ideal generated by $f_1, ..., f_s$ based on Buchberger's algorithm (e.g., [65, 66]). The

implementation can be found in most symbolic mathematical computation languages (see for instance `gbasis(.)` built-in function in Matlab).

- `StandardBasis(`G`)`: This subroutine computes the basis of standard monomials B defined in Eq. (6.12) corresponding to the Gröbner basis $G = \{g_1, ..., g_t\}$. Indicatively, B is constructed by selecting all monomials that are not divisible by $LT(g_i)$ for any $i = 1, ..., t$.

- `NormalForm(`h`,`G`)`: This subroutine computes the unique remainder of the division of an arbitrary polynomial h by the Gröbner basis G via the Division Algorithm in Definition 6.2.1. The column vector of coefficients of this remainder with respect to basis B, is denoted as $[$`NormalForm(`h`,`G`)`$]_B$. The interested reader is directed to [168] for an indicative implementation in a symbolic language system.

Algorithm 1 `MultMatrix(`$f, f_1, ..., f_s$`)` - Computation of multiplication matrix M_f

Input: $f, f_1, ..., f_s \in \mathbb{R}[z_1, ..., z_p]$
Output: M_f
1: $G =$ `Groebner(`$f_1, ..., f_s$`)`
2: $B =$ `StandardBasis(`G`)`
3: $\mu = \text{length}(B)$
4: Initialize M_f as an empty $\mu \times \mu$ matrix
5: **for** $i = 1$ to μ **do**
6: $\quad M_f(:, i) = [$`NormalForm(`$B(i) \cdot f$`,`G`)`$]_B$ ▷ Computation of the i-th column of M_f
7: **end for**
8: **return** M_f

Next, consider the system of polynomial equations of Eq. (6.1) and the ideal generated by these polynomials $I = \langle f_1, ..., f_s \rangle$. According to Eq. (6.4), the affine variety $\boldsymbol{V}(I)$ is the set of all solutions of Eq. (6.1) and thus, the real solutions of Eq. (6.1) are the real elements of $\boldsymbol{V}(I)$. The determination of $\boldsymbol{V}(I)$ can be achieved with the aid of Theorem 3. Specifically, Theorem 3 suggests that all the real values of an arbitrary polynomial f on $\boldsymbol{V}(I)$ are precisely the real eigenvalues of matrix M_f which is constructed according to Algorithm 1 as $M_f =$ `MultMatrix(`$f, f_1, ..., f_s$`)`. Next, assuming that Eq. (6.1) has n real solutions and

denoting by $\boldsymbol{z}(k)$ the k-th solution, the first components of all n solutions, i.e., $z_1^{(1)}, ..., z_1^{(n)}$, can be determined as the real eigenvalues of the matrix $M_{z_1} = \texttt{MultMatrix}(z_1, f_1, ..., f_s)$. In the same exact manner, all components i of the n real solutions i.e., $z_i^{(1)}, ..., z_i^{(n)}$, can be determined as the real eigenvalues of M_{z_i} for all $i = 1, ..., p$.

It is noted however, that the computation of the eigenvalues for each M_{z_i} does not provide a natural ordering of these eigenvalues, and thus, the process of obtaining each $z_i^{(k)}$ as described above, implies that, in general, $z_i^{(k)}$ and $z_j^{(k)}$ (where $i \neq j$) are not necessarily components of the same solution k. In other words, the components of the different solutions are unordered. This would not be a problem in the case of $n = 1$, i.e., if there was only one solution of the system in Eq. (6.1). One way to treat this issue is by considering all possible combinations $\boldsymbol{z}^{candidate} = [z_1, ..., z_p]^T$ from the obtained results by selecting one z_i from $(z_i^{(1)}, ..., z_i^{(n)})$ at a time, and verifying whether $\boldsymbol{z}^{candidate}$ is a valid solution by substituting it into Eq. (6.1). This leads to a number of possible solutions of n^p which increases exponentially with p. For example, in the case of a 2 dimensional oscillator, i.e., $n = 2$ and assuming an up to 3-rd order expansion in Eq. (8.8), leads to a polynomial system of $p = 18$ equations with p unknowns which has $n = 2$ solutions. In this case, there exist 2^18 candidate solutions $\boldsymbol{z}^{candidate}$. Even though, 2^{18} appears as a tractable number of candidate solutions to verify, by slightly increasing n and/or p can lead to a number of candidate solutions in the order of billions or even trillions which constitutes a significant limitation of this approach.

In passing, it is noted that the graded lexicographical order

$$x_1^d > ... > x_n^d > x_1^{d-1}x_2 > ... > x_1 > ... > x_n > 1 \tag{6.14}$$

is considered in the numerical examples of this thesis.

Chapter 7: Convexity of the Wiener path integral technique most probable path optimization problem

7.1 Formulation of the WPI most probable path optimization problem as an algebraic system of polynomial equations

For a wide range of dynamical systems (e.g., systems with a nonlinearity function in Eq. (2.46) of polynomial form), not only the entire set of solutions corresponding to the first-order optimality condition $\nabla J(\boldsymbol{z}) = \boldsymbol{0}$ in Eq. (2.35) can be determined, but also convexity of $J(\boldsymbol{z})$ is implied if the technique yields only one solution. In the latter case, clearly, the Newton's optimization scheme of Sec. 2.3.2 converges to the same global minimum determined by the herein proposed computational algebraic technique presented in Chapter 6. In fact, it is noted that, in its standard implementation, the technique determines the values of J corresponding to all real solutions of the system in Eq. (6.1), i.e., J is evaluated on the entire set of points defined by $\nabla J(\boldsymbol{z}) = \boldsymbol{0}$. Of course, as discussed in Sec. 6.3, the technique can be utilized for determining the actual solutions $\boldsymbol{z}^*$ as well (and not only the values $J(\boldsymbol{z}^*)$) (e.g., [73]). However, this implies significant additional computational cost. In this regard, coupling the Newton's optimization scheme of Sec. 2.3.2 with the herein proposed computational algebraic technique for showing that the $\boldsymbol{z}^*$ provided by the Newton's scheme corresponds, indeed, to the global minimum of $J(\boldsymbol{z})$, appears to be an efficient alternative.

Next, considering a polynomial nonlinearity function $\boldsymbol{g}_{nl}$ in Eq. (2.46) of degree d, the term $g_1(\boldsymbol{z})$ in Eq. (2.54) becomes a multivariate polynomial of degree $d + 1$ in $p := nL$ variables, whereas the term $g_2(\boldsymbol{z})$ in Eq. (2.55) becomes a multivariate polynomial of degree $2d$ in p variables. Therefore, the objective function $J(\boldsymbol{z})$ takes the form of a multivariate polynomial of degree $2d$ in p variables and the first-order optimality condition of Eq. (2.35)

leads to an algebraic system of p equations of the form of Eq. (6.1). In Eq. (6.1), each f_i is a polynomial of degree at most $2d-1$ with coefficients in $\mathbb{R}$. In this regard, the convexity of the objective function $J(\boldsymbol{z})$ can be proved by showing that the system of Eq. (6.1) has a unique real solution. Also, $s = p$ is considered in the ensuing analysis, although this is not a necessary requirement for the technique (e.g., [73]).

Next, consider the optimization problem of Eq. (2.34) and set

$$J^* = \min_{\boldsymbol{z}\in\mathbb{R}^n} J(\boldsymbol{z}) \tag{7.1}$$

Then, J^* is equal to the smallest real eigenvalue of matrix $\boldsymbol{M_J}$ representing the linear map $m_{J_\epsilon} : A \rightarrow A$ (defined in Eq. (6.13)) with respect to the monomial basis $\boldsymbol{B}$ (defined in Eq. (6.12)), where $A = \mathbb{C}[z_1, ..., z_p]/I$ with $I = \langle \frac{\partial J}{\partial z_1}, ..., \frac{\partial J}{\partial z_n} \rangle$. In other words, the globally minimum value of $J(\boldsymbol{z})$, as well as all its values on its critical points (i.e., points where $\boldsymbol{\nabla J = 0}$), can be found by determining matrix $\boldsymbol{M_J}$.

Moreover, as shown in Sec. 2.3.2, the convergence rate expressed in Eq. (2.56) is increasing for decreasing nonlinearity degree. This is demonstrated further in the numerical examples of Sec. 7.2; see Tables 7.1 and 7.2. Finally, it is important to note that although it has been shown in Section 2.3.2 that a Newton's optimization scheme for determining the most probable path appears to be a suitable choice, the convergence rate shown in Eq.(2.56) can be construed as local (see also [25]). In other words, there is no guarantee about existence and convergence to a global minimum. In fact, proving the potential convexity of $J(\boldsymbol{z})$ (and thus, the existence of a global extremum) is addressed by resorting to the computational algebraic geometry concepts and tools presented in Chapter 6 such as Gröbner bases.

7.2 Numerical examples

In this section, various numerical examples pertaining to oscillators with diverse nonlinear behaviors are considered for demonstrating the reliability of the WPI technique to evaluate

the joint response PDF, in conjunction with the proposed Newton's scheme for determining the most probable path. Further, the herein developed Gröbner basis approach is also employed for demonstrating the existence of a unique solution (and thus, the convexity of the objective function) of the most probable path optimization problem.

7.2.1 Linear oscillator

Consider a SDOF linear oscillator whose governing equation is a scalar version of Eq. (2.17), i.e.,

$$m\ddot{x} + c\dot{x} + kx = w(t), \tag{7.2}$$

where $m = 5,\ c = 0.2,\ k = 1$, and $E(w(t)w(t+\tau)) = 2\pi S_0\delta(\tau)$ with $S_0 = 0.5$.

As pointed out in Sec. 2.3.2, for linear systems the Newton's optimization scheme converges to the exact solution $\boldsymbol{z}^* = -\mathbf{Q}^{-1}\mathbf{b}$ in only one iteration for any arbitrarily selected starting point $\boldsymbol{z}^{(0)}$. In this regard, for an indicative final time instant $t_f = 1s$ and for boundary conditions $(x(0), \dot{x}(0), x(t_f), \dot{x}(t_f)) = (0, 0, -0.5, -1.0)$, the objective function of Eq. (2.39) is shown in Fig. 7.1 by utilizing $L = 2$ trial functions. Further, as also stated in Sec. 2.3.2 and proved in B, it is readily seen that the objective function $J(\boldsymbol{z})$ of Eq. (2.39) is convex, and thus, the Newton's scheme converges to the exact optimal solution $\boldsymbol{z}^* = -\mathbf{Q}^{-1}\mathbf{b} = (0.0173, 0.00014)$ in a single iteration starting from the arbitrarily chosen point $\boldsymbol{z}^{(0)} = (50, 50)$. Further, employing the Gröbner basis approach developed in Chapter 6 and discussed in Sec. 7.1 yields a single solution and the corresponding objective function value becomes $J(\boldsymbol{z}^*) = 4.4204$, which coincides practically with the estimate based on Newton's scheme.

Finally, utilizing a brute-force discretization of the PDF effective domain (e.g. [22]), the joint response PDF at a specific time instant is determined via the solution of $N^2 = 961$ boundary value problems. In Fig. 7.2, the corresponding marginal response displacement and velocity PDFs at various time instants are plotted. It is shown that the WPI-based estimates utilizing Newton's scheme coincide with the estimates based on the Gröbner basis approach. Comparisons with MCS data (10,000 realizations) are included as well demonstrating the

high accuracy degree exhibited by the WPI technique.

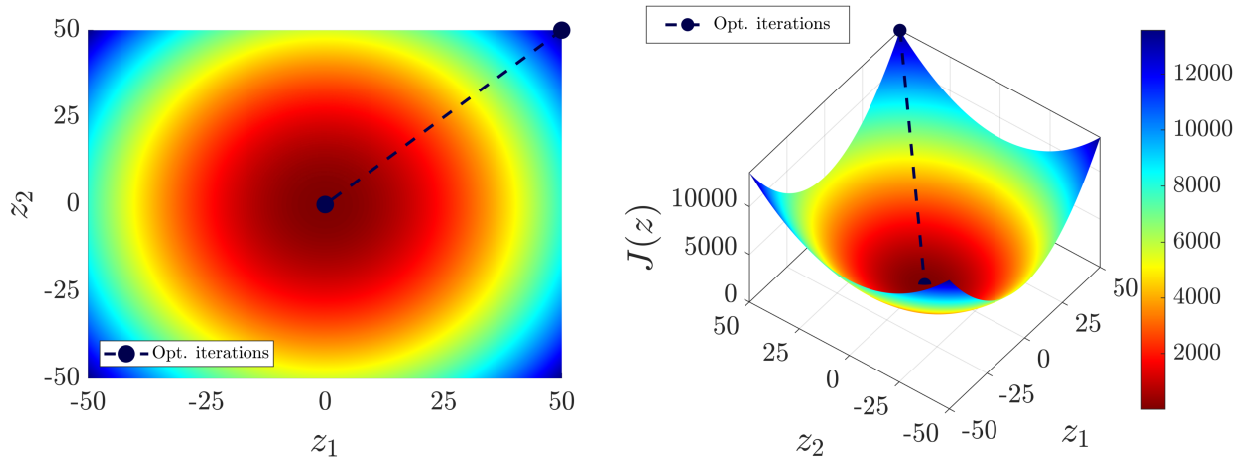

Figure 7.1: Most probable path optimization problem objective function using $L = 2$ trial functions and corresponding to a linear oscillator under white noise ($t_f = 1s$, $x(t_f) = -0.5$, $\dot{x}(t_f) = -1.0$). The Newton's optimization scheme iterations are also included.

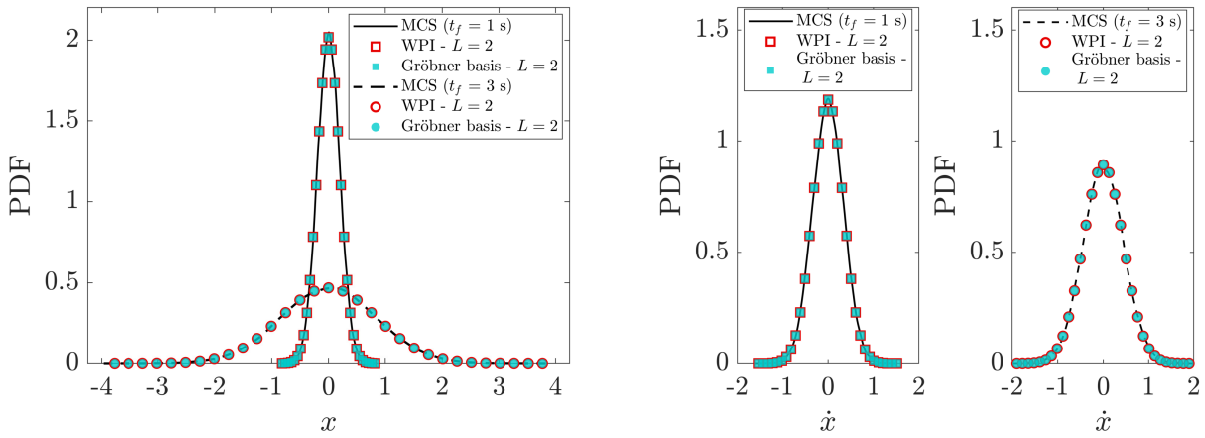

(a) Response displacement PDF

(b) Response velocity PDF

Figure 7.2: Response displacement and velocity PDFs at various time instants corresponding to a linear oscillator under white noise. Comparisons between WPI-based estimates utilizing the Newton's scheme and the Gröbner basis approaches for the most probable path determination. MCS-based estimates are also included (10,000 realizations).

7.2.2 Duffing nonlinear oscillator

In this example, consider a SDOF Duffing nonlinear oscillator whose governing equation is a scalar version of Eq. (2.17), i.e.,

$$m\ddot{x} + c\dot{x} + kx + \varepsilon g_{nl}(x, \dot{x}) = w(t) \tag{7.3}$$

where

$$g_{nl}(x, \dot{x}) = kx^3 \tag{7.4}$$

In Eqs. (7.3)-(7.4), the same parameters values are used for m, c, k and S_0 as in example 7.2.1.

Next, for an indicative final time instant $t_f = 1s$ and for boundary conditions $(x(0), \dot{x}(0), x(t_f), \dot{x}(t_f)) = (0, 0, -0.5, -1.0)$, the objective functions $J(\boldsymbol{z})$ of the most probable path optimization problem for $\varepsilon = 1, 10$, and 20 are shown in Figs. 7.3, 7.4 and 7.5, respectively. The iteration points of the Newton's scheme are also included in the figures corresponding both to an arbitrarily selected starting point (i.e., $\boldsymbol{z}^{(0)} = (50, -50)$), and to a starting point equal to the exact optimum $\boldsymbol{z}^{(0)} = \boldsymbol{z}_{lin} = -\mathbf{Q}^{-1}\mathbf{b}$ corresponding to the associated linear system (i.e., $\varepsilon = 0$). Clearly, as pointed out in Sec. 2.3.2, $\boldsymbol{z}^{(0)} = \boldsymbol{z}_{lin}$ is shown to be a reasonable choice as a starting point in the optimization scheme, since for all cases the number of iterations is significantly smaller than the respective one based on an arbitrarily selected starting point. Also, as dictated by Eq. (2.56), it can be readily seen that the convergence rate increases for smaller values of the nonlinearity parameter ε. Numerical results related to the iterations of the Newton's scheme are summarized in Table 7.1, which includes also results based on the Gröbner basis approach. It is seen that, for all nonlinearity parameter values, the Gröbner approach yields a single solution and the corresponding objective function value coincides practically with the estimate based on the Newton's scheme. This proves the convexity of the objective function and that the Newton's scheme converges, indeed, to the global minimum.

In Fig. 7.6, the WPI-based marginal response displacement and velocity PDFs are plotted for various nonlinearity magnitude values at two indicative time instants. It is shown that the WPI-based estimates utilizing the Newton's scheme coincide with the estimates based on the Gröbner basis approach. Comparisons with MCS data (10,000 realizations) are included as well demonstrating the high accuracy degree exhibited by the WPI technique.

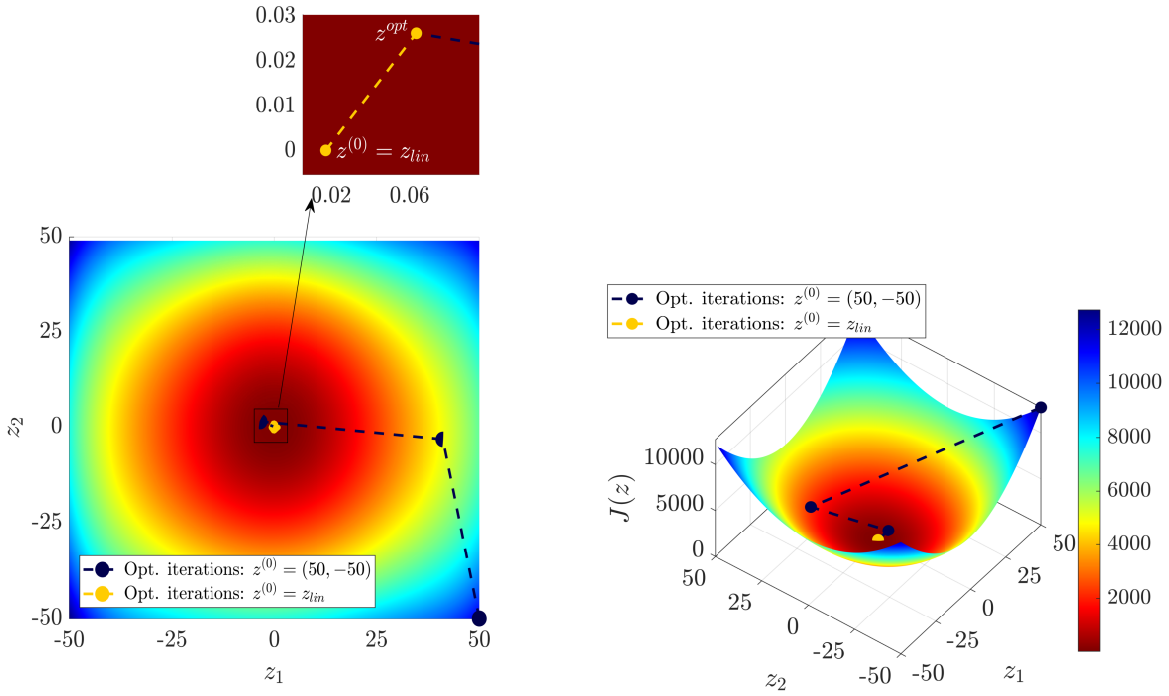

Figure 7.3: Most probable path optimization problem objective function using $L = 2$ trial functions and corresponding to a Duffing oscillator with $\varepsilon = 1.0$ under white noise ($t_f = 1s$, $x(t_f) = -0.5$, $\dot{x}(t_f) = -1.0$). The Newton's optimization scheme iterations are also included.

7.2.3 Nonlinear oscillator with an asymmetric response PDF

In this example, consider a SDOF nonlinear oscillator with an asymmetric response PDF, whose governing equation is given by Eqs. (7.5)-(7.6), i.e.,

$$m\ddot{x} + c\dot{x} + kx + \varepsilon g_{nl}(x, \dot{x}) = w(t) \tag{7.5}$$

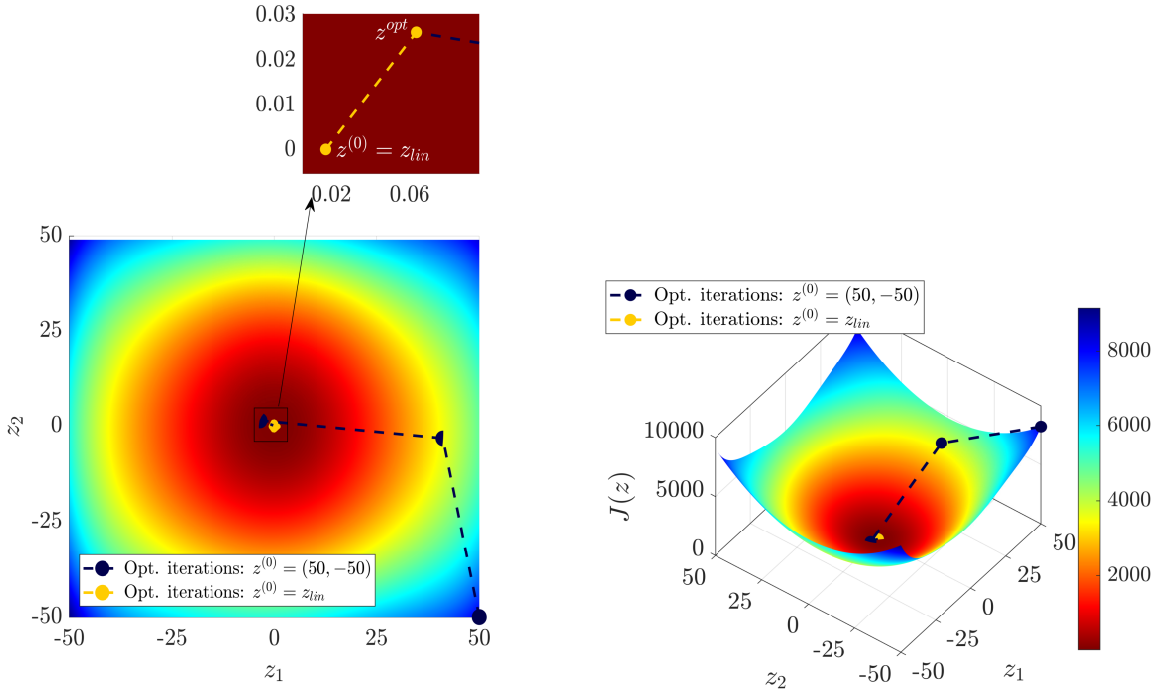

Figure 7.4: Most probable path optimization problem objective function using $L = 2$ trial functions and corresponding to a Duffing oscillator with $\varepsilon = 10$ under white noise ($t_f = 1s$, $x(t_f) = -0.5$, $\dot{x}(t_f) = -1.0$). The Newton's optimization scheme iterations are also included.

Table 7.1: Convergence rate and objective function values for a Duffing oscillator

$\varepsilon = 1.0$		$\varepsilon = 10$		$\varepsilon = 20$		$\varepsilon = 100$	
$\|z^{(k)} - z^*\|$	$J(\mathbf{z}^{(k)})$	$\|z^{(k)} - z^*\|$	$J(\mathbf{z}^{(k)})$	$\|z^{(k)} - z^*\|$	$J(\mathbf{z}^{(k)})$	$\|z^{(k)} - z^*\|$	$J(\mathbf{z}^{(k)})$
Newton's numerical optimization scheme - Arbitrarily selected starting point $z^{(0)}$							
70.697	1.26E4	70.685	8.23E3	70.671	1.30E4	70.138	8.81E4
37.666	4.14E3	44.568	3.97E3	50.835	5.26E3	58.718	2.34E4
7.735	1.92E2	18.447	9.96E2	38.458	2.81E3	49.450	6.92E3
4.63E-2	4.458	12.425	4.59E2	29.451	1.83E3	40.993	2.52E3
5.37E-7	4.452	3.571	45.024	9.694	2.76E2	31.862	1.10E3
1.08E-16	4.452	2.93E-2	4.745	3.467	43.157	23.047	6.10E2
		1.56E-6	4.743	5.588E-2	5.096	17.922	4.28E2
		7.03E-15	4.743	1.08E-5	5.086	14.318	1.04E2
				6.44E-13	5.086	5.787	28.117
						2.459	8.534
						0.118	8.491
						1.32E-4	8.491
						2.97E-10	8.491
						1.41E-15	8.491
Newton's numerical optimization scheme - Starting point $\mathbf{z}^{(0)} = -\mathbf{Q}^{-1}\mathbf{b}$ corresponding to a linear oscillator with $\varepsilon = 0$							
5.24E-3	4.452	5.29E-2	4.751	1.07E-1	5.120	5.74E-1	9.446
8.49E-9	4.452	8.49E-6	4.743	6.77E-5	5.086	7.68E-3	8.491
		2.15E-13	4.743	2.617E-11	5.086	1.11E-6	8.491
						2.28E-14	8.491
Computational algebraic geometry approach based on Gröbner bases							
	4.452		4.743				8.490

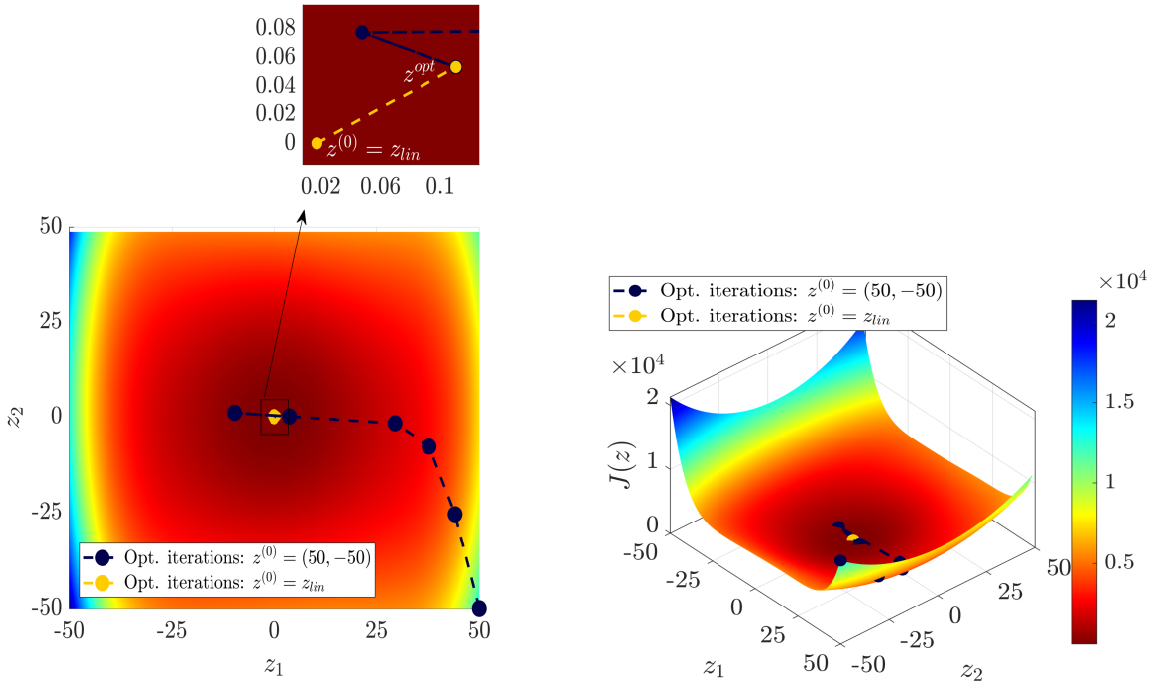

Figure 7.5: Most probable path optimization problem objective function using $L = 2$ trial functions and corresponding to a Duffing oscillator with $\varepsilon = 20$ under white noise ($t_f = 1s$, $x(t_f) = -0.5$, $\dot{x}(t_f) = -1.0$). The Newton's optimization scheme iterations are also included.

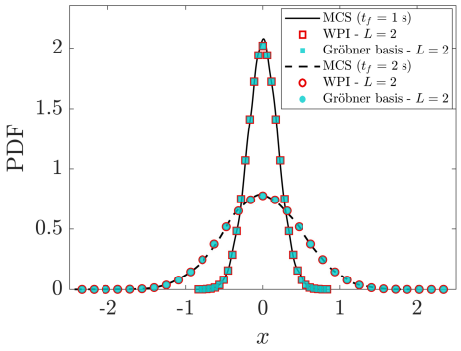

(a) $\varepsilon = 1$: Response displacement PDF

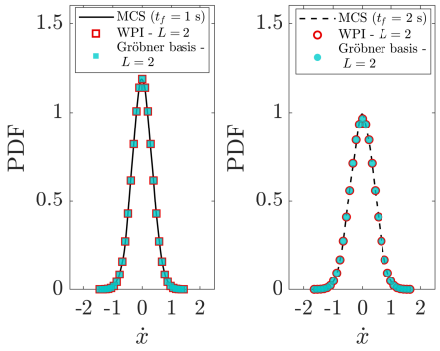

(b) $\varepsilon = 1$: Response velocity PDF

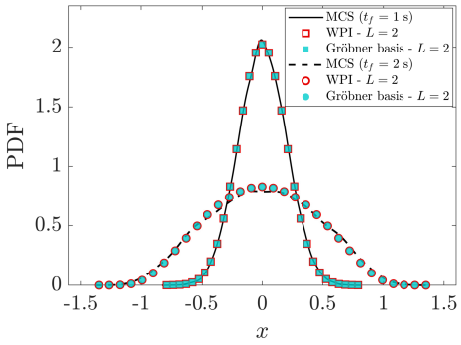

(c) $\varepsilon = 10$: Response displacement PDF

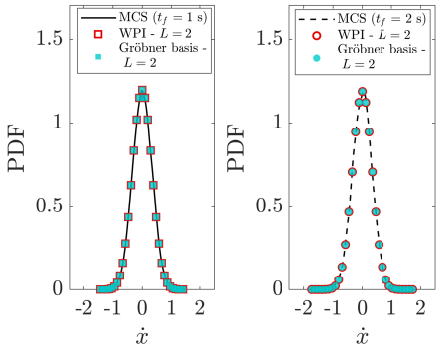

(d) $\varepsilon = 10$: Response velocity PDF

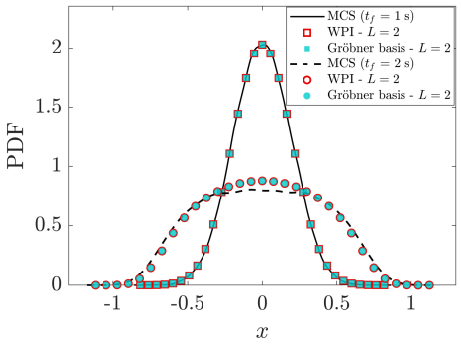

(e) $\varepsilon = 20$: Response displacement PDF

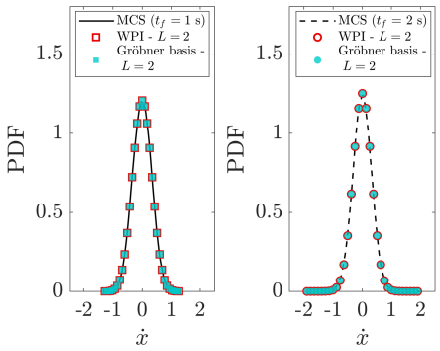

(f) $\varepsilon = 20$: Response velocity PDF

Figure 7.6: Response displacement and velocity PDFs at various time instants corresponding to a Duffing oscillator under white noise. Comparisons between WPI-based estimates utilizing the Newton's scheme and the Gröbner basis approaches for the most probable path determination. MCS-based estimates are also included (10,000 realizations).

where

$$g_{nl}(x, \dot{x}) = ax^2 + x^3 \tag{7.6}$$

In Eq. (7.5)-(7.6), the parameters values used are, $m = 1,\ c = 0.2,\ k = 1,\ E(w(t)w(t+\tau)) = 2\pi S_0 \delta(\tau)$ with $S_0 = 0.05$, and a is constant.

Further, for an indicative final time instant $t_f = 1s$ and for boundary conditions $(x(0), \dot{x}(0), x(t_f), \dot{x}(t_f)) = (0, 0, -0.3, -0.8)$, the objective functions $J(\mathbf{z})$ of the most probable path optimization problem for $\varepsilon = 1$ and $a = 1.5$, $\varepsilon = 10$ and $a = \frac{3\sqrt{10}}{20}$, and $\varepsilon = 50$ and $a = \frac{3\sqrt{2}}{20}$ are shown in Figs. 7.7, 7.8 and 7.9, respectively. The iteration points of the Newton's scheme are also included in the figures corresponding both to an arbitrarily selected starting point (i.e., $\mathbf{z}^{(0)} = (50, -50)$ or $\mathbf{z}^{(0)} = (-50, 50)$), and to a starting point equal to the exact optimum $\mathbf{z}^{(0)} = \mathbf{z}_{lin} = -\mathbf{Q}^{-1}\mathbf{b}$ corresponding to the associated linear system (i.e., $\varepsilon = 0$). In a similar manner as in example 7.2.2, $\mathbf{z}^{(0)} = \mathbf{z}_{lin}$ proves to be an excellent choice as a starting point in the optimization scheme, whereas it is seen that the convergence rate increases for smaller values of the nonlinearity parameter ε. Numerical results related to the iterations of the Newton's scheme are summarized in Table 7.2, which includes also results based on the Gröbner basis approach. The convexity of the objective function and the convergence of Newton's scheme to the global minimum is demonstrated by noticing that for all nonlinearity parameter values, the Gröbner approach yields a single solution and the corresponding objective function value coincides practically with the estimate based on the Newton's scheme.

In Fig. 7.10, the WPI-based marginal response displacement and velocity PDFs are plotted for various nonlinearity magnitude values at two indicative time instants. It is shown that the WPI-based estimates utilizing Newton's scheme coincide with the estimates based on the Gröbner basis approach. Comparisons with MCS data $(20,000$ realizations) are included as well demonstrating the high accuracy degree exhibited by the WPI technique.

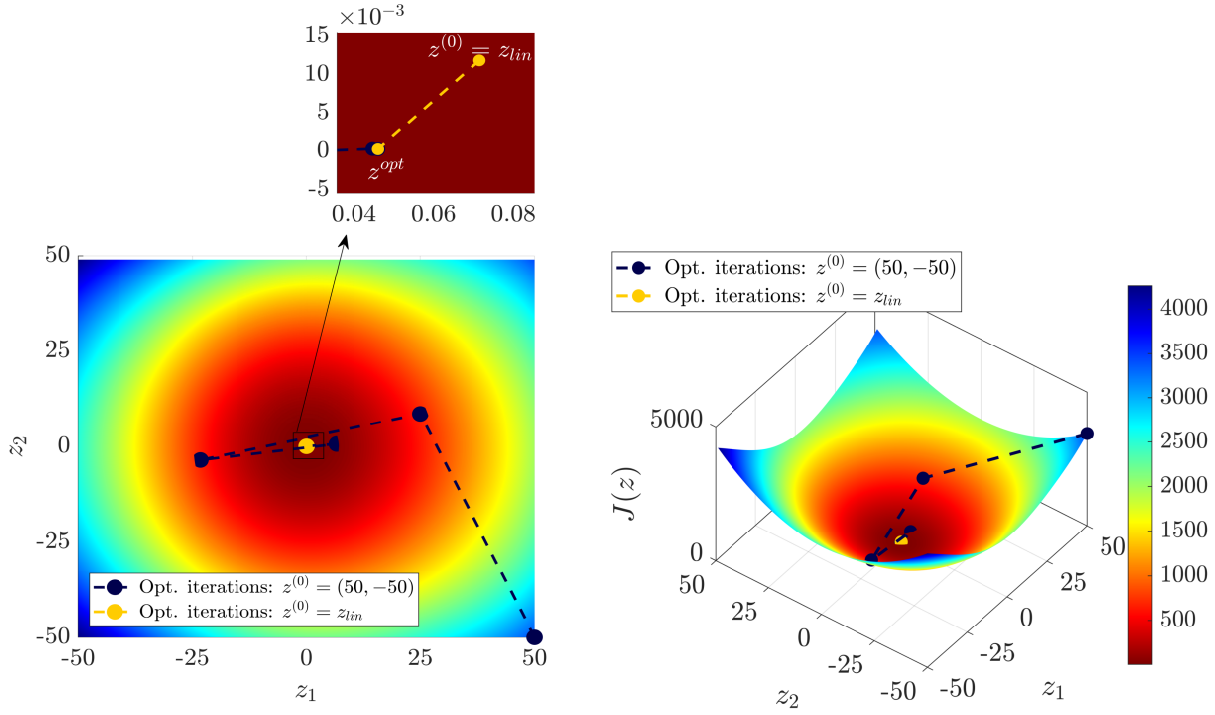

Figure 7.7: Most probable path optimization problem objective function using $L = 2$ trial functions and corresponding to a nonlinear oscillator with an asymmetric response PDF with $\varepsilon = 1$ and $a = 1.5$ under white noise ($t_f = 1s$, $x(t_f) = -0.3$, $\dot{x}(t_f) = -0.8$). The Newton's optimization scheme iterations are also included.

Table 7.2: Convergence rate and objective function values for a nonlinear oscillator with an asymmetric response PDF.

$\varepsilon = 1$, $a = 1.50$		$\varepsilon = 10$, $a = \frac{3\sqrt{10}}{20}$		$\varepsilon = 50$, $a = \frac{3\sqrt{2}}{20}$		$\varepsilon = 100$, $a = 0.150$	
$\|z^{(k)} - z^*\|$	$J(\mathbf{z}^{(k)})$	$\|z^{(k)} - z^*\|$	$J(\mathbf{z}^{(k)})$	$\|z^{(k)} - z^*\|$	$J(\mathbf{z}^{(k)})$	$\|z^{(k)} - z^*\|$	$J(\mathbf{z}^{(k)})$
Newton's numerical optimization scheme - Arbitrarily selected starting point $z^{(0)}$							
70.678	3.49E+03	70.730	3.30E4	70.732	1.28E6	70.374	5.40E6
25.173	6.21E2	58.642	9.16E3	57.614	3.33E5	57.053	1.41E6
17.770	3.88E2	47.166	2.96E3	47.261	8.62E4	46.490	3.65E5
1.786	5.536	35.498	1.19E3	39.109	2.23E4	38.153	9.45E4
2.31E-2	1.683	26.321	5.92E2	32.603	5.90E3	31.606	2.43E4
3.21E-6	1.683	20.316	3.64E2	27.040	1.68E3	26.449	6.27E3
6.18E-14	1.683	7.104	63.160	21.494	5.72E2	22.213	1.67E3
		1.943	6.109	15.672	2.39E2	18.191	4.96E2
		1.15E-1	1.615	11.019	1.16E2	13.697	1.78E2
		2.08E-4	1.598	7.990	63.940	9.385	71.774
		7.29E-10	1.598	0.782	2.554	6.971	35.490
				6.73E-3	1.794	5.514	23.641
				2.35E-7	1.794	1.570	5.110
				1.07E-15	1.794	0.520	2.616
						6.55E-3	2.271
						1.93E-6	2.271
						1.99E-13	2.271
Newton's numerical optimization scheme - Starting point $z^{(0)} = -\mathbf{Q}^{-1}\mathbf{b}$ corresponding to a linear oscillator with $\varepsilon = 0$							
0.0278	1.684	0.046	1.601	0.077	1.800	0.278	2.357
3.955E-6	1.683	3.205E-5	1.598	2.305E-5	1.794	0.0010	2.2715
9.116E-14	1.683	1.711E-11	1.598	8.485E-12	1.794	1.831E-8	2.271
Computational algebraic geometry approach based on Gröbner bases							
	1.683		1.598		1.793		2.271

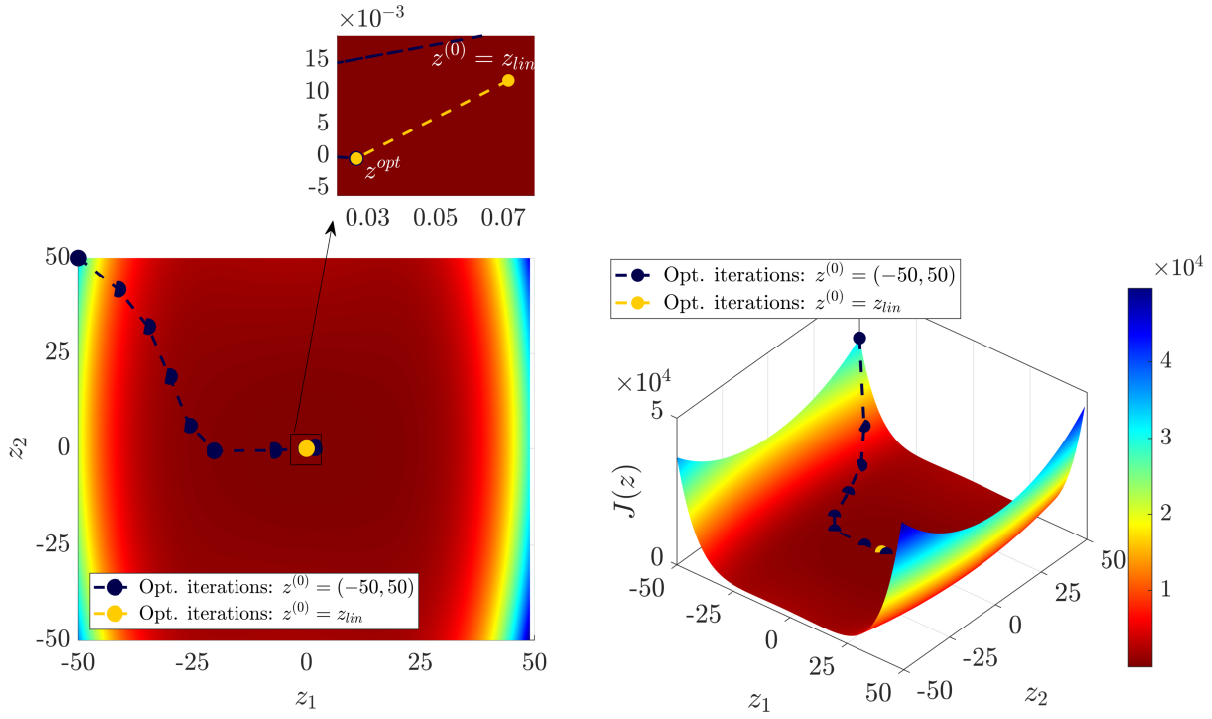

Figure 7.8: Most probable path optimization problem objective function using $L = 2$ trial functions and corresponding to a nonlinear oscillator with an asymmetric response PDF with $\varepsilon = 10$ and $a = \frac{3\sqrt{10}}{20}$ under white noise ($t_f = 1s,\ x(t_f) = -0.3,\ \dot{x}(t_f) = -0.8$). The Newton's optimization scheme iterations are also included.

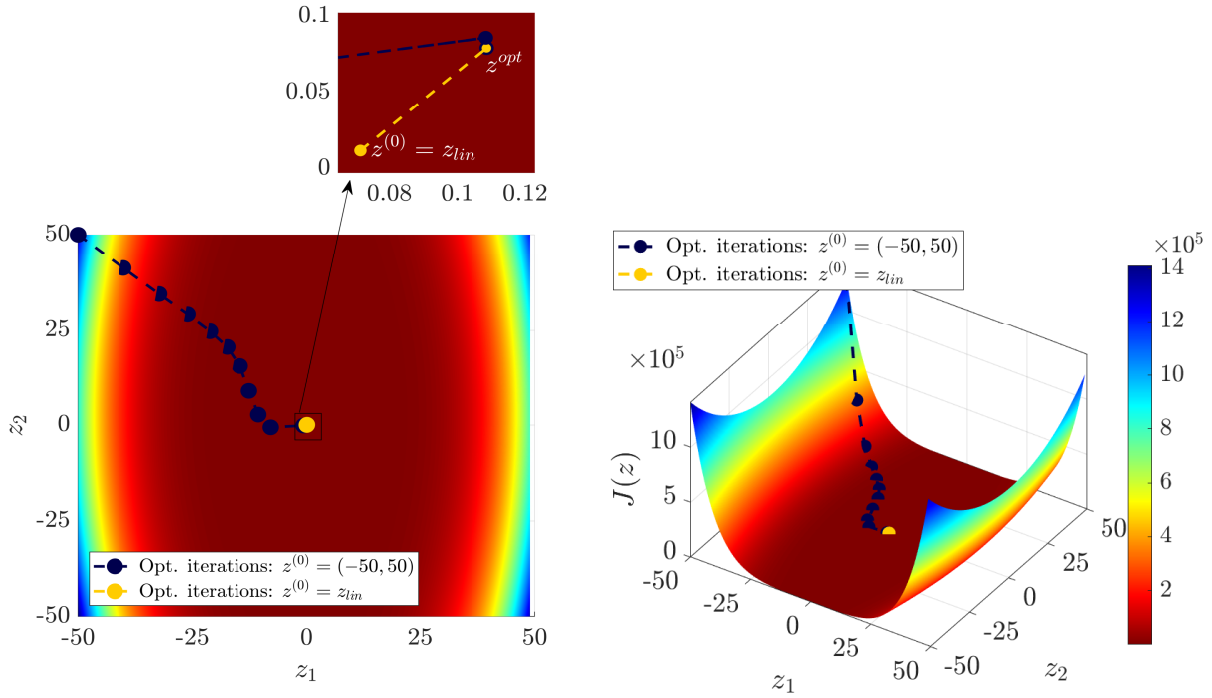

Figure 7.9: Most probable path optimization problem objective function using $L = 2$ trial functions and corresponding to a nonlinear oscillator with an asymmetric response PDF with $\varepsilon = 50$ and $a = \frac{3\sqrt{2}}{20}$ under white noise ($t_f = 1s,\ x(t_f) = -0.3,\ \dot{x}(t_f) = -0.8$). The Newton's optimization scheme iterations are also included.

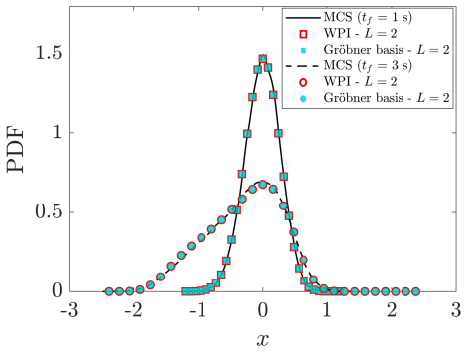

(a) ε = 1: Response displacement PDF

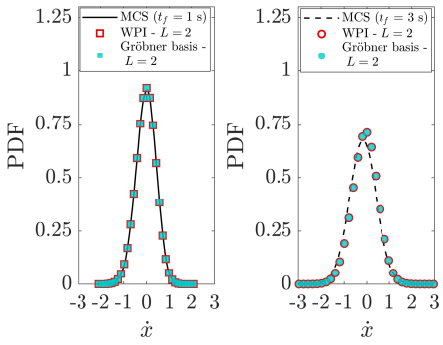

(b) ε = 1: Response velocity PDF

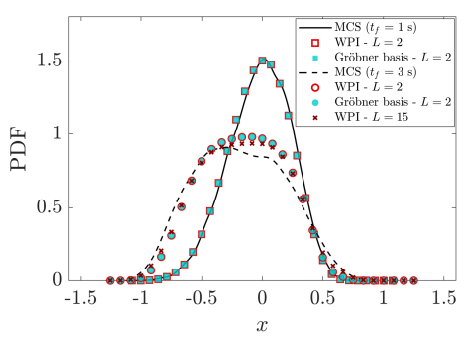

(c) ε = 10: Response displacement PDF

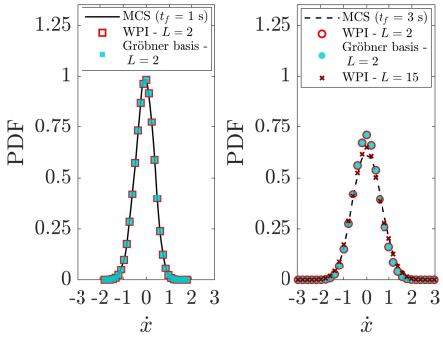

(d) ε = 10: Response velocity PDF

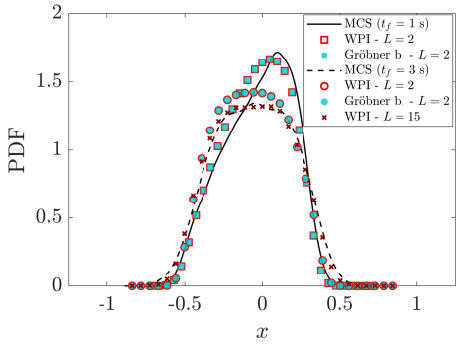

(e) ε = 50: Response displacement PDF

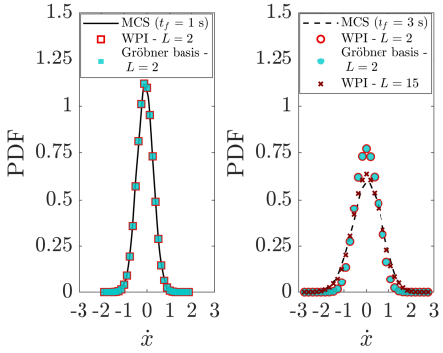

(f) ε = 50: Response velocity PDF

Figure 7.10: Response displacement and velocity PDFs at various time instants corresponding to a nonlinear oscillator with an asymmetric response PDF. Comparisons between WPI-based estimates utilizing the Newton's scheme and the Gröbner basis approaches for the most probable path determination. MCS-based estimates are also included (20,000 realizations).

7.2.4 Nonlinear oscillator with a bimodal response PDF

Consider a SDOF nonlinear oscillator exhibiting a bimodal response PDF, whose governing equation is given by

$$m\ddot{x} + c\dot{x} + kx + \varepsilon g_{nl}(x, \dot{x}) = w(t) \tag{7.7}$$

where

$$g_{nl}(x, \dot{x}) = -ax + x^3 \tag{7.8}$$

In Eq. (7.7)-(7.8), the parameters values utilized are, $m = 1,\ c = 1.0, k = 1.0,\ E(w(t)w(t+\tau)) = 2\pi S_0 \delta(\tau)$ with $S_0 = 0.0637$ and a is constant.

Next, for an indicative final time instant $t_f = 1s$ and for boundary conditions $(x(0), \dot{x}(0), x(t_f), \dot{x}(t_f)) = (0, 0, 0.8, 0.9)$, the objective functions $J(\mathbf{z})$ of the most probable path optimization problem for $a = 1.3,\ 1.5$ and 1.8, considering $\varepsilon = 1$ are shown in Figs. 7.11, 7.12 and 7.13, respectively. The Newton's scheme iteration points are also included in the figures corresponding both to an arbitrarily selected starting point $\mathbf{z}^{(0)} = (-100, 100)$, and to a starting point equal to the exact optimum $\mathbf{z}^{(0)} = \mathbf{z}_{lin} = -\mathbf{Q}^{-1}\mathbf{b}$ corresponding to the associated linear system (i.e., $\varepsilon = 0$). Obviously, the convergence behavior is highly improved when $\mathbf{z}^{(0)} = \mathbf{z}_{lin}$ is used. Numerical results related to the iterations of the Newton's scheme are summarized in Table 7.3, which includes also results based on the Gröbner basis approach. In a similar manner as in the previous examples, the single solution obtained by the Gröbner basis approach demonstrates the convexity of the objective function and the existence of a single global minimum.

In Fig. 7.14, it is shown that the WPI-based estimates utilizing the Newton's scheme coincide with the estimates based on the Gröbner basis approach. Comparisons with MCS data $(50,000$ realizations) are included as well demonstrating the high accuracy degree exhibited by the WPI technique.

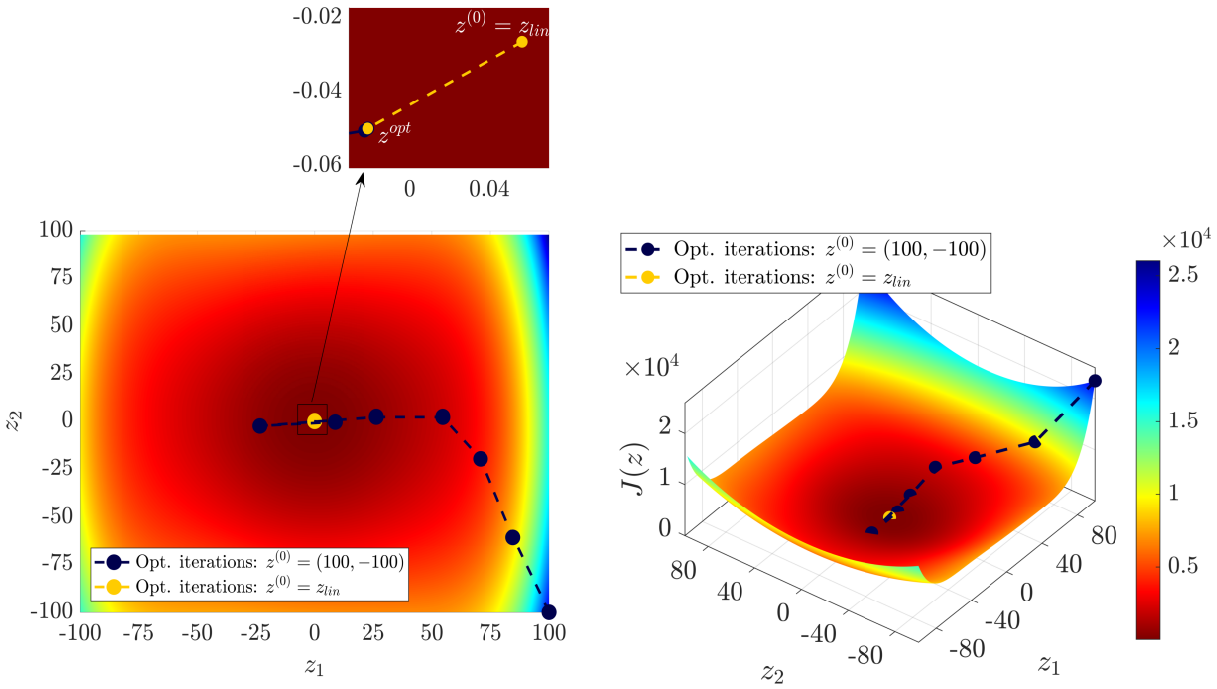

Figure 7.11: Most probable path optimization problem objective function using $L = 2$ trial functions and corresponding to a nonlinear oscillator with a bimodal response PDF with $a = 1.3$ and $\varepsilon = 1$ under white noise ($t_f = 1s$, $x(t_f) = 0.8$, $\dot{x}(t_f) = 0.9$). The Newton's optimization scheme iterations are also included.

Table 7.3: Convergence rate and objective function values for a nonlinear oscillator with a bimodal response PDF.

$a = 1.3$		$a = 1.5$		$a = 1.8$	
$\|z^{(k)} - z^*\|$	$J(\mathbf{z}^{(k)})$	$\|z^{(k)} - z^*\|$	$J(\mathbf{z}^{(k)})$	$\|z^{(k)} - z^*\|$	$J(\mathbf{z}^{(k)})$
Newton's numerical optimization scheme - Arbitrarily selected starting point $\mathbf{z}^{(0)}$					
141.401	2.35E4	141.386	2.33E4	141.366	2.30E4
104.044	8.73E3	103.987	8.66E3	103.905	8.57E3
73.449	3.79E3	73.522	3.78E3	73.635	3.77E3
54.720	2.02E3	54.932	2.04E3	55.255	2.06E3
26.456	6.13E2	26.538	6.21E2	26.665	6.32E2
23.386	5.47E2	24.484	6.01E2	26.232	6.92E2
8.777	81.474	10.692	1.18E2	14.577	2.13E2
0.742	5.232	1.302	6.274	3.305	15.852
1.75E-3	4.667	4.88E-3	4.514	1.91E-2	4.316
1.15E-8	4.667	9.02E-8	4.514	1.30E-6	4.316
		2.95E-17	4.514	6.38E-15	4.316
Newton's numerical optimization scheme - Starting point $\mathbf{z}^{(0)} = -\mathbf{Q}^{-1}\mathbf{b}$ corresponding to a linear oscillator with $\varepsilon = 0$.					
0.072	4.671	0.084	4.520	0.1028	4.325
3.374E-6	4.667	6.193E-6	4.514	1.205E-5	4.316
2.990E-14	4.667	1.058E-13	4.514	4.436E-13	4.316
Computational algebraic geometry approach based on Gröbner bases.					
	4.667		4.514		4.316

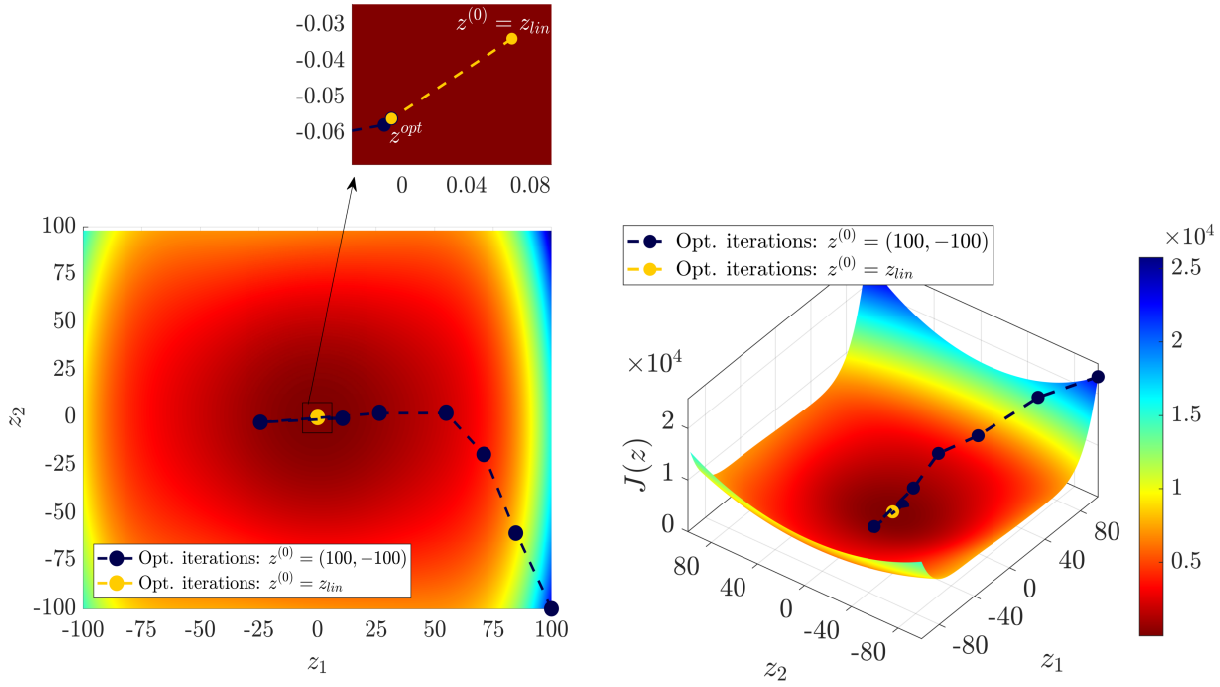

Figure 7.12: Most probable path optimization problem objective function using $L = 2$ trial functions and corresponding to a nonlinear oscillator with a bimodal response PDF with $a = 1.5$ and $\varepsilon = 1$ under white noise ($t_f = 1s$, $x(t_f) = 0.8$, $\dot{x}(t_f) = 0.9$). The Newton's optimization scheme iterations are also included.

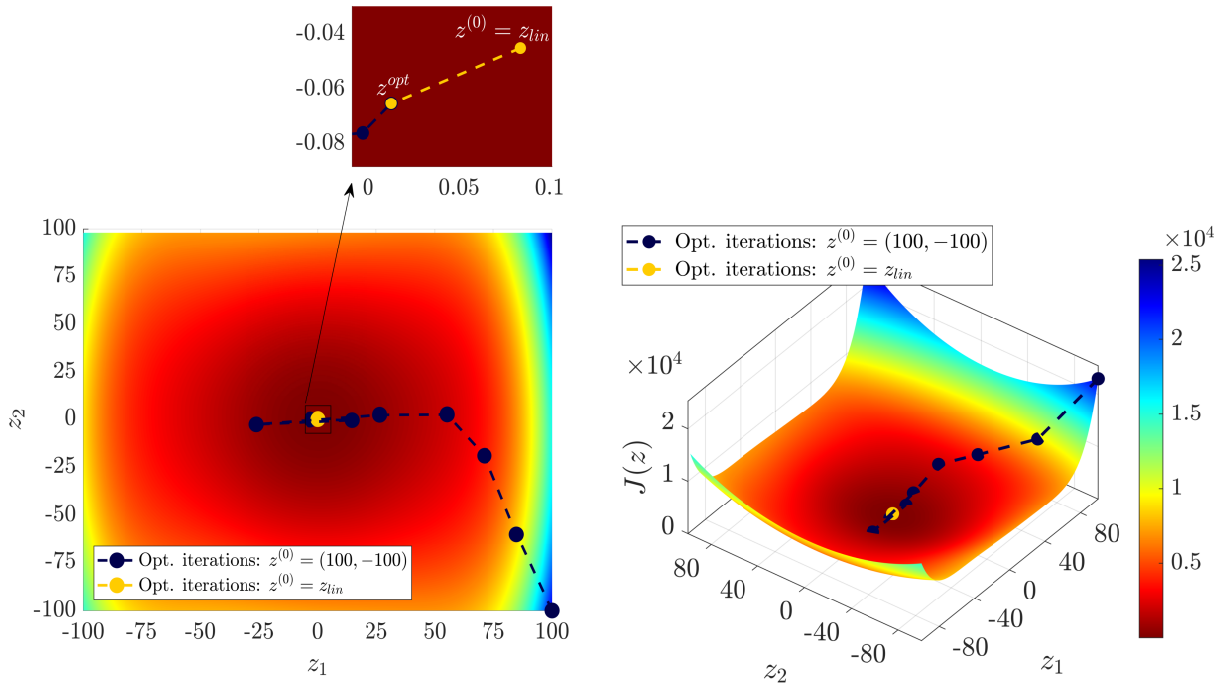

Figure 7.13: Most probable path optimization problem objective function using $L = 2$ trial functions and corresponding to a nonlinear oscillator with a bimodal response PDF with $a = 1.8$ and $\varepsilon = 1$ under white noise ($t_f = 1s$, $x(t_f) = 0.8$, $\dot{x}(t_f) = 0.9$). The Newton's optimization scheme iterations are also included.

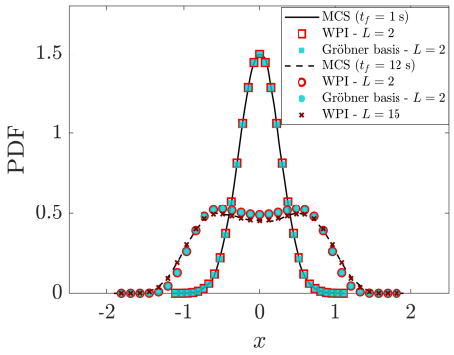

(a) a = 1.3: Response displacement PDF

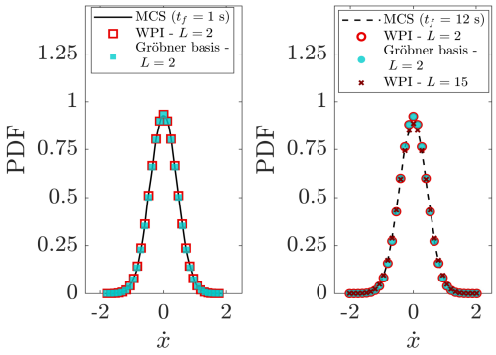

(b) a = 1.3: Response velocity PDF

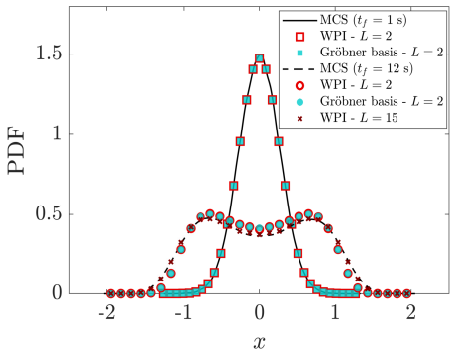

(c) a = 1.5: Response displacement PDF

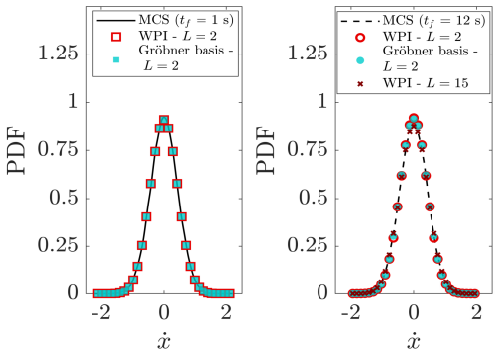

(d) a = 1.5: Response velocity PDF

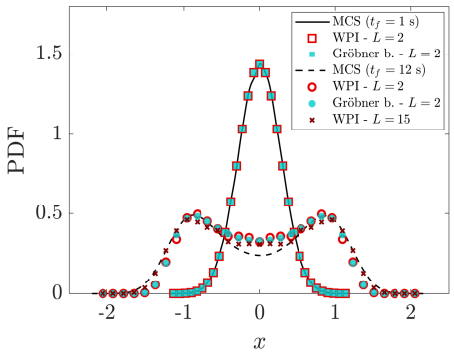

(e) a = 1.8: Response displacement PDF

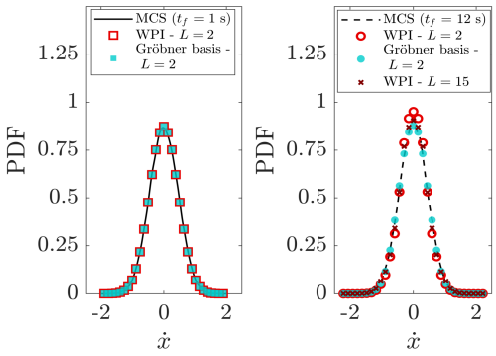

(f) a = 1.8: Response velocity PDF

Figure 7.14: Response displacement and velocity PDFs at various time instants corresponding to a nonlinear oscillator with a bimodal response PDF under white noise. Comparisons between WPI-based estimates utilizing both the Newton's scheme and the Gröbner basis approaches for the most probable path determination. MCS-based estimates are also included (50,000 realizations).

Chapter 8: Nonlinear normal modes (NNMs)

8.1 The Shaw–Pierre formulation

8.1.1 Center manifold technique

The nonlinear equations of motion are written in the state variable form

$$\left.\begin{aligned} \dot{x}_i &= y_i && (8.1a)\\ \dot{y}_i &= g_i(\boldsymbol{x};\boldsymbol{y}) && (8.1b)\end{aligned}\right\} \; i = 1, ..., n$$

where $\boldsymbol{x} = [x_1, x_2, ..., x_n]^T$ is the displacement vector, $\boldsymbol{y} = [y_1, y_2, ..., y_n]^T$ is the velocity vector and $\mathbf{g} = [g_1, g_2, ..., g_n]^T$ is an arbitrary nonlinear vector function.

Following [1], it is assumed next that there exists at least one motion for which all displacements and velocities are functionally related to a single displacement-velocity pair. Without loss of generality, this pair is chosen as the first displacement x_1 and velocity y_1, and the notation $u = x_1$ and $v = y_1$ is employed for convenience. In this regard, the rest x_i's and y_i's are expressed functionally in terms of u and v as

$$\left.\begin{aligned} x_i &= X_i(u, v) && (8.2a)\\ y_i &= Y_i(u, v) && (8.2b)\end{aligned}\right\} \; i = 1, ..., n$$

where $X_1(u,v) = u$ and $Y_1(u,v) = v$. Eq. (8.2) can be written in vector form as

$$\begin{bmatrix} x_1 \\ y_1 \\ x_2 \\ y_2 \\ \vdots \\ x_n \\ y_n \end{bmatrix} = \begin{bmatrix} u \\ v \\ X_2(u,v) \\ Y_2(u,v) \\ \vdots \\ X_n(u,v) \\ Y_n(u,v) \end{bmatrix} \tag{8.3}$$

It is noted that that for the cases considered in this thesis, a representation of the form of Eq. (8.2) is possible. The interested reader is referred to [1] for more details about the applicability of this representation.

Eq. (8.2) represents a 2-dimensional constraint surface in the $2n$-dimensional phase space. Thus, according to [1], a normal mode of motion for the nonlinear system of Eq. (8.1) is defined as a motion which takes place on a 2-dimensional invariant manifold in the system's phase space. This manifold has the following two properties, (a) it passes through a stable equilibrium point of the system, and (b) at that point, it is tangent to a plane which is an eigenspace of the system linearized around that equilibrium.

Next, restraining the solutions of the equations of motion (Eq. (8.1)) to satisfy the constraint equations (Eq. (8.2)) as well, yields a set of equations which can be solved for the constraint surface defined by the X_i's and Y_i's. This is accomplished by eliminating the time dependence and leads to a set of equations for the geometry of the invariant manifold (see e.g., [170, 171]). In this regard, differentiating the constraint equations Eq. (8.2) with respect to time yields

$$\left.\begin{aligned} \dot{x}_i &= \frac{\partial X_i}{\partial u}\dot{u} + \frac{\partial X_i}{\partial v}\dot{v} && \text{(8.4a)} \\ \dot{y}_i &= \frac{\partial Y_i}{\partial u}\dot{u} + \frac{\partial Y_i}{\partial v}\dot{v} && \text{(8.4b)} \end{aligned}\right\} \; i = 1, \ldots, n$$

Next, substituting the equations of motion Eq. (8.1) into Eq. (8.4) and replacing x_i and y_i by X_i and Y_i respectively, leads to $2n-2$ equations of the form

$$Y_i(u,v) = \frac{\partial X_i}{\partial u} v + \frac{\partial X_i}{\partial v} g_1(u, X_2(u,v), ..., X_n(u,v); v, Y_2(u,v), ..., Y_n(u,v))$$

$$g_i(u, X_2(u,v), ..., X_n(u,v); v, Y_2(u,v), ..., Y_n(u,v)) = \frac{\partial Y_i}{\partial u} v + \frac{\partial Y_i}{\partial v} g_1(u, X_2(u,v), ..., X_n(u,v); v, Y_2(u,v), ..., Y_n(u,v))$$

which can be solved for X_i and Y_i. It is noted that for $i = 1$, Eq. (8.5) is satisfied trivially. Even though Eq. (8.5) are not simpler than the original equations of motion, they allow for an approximate solution based on power series expansions. Once the X_i's and Y_i's have been obtained, the normal mode dynamics, i.e., the dynamics on the invariant manifold can be determined by substituting the X_i's and Y_i's in place of x_i and y_i in the first pair of the equations of motion, i.e., the ones for x_1 and x_2. In this regard, the modal dynamic equation becomes

$$\dot{u} = v \tag{8.6a}$$

$$\dot{v} = g_1(u, X_2(u,v), ..., X_n(u,v); v, Y_2(u,v), ..., Y_n(u,v)) \tag{8.6b}$$

where u and v represent the variables on the invariant manifold and correspond to projections of the modal dynamics on the (x_1, y_1) plane. In general, at every equilibrium point there are n solutions for the X_i's and Y_i's which correspond to n sets of equations of the form of Eq. (8.6), one set for each mode.

8.1.2 Approximation of the modal dynamics

Following [1], this section presents a technique for approximating the normal mode invariant manifolds, as well as the dynamics on these manifolds near the equilibrium point. Despite its local nature, this technique yields exact results for similar normal modes, since they they are represented by flat manifolds, and asymptotic results for non-similar normal modes. The adopted approximations take the form of power series expansions and can, in

principle, be generated for arbitrary order.

More specifically, a Taylor series expansion about the equilibrium configuration of the systems is employed. Without loss of generality, it is assumed that the equilibrium point of interest is at $\boldsymbol{x} = \boldsymbol{0}$. In this regard, the dynamics of the system near the equilibrium point can be approximated as

$$\begin{aligned}
\dot{x}_j =& y_j \\
\dot{y}_j =& \alpha_{jk} x_k + \beta_{jk} y_k + \delta_{jkm} x_k x_m + \epsilon_{jkm} x_k y_m + \gamma_{jkm} y_k y_m \\
&+ \mu_{jkmq} x_k x_m x_q + \nu_{jkmq} x_k x_m y_q + \rho_{jkmq} x_k y_m y_q + \xi_{jkmq} y_k y_m y_q + \ldots
\end{aligned}$$

where the coefficients in the expansions are derived form straightforward differentiation of the forces g_j $(j = 1, ..., n)$ with respect to $\boldsymbol{x}$ and $\boldsymbol{y}$, and where the implicit summation notation is used.

Next, it is assumed that the normal modes for the non-linear system, as given in Eq. (8.2), can also be expanded with the aid of a Taylor series as

$$\left.\begin{aligned}
X_i(u,v) =& a_{1,i} u + a_{2,i} v + a_{3,i} u^2 + a_{4,i} uv + a_{5,i} v^2 && \text{(8.8a)} \\
&+ a_{6,i} u^3 + a_{7,i} u^2 v + a_{8,i} uv^2 + a_{9,i} v^3 + \ldots && \text{(8.8b)} \\
Y_i(u,v) =& b_{1,i} u + b_{2,i} v + b_{3,i} u^2 + b_{4,i} uv + b_{5,i} v^2 && \text{(8.8c)} \\
&+ b_{6,i} u^3 + b_{7,i} u^2 v + b_{8,i} uv^2 + b_{9,i} v^3 + \ldots && \text{(8.8d)}
\end{aligned}\right\} \; i = 1, ..., n$$

The expansion of Eq. (8.8) can be written in vector form as

$$\begin{bmatrix} x_1 \\ y_1 \\ x_2 \\ y_2 \\ \vdots \\ x_n \\ y_n \end{bmatrix} = \left\{ \begin{bmatrix} 1 & 0 \\ 0 & 1 \\ a_{1,2} & a_{2,2} \\ b_{1,2} & b_{2,2} \\ \vdots & \vdots \\ a_{1,n} & a_{2,n} \\ b_{1,n} & b_{2,n} \end{bmatrix} + \begin{bmatrix} 0 & 0 \\ 0 & 0 \\ a_{3,2}u + a_{4,2}v & a_{5,2}v \\ b_{3,2}u + b_{4,2}v & b_{5,2}v \\ \vdots & \vdots \\ a_{3,n}u + a_{4,n}v & a_{5,n}v \\ b_{3,n}u + b_{4,n}v & b_{5,n}v \end{bmatrix} + \begin{bmatrix} 0 & 0 \\ 0 & 0 \\ a_{6,2}u^2 + a_{8,2}v^2 & a_{7,2}u^2 + a_{9,2}v^2 \\ b_{6,2}u^2 + b_{8,2}v^2 & b_{7,2}u^2 + b_{9,2}v^2 \\ \vdots & \vdots \\ a_{6,n}u^2 + a_{8,n}v^2 & a_{7,n}u^2 + a_{9,n}v^2 \\ b_{6,n}u^2 + b_{8,n}v^2 & b_{7,n}u^2 + b_{9,n}v^2 \end{bmatrix} \right\} \begin{bmatrix} u \\ v \end{bmatrix} + \ldots \tag{8.9}$$

which leads to a more compact notation of the form

$$\boldsymbol{q} = \left\{ \mathbf{m}_0 + \mathbf{m}_1(u, v) + \mathbf{m}_2(u, v) \right\} \begin{bmatrix} u \\ v \end{bmatrix} + \ldots \tag{8.10}$$

where $\boldsymbol{q} = [x_1, y_1, x_2, y_2, ..., x_n, y_n]^T$ and $\mathbf{m}_0$, $\mathbf{m}_1$, $\mathbf{m}_2$ are $2n \times n$ matrices. The matrix $\mathbf{m}_0$ is the linear modal component, whereas $\mathbf{m}_1$ and $\mathbf{m}_2$ incorporate the effects of quadratic and cubic non-linear terms, respectively.

The coefficients of the linear terms represent the ratios for the usual linear normal modes. For an undamped system it can be shown that the cross-terms between displacement and velocity, $a_{2,i}$ and $b_{1,i}$, equal zero, while $a_{1,i} = b_{2,i}$ represent the usual amplitude rations for a conservative vibratory system. For a damped system, the linear coupling terms between

displacement and velocity are generally non-zero and have no special relationship with one another (other than being the linear approximation to the modal subspace), except in cases such as proportional damping, where the modes of the damped system are identical to those of its undamped counterpart. These non-zero cross-terms allow for phase differences between the displacements for non-conservative systems.

The non-linear terms in Eq. (8.10) describe the bending of the modal subspace. Their associated coefficients can all be zero for a mode in which the amplitude ratios are fixed constants, as happens in systems which posses similar normal modes, but in general they are non-zero. These terms capture the effects of the non-linear forces, and result in the fact that the displacement and velocity ratios are dependent on the amplitude of the motion.

Next, substituting Eq. (8.8) into Eq. (8.5), gathering terms of the same order in the monomials of u and v and requiring that the corresponding coefficients vanish, leads to a system of algebraic equations for the coefficients a_{ki} and b_{ki} in Eq. (8.8). This system, consists of $18(n-1)$ algebraic equations if the Taylor expansions of Eq. (8.8) are truncated after the 3-rd order terms. In the case that 4-th order terms are included in the Taylor expansions, the number of algebraic equations becomes $28(n-1)$ and including 5-th order terms it becomes $40(n-1)$. In general, the system of algebraic equations to be solved has $[(r+1)(r+2)-2](n-1)$ equations and the same number of unknowns where r is the order of the expansion in Eq. (8.8).

Solving the $18(n-1)$ system of equations leads to a cubic series approximation of the n nonlinear normal modes and provides a geometric representation of the invariant manifolds near the equilibrium point. A local approximation of the dynamical equations for each mode can be constructed via Eq. (8.6) by utilizing the series expansion for g_1 shown in Eq. (8.7) and replacing (x_j, y_j) with $X_j(u,v), Y_j(u,v)$ for all $j = 1, ..., n$. This yields a single-degree-of-freedom nonlinear oscillator equation which describes the dynamics of the system on an invariant, two-dimensional subspace which is tangent to the linear normal mode eigenspace at the equilibrium point. There are n such oscillators, one for each normal mode. It is noted,

that in the case where the nonlinear functions g_j in the equations of motion Eq. (8.1) are polynomial functions of $\boldsymbol{x}$ and $\boldsymbol{y}$, the series representation of Eq. (8.7) is not necessary, since the quantities $\dot{x}_j$ and $\dot{y}_j$ will be polynomials in u and v by construction.

8.1.3 Transformation from nonlinear modal to physical coordinates

Next, a complete nonlinear modal matrix $\mathbf{M}$ can be constructed which depends on the modal coordinates denoted as $\boldsymbol{w}$. The $2n \times 2n$ modal matrix $\mathbf{M}$ is constructed by concatenating the n $2n \times 2$ matrices of Eq. (8.10). Similarly, $\boldsymbol{w}$ is constructed by noting that each mode will have its own (u, v) pair, which is labeled as (u_k, v_k) for $k = 1, ..., n$, i.e., $\boldsymbol{w} = [u_1, v_1, ..., u_k, v_k]^T$. The complete transformation from modal coordinates $\boldsymbol{w}$ to physical coordinates $\boldsymbol{q}$ can be written as

$$\boldsymbol{q} = \mathbf{M}(\boldsymbol{w})\boldsymbol{w} = \left\{\mathbf{M}_0 + \mathbf{M}_1(\boldsymbol{w}) + \mathbf{M}_2(\boldsymbol{w})\right\} \boldsymbol{w} + ... \tag{8.11}$$

where the matrices $\mathbf{M}_p$ are assembled from the matrices $\mathbf{m}_p$ of Eq. (8.10) for $p = 0, 1, 2$. It is noted that the coefficients $a_{i,j}$ and $b_{i,j}$ will be different for each mode, and an explicit representation of Eq. (8.11) with respect to these coefficients would require an additional index representing the each mode, i.e., $a_{i,j,k}$ and $b_{i,j,k}$.

8.1.4 Transformation from physical to nonlinear modal coordinates

A nonlinear extension of the corresponding linear modal superposition is described in this section, which of course is not strictly the same as its linear counterpart. Specifically, it is a nonlinear coordinate transformation that allows for assembling a complete solution from a sum of simpler ones. In general, the coupling between the nonlinear equations of motion cannot be fully eliminated. Nevertheless, as shown in Sec. 8.2 the herein described nonlinear transformation of the equations of motion leads to a relatively accurate description of the system dynamics simply by ignoring the coupling terms and applying superposition of

the resultant uncoupled nonlinear equations. Moreover, this approach reduces to its linear counterpart when nonlinearities are not present or ignored.

In linear system, the eigenspaces are planar and the overall system response can be decomposed into modal components via linear projection onto these eigenspaces, or reassembled by linear recombination of the modal responses. In the presence of nonlinearities, the modal subspaces are curved in general and curvilinear coordinates need to be utilized for reflecting the nature of these subspaces.

The aforementioned nonlinear modal superposition approach, involves a transformation from physical coordinates to modal coordinates and a subsequent recombination of the modal dynamics to the physical coordinates via $\boldsymbol{q} = \mathbf{M}(\boldsymbol{w})\boldsymbol{w}$ of Eq. (8.11). This process requires an inversion of the transformation of Eq. (8.11). As described in [1], this inversion is much simpler in the case where only cubic nonlinearities are present. The inversion is presented here under this assumption and the interested reader is referred to Appendix C in [1] for a detailed presentation of the general case.

The inversion process begins by setting $M_1(\boldsymbol{w})$ equal to zero and rewriting equation Eq. (8.11) as

$$\begin{aligned} \boldsymbol{w} &= \left\{\mathbf{M}_0 + \mathbf{M}_2(\boldsymbol{w})\right\}^{-1} \boldsymbol{q} + \ldots \\ &= \left\{\mathbf{I} + \mathbf{M}_0^{-1}\mathbf{M}_2(\boldsymbol{w})\right\}^{-1} \mathbf{M}_0^{-1}\boldsymbol{q} + \ldots \\ &= \left\{\mathbf{I} - \mathbf{M}_0^{-1}\mathbf{M}_2(\boldsymbol{w})\right\} \mathbf{M}_0^{-1}\boldsymbol{q} + \ldots \end{aligned} \tag{8.12}$$

where $\mathbf{I}$ is the $2n \times 2n$ identity matrix. The right hand side of Eq. (8.12) involves both $\boldsymbol{q}$ and $\boldsymbol{w}$. This can be remedied by observing that $\mathbf{M}_2(\boldsymbol{w})$ is quadratic in $\boldsymbol{w}$ and that the leading order argument of $\mathbf{M}_2$ is simply $\mathbf{M}_0^{-1}\boldsymbol{q}$. Hence, $\boldsymbol{w}$ in the right hand side of Eq. (8.12) is replaced by $\mathbf{M}_0^{-1}\boldsymbol{q}$ and higher order terms are ignored. This yields the inverse transformation

$$\boldsymbol{w} = \left\{\mathbf{I} - \mathbf{M}_0^{-1}\mathbf{M}_2(\mathbf{M}_0^{-1}\boldsymbol{q})\right\} \mathbf{M}_0^{-1}\boldsymbol{q} + \ldots \tag{8.13}$$

which is correct up to cubic terms in $\boldsymbol{q}$.

Next, the equations of motion are being transformed to a modal coordinate representation. Specifically, near the equilibrium $\boldsymbol{q} = \boldsymbol{0}$, the equations of motion are written as

$$\dot{\boldsymbol{q}} = \boldsymbol{A}(\boldsymbol{q})\boldsymbol{q} = \Big\{\boldsymbol{A}_0 + \boldsymbol{A}_1(\boldsymbol{q}) + \boldsymbol{A}_2(\boldsymbol{q})\Big\}\,\boldsymbol{q} + \ldots \tag{8.14}$$

where $\boldsymbol{A}_0\boldsymbol{q}$ represents the linearized dynamics, $\boldsymbol{A}_1(\boldsymbol{q})\boldsymbol{q}$ the quadratic terms and $\boldsymbol{A}_2(\boldsymbol{q})\boldsymbol{q}$ the cubic terms. Next, the time derivative of $\boldsymbol{q}$ is expressed as

$$\dot{\boldsymbol{q}} = \frac{\partial \bar{\mathbf{M}}(\boldsymbol{w})}{\partial \boldsymbol{w}}\dot{\boldsymbol{w}} \tag{8.15}$$

which is a direct consequence of Eq. (8.11) after defining

$$\bar{\mathbf{M}}(\boldsymbol{w}) = \mathbf{M}(\boldsymbol{w})\boldsymbol{w} = \boldsymbol{q} \tag{8.16}$$

Substituting Eqs. (8.15) and (8.16) into Eq. (8.14) yields

$$\frac{\partial \bar{\mathbf{M}}(\boldsymbol{w})}{\partial \boldsymbol{w}}\dot{\boldsymbol{w}} = \boldsymbol{A}(\bar{\mathbf{M}}(\boldsymbol{w}))\bar{\mathbf{M}}(\boldsymbol{w}) \tag{8.17}$$

and thus the equations of motion in terms of the modal coordinates can be expressed as

$$\dot{\boldsymbol{w}} = \left[\frac{\partial \bar{\mathbf{M}}(\boldsymbol{w})}{\partial \boldsymbol{w}}\right]^{-1} \boldsymbol{A}(\bar{\mathbf{M}}(\boldsymbol{w}))\bar{\mathbf{M}}(\boldsymbol{w}) \tag{8.18}$$

Even though the modal equations in Eq. (8.18) are generally coupled, it is shown in Sec. 8.2 that in some cases, ignoring the coupling terms the nonlinear modal responses can be recombined into a sufficiently accurate general motion. This is achieved by solving an initial value problem. Specifically, let $\boldsymbol{q}_0$ be the initial conditions of the system in physical coordinates. The inverse transformation of Eq. (8.13) is employed for determining the initial value vector $\boldsymbol{w}_0$ in terms of modal coordinates, which corresponds to the coupled system of nonlinear

modal oscillators of Eq. (8.18). In Sec. 8.2, the coupling terms are ignored yielding a set of n "decoupled" nonlinear modal equations of motion which are individually solved using numerical integration. The results are compared with numerical integration results of the original equations of motion in physical coordinates, demonstrating very good agreement in the considered examples.

8.2 Examples

8.2.1 Linear oscillator with damping

The first example considered in this section is a 2-dimensional linear oscillator described by the following equations of motion.

$$\dot{x}_1 = y_1, \quad \dot{y_1} = g_1(x_1, y_1; x_2, y_2) = -(1+k)x_1 + kx_2 - cy_1 + cy_2 \tag{8.19a}$$

$$\dot{x}_2 = y_2, \quad \dot{y_2} = g_2(x_1, y_1; x_2, y_2) = kx_1 - (1+k)x_2 + cy_1 - 2cy_2 \tag{8.19b}$$

where the parameter values are $k = 1$ and $c = 0.3$. The expansions of Eq. (8.2) are utilized and truncated to up to 3-rd order terms and the procedure outlined in Sec. 8.1.1 yields a system of 18 polynomial equations in 18 unknowns, namely the 9 coefficients $a_1, ..., a_9$ of the expansion of $X_2(u, v)$ and the 9 coefficients $b_1, ..., b_9$ for the expansion of $Y_2(u, v)$ shown in Eq. (8.2). This system of polynomial equations has 2 real solutions, one for each mode.

The Gröbner basis approach outlined in Chapter 6 is utilized next for the solution of the aforementioned polynomial system. The corresponding Gröbner basis, shown in Eq. (C.1) in Appendix C, has 24 elements and the basis of standard monomials B, shown in Eq. (8.20), has only 6 elements, i.e., the polynomial system of equations has 6 solutions (2 real and 4 complex).

$$B = \begin{bmatrix} 1 & a_1 & a_2 & b_1 & b_2 & b_2^2 \end{bmatrix} \tag{8.20}$$

The two solutions of the polynomial system of equations corresponding to the two normal

modes are given in Tab. 8.1. It can be seen that only the coefficients of the linear parts of the expansions, i.e., a_1, a_2, b_1 and b_2 are nonzero.

Table 8.1: Solutions for the linear system

	Mode 1	Mode 2		Mode 1	Mode 2
a_1	-1.1056	0.9471	b_1	0.4599	0.1401
a_2	-0.1550	-0.1386	b_2	-0.9891	0.9676
a_3	0	0	b_3	0	0
a_4	0	0	b_4	0	0
a_5	0	0	b_5	0	0
a_6	0	0	b_6	0	0
a_7	0	0	b_7	0	0
a_8	0	0	b_8	0	0
a_9	0	0	b_9	0	0

The shapes of the invariant manifolds $X_2(u, v) = x_2$ and $Y_2(u, v) = \dot{x}_2$ within the phase space $(u, v) = (x_1, \dot{x}_1)$ is shown in Fig. 8.1. As expected, these manifolds corresponding to the linear system of Eq. (8.19) have planar shapes. Moreover, the linear equations of motion

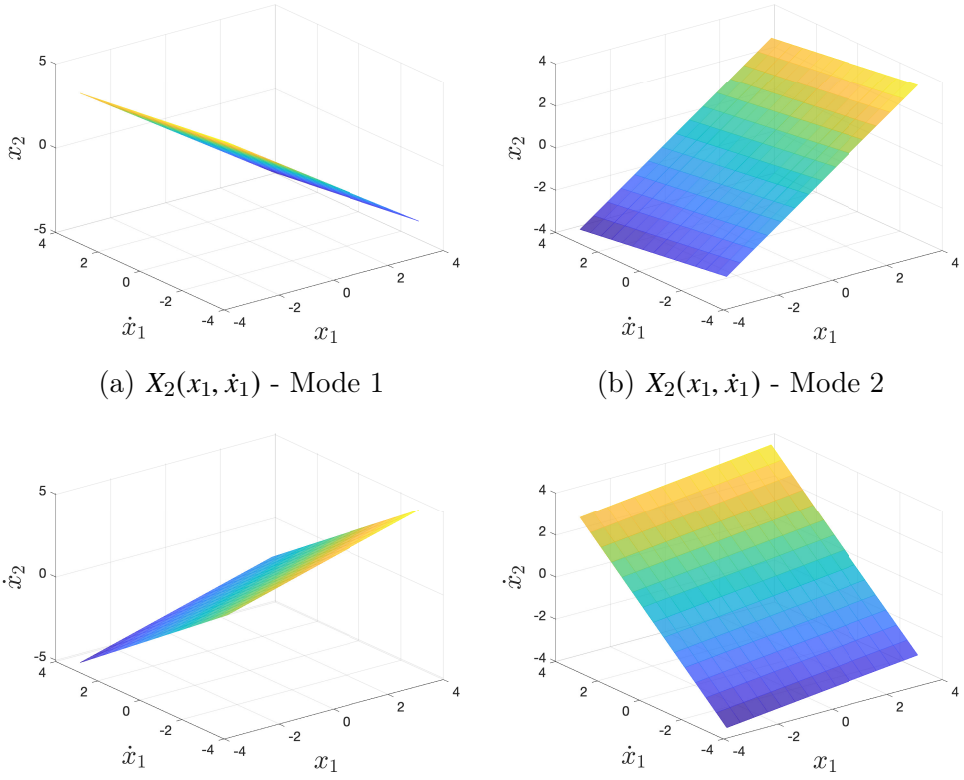

(a) $X_2(x_1, \dot{x}_1)$ - Mode 1

(b) $X_2(x_1, \dot{x}_1)$ - Mode 2

(c) $Y_2(x_1, \dot{x}_1)$ - Mode 1

(d) $Y_2(x_1, \dot{x}_1)$ - Mode 2

Figure 8.1: Invariant manifolds of the linear system.

in Eq. (8.19) are projected onto the linear modal subspaces which leads to the uncoupled system of modal equations of motion as

$$\text{mode 1:} \quad \ddot{u}_1 + 0.7517\dot{u}_1 + 2.9676u_1 = 0 \tag{8.21a}$$

$$\text{mode 2:} \quad \ddot{u}_2 + 0.1483\dot{u}_2 + 1.0109u_2 = 0 \tag{8.21b}$$

Next, assuming a vector of initial conditions $\boldsymbol{q}_0 = (x_1, y_1, x_2, y_2) = (0, 0, 2, 0)$, the original equations of motion Eq. (8.19) are solved numerically. Moreover, $\boldsymbol{q}_0$ is transformed to modal coordinates using Eq.(8.13) as $\boldsymbol{w}_0 = (u_1, v_1, u_2, v_2) = (-0.97309, -0.15905, 0.97309, 0.15905)$ and the uncoupled modal equations of motion Eq. (8.21) are solved separately for each mode and subsequently recombined into a general motion in terms of physical coordinates. The results of the two solution approaches are compared in Fig. 8.2 where perfect agreement is observed. This is due to the linear form of the original equations of motion which allows for perfect decoupling and modal superposition.

8.2.2 Nonlinear oscillator with cubic nonlinearity

The second example of this section is a 2-dimensional nonlinear system with cubic nonlinearity described by the following equations of motion.

$$\dot{x}_1 = y_1, \quad \dot{y}_1 = g_1(x_1, y_1; x_2, y_2) = -(1+k)x_1 + kx_2 - \gamma x_1^3 - cy_1 + cy_2 \tag{8.22a}$$

$$\dot{x}_2 = y_2, \quad \dot{y}_2 = g_2(x_1, y_1; x_2, y_2) = kx_1 - (1+k)x_2 + cy_1 - 2cy_2 \tag{8.22b}$$

where the parameter values are $k = 1$, $c = 0.3$ and $\gamma = 0.5$. The expansions of Eq. (8.2) are utilized and truncated to up to 3-rd order terms and the procedure outlined in Sec. 8.1.1 yields a system of 18 polynomial equations in 18 unknowns, namely the 9 coefficients $a_1, ..., a_9$ of the expansion of $X_2(u, v)$ and the 9 coefficients $b_1, ..., b_9$ for the expansion of $Y_2(u, v)$ shown in Eq. (8.2). This system of polynomial equations again has 2 real solutions, one for each mode.

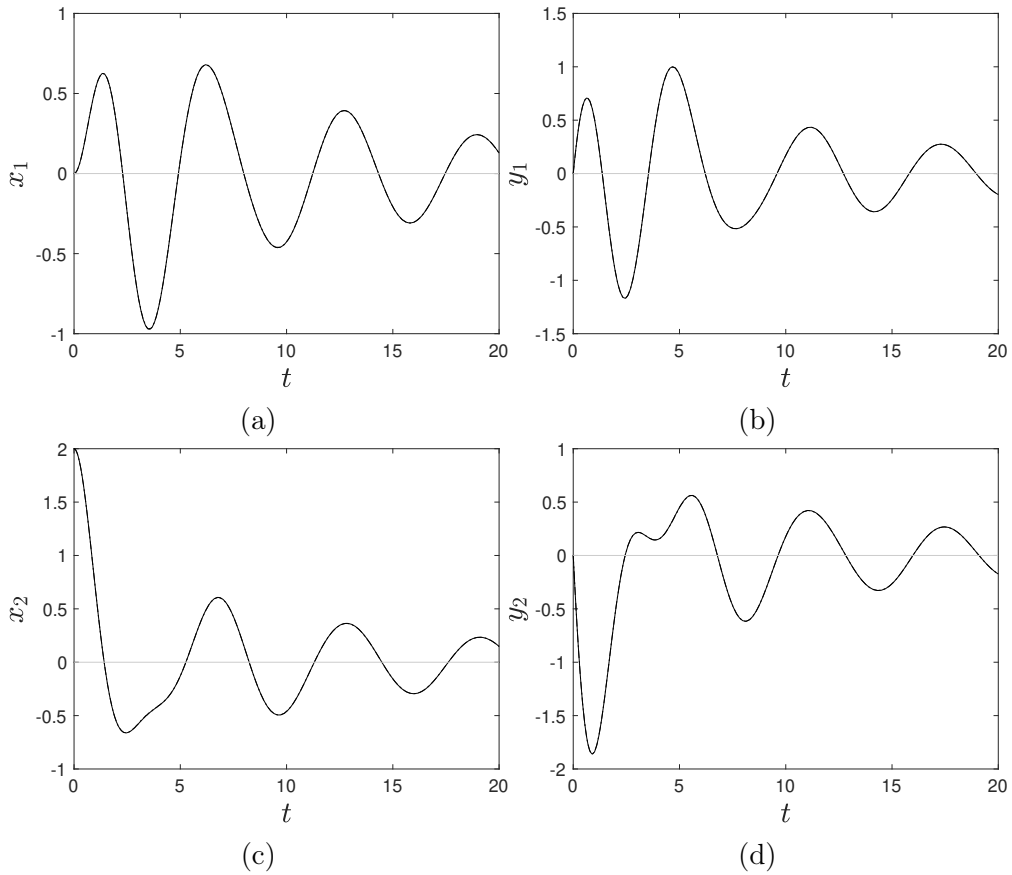

Figure 8.2: Numerical solutions of original and modal equations of motion. **Solid line**: original equations of motion. **Dashed line**: linear modal equations of motion.

The Gröbner basis approach outlined in Chapter 6 is utilized next for the solution of the aforementioned polynomial system. In this case, the Gröbner basis has 28 elements which have a much more complicated form compared to the elements of the Gröbner basis in the linear system case. The basis of standard monomials $\boldsymbol{B}$, shown in Eq. (8.23), again has only 6 elements, i.e., the polynomial system of equations has 6 solutions (2 real and 4 complex).

$$\boldsymbol{B} = \begin{bmatrix} 1 & b_2 & b_6 & b_7 & b_8 & b_9 \end{bmatrix} \tag{8.23}$$

The two solutions of the polynomial system of equations corresponding to the two normal modes are given in Tab. 8.2.

The shapes of the invariant manifolds $X_2(u, v) = x_2$ and $Y_2(u, v) = \dot{x}_2$ within the phase

Table 8.2: Solutions for the system with cubic nonlinearity

	Mode 1	Mode 2		Mode 1	Mode 2
a_1	-1.1056	0.9471	b_1	0.4599	0.1401
a_2	-0.1550	-0.1386	b_2	-0.9891	0.9676
a_3	0	0	b_3	0	0
a_4	0	0	b_4	0	0
a_5	0	0	b_5	0	0
a_6	0.0327	0.1554	b_6	0.2088	0.0531
a_7	-0.0492	-0.0074	b_7	0.1991	0.0244
a_8	-0.0110	0.2191	b_8	0.0821	0.0768
a_9	-0.0187	-0.0627	b_9	0.0324	0.2455

space $(u, v) = (x_1, \dot{x}_1)$ is shown in Fig. 8.3. In this case, the manifolds corresponding to the nonlinear system of Eq. (8.22) have curved shapes and they are tangent to their linear counterparts at the equilibrium point, i.e., the point $(0, 0)$ in this example. Moreover, the

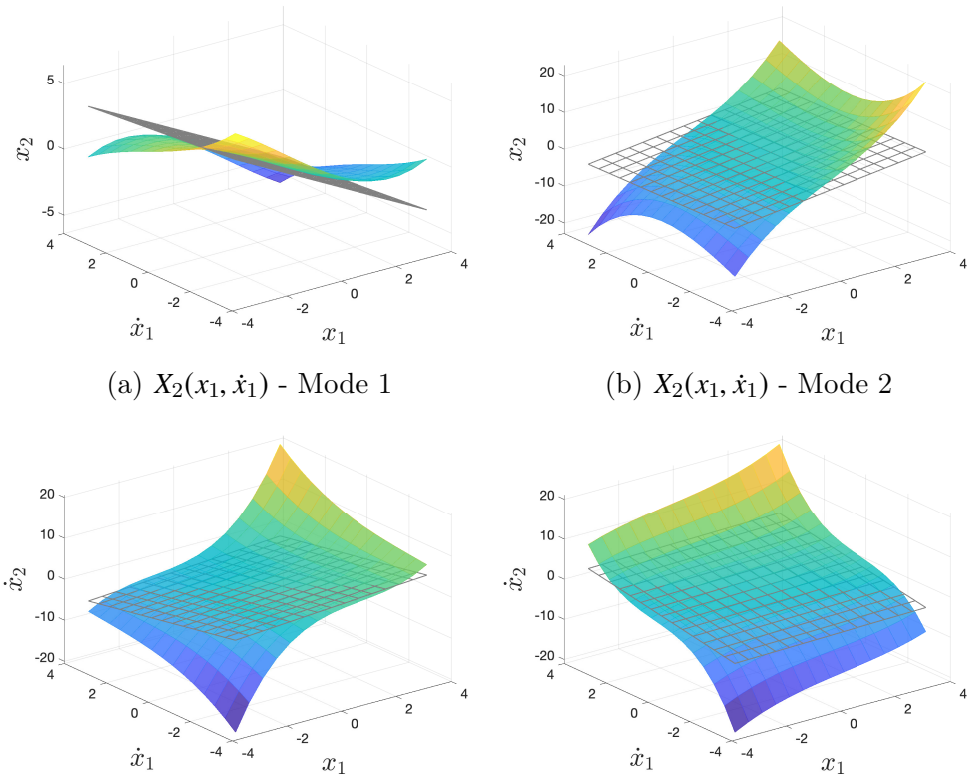

(a) $X_2(x_1, \dot{x}_1)$ - Mode 1

(b) $X_2(x_1, \dot{x}_1)$ - Mode 2

(c) $Y_2(x_1, \dot{x}_1)$ - Mode 1

(d) $Y_2(x_1, \dot{x}_1)$ - Mode 2

Figure 8.3: Invariant manifolds of the nonlinear system with cubic nonlinearity.

nonlinear equations of motion in Eq. (8.22) are projected onto the nonlinear modal subspaces which, after ignoring the coupling terms, leads to the "decoupled" system of modal equations

of motion

$$\text{mode 1:} \quad \ddot{u}_1 + 0.7517\dot{u}_1 + 2.9676u_1 + 0.4046u_1^3 - 0.0105u_1^2\dot{u}_1 - 0.0136u_1\dot{u}_1^2 + 0.0089\dot{u}_1^3 = 0 \tag{8.24a}$$

$$\text{mode 2:} \quad \ddot{u}_2 + 0.1483\dot{u}_2 + 1.0109u_2 + 0.3287u_2^3 + 0.0002u_2^2\dot{u}_2 - 0.2421u_2\dot{u}_2^2 - 0.0109\dot{u}_2^3 = 0 \tag{8.24b}$$

For the same nonlinear system described in Eq. (8.22), the expansions of Eq. (8.2) are utilized but truncated to up to 5-th order terms this time. The procedure outlined in Sec. 8.1.1 yields a system of 40 polynomial equations in 40 unknowns, where the coefficients $a_{10}, ..., a_{20}$ are included in the expansion of $X_2(u, v)$ and the coefficients $b_{10}, ..., b_{20}$ in the expansion of $Y_2(u, v)$. This system of polynomial equations again has 2 real solutions, one for each mode. This polynomial system is solved using the Gröbner basis approach outlined in Chapter 6. The values of the coefficients $a_1, ..., a_9$ and $b_1, ..., b_9$ are the same with the ones in Tab. 8.2, whereas the values of the additional 4-th and 5-th order coefficients are shown in Tab. 8.3. It is seen that the 5-th order coefficients are nonzero indicating that the accuracy of the invariant manifolds shown in Fig. 8.3 increases with increasing expansion order even beyond the order of the nonlinearity present in the equations of motion. Projection onto the

Table 8.3: Additional 4-th and 5-th order coefficients for the system with cubic nonlinearity

	Mode 1	Mode 2		Mode 1	Mode 2
a_{10}	0	0	b_{10}	0	0
a_{11}	0	0	b_{11}	0	0
a_{12}	0	0	b_{12}	0	0
a_{13}	0	0	b_{13}	0	0
a_{14}	0	0	b_{14}	0	0
a_{15}	0.0803	0.1144	b_{15}	-0.1685	0.1180
a_{16}	0.1157	-0.1155	b_{16}	-0.2342	0.3684
a_{17}	0.1041	-0.5317	b_{17}	-0.2022	0.0329
a_{18}	0.0783	0.0906	b_{18}	-0.1015	-0.7289
a_{19}	0.0190	0.0162	b_{19}	-0.0266	0.0937
a_{20}	0.0080	-0.0584	b_{20}	-0.0076	0.0471

nonlinear modal subspaces approximated by the 5-th order expansion, and after ignoring the coupling terms, leads to the "decoupled" system of modal equations of motion similar the one in Eq. (8.24) but terms of up to 5-th order in this case.

Next, assuming a vector of initial conditions $\boldsymbol{q}_0 = (0, 0, 2, 0)$, the original equations of motion Eq. (8.22) are solved numerically. Moreover, $\boldsymbol{q}_0$ is transformed to nonlinear modal coordinates using Eq.(8.13) yielding $\boldsymbol{w}_0 = (-0.91743, -0.22736, 0.91743, 0.22736)$ and the "decoupled" modal equations of motion Eq. (8.24) are solved separately for each mode and subsequently recombined into a general motion in terms of physical coordinates. The same procedure is followed again twice. First, the original equations of motion and the vector of initial conditions are projected onto the linear modal subspaces, yielding the "linear" modal equations of motion

$$\text{mode 1:} \quad \ddot{u}_1 + 0.7517\dot{u}_1 + 2.9676u_1 + 0.5u_1^3 = 0 \tag{8.25a}$$

$$\text{mode 2:} \quad \ddot{u}_2 + 0.1483\dot{u}_2 + 1.0109u_2 + 0.5u_2^3 = 0 \tag{8.25b}$$

with initial conditions $\boldsymbol{w}_0 = (-0.97309, -0.15905, 0.97309, 0.15905)$. Second, the original equations of motion and the vector of initial conditions are projected onto the nonlinear subspaces approximated by the 5-th order expansion. The results of the four solution approaches are compared in Fig. 8.4 where it can be observed that the solution of the nonlinear modal equations Eq. (8.24) captures the solution of the original equations of motion relatively accurately. The discrepancy between these two solutions is attributed to the fact that coupling terms have been ignored in Eq. (8.24). On the contrary, the solution of the "linear" modal equations Eq. (8.25) diverges from the solution of the original equations significantly. Finally, the solution of the modal equations of motion obtained after projection onto the nonlinear modal subspaces approximated by the 5-th order expansions yields an obvious improvement over the solution where only a 3-rd order expansion is used.

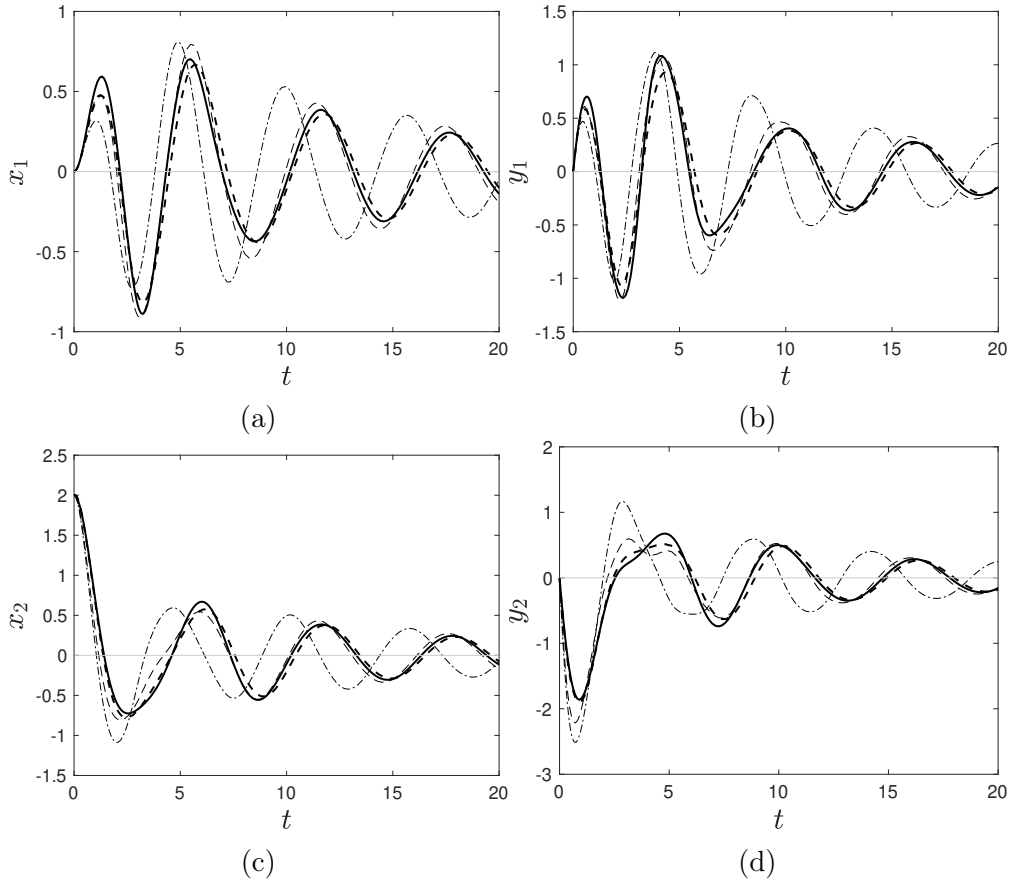

Figure 8.4: Numerical solutions of original and modal equations of motion. **Thick solid line**: original equations of motion. **Thick dashed line**: nonlinear modal equations of motion approximated to 5-th order. **Thin dashed line**: nonlinear modal equations of motion approximated to 3-rd order. **Thin dashed-dotted line**: linear modal equations of motion.

8.2.3 Nonlinear oscillator with cubic and quintic nonlinearities

The third example of this section is a 2-dimensional nonlinear system with cubic and quintic nonlinearities described by the following equations of motion.

$$\dot{x}_1 = y_1, \quad \dot{y}_1 = g_1(x_1, y_1; x_2, y_2) = -(1+k)x_1 + kx_2 - \gamma x_1^3 - \delta x_1^5 - cy_1 + cy_2 \tag{8.26a}$$

$$\dot{x}_2 = y_2, \quad \dot{y}_2 = g_2(x_1, y_1; x_2, y_2) = kx_1 - (1+k)x_2 + cy_1 - 2cy_2 \tag{8.26b}$$

where the parameter values are $k = 1$, $c = 0.3$, $\gamma = 0.5$ and $\delta = 1.5$. The expansions of Eq. (8.2) are utilized and truncated to up to 5-th order terms and the procedure outlined in Sec.

8.1.1 yields a system of 40 polynomial equations in 40 unknowns, namely the 20 coefficients $a_1, ..., a_{20}$ of the expansion of $X_2(u, v)$ and the 20 coefficients $b_1, ..., b_{20}$ for the expansion of $Y_2(u, v)$ shown in Eq. (8.2). This system of polynomial equations again has 2 real solutions, one for each mode.

The Gröbner basis approach outlined in Chapter 6 is utilized next for the solution of the aforementioned polynomial system. In this case, the Gröbner basis has 50 elements and the basis of standard monomials B, shown in Eq. (8.27), again has only 6 elements, i.e., the polynomial system of equations has 6 solutions (2 real and 4 complex).

$$B = \begin{bmatrix} 1 & b_{16} & b_{17} & b_{18} & b_{19} & b_{20} \end{bmatrix} \tag{8.27}$$

The two solutions of the polynomial system of equations corresponding to the two normal modes are given in Tab. 8.4. It is noted, that for the nonlinear system of this example, a second approach has been utilized, where the expansions of Eq. (8.2) are truncated after the 3-rd order terms, even though the nonlinear system includes a quintic term as well. The results, i.e., the Gröbner basis, the basis of standard monomials and the solutions of the polynomial system of equations, were identical to the previous example.

Table 8.4: Solutions for the system with cubic and quintic nonlinearities

	Mode 1	Mode 2		Mode 1	Mode 2
a_1	-1.1056	0.9471	b_1	0.4599	0.1401
a_2	-0.1550	-0.1386	b_2	-0.9891	0.9676
a_3	0	0	b_3	0	0
a_4	0	0	b_4	0	0
a_5	0	0	b_5	0	0
a_6	0.0327	0.1554	b_6	0.2088	0.0531
a_7	-0.0492	-0.0074	b_7	0.1991	0.0244
a_8	-0.0110	0.2191	b_8	0.0821	0.0768
a_9	-0.0187	-0.0627	b_9	0.0324	0.2455
a_{10}	0	0	b_{10}	0	0
a_{11}	0	0	b_{11}	0	0
a_{12}	0	0	b_{12}	0	0
a_{13}	0	0	b_{13}	0	0
a_{14}	0	0	b_{14}	0	0
a_{15}	0.0095	0.4282	b_{15}	0.4926	-0.0379
a_{16}	-0.0892	0.1884	b_{16}	0.5264	-0.2200
a_{17}	-0.0698	1.0743	b_{17}	0.3492	0.0771
a_{18}	-0.0657	0.0876	b_{18}	0.1776	0.6983
a_{19}	-0.0200	0.6308	b_{19}	0.0536	0.2076
a_{20}	-0.0084	-0.1075	b_{20}	0.0128	0.6944

The shapes of the invariant manifolds $X_2(u, v) = x_2$ and $Y_2(u, v) = \dot{x}_2$ within the phase space $(u, v) = (x_1, \dot{x}_1)$ is shown in Fig. 8.3. In this case, the manifolds corresponding to the nonlinear system of Eq. (8.22) have curved shapes and they are tangent to their linear counterparts at the equilibrium point, i.e., the point $(0, 0)$ in this example. Moreover, the

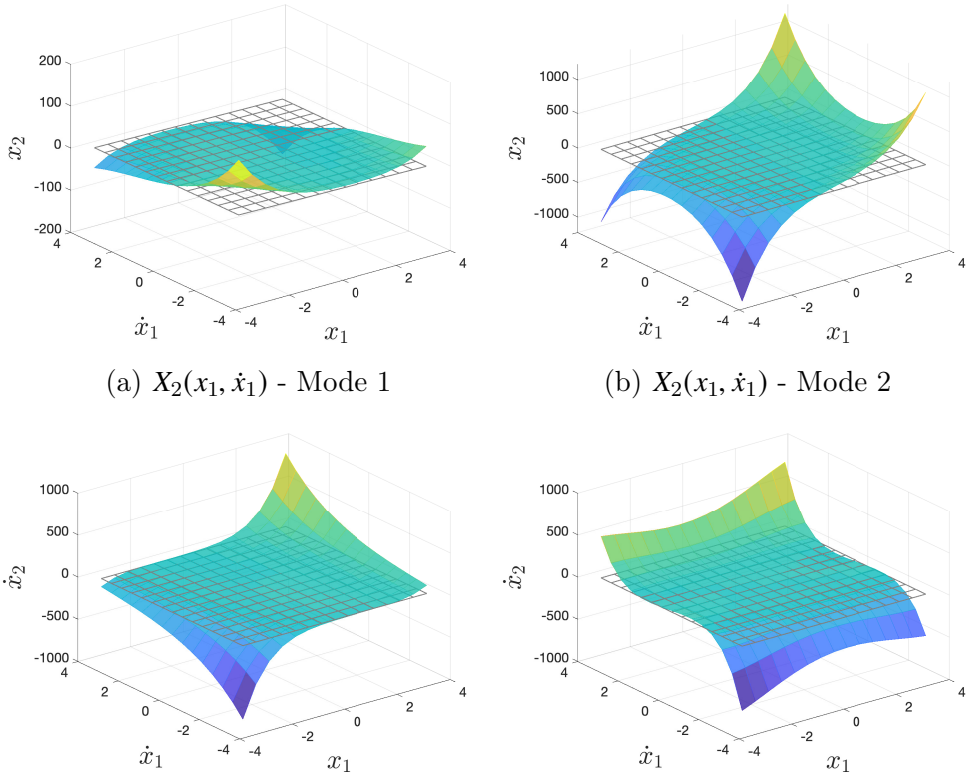

(a) $X_2(x_1, \dot{x}_1)$ - Mode 1

(b) $X_2(x_1, \dot{x}_1)$ - Mode 2

(c) $Y_2(x_1, \dot{x}_1)$ - Mode 1

(d) $Y_2(x_1, \dot{x}_1)$ - Mode 2

Figure 8.5: Invariant manifolds of the nonlinear system with cubic and quintic nonlinearities.

nonlinear equations of motion in Eq. (8.26) are projected onto the nonlinear modal subspaces approximated to 5-th order (see Eq. (8.8)) which, after ignoring the coupling terms, leads

to the "decoupled" system of modal equations of motion

$$\begin{aligned}
\text{mode 1:}\quad & \ddot{u}_1 + 0.7517\dot{u}_1 + 2.9676u_1 + 0.4046u_1^3 - 0.0105u_1^2\dot{u}_1 \\
& - 0.0136u_1{\dot{u}_1}^2 + 0.0089{\dot{u}_1}^3 + 1.3428u_1^5 - 0.0687u_1^4\dot{u}_1 \\
& - 0.0350u_1^3{\dot{u}_1}^2 + 0.0124u_1^2{\dot{u}_1}^3 + 0.0039u_1{\dot{u}_1}^4 + 0.0046{\dot{u}_1}^5 = 0 \qquad (8.28a) \\
\text{mode 2:}\quad & \ddot{u}_2 + 0.1483\dot{u}_2 + 1.0109u_2 + 0.3287u_2^3 + 0.0001u_2^2\dot{u}_2 \\
& - 0.2421u_2{\dot{u}_2}^2 - 0.0109{\dot{u}_2}^3 + 1.0832u_2^5 - 0.1224u_2^4\dot{u}_2 \\
& - 1.0975u_2^3{\dot{u}_2}^2 - 0.2971u_2^2{\dot{u}_2}^3 - 0.6931u_2{\dot{u}_2}^4 - 0.1008{\dot{u}_2}^5 = 0 \qquad (8.28b)
\end{aligned}$$

Next, assuming a vector of initial conditions $\boldsymbol{q}_0 = (0, 0, 2, 0)$, the original equations of motion Eq. (8.26) are solved numerically. Moreover, $\boldsymbol{q}_0$ is transformed to nonlinear modal coordinates using Eq.(8.13) yielding $\boldsymbol{w}_0 = (-0.80372, -0.33127, 0.80372, 0.33127)$ and the "decoupled" modal equations of motion Eq. (8.28) are solved separately for each mode and subsequently recombined into a general motion in terms of physical coordinates. The same procedure is followed again twice. First, the original equations of motion and the vector of initial conditions are projected onto the nonlinear modal subspaces approximated to 3-rd order (see Eq. (8.8)) which, after ignoring the coupling terms, leads to the "decoupled" system of modal equations of motion

$$\begin{aligned}
\text{mode 1:}\quad & \ddot{u}_1 + 0.7517\dot{u}_1 + 2.9676u_1 + 0.4046u_1^3 \qquad (8.29a) \\
& - 0.0105u_1^2\dot{u}_1 - 0.0136u_1\dot{u}_1^2 + 0.0089\dot{u}_1^3 + 1.5u_1^5 = 0 \qquad (8.29b) \\
\text{mode 2:}\quad & \ddot{u}_2 + 0.1483\dot{u}_2 + 1.0109u_2 + 0.3287u_2^3 \qquad (8.29c) \\
& + 0.0002u_2^2\dot{u}_2 - 0.2421u_2\dot{u}_2^2 - 0.0109\dot{u}_2^3 + 1.5u_2^5 = 0 \qquad (8.29d)
\end{aligned}$$

with initial conditions $\boldsymbol{w}_0 = (-0.97309, -0.15905, 0.97309, 0.15905)$. Second, the original equations of motion and the vector of initial conditions are projected onto the linear modal

subspaces, yielding the "linear" modal equations of motion

$$\text{mode 1:} \quad \ddot{u}_1 + 0.7517\dot{u}_1 + 2.9676u_1 + 0.5u_1^3 + 0.5u_1^3 + 1.5u_1^5 = 0 \tag{8.30a}$$

$$\text{mode 2:} \quad \ddot{u}_2 + 0.1483\dot{u}_2 + 1.0109u_2 + 0.5u_2^3 + 0.5u_2^3 + 1.5u_2^5 = 0 \tag{8.30b}$$

with initial conditions $\boldsymbol{w}_0 = (-0.97309, -0.15905, 0.97309, 0.15905)$.

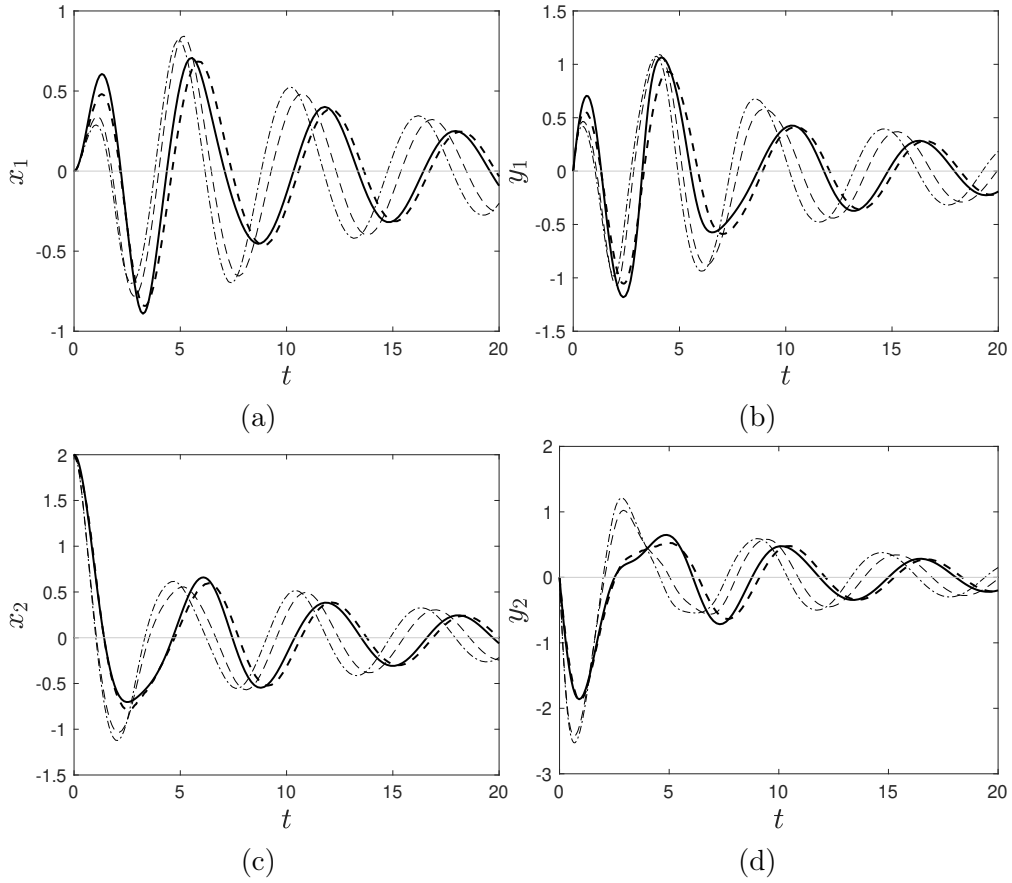

Figure 8.6: Numerical solutions of original and modal equations of motion. **Thick solid line**: original equations of motion. **Thick dashed line**: nonlinear modal equations of motion approximated to 5-th order. **Thin dashed line**: nonlinear modal equations of motion approximated to 3-rd order. **Thin dashed-dotted line**: linear modal equations of motion.

The results of the four solution approaches are compared in Fig. 8.6 where it can be observed that the solution of the nonlinear modal equations approximated to 5-th order, i.e., Eq. (8.28), captures the solution of the original equations of motion relatively accurately.

The discrepancy between these two solutions is attributed to the fact that coupling terms have been ignored in Eq. (8.28). On the contrary, the solution of the nonlinear modal equations approximated to 3-rd order, i.e., Eq. (8.29), as well as, the solution of the "linear" modal equations, i.e., Eq. (8.30) diverge from the solution of the original equations significantly.

8.2.4 3-Dimensional nonlinear oscillator with cubic nonlinearity

The first example considered in this section is a 3-dimensional linear oscillator described by the following equations of motion.

$$\dot{x}_1 = y_1, \quad \dot{y}_1 = g_1(x_1, y_1; x_2, y_2; x_3, y_3) = -(1+k)x_1 + kx_2 - \gamma x_1^3 - cy_1 + cy_2 \tag{8.31a}$$

$$\dot{x}_2 = y_2, \quad \dot{y}_2 = g_2(x_1, y_1; x_2, y_2; x_3, y_3) = kx_1 - (1+k)x_2 + kx_3 + cy_1 - 2cy_2 + cy_3 \tag{8.31b}$$

$$\dot{x}_3 = y_3, \quad \dot{y}_3 = g_3(x_1, y_1; x_2, y_2; x_3, y_3) = kx_2 - (1+k)x_3 + cy_2 - 2cy_3 \tag{8.31c}$$

where the parameter values are $k = 1$ and $c = 0.3$. The expansions of Eq. (8.2) are utilized and truncated to up to 3-rd order terms and the procedure outlined in Sec. 8.1.1 yields a system of 36 polynomial equations in 36 unknowns, namely the 9 coefficients $a_{1,2}, ..., a_{9,2}$ of the expansion of $X_2(u, v)$, the 9 coefficients $b_{1,2}, ..., b_{9,2}$ for the expansion of $Y_2(u, v)$, the 9 coefficients $a_{1,3}, ..., a_{9,3}$ of the expansion of $X_3(u, v)$ and the 9 coefficients $b_{1,3}, ..., b_{9,3}$ for the expansion of $Y_3(u, v)$ shown in Eq. (8.2). This system of polynomial equations has 3 real solutions, one for each mode.

The Gröbner basis approach outlined in Chapter 6 is utilized next for the solution of the aforementioned polynomial system. In this case, the Gröbner basis has 127 elements. The basis of standard monomials $\boldsymbol{B}$, shown in Eq. (8.32), has only 15 elements, i.e., the polynomial system of equations has 15 solutions (3 real and 12 complex).

$$\boldsymbol{B} = [1,\ a_{8,3},\ a_{9,3},\ b_{1,2},\ b_{2,2},\ b_{6,2},\ b_{7,2},\ b_{8,2},\ b_{9,2},\ b_{1,3},\ b_{2,3},\ b_{6,3},\ b_{7,3},\ b_{8,3},\ b_{9,3}] \tag{8.32}$$

The two solutions of the polynomial system of equations corresponding to the three normal modes are given in Tab. 8.5.

Table 8.5: Solutions for the system with cubic nonlinearity corresponding to the 3-D nonlinear oscillator

	Mode 1	Mode 2	Mode 3		Mode 1	Mode 2	Mode 3
$a_{1,2}$	-1.6209	1.3697	-0.0822	$b_{1,2}$	0.7883	0.1289	0.2820
$a_{2,2}$	-0.2329	-0.2179	-0.1412	$b_{2,2}$	-1.3990	1.3916	-0.0191
$a_{3,2}$	0	0	0	$b_{3,2}$	0	0	0
$a_{4,2}$	0	0	0	$b_{4,2}$	0	0	0
$a_{5,2}$	0	0	0	$b_{5,2}$	0	0	0
$a_{6,2}$	0.0139	0.2144	0.1381	$b_{6,2}$	0.3017	0.0554	0.0197
$a_{7,2}$	-0.0619	0.0054	0.0153	$b_{7,2}$	0.2502	-0.2379	0.1555
$a_{8,2}$	-0.0225	0.7563	0.0609	$b_{8,2}$	0.1017	-0.0632	0.0448
$a_{9,2}$	-0.0182	-0.1344	-0.0132	$b_{9,2}$	0.0314	0.7754	0.0772
$a_{1,3}$	1.1912	0.9570	-0.9663	$b_{1,3}$	-0.7507	0.1213	0.0309
$a_{2,3}$	0.2218	-0.2051	-0.0155	$b_{2,3}$	0.9799	0.9776	-0.9594
$a_{3,3}$	0	0	0	$b_{3,3}$	0	0	0
$a_{4,3}$	0	0	0	$b_{4,3}$	0	0	0
$a_{5,3}$	0	0	0	$b_{5,3}$	0	0	0
$a_{6,3}$	-0.0123	0.2226	-0.0722	$b_{6,3}$	-0.2404	0.0196	0.1885
$a_{7,3}$	0.0451	0.0600	-0.0916	$b_{7,3}$	-0.1953	-0.0623	0.0832
$a_{8,3}$	0.0175	0.6235	-0.0650	$b_{8,3}$	-0.0831	0.1262	0.0685
$a_{9,3}$	0.0140	-0.1592	-0.0325	$b_{9,3}$	-0.0244	0.6513	-0.0216

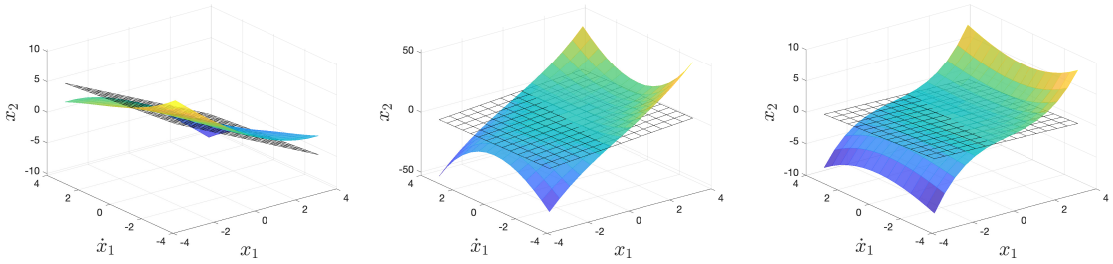

(a) $X_2(x_1, \dot{x}_1)$ - Mode 1 (b) $X_2(x_1, \dot{x}_1)$ - Mode 2 (c) $X_2(x_1, \dot{x}_1)$ - Mode 3

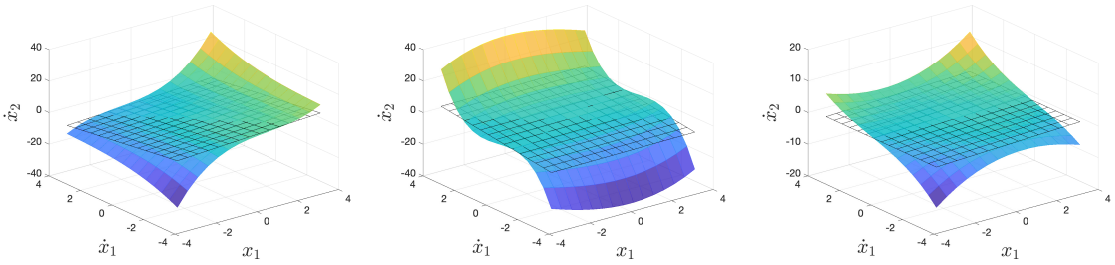

(d) $Y_2(x_1, \dot{x}_1)$ - Mode 1 (e) $Y_2(x_1, \dot{x}_1)$ - Mode 2 (f) $Y_2(x_1, \dot{x}_1)$ - Mode 3

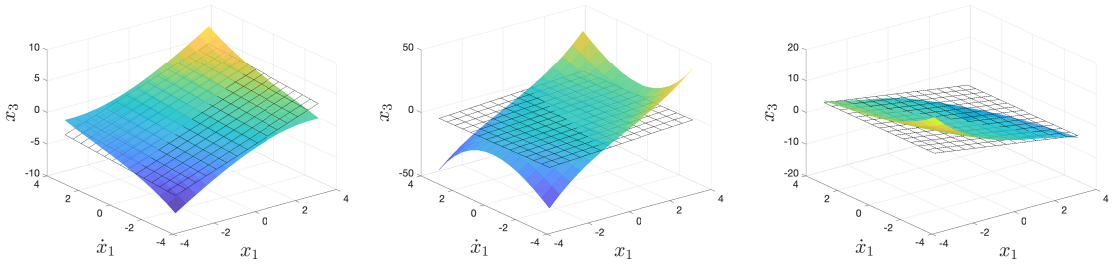

(g) $X_3(x_1, \dot{x}_1)$ - Mode 1 (h) $X_3(x_1, \dot{x}_1)$ - Mode 2 (i) $X_3(x_1, \dot{x}_1)$ - Mode 3

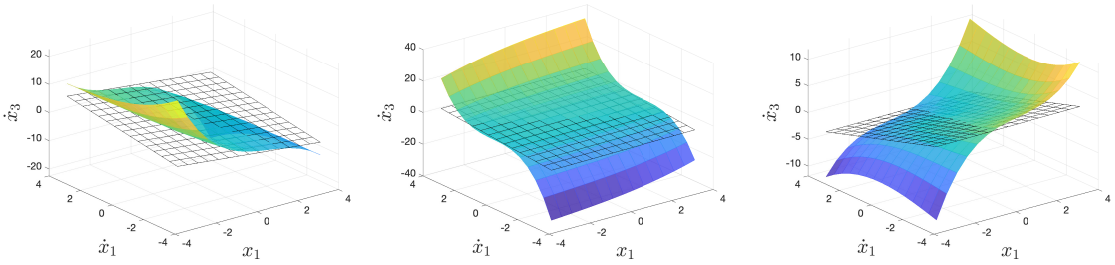

(j) $Y_3(x_1, \dot{x}_1)$ - Mode 1 (k) $Y_3(x_1, \dot{x}_1)$ - Mode 2 (l) $Y_3(x_1, \dot{x}_1)$ - Mode 3

Figure 8.7: Invariant manifolds of the 3-D nonlinear system with cubic nonlinearity.

The shapes of the invariant manifolds $X_2(u, v) = x_2$, $Y_2(u, v) = \dot{x}_2$, $X_3(u, v) = x_3$ and $Y_3(u, v) = \dot{x}_3$ within the phase space $(u, v) = (x_1, \dot{x}_1)$ is shown in Fig. 8.7 for each of the three normal modes. In this case, the manifolds corresponding to the nonlinear system of Eq. (8.31) have curved shapes and they are tangent to their linear counterparts at the

equilibrium point, i.e., the point $(0, 0)$ in this example.

Conclusions

The first part of this thesis is devoted to presenting important developments of the Wiener path integral (WPI) technique. Originated from theoretical physics, path integral techniques have recently attracted attention in the engineering mechanics community, primarily due to their unique characteristics in treating uncertainty propagation problems related to nonlinear dynamical systems under random excitation. The adaptation of path integration concepts in engineering dynamics problems, has been significantly aided by the contributions of Kougioumtzoglou and co-workers, focusing primarily on variational approaches that lead to the development of the WPI technique presented in Chapter 2. Following the initial research efforts in the area of engineering mechanics (e.g., [17]), attention was directed towards improving the WPI technique with respect to three distinct aspects; namely, numerical efficiency, accuracy and versatility in treating a wider range of engineering dynamics problems. In this thesis, significant improvements in the efficiency and versatility of the WPI technique are presented.

Specifically, in Chapter 3, a novel WPI variational formulation with free boundaries is developed for determining the stochastic response of high-dimensional nonlinear dynamical systems in a computationally efficient manner. In this regard, the determination of the complete joint response PDF, required by the standard WPI implementation, has been circumvented herein by utilizing a novel variational formulation involving free boundaries. The developed technique is capable of determining any lower-dimensional joint response PDF directly by properly selecting a combination of fixed and free boundaries at the end time point. Therefore, if knowledge of few only marginal or lower-dimensional joint response PDFs corresponding to a high-dimensional system is of interest, the technique constitutes a powerful tool that appears to be orders of magnitude more efficient than a standard MCS

scheme.

Next, in Chapter 4, a methodology based on the WPI is developed for determining the joint response transition PDF of a broad class of nonlinear dynamical systems with singular diffusion matrices. In this regard, the WPI technique has been extended herein to account for systems that can be represented, generally, as an underdetermined system of SDEs coupled with a set of ODEs. Indicative examples include (but are not limited to) systems with only some of the DOFs excited, hysteresis modeling via additional auxiliary state equations, and energy harvesters with coupled electro-mechanical equations. Next, interpreting the set of ODEs as constraint equations leads to a constrained variational problem to be solved for the most probable path, and thus, the joint response PDF is determined. To this aim, a direct functional minimization formulation has been applied, coupled with a standard Rayleigh-Ritz solution approach. This has reduced the constrained variational problem to an ordinary constrained optimization problem. The reliability of the technique has been demonstrated by considering diverse numerical examples, including various 2-DOF oscillators with only one DOF excited. Interestingly, it has been shown that the special case of a linear oscillator under Kanai-Tajimi earthquake excitation, which yields a singular diffusion matrix, can also be cast in the aforementioned form and treated under the same framework. Further, the SDOF Bouc-Wen nonlinear hysteretic oscillator has also been considered. Comparisons with pertinent MCS data have demonstrated a relatively high degree of accuracy. Moreover, in Chapter 5, this methodology is applied for the stochastic response determination and reliability-based design optimization of a class of energy harvesters exhibiting asymmetric nonlinearities and endowed with fractional derivative elements. It is shown, that the WPI technique provides an efficient computational framework for designing such devices, and the results verify several theoretically established facts reported in the vibratory energy harvesting literature.

The second part of this thesis, serves as a demonstration of the potential merit of recently developed computational algebraic geometry techniques in a wide variety of problems in en-

gineering mechanics. Computational methods that exploit results from algebraic geometry have flourished in recent years and provide powerful tools for the analysis of mathematical problems via computational algebra frameworks. In Chapter 6, one such technique is presented, which relies on the concept of a Gröbner basis to yield all solutions of an algebraic system of polynomial equations. Even though this technique is confined to treating polynomial systems of relatively low dimensionality, it has been proven very useful in treating two challenging problems related to engineering mechanics.

First, it is shown in Chapter 7, that the convexity of the objective function involved in the solution of the WPI can be demonstrated with the aid of Gröbner bases. Specifically, the Rayleigh–Ritz solution approach to the WPI leads to an optimization problem that requires the minimization of a multivariate polynomial. Unless the corresponding objective function is convex, there is no guarantee that a numerical optimization scheme will lead to the global optimum and not to a possibly local optimum. However, considering first order optimality conditions, leads to a system of polynomial equations which is amenable to the solution technique described in Chapter 6. In this regard, all solutions of the algebraic polynomial system are obtained and it is shown that at least for the herein considered nonlinear oscillators, there is only one solution to the associated polynomial system. Therefore, the objective function corresponding to the original minimization problem is convex, and thus, any appropriate numerical scheme is guaranteed to converge to the global optimum.

Second, in Chapter 8, the Gröbner basis approach is applied to the calculation of nonlinear normal modes (NNMs) of a class of nonlinear dynamical systems. NNMs are the nonlinear counterparts of the well known linear normal modes of linear systems and their calculation is a particularly tedious task. For systems with polynomial nonlinearities, the calculation of the NNMs typically resorts to obtaining all solutions of an algebraic system of polynomial equations. In Chapter 8, the Shaw–Pierre formulation for approximating NNMs is adopted and the related polynomial system of equations is solved with the aid of the Gröbner basis approach. As shown in Sec. 8.2, this solution treatment allows for considering higher order

terms in the associated Taylor expansion, which improves the accuracy of the corresponding approximation. Moreover, in order to reduce the associated computational cost, information about the linear part of the Taylor expansion is utilized in obtaining the remaining nonlinear terms, which renders the calculation of the NNMs of a 3-DOF dynamical system possible. To the knowledge of the author, this is achieved for the first time without resorting to numerical continuation schemes.

References

[1] S. W. Shaw and C. Pierre, "Normal modes for non-linear vibratory systems," *Journal of Sound and Vibration*, vol. 164, no. 1, pp. 85–124, 1993.

[2] M. Grigoriu, *Applied Non-Gaussian Processes: Examples, Theory, Simulation, Linear Random Vibration, and MATLAB Solutions*. PTR Prentice Hall Upper Saddle River, NJ, 1995.

[3] M. Grigoriu, *Stochastic Calculus: Applications in Science and Engineering*. Birkhäuser, Boston-Basel-Baein, 2002.

[4] P. D. Spanos and B. A. Zeldin, "Monte carlo treatment of random fields: A broad perspective," *Applied Mechanics Reviews*, 1998.

[5] G. Deodatis, "Simulation of ergodic multivariate stochastic processes," *Journal of Engineering Mechanics*, vol. 122, no. 8, pp. 778–787, 1996.

[6] E. Vanmarcke, *Random Fields: Analysis and Synthesis*. World Scientific, 2010.

[7] S.-K. Au and Y. Wang, *Engineering Risk Assessment with Subset Simulation*. John Wiley & Sons, New York, 2014.

[8] Y.-K. Lin, *Probabilistic Theory of Structural Dynamics*. Krieger Publishing Company, 1976.

[9] I. Elishakoff, *Probabilistic Methods in the Theory of Structures*. Dover Publications, Mineola, New York, 1999.

[10] J. B. Roberts and P. D. Spanos, *Random Vibration and Statistical Linearization (Dover Civil and Mechanical Engineering)*. Dover Publications, Mineola, NY, 2003, ISBN: 0486432408.

[11] R. G. Ghanem and P. D. Spanos, *Stochastic Finite Elements: A Spectral Approach*. Courier Corporation, 2003.

[12] J. Li and J. Chen, *Stochastic Dynamics of Structures*. John Wiley & Sons, 2009.

[13] M. Grigoriu, *Stochastic Systems: Uncertainty Quantification and Propagation*. Springer Science & Business Media, 2012.

[14] N. Wiener, "The average of an analytical functional and the Brownian movement," *Proc. Natl. Acad. Sci*, vol. 7, pp. 294–298, 1921.

[15] M. Chaichian and A Demichev, *Path Integrals in Physics: Stochastic Processes and Quantum Mechanics*. Institute of Physics Publishing, Bristol, U.K., 2001.

[16] I. Kougioumtzoglou and P. Spanos, "An analytical Wiener path integral technique for non-stationary response determination of nonlinear oscillators," *Probabilistic Engineering Mechanics*, vol. 28, pp. 125–131, 2012.

[17] I. A. Kougioumtzoglou and P. D. Spanos, "Nonstationary stochastic response determination of nonlinear systems: A Wiener path integral formalism," *Journal of Engineering Mechanics*, vol. 140, no. 9, p. 04 014 064, 2014.

[18] I. Petromichelakis, A. F. Psaros, and I. A. Kougioumtzoglou, "Stochastic response determination and optimization of a class of nonlinear electromechanical energy harvesters: A Wiener path integral approach," *Probabilistic Engineering Mechanics*, vol. 53, pp. 116–125, 2018.

[19] A. F. Psaros, I. A. Kougioumtzoglou, and I. Petromichelakis, "Sparse representations and compressive sampling for enhancing the computational efficiency of the Wiener path integral technique," *Mechanical Systems and Signal Processing*, vol. 111, pp. 87–101, 2018.

[20] A. F. Psaros, O. Brudastova, G. Malara, and I. A. Kougioumtzoglou, "Wiener path integral based response determination of nonlinear systems subject to non-white, non-Gaussian, and non-stationary stochastic excitation," *Journal of Sound and Vibration*, vol. 433, pp. 314–333, 2018.

[21] I. A. Kougioumtzoglou, A. Di Matteo, P. D. Spanos, A. Pirrotta, and M. Di Paola, "An efficient Wiener path integral technique formulation for stochastic response determination of nonlinear mdof systems," *Journal of Applied Mechanics*, vol. 82, no. 10, p. 101 005, 2015.

[22] I. Petromichelakis, A. F. Psaros, and I. A. Kougioumtzoglou, "Stochastic response determination of nonlinear structural systems with singular diffusion matrices: A Wiener path integral variational formulation with constraints," *Probabilistic Engineering Mechanics*, vol. 60, p. 103 044, 2020.

[23] A. Di Matteo, I. A. Kougioumtzoglou, A. Pirrotta, P. D. Spanos, and M. Di Paola, "Stochastic response determination of nonlinear oscillators with fractional derivatives elements via the Wiener path integral," *Probabilistic Engineering Mechanics*, vol. 38, pp. 127–135, 2014.

[24] A. F. Psaros, I. Petromichelakis, and I. A. Kougioumtzoglou, "Wiener path integrals and multi-dimensional global bases for non-stationary stochastic response determination of structural systems," *Mechanical Systems and Signal Processing*, vol. 128, pp. 551–571, 2019.

[25] J. Nocedal and S. Wright, *Numerical Optimization (Springer Series in Operations Research and Financial Engineering)*. Springer, New York, 2006, ISBN: 0387303030.

[26] A. Doucet, N. De Freitas, and N. Gordon, *An Introduction to Sequential Monte Carlo Methods*. Springer-Verlag, 2001.

[27] D. Venturi and G. E. Karniadakis, "Convolutionless Nakajima–Zwanzig equations for stochastic analysis in nonlinear dynamical systems," *Proceedings of the Royal Society A: Mathematical, Physical and Engineering Sciences*, vol. 470, no. 2166, p. 20 130 754, 2014.

[28] N. Chen and A. J. Majda, "Beating the curse of dimension with accurate statistics for the Fokker–Planck equation in complex turbulent systems," *Proceedings of the National Academy of Sciences*, vol. 114, no. 49, pp. 12 864–12 869, 2017.

[29] D. Xiu and J. S. Hesthaven, "High-order collocation methods for differential equations with random inputs," *SIAM Journal on Scientific Computing*, vol. 27, no. 3, pp. 1118–1139, 2005.

[30] X. Ma and N. Zabaras, "An adaptive high-dimensional stochastic model representation technique for the solution of stochastic partial differential equations," *Journal of Computational Physics*, vol. 229, no. 10, pp. 3884–3915, 2010.

[31] C. Beck, E Weinan, and A. Jentzen, "Machine learning approximation algorithms for high-dimensional fully nonlinear partial differential equations and second-order backward stochastic differential equations," *Journal of Nonlinear Science*, vol. 29, no. 4, pp. 1563–1619, 2019.

[32] P. Hänggi, "Path integral solutions for non-Markovian processes," *Zeitschrift für Physik B Condensed Matter*, vol. 75, no. 2, pp. 275–281, 1989.

[33] A. N. Drozdov and P. Talkner, "Path integrals for Fokker–Planck dynamics with singular diffusion: Accurate factorization for the time evolution operator," *The Journal of Chemical Physics*, vol. 109, no. 6, pp. 2080–2091, 1998.

[34] A. McKane, H. Luckock, and A. Bray, "Path integrals and non-Markov processes. i. general formalism," *Physical Review A*, vol. 41, no. 2, p. 644, 1990.

[35] H. S. Wio, P Colet, M San Miguel, L Pesquera, and M. Rodriguez, "Path-integral formulation for stochastic processes driven by colored noise," *Physical Review A*, vol. 40, no. 12, p. 7312, 1989.

[36] P Colet, H. S. Wio, and M San Miguel, "Colored noise: A perspective from a path-integral formalism," *Physical Review A*, vol. 39, no. 11, p. 6094, 1989.

[37] S. Einchcomb and A. McKane, "Use of Hamiltonian mechanics in systems driven by colored noise," *Physical Review E*, vol. 51, no. 4, p. 2974, 1995.

[38] F. Ikhouane and J. Rodellar, *Systems with Hysteresis: Analysis, Identification and Control using the Bouc-Wen Model*. John Wiley & Sons, 2007.

[39] P. D. Spanos, F. M. Strati, G. Malara, and F. Arena, "An approach for non-linear stochastic analysis of u-shaped OWC wave energy converters," *Probabilistic Engineering Mechanics*, vol. 54, pp. 44–52, 2018.

[40] F. Wiegel, "Path integrals with topological constraints: Aharonov-Bohm effect and polymer entanglements," *Physica A: Statistical Mechanics and its Applications*, vol. 109, no. 3, pp. 609–617, 1981.

[41] S. N. Majumdar, "Brownian functionals in physics and computer science," in *The Legacy Of Albert Einstein: A Collection of Essays in Celebration of the Year of Physics*, World Scientific, 2007, pp. 93–129.

[42] S. N. Majumdar, J. Randon-Furling, M. J. Kearney, and M. Yor, "On the time to reach maximum for a variety of constrained Brownian motions," *Journal of Physics A: Mathematical and Theoretical*, vol. 41, no. 36, p. 365 005, 2008.

[43] H. A. Sodano, D. J. Inman, and G. Park, "A review of power harvesting from vibration using piezoelectric materials," *Shock and Vibration Digest*, vol. 36, no. 3, pp. 197–206, 2004.

[44] ——, "Generation and storage of electricity from power harvesting devices," *Journal of Intelligent Material Systems and Structures*, vol. 16, no. 1, pp. 67–75, 2005.

[45] W.-J. Wu, Y.-Y. Chen, B.-S. Lee, J.-J. He, and Y.-T. Peng, "Tunable resonant frequency power harvesting devices," in *Smart Structures and Materials 2006: Damping and Isolation*, International Society for Optics and Photonics, vol. 6169, 2006, 61690A.

[46] M. Soliman, E. Abdel-Rahman, E. El-Saadany, and R. Mansour, "A wideband vibration-based energy harvester," *Journal of Micromechanics and Microengineering*, vol. 18, no. 11, p. 115 021, 2008.

[47] M. F. Daqaq, R. Masana, A. Erturk, and D. D. Quinn, "On the role of nonlinearities in vibratory energy harvesting: A critical review and discussion," *Applied Mechanics Reviews*, vol. 66, no. 4, p. 040 801, 2014.

[48] L Gammaitoni, I Neri, and H Vocca, "Nonlinear oscillators for vibration energy harvesting," *Applied Physics Letters*, vol. 94, no. 16, p. 164 102, 2009.

[49] S Adhikari, M. Friswell, and D. Inman, "Piezoelectric energy harvesting from broadband random vibrations," *Smart Materials and Structures*, vol. 18, no. 11, p. 115 005, 2009.

[50] D. A. Barton, S. G. Burrow, and L. R. Clare, "Energy harvesting from vibrations with a nonlinear oscillator," *Journal of Vibration and Acoustics*, vol. 132, no. 2, p. 021 009, 2010.

[51] M. F. Daqaq, "Transduction of a bistable inductive generator driven by white and exponentially correlated Gaussian noise," *Journal of Sound and Vibration*, vol. 330, no. 11, pp. 2554–2564, 2011.

[52] H. Yoon and B. D. Youn, "Stochastic quantification of the electric power generated by a piezoelectric energy harvester using a time–frequency analysis under non-stationary random vibrations," *Smart Materials and Structures*, vol. 23, no. 4, p. 045 035, 2014.

[53] T. J. Freeborn, B. Maundy, and A. S. Elwakil, "Fractional-order models of supercapacitors, batteries and fuel cells: A survey," *Materials for Renewable and Sustainable Energy*, vol. 4, no. 3, p. 9, 2015.

[54] A. Allagui, T. J. Freeborn, A. S. Elwakil, M. E. Fouda, B. J. Maundy, A. G. Radwan, Z. Said, and M. A. Abdelkareem, "Review of fractional-order electrical characterization of supercapacitors," *Journal of Power Sources*, vol. 400, pp. 457–467, 2018.

[55] G. M. Ngueuteu and P Woafo, "Dynamics and synchronization analysis of coupled fractional-order nonlinear electromechanical systems," *Mechanics Research Communications*, vol. 46, pp. 20–25, 2012.

[56] C. K. Kwuimy, G Litak, and C Nataraj, "Nonlinear analysis of energy harvesting systems with fractional order physical properties," *Nonlinear Dynamics*, vol. 80, no. 1-2, pp. 491–501, 2015.

[57] A. Erturk and D. J. Inman, *Piezoelectric Energy Harvesting*. John Wiley & Sons, New Jersey, 2011.

[58] G Litak, M. Friswell, and S Adhikari, "Magnetopiezoelastic energy harvesting driven by random excitations," *Applied Physics Letters*, vol. 96, no. 21, p. 214 103, 2010.

[59] M. F. Daqaq, "Response of uni-modal duffing-type harvesters to random forced excitations," *Journal of Sound and Vibration*, vol. 329, no. 18, pp. 3621–3631, 2010.

[60] P. Green, K Worden, K Atallah, and N. Sims, "The benefits of duffing-type nonlinearities and electrical optimisation of a mono-stable energy harvester under white Gaussian excitations," *Journal of Sound and Vibration*, vol. 331, no. 20, pp. 4504–4517, 2012.

[61] S Adhikari, M. Friswell, G Litak, and H. H. Khodaparast, "Design and analysis of vibration energy harvesters based on peak response statistics," *Smart Materials and Structures*, vol. 25, no. 6, p. 065 009, 2016.

[62] Q. He and M. F. Daqaq, "Electric load optimization of a nonlinear mono-stable duffing harvester excited by white noise," *Meccanica*, vol. 51, no. 5, pp. 1027–1039, 2016.

[63] S. Ali, S Adhikari, M. Friswell, and S Narayanan, "The analysis of piezomagnetoelastic energy harvesters under broadband random excitations," *Journal of Applied Physics*, vol. 109, no. 7, p. 074 904, 2011.

[64] I. A. Kougioumtzoglou, "A Wiener path integral solution treatment and effective material properties of a class one-dimensional stochastic mechanics problems," *Journal of Engineering Mechanics*, vol. 143, no. 6, p. 04 017 014, 2017.

[65] B. Buchberger, "Ein algorithmus zum auffinden der basiselemente des restklassenringes nach einem nulldimensionalen polynomideal," *PhD thesis, Universitat Insbruck*, 1965.

[66] ——, "Ein algorithmisches kriterium für die lösbarkeit eines algebraischen gleichungssystems," *Aequationes Math*, vol. 4, no. 3, pp. 374–383, 1970.

[67] D. Lazard, "Gröbner bases, Gaussian elimination and resolution of systems of algebraic equations," in *European Conference on Computer Algebra*, Springer, 1983, pp. 146–156.

[68] D. S. Arnon, G. E. Collins, and S. McCallum, "Cylindrical algebraic decomposition i: The basic algorithm," *SIAM Journal on Computing*, vol. 13, no. 4, pp. 865–877, 1984.

[69] W. W. Adams and P. Loustaunau, *An Introduction to Grobner Bases*. American Mathematical Soc., 1994.

[70] W. Vasconcelos, *Computational Methods in Commutative Algebra and Algebraic Geometry*. Springer Science & Business Media, 2004.

[71] D. Eisenbud, *Commutative Algebra: with a View Toward Algebraic Geometry*. Springer Science & Business Media, 2013.

[72] D. Cox, J. Little, and D. O'Shea, *Ideals, varieties, and algorithms. undergraduate texts in mathematics*, 1997.

[73] D. A. Cox, J. Little, and D. O'shea, *Using Algebraic Geometry*. Springer Science & Business Media, 2006, vol. 185.

[74] R. M. Rosenberg, "Normal modes of nonlinear dual-mode systems," *Journal of Applied Mechanics*, vol. 27, pp. 263–268, 1960.

[75] ——, "The normal modes of nonlinear n-degree-of-freedom systems," *Journal of Applied Mechanics*, vol. 29, pp. 7–14, 1962.

[76] ——, "On nonlinear vibrations of systems with many degrees of freedom," in *Advances in applied mechanics*, vol. 9, Elsevier, 1966, pp. 155–242.

[77] R. H. Rand, "Nonlinear normal modes in two-degree-of-freedom systems," *Journal of Applied Mechanics*, vol. 38, no. 2, pp. 561–561, 1971.

[78] ——, "A direct method for non-linear normal modes," *International Journal of Non-Linear Mechanics*, vol. 9, no. 5, pp. 363–368, 1974.

[79] S. Shaw and C. Pierre, "Non-linear normal modes and invariant manifolds," *Journal of Sound and Vibration*, vol. 150, pp. 170–173, 1991.

[80] S. W. Shaw and C. Pierre, "Normal modes of vibration for non-linear continuous systems," *Journal of Sound and Vibration*, vol. 169, no. 3, pp. 319–347, 1994.

[81] C. Pierre, D. Jiang, and S. Shaw, "Nonlinear normal modes and their application in structural dynamics," *Mathematical Problems in Engineering*, vol. 2006, 2006.

[82] A. F. Vakakis, "Analysis and identification of linear and nonlinear normal modes in vibrating systems.," *Ph.D. Dissertation, California Institute of Technology*, 1991.

[83] ——, "Non-similar normal oscillations in a strongly non-linear discrete system," *Journal of Sound and Vibration*, vol. 158, no. 2, pp. 341–361, 1992.

[84] A. Nayfeh, C Chin, and S. Nayfeh, "Nonlinear normal modes of a cantilever beam," *Journal of Vibration and Acoustics*, vol. 117, no. 4, pp. 477–481, 1995.

[85] A. H. Nayfeh, W. Lacarbonara, and C.-M. Chin, "Nonlinear normal modes of buckled beams: Three-to-one and one-to-one internal resonances," *Nonlinear Dynamics*, vol. 18, no. 3, pp. 253–273, 1999.

[86] E. Pesheck, C. Pierre, and S. W. Shaw, "Modal reduction of a nonlinear rotating beam through nonlinear normal modes," *Journal of Vibration and Acoustics*, vol. 124, no. 2, pp. 229–236, 2002.

[87] O. V. Gendelman, "Bifurcations of nonlinear normal modes of linear oscillator with strongly nonlinear damped attachment," *Nonlinear Dynamics*, vol. 37, no. 2, pp. 115–128, 2004.

[88] C. Touzé and M Amabili, "Nonlinear normal modes for damped geometrically nonlinear systems: Application to reduced-order modelling of harmonically forced structures," *Journal of Sound and Vibration*, vol. 298, no. 4-5, pp. 958–981, 2006.

[89] F. Wang and A. K. Bajaj, "Nonlinear normal modes in multi-mode models of an inertially coupled elastic structure," *Nonlinear Dynamics*, vol. 47, no. 1-3, pp. 25–47, 2007.

[90] M. Peeters, G. Kerschen, and J.-C. Golinval, "Dynamic testing of nonlinear vibrating structures using nonlinear normal modes," *Journal of Sound and Vibration*, vol. 330, no. 3, pp. 486–509, 2011.

[91] ——, "Modal testing of nonlinear vibrating structures based on nonlinear normal modes: Experimental demonstration," *Mechanical Systems and Signal Processing*, vol. 25, no. 4, pp. 1227–1247, 2011.

[92] J.-P. Noël, L. Renson, C. Grappasonni, and G. Kerschen, "Identification of nonlinear normal modes of engineering structures under broadband forcing," *Mechanical Systems and Signal Processing*, vol. 74, pp. 95–110, 2016.

[93] A. F. Vakakis, L. I. Manevitch, Y. V. Mikhlin, V. N. Pilipchuk, and A. A. Zevin, *Normal Modes and Localization in Nonlinear Systems*. Springer, 2001.

[94] G. Kerschen, S. Shaw, C Touzé, O. Gendelman, B Cochelin, and A. Vakakis, *Modal Analysis of Nonlinear Mechanical Systems*. Springer, 2014, vol. 555.

[95] A. Vakakis, "Non-linear normal modes (nnms) and their applications in vibration theory: An overview," *Mechanical Systems and Signal Processing*, vol. 11, pp. 3–22, 1997.

[96] G. Kerschen, M. Peeters, J.-C. Golinval, and A. F. Vakakis, "Nonlinear normal modes, part i: A useful framework for the structural dynamicist," *Mechanical systems and signal processing*, vol. 23, no. 1, pp. 170–194, 2009.

[97] M. Peeters, R. Viguié, G. Sérandour, G. Kerschen, and J.-C. Golinval, "Nonlinear normal modes, part ii: Toward a practical computation using numerical continuation

techniques," *Mechanical Systems and Signal Processing*, vol. 23, no. 1, pp. 195–216, 2009.

[98] C. W. Gardiner, *Handbook of Stochastic Methods for Physics, Chemistry and the Natural Sciences*, Third, ser. Springer Series in Synergetics. Berlin: Springer-Verlag, 2004, vol. 13, pp. xviii+415, ISBN: 3-540-20882-8.

[99] L. Arnold, *Stochastic Differential Equations: Theory and Applications*. Dover Publications, New York, 1974, ISBN: 978-0486482361.

[100] T. T. Soong and M. Grigoriu, *Random Vibration of Mechanical and Structural Systems*. Prentice Hall, New Jersey, 1992, ISBN: 0137523610.

[101] I. I. Gihman and A. V. Skorohod, *Stochastic Differential Equations (Ergebnisse der Mathematik und ihrer Grenzgebiete. 2. Folge)*. Springer-Verlag, Berlin Heidelberg, 1972, ISBN: 3540059466.

[102] H. Risken, "Fokker-planck equation," in *The Fokker-Planck Equation*, Springer, 1996, pp. 63–95.

[103] L. Onsager and S Machlup, "Fluctuations and irreversible processes," *Physical Review*, vol. 91, no. 6, p. 1505, 1953.

[104] H. S. Wio, *Path Integrals for Stochastic Processes: An Introduction*. World Scientific Pub Co Inc, 2013, ISBN: 9814447994.

[105] M. F. Weber and E. Frey, "Master equations and the theory of stochastic path integrals," *Reports on Progress in Physics*, vol. 80, no. 4, p. 046 601, 2017.

[106] L. F. Cugliandolo, V. Lecomte, and F. Van Wijland, "Building a path-integral calculus," *arXiv preprint arXiv:1806.09486*, 2018.

[107] F Langouche, D Roekaerts, and E Tirapegui, "Functional integrals and the Fokker-Planck equation," *Il Nuovo Cimento B (1971-1996)*, vol. 53, no. 1, pp. 135–159, 1979.

[108] A Naess and V Moe, "Stationary and non-stationary random vibration of oscillators with bilinear hysteresis," *International Journal of Non-Linear Mechanics*, vol. 31, no. 5, pp. 553–562, 1996.

[109] I. M. Gelfand, S. V. Fomin, and R. A. Silverman, *Calculus of Variations*. Courier Corporation, North Chelmsford, MA, 2000.

[110] G. M. Ewing, *Calculus of Variations with Applications*. Dover, New York, 1985.

[111] L. D. Elsgolc, *Calculus of Variations*. Mineola, N.Y: Dover Publications, 2007, ISBN: 978-0486457994.

[112] U. M. Ascher, R. M. Mattheij, and R. D. Russell, *Numerical Solution of Boundary Value Problems for Ordinary Differential Equations*. SIAM, 1995.

[113] J. Stoer and R. Bulirsch, *Introduction to Numerical Analysis*. Springer Science & Business Media, 2013.

[114] U. M. Ascher and L. R. Petzold, *Computer Methods for Ordinary Differential Equations and Differential-Algebraic Equations*. SIAM, 1998, vol. 61.

[115] W. H. Press, B. P. Flannery, S. A. Teukolsky, W. T. Vetterling, *et al.*, *Numerical recipes*, 1989.

[116] L. F. Shampine, J. Kierzenka, M. W. Reichelt, *et al.*, "Solving boundary value problems for ordinary differential equations in matlab with bvp4c," *Tutorial Notes*, vol. 2000, pp. 1–27, 2000.

[117] O. C. Zienkiewicz, *Finite Elements and Approximation*. Mineola, N.Y: Dover Publications, 2006, ISBN: 978-0486453019.

[118] R. Storn and K. Price, "Differential evolution–a simple and efficient heuristic for global optimization over continuous spaces," *Journal of Global Optimization*, vol. 11, no. 4, pp. 341–359, 1997.

[119] C. Audet and J. E. Dennis Jr, "Analysis of generalized pattern searches," *SIAM Journal on Optimization*, vol. 13, no. 3, pp. 889–903, 2002.

[120] A. F. Psaros, Y. Zhao, and I. A. Kougioumtzoglou, "An exact closed-form solution for linear multi-degree-of-freedom systems under Gaussian white noise via the Wiener path integral technique," *Probabilistic Engineering Mechanics*, vol. 60, p. 103 040, 2020.

[121] J. R. Morison, M. P. O'Brien, J. W. Johnson, and S. A. Schaaf, "The force exerted by surface waves on piles," *Journal of Petroleum Technology*, vol. 2, no. 05, pp. 149–154, 1950.

[122] E. Perkins, M. Kimura, T. Hikihara, and B. Balachandran, "Effects of noise on symmetric intrinsic localized modes," *Nonlinear Dynamics*, vol. 85, no. 1, pp. 333–341, 2016.

[123] R. Lifshitz and M. C. Cross, "Response of parametrically driven nonlinear coupled oscillators with application to micromechanical and nanomechanical resonator arrays," *Physical Review B*, vol. 67, no. 13, p. 134 302, 2003.

[124] K. Eom, H. S. Park, D. S. Yoon, and T. Kwon, "Nanomechanical resonators and their applications in biological/chemical detection: Nanomechanics principles," *Physics Reports*, vol. 503, no. 4-5, pp. 115–163, 2011.

[125] S. Ramakrishnan and B. Balachandran, "Energy localization and white noise-induced enhancement of response in a micro-scale oscillator array," *Nonlinear dynamics*, vol. 62, no. 1-2, pp. 1–16, 2010.

[126] C. Lanczos, *The Variational Principles of Mechanics (Dover Books on Physics)*. Dover Publications, Mineola, NY, 1986, ISBN: 9780486650678.

[127] M. Giaquinta and S. Hildebrandt, *Calculus of Variations I (Grundlehren der mathematischen Wissenschaften) (Vol 1)*. Springer, Berlin, 2006, ISBN: 354050625X.

[128] C. W. Gear, B. Leimkuhler, and G. K. Gupta, "Automatic integration of Euler-Lagrange equations with constraints," *Journal of Computational and Applied Mathematics*, vol. 12, pp. 77–90, 1985.

[129] G. Strang, *Linear Algebra and its Applications, 4th Edition*. Thomson Higher Education, Belmont, CA, 2006, ISBN: 0030105676.

[130] G. E. Shilov, *Linear Algebra (Dover Books on Mathematics)*. Dover Publications, Mineola, NY, 1977, ISBN: 048663518X.

[131] E. N. Antoniou, A. A. Pantelous, I. A. Kougioumtzoglou, and A. Pirrotta, "Response determination of linear dynamical systems with singular matrices: A polynomial matrix theory approach," *Applied Mathematical Modelling*, vol. 42, pp. 423–440, 2017.

[132] R. H. Byrd and J. Nocedal, "A tool for the analysis of quasi-Newton methods with application to unconstrained minimization," *SIAM Journal on Numerical Analysis*, vol. 26, no. 3, pp. 727–739, 1989.

[133] D. Goldfarb, "A family of variable-metric methods derived by variational means," *Mathematics of Computation*, vol. 24, no. 109, pp. 23–26, 1970.

[134] D. C. Liu and J. Nocedal, "On the limited memory BFGS method for large scale optimization," *Mathematical Programming*, vol. 45, no. 1-3, pp. 503–528, 1989.

[135] M. R. Hestenes, "Multiplier and gradient methods," *Journal of Optimization Theory and Applications*, vol. 4, no. 5, pp. 303–320, 1969.

[136] R. T. Rockafellar, "The multiplier method of hestenes and powell applied to convex programming," *Journal of Optimization Theory and Applications*, vol. 12, no. 6, pp. 555–562, 1973.

[137] M. J. Powell, "A fast algorithm for nonlinearly constrained optimization calculations," in *Numerical Analysis*, Springer, 1978, pp. 144–157.

[138] D. P. Bertsekas, *Constrained Optimization and Lagrange Multiplier Methods*. Athena Scientific, Nashua, NH, 1982, ISBN: 1-886529-04-3.

[139] K. Kanai, "Semi-empirical formula for the seismic characteristics of the ground," *Bulletin of the Earthquake Research Institute*, vol. 35, pp. 309–325, 1957.

[140] H. Tajimi, "A statistical method of determing the maximum response of a building structure during an earthquake.," in *Proc. 2nd World Conf. Earthq. Eng.*, 1960, pp. 781–797.

[141] R. W. Clough and J. Penzien, "Dynamics of structures, computers & structures," *Inc., Berkeley, CA*, 1995.

[142] G Alotta, M Di Paola, and A Pirrotta, "Fractional Tajimi–Kanai model for simulating earthquake ground motion," *Bulletin of Earthquake Engineering*, vol. 12, no. 6, pp. 2495–2506, 2014.

[143] M. Shinozuka and G. Deodatis, "Simulation of stochastic processes by spectral representation," *Applied Mechanics Reviews*, vol. 44, no. 4, pp. 191–204, 1991.

[144] R Bouc, "Forced vibrations of mechanical systems with hysteresis," in *Proc. of the Fourth Conference on Nonlinear Oscillations, Prague, 1967*, 1967.

[145] Y.-K. Wen, "Method for random vibration of hysteretic systems," *Journal of the Engineering Mechanics Division*, vol. 102, no. 2, pp. 249–263, 1976.

[146] J. E. Hurtado and A. H. Barbat, "Equivalent linearization of the Bouc–Wen hysteretic model," *Engineering Structures*, vol. 22, no. 9, pp. 1121–1132, 2000.

[147] Y. Wen, "Equivalent linearization for hysteretic systems under random excitation," *Journal of Applied Mechanics*, vol. 47, no. 1, pp. 150–154, 1980.

[148] P. Spanos and I. Kougioumtzoglou, "Harmonic wavelet-based statistical linearization of the Bouc-Wen hysteretic model," in *Proceedings of the 11th International Conference on Applications of Statistics and Probability in Civil Engineering, ICASP*, vol. 11, 2011, pp. 2649–2656.

[149] K. Papakonstantinou, P. Dimizas, and V. Koumousis, "An inelastic beam element with hysteretic damping," *Shock and Vibration*, vol. 15, no. 3, 4, pp. 273–290, 2008.

[150] A. Charalampakis and V. Koumousis, "A Bouc–Wen model compatible with plasticity postulates," *Journal of Sound and Vibration*, vol. 322, no. 4-5, pp. 954–968, 2009.

[151] Y. Wen, "Methods of random vibration for inelastic structures," *Applied Mechanics Reviews*, vol. 42, no. 2, pp. 39–52, 1989.

[152] M. Ismail, F. Ikhouane, and J. Rodellar, "The hysteresis Bouc-Wen model, a survey," *Archives of Computational Methods in Engineering*, vol. 16, no. 2, pp. 161–188, 2009.

[153] F. Cottone, H. Vocca, and L Gammaitoni, "Nonlinear energy harvesting," *Physical Review Letters*, vol. 102, no. 8, p. 080 601, 2009.

[154] S. D. Nguyen and E. Halvorsen, "Nonlinear springs for bandwidth-tolerant vibration energy harvesting," *Journal of Microelectromechanical Systems*, vol. 20, no. 6, pp. 1225–1227, 2011.

[155] M. F. Daqaq, "On intentional introduction of stiffness nonlinearities for energy harvesting under white Gaussian excitations," *Nonlinear Dynamics*, vol. 69, no. 3, pp. 1063–1079, 2012.

[156] E. Halvorsen, "Fundamental issues in nonlinear wideband-vibration energy harvesting," *Physical Review E*, vol. 87, no. 4, p. 042 129, 2013.

[157] R. Harne and K. Wang, "A review of the recent research on vibration energy harvesting via bistable systems," *Smart Materials and Structures*, vol. 22, no. 2, p. 023 001, 2013.

[158] H. K. Joo and T. P. Sapsis, "Performance measures for single-degree-of-freedom energy harvesters under stochastic excitation," *Journal of Sound and Vibration*, vol. 333, no. 19, pp. 4695–4710, 2014.

[159] R. Langley, "A general mass law for broadband energy harvesting," *Journal of Sound and Vibration*, vol. 333, no. 3, pp. 927–936, 2014.

[160] R. S. Langley, "Bounds on the vibrational energy that can be harvested from random base motion," *Journal of Sound and Vibration*, vol. 339, pp. 247–261, 2015.

[161] Q. He and M. F. Daqaq, "Influence of potential function asymmetries on the performance of nonlinear energy harvesters under white noise," in *ASME 2014 International Design Engineering Technical Conferences and Computers and Information in Engineering Conference*, American Society of Mechanical Engineers, 2014, V006T10A060–V006T10A060.

[162] K. Oldham and J. Spanier, *The Fractional Calculus Theory and Applications of Differentiation and Integration to Arbitrary Order*. Elsevier, 1974, vol. 111.

[163] V. Torczon, "On the convergence of pattern search algorithms," *SIAM Journal on Optimization*, vol. 7, no. 1, pp. 1–25, 1997.

[164] R. M. Lewis and V. Torczon, "Pattern search algorithms for bound constrained minimization," *SIAM Journal on Optimization*, vol. 9, no. 4, pp. 1082–1099, 1999.

[165] R. H. Byrd, J. C. Gilbert, and J. Nocedal, "A trust region method based on interior point techniques for nonlinear programming," *Mathematical programming*, vol. 89, no. 1, pp. 149–185, 2000.

[166] R. A. Waltz, J. L. Morales, J. Nocedal, and D. Orban, "An interior algorithm for nonlinear optimization that combines line search and trust region steps," *Mathematical programming*, vol. 107, no. 3, pp. 391–408, 2006.

[167] M. Raghavan and B. Roth, "Solving polynomial systems for the kinematic analysis and synthesis of mechanisms and robot manipulators," *Journal of Mechanical Design*, vol. 117, no. B, pp. 71–79, 1995.

[168] L. Gonzalez-Vega, F. Rouillier, and M. Roy, "Symbolic recipes for polynomial system solving," in *Some tapas of computer algebra*, Springer, 1999, pp. 34–65.

[169] P. A. Parrilo and B. Sturmfels, "Minimizing polynomial functions," *Algorithmic and Quantitative Real Algebraic Geometry, DIMACS Series in Discrete Mathematics and Theoretical Computer Science*, vol. 60, pp. 83–99, 2003.

[170] J. Carr, *Applications of Centre Manifold Theory*. Springer Science & Business Media, 2012, vol. 35.

[171] R. H. Rand and D. Armbruster, *Perturbation Methods, Bifurcation Theory and Computer Algebra*. Springer Science & Business Media, 2012, vol. 65.

Appendix A: Derivation of Euler-Lagrange equations and free-boundary conditions

Some basic variational calculus concepts are reviewed for completeness.

A.1 First-order system of SDEs

The most probable path $\bar{\boldsymbol{a}}(t)$ corresponding to (2.1) is the function that minimizes the functional

$$S = \int_{t_0}^{t_f} \mathcal{L}\left(\boldsymbol{a}, \dot{\boldsymbol{a}}\right) \mathrm{d}t \tag{A.1}$$

where the Lagrangian $\mathcal{L}$ is given in (2.10). Such a function is typically referred to as an *extremal* of functional S. According to the fundamental theorem of calculus of variations [109], an extremal can be evaluated by utilizing the necessary condition that the first variation of the functional vanishes, i.e.

$$\delta S = 0 \tag{A.2}$$

in conjunction with appropriate boundary conditions. Assuming that the initial and final times t_0 and t_f are fixed, the first variation δS can be written as

$$\delta S = \int_{t_0}^{t_f} \left[\mathcal{L}\left(\boldsymbol{a} + \delta\boldsymbol{a}, \dot{\boldsymbol{a}} + \delta\dot{\boldsymbol{a}}\right) - \mathcal{L}\left(\boldsymbol{a}, \dot{\boldsymbol{a}}\right)\right] \mathrm{d}t \tag{A.3}$$

where $\delta\boldsymbol{a}$ and $\delta\dot{\boldsymbol{a}}$ are the variations of functions $\boldsymbol{a}$ and $\dot{\boldsymbol{a}}$, respectively. By employing Taylor's formula, the first term of the integrand in (A.3) can be written as

$$\mathcal{L}\left(\boldsymbol{a} + \delta\boldsymbol{a}, \dot{\boldsymbol{a}} + \delta\dot{\boldsymbol{a}}\right) = \mathcal{L}\left(\boldsymbol{a}, \dot{\boldsymbol{a}}\right) + \sum_{i=1}^{n} \frac{\partial}{\partial a_i} \mathcal{L}\left(\boldsymbol{a}, \dot{\boldsymbol{a}}\right) \delta a_i + \sum_{i=1}^{n} \frac{\partial}{\partial \dot{a}_i} \mathcal{L}\left(\boldsymbol{a}, \dot{\boldsymbol{a}}\right) \delta \dot{a}_i + R \tag{A.4}$$

where $\boldsymbol{R}$ is an infinitesimal of higher order than $\delta\boldsymbol{a}$ and $\delta\dot{\boldsymbol{a}}$. Next, combining equations (A.2), (A.3) and (A.4), ignoring $\boldsymbol{R}$ and defining $\mathcal{L}_{a_i} = \frac{\partial}{\partial a_i}\mathcal{L}(\boldsymbol{a}, \dot{\boldsymbol{a}})$ and $\mathcal{L}_{\dot{a}_i} = \frac{\partial}{\partial \dot{a}_i}\mathcal{L}(\boldsymbol{a}, \dot{\boldsymbol{a}})$, the first variation of (A.3) takes the form

$$\begin{aligned}\delta S &= \int_{t_0}^{t_f} \sum_{i=1}^{n} \left[\mathcal{L}_{a_i}\delta a_i + \mathcal{L}_{\dot{a}_i}\delta\dot{a}_i\right] \mathrm{d}t \\ &= \sum_{i=1}^{n} \int_{t_0}^{t_f} \mathcal{L}_{a_i}\delta a_i \mathrm{d}t + \int_{t_0}^{t_f} \mathcal{L}_{\dot{a}_i}\delta\dot{a}_i \mathrm{d}t \end{aligned} \tag{A.5}$$

Applying integration by parts on the second integral within the sum of (A.5) yields

$$\int_{t_0}^{t_f} \mathcal{L}_{\dot{a}_i}\delta\dot{a}_i \mathrm{d}t = \left[\mathcal{L}_{\dot{a}_i}\delta a_i\right]_{t_0}^{t_f} - \int_{t_0}^{t_f} \frac{\mathrm{d}}{\mathrm{d}t}\mathcal{L}_{\dot{a}_i}\delta a_i \mathrm{d}t \tag{A.6}$$

Substituting (A.6) into (A.5), the necessary condition (i.e., (A.2)) for the minimization of functional S becomes

$$\delta S = \sum_{i=1}^{n} \left[\mathcal{L}_{\dot{a}_i}\delta a_i\right]_{t_0}^{t_f} + \sum_{i=1}^{n} \int_{t_0}^{t_f} \left(\mathcal{L}_{a_i} - \frac{\mathrm{d}}{\mathrm{d}t}\mathcal{L}_{\dot{a}_i}\right) \delta a_i \mathrm{d}t = 0 \tag{A.7}$$

A.1.1 Fixed boundaries

Next, considering fixed initial and final conditions of the form

$$a_i(t_0) = a_{i,0} \quad \text{and} \quad a_i(t_f) = a_{i,f} \quad \text{for all} \quad i = 1, ..., n \tag{A.8}$$

all variations δa_i vanish at the boundaries, i.e.,

$$[\delta a_i]_{t=t_0} = [\delta a_i]_{t=t_f} = 0 \quad \text{for all} \quad i = 1, ..., n \tag{A.9}$$

and thus, (A.7) becomes

$$\sum_{i=1}^{n} \int_{t_0}^{t_f} \left(\mathcal{L}_{a_i} - \frac{\mathrm{d}}{\mathrm{d}t} \mathcal{L}_{\dot{a}_i} \right) \delta a_i \mathrm{d}t = 0 \tag{A.10}$$

Utilizing the fundamental lemma of calculus of variations [111], leads to the well known Euler-Lagrange (E-L) equations of (2.15) which is a system of n coupled second-order ordinary differential equations (ODE) that can be solved together with the $2n$ boundary conditions of (2.16) for the determination of the most probable path $\bar{\boldsymbol{a}}(t)$.

A.1.2 Free boundaries

The problem of determining the most probable path $\tilde{\boldsymbol{a}}(t)$ is considered next, in which some of the endpoint boundaries are considered free. Thus, it is assumed that the initial conditions are fixed and that only a subset of the endpoint boundaries are fixed at $t = t_f$, i.e.,

$$\left.\begin{aligned} a_i(t_0) &= a_{i,0} && \text{(A.11a)} \\ a_i(t_f) &= a_{i,f} \quad \text{if} \quad i \in U && \text{(A.11b)} \end{aligned}\right\} \; i = 1, ..., n$$

whereas the rest $a_i(t_f)$ for which $i \notin U$ are considered free. It is noted that the set U, that determines which endpoint boundaries are fixed, is an arbitrary subset $U \subseteq \{1, ..., n\}$.

In this case, the variations at the boundaries take the form

$$[\delta a_i]_{t=t_0} = 0 \tag{A.12a}$$

$$\left.\begin{cases} [\delta a_i]_{t=t_f} = 0 & \text{if} \quad i \in U \\ [\delta a_i]_{t=t_f} = \delta a_{i,f} & \text{otherwise} \end{cases}\right\} \; i = 1, ..., n \tag{A.12b}$$

Note that $\tilde{\boldsymbol{a}}(t)$ is also an extremal with respect to the more restricted class of functions $\boldsymbol{a}(t)$ that have their boundaries fixed. Consequently, $\tilde{\boldsymbol{a}}(t)$ satisfies the E-L equation (2.15). In this regard, the second sum in (A.7) vanishes and taking (A.12) into account, (A.7) reduces

to

$$\sum_{i\notin U}\left[\mathcal{L}_{\dot{a}_i}\delta a_i\right]_{t=t_f}=\sum_{i\notin U}\left[\mathcal{L}_{\dot{a}_i}\right]_{t=t_f}\delta a_{i,f}=0 \tag{A.13}$$

Since the variations $\delta a_{i,f}$ are arbitrary, (A.13) leads to the additional boundary conditions $\left[\mathcal{L}_{\dot{a}_i}\right]_{t=t_f}$ for all $i\notin U$. Overall, the most probable path $\tilde{\boldsymbol{a}}(t)$ can be determined by solving the system of the n E-L equations in (2.15) together with the $2n$ modified boundary conditions of (3.2); see also [109, 111] for a broader perspective.

A.2 Higher-order system of SDEs

In this section, a generalization of the herein developed methodology is presented, which accounts for higher-order systems of the form of (3.4). The most probable path $\bar{\boldsymbol{x}}(t)$ corresponding to (3.4) is the function that minimizes the functional

$$S=\int_{t_0}^{t_f}\mathcal{L}\left(\boldsymbol{x},...,\boldsymbol{x}^{(m)}\right)\mathrm{d}t \tag{A.14}$$

where $\mathcal{L}\left(\boldsymbol{x},...,\boldsymbol{x}^{(m)}\right)$ is shown in (3.5).

Similarly as in the first-order case, $\bar{\boldsymbol{x}}(t)$ can be determined by considering the first-order extremality condition of (A.2). In the case of higher-order SDEs considered in this section, assuming that the initial and final times t_0 and t_f are fixed, the first variation δS takes the form

$$\delta S=\int_{t_0}^{t_f}\left[\mathcal{L}\left(\boldsymbol{x}+\delta\boldsymbol{x},...,\boldsymbol{x}^{(m)}+\delta\boldsymbol{x}^{(m)}\right)-\mathcal{L}\left(\boldsymbol{x},...,\boldsymbol{x}^{(m)}\right)\right]\mathrm{d}t \tag{A.15}$$

where $\delta\boldsymbol{x},...,\delta\boldsymbol{x}^{(m-1)}$ and $\delta\boldsymbol{x}^{(m)}$ are the variations of functions $\boldsymbol{x},...,\boldsymbol{x}^{(m-1)}$ and $\boldsymbol{x}^{(m)}$, respectively. By employing Taylor's formula, the first term of the integrand in (A.15) can be

written as

$$\begin{aligned}
&\mathcal{L}\left(\boldsymbol{x}+\delta\boldsymbol{x},...,\boldsymbol{x}^{(m)}+\delta\boldsymbol{x}^{(m)}\right)= \\
&\mathcal{L}\left(\boldsymbol{x},...,\boldsymbol{x}^{(m)}\right)+\sum_{i=1}^{n}\frac{\partial}{\partial x_i}\mathcal{L}\left(\boldsymbol{x},...,\boldsymbol{x}^{(m)}\right)\delta x_i+\sum_{i=1}^{n}\frac{\partial}{\partial \dot{x}_i}\mathcal{L}\left(\boldsymbol{x},...,\boldsymbol{x}^{(m)}\right)\delta \dot{x}_i+... \\
&+\sum_{i=1}^{n}\frac{\partial}{\partial x_i^{(m)}}\mathcal{L}\left(\boldsymbol{x},...,\boldsymbol{x}^{(m)}\right)\delta x_i^{(m)}+R \\
&=\mathcal{L}\left(\boldsymbol{x},...,\boldsymbol{x}^{(m)}\right)+\sum_{k=0}^{m}\sum_{i=1}^{n}\frac{\partial}{\partial x_i^{(k)}}\mathcal{L}\left(\boldsymbol{x},...,\boldsymbol{x}^{(m)}\right)\delta x_i^{(k)}+R
\end{aligned} \tag{A.16}$$

where $\boldsymbol{R}$ is an infinitesimal of higher order than $\delta\boldsymbol{x},...,\delta\boldsymbol{x}^{(m-1)}$ and $\delta\boldsymbol{x}^{(m)}$. Next, combining equations (A.2), (A.15) and (A.16), ignoring $\boldsymbol{R}$ and defining $\mathcal{L}_{x_i^{(k)}}=\frac{\partial}{\partial x_i^{(k)}}\mathcal{L}\left(\boldsymbol{x},...,\boldsymbol{x}^{(m)}\right)$, the first variation of (A.15) takes the form

$$\delta S=\sum_{k=0}^{m}\sum_{i=1}^{n}\int_{t_0}^{t_f}\mathcal{L}_{x_i^{(k)}}\delta x_i^{(k)}\mathrm{d}t \tag{A.17}$$

Applying integration by parts once on the terms of (A.17) corresponding to $k=1$, twice on the terms corresponding to $k=2$, etc. yields

$$\begin{aligned}
\int_{t_0}^{t_f}\mathcal{L}_{\dot{x}_i}\delta\dot{x}_i\mathrm{d}t&=\left[\mathcal{L}_{\dot{x}_i}\delta x_i\right]_{t_0}^{t_f}-\int_{t_0}^{t_f}\frac{\mathrm{d}}{\mathrm{d}t}\mathcal{L}_{\dot{x}_i}\delta x_i\mathrm{d}t \\
\int_{t_0}^{t_f}\mathcal{L}_{\ddot{x}_i}\delta\ddot{x}_i\mathrm{d}t&=\left[\mathcal{L}_{\ddot{x}_i}\delta\dot{x}_i\right]_{t_0}^{t_f}-\left[\frac{\mathrm{d}}{\mathrm{d}t}\mathcal{L}_{\ddot{x}_i}\delta x_i\right]_{t_0}^{t_f}+\int_{t_0}^{t_f}\frac{\mathrm{d}^2}{\mathrm{d}t^2}\mathcal{L}_{\ddot{x}_i}\delta x_i\mathrm{d}t \\
&\vdots \\
\int_{t_0}^{t_f}\mathcal{L}_{x_i^{(m)}}\delta x_i^{(m)}\mathrm{d}t&=\sum_{k=0}^{m-1}(-1)^k\left[\frac{\mathrm{d}^{m-k-1}}{\mathrm{d}t^{m-k-1}}\mathcal{L}_{x_i^{(m)}}\delta x_i^{(k)}\right]_{t_0}^{t_f}+(-1)^m\int_{t_0}^{t_f}\frac{\mathrm{d}^m}{\mathrm{d}t^m}\mathcal{L}_{x_i^{(m)}}\delta x_i\mathrm{d}t
\end{aligned} \tag{A.18}$$

Substituting (A.18) into (A.17) and gathering terms of the same order k in variations

$\delta x_i^{(k)}$, the necessary condition ((A.2)) for the minimization of functional S becomes

$$\begin{aligned}
\delta S = &\sum_{i=1}^{n}\Bigg\{\left[\left(\sum_{k=0}^{m-1}(-1)^k\frac{\mathrm{d}^k}{\mathrm{d}t^k}\mathcal{L}_{x_i^{(k+1)}}\right)\delta x_i\right]_{t_0}^{t_f}+\left[\left(\sum_{k=0}^{m-2}(-1)^k\frac{\mathrm{d}^k}{\mathrm{d}t^k}\mathcal{L}_{x_i^{(k+2)}}\right)\delta\dot{x}_i\right]_{t_0}^{t_f}+\ldots\\
&+\left[\mathcal{L}_{x_i^{(m)}}\delta x_i^{(m-1)}\right]_{t_0}^{t_f}+\int_{t_0}^{t_f}\left(\sum_{k=0}^{m}(-1)^k\frac{\mathrm{d}^k}{\mathrm{d}t^k}\mathcal{L}_{x_i^{(k)}}\right)\delta x_i\mathrm{d}t\Bigg\}\\
&=\sum_{i=1}^{n}\Bigg\{\sum_{l=0}^{m-1}\left[\left(\sum_{k=0}^{m-l-1}(-1)^k\frac{\mathrm{d}^k}{\mathrm{d}t^k}\mathcal{L}_{x_i^{(k+l+1)}}\right)\delta x_i^{(l)}\right]_{t_0}^{t_f}\Bigg\}\\
&+\sum_{i=1}^{n}\int_{t_0}^{t_f}\left(\sum_{k=0}^{m}(-1)^k\frac{\mathrm{d}^k}{\mathrm{d}t^k}\mathcal{L}_{x_i^{(k)}}\right)\delta x_i\mathrm{d}t=0
\end{aligned}\tag{A.19}$$

A.2.1 Fixed boundaries

Next, considering fixed initial and final conditions of the form

$$x_i^{(k)}(t_0)=x_{i,0}^{(k)}\quad\text{and}\quad x_i^{(k)}(t_f)=x_{i,f}^{(k)}\quad\text{for all}\quad i=1,\ldots,n\quad\text{and}\quad k=0,\ldots,m-1 \tag{A.20}$$

all variations $\delta x_i^{(k)}$ vanish at the boundaries, i.e.,

$$\left[\delta x_i^{(k)}\right]_{t=t_0}=\left[\delta x_i^{(k)}\right]_{t=t_f}=0\quad\text{for all}\quad i=1,\ldots,n\quad\text{and}\quad k=0,\ldots,m-1 \tag{A.21}$$

and thus, (A.19) becomes

$$\sum_{i=1}^{n}\int_{t_0}^{t_f}\left(\sum_{k=0}^{m}(-1)^k\frac{\mathrm{d}^k}{\mathrm{d}t^k}\mathcal{L}_{x_i^{(k)}}\right)\delta x_i\mathrm{d}t=0 \tag{A.22}$$

Utilizing the fundamental lemma of calculus of variations [111], leads to the Euler-Lagrange (E-L) equations shown in (3.7) which is a system of n coupled $2m$th-order ODEs that can be solved together with the $2nm$ boundary conditions of (A.20) for the determination of the most probable path $\bar{\boldsymbol{x}}(t)$.

A.2.2 Free boundaries

The problem of determining the most probable path $\tilde{\boldsymbol{x}}(t)$ is considered next, in which some of the endpoint boundaries are considered free. Thus, it is assumed that the initial conditions are fixed and that only a subset of the endpoint boundaries are fixed at $t = t_f$, i.e.,

$$\left.\begin{aligned} x_i^{(k)}(t_0) &= x_{i,0}^{(k)} && \text{(A.23a)} \\ x_i^{(k)}(t_f) &= x_{i,f}^{(k)} \quad \text{if} \quad i \in U_k && \text{(A.23b)} \end{aligned}\right\} \; i = 1, ..., n \quad \text{and} \quad k = 0, ..., m-1$$

whereas the rest $x_i^{(k)}(t_f)$ for which $i \notin U_k$ are considered free. It is noted that the sets U_k, that determine which endpoint boundaries of kth-order are fixed, are arbitrary subset $U_k \subseteq \{1, ..., n\}$ for all $k = 0, ..., m-1$.

In this case, the variations at the boundaries take the form

$$\left.\begin{aligned} &\left[\delta x_i^{(k)}\right]_{t=t_0} = 0 && \text{(A.24a)} \\ &\begin{cases} \left[\delta x_i^{(k)}\right]_{t=t_f} = 0 & \text{if} \quad i \in U_k \\ \left[\delta x_i^{(k)}\right]_{t=t_f} = \delta x_{i,f}^{(k)} & \text{otherwise} \end{cases} && \text{(A.24b)} \end{aligned}\right\} \; i = 1, ..., n \quad \text{and} \quad k = 0, ..., m-1$$

Note that $\tilde{\boldsymbol{x}}(t)$ is also an extremal with respect to the more restricted class of functions $\boldsymbol{x}(t)$ that have their boundaries fixed. Consequently, $\tilde{\boldsymbol{x}}(t)$ satisfies the E-L equation (3.7). In this regard, the corresponding sum in (A.19) vanishes and taking (A.24) into account, the remaining terms of (A.19) yield a set of boundary conditions corresponding to the free boundaries, i.e., the components $x_i^{(k)}$ for which $i \notin U_k$. The complete set of boundary conditions, considering a combination of fixed and free conditions, is shown in (3.8). Concisely, the most probable path $\tilde{\boldsymbol{x}}(t)$ can be determined by solving the system of the n E-L equations in (3.7) together with the $2nm$ modified boundary conditions of (3.8).

Appendix B: Positive definiteness of matrix Q

In this Appendix, the positive definiteness of matrix $\mathbf{Q}$ is proved, and thus, convexity of Eq. (2.43) is also implied. For tutorial effectiveness, the proof is shown hereinafter for a SDOF linear oscillator. In this regard, consider a normalized version of Eq. (7.2) in the form

$$\ddot{x} + 2\zeta_0\omega_0\dot{x} + \omega_0^2 x = \frac{w(t)}{m} \tag{B.1}$$

where ζ_0 is the damping ratio and ω_0 is the natural frequency of the system. Next, employing two trial functions (i.e., $L = 2$) and considering arbitrary initial and final time instants (t_0 and t_f) in Eq. (2.40), matrix $\mathbf{Q}$ is expressed in the form

$$\mathbf{Q} = \begin{bmatrix} Q_{11} & 0 \\ 0 & Q_{22} \end{bmatrix} \tag{B.2}$$

where

$$Q_{11} = \frac{(t_f - t_0)^5}{630}\left(\omega_0{}^4 t_f{}^4 - 4\,\omega_0{}^4 t_f{}^3 t_0 + 6\,\omega_0{}^4 t_f{}^2 t_0{}^2 - 4\,\omega_0{}^4 t_f t_0{}^3 + \omega_0{}^4 t_0{}^4 + 48\,\omega_0{}^2 t_f{}^2 \zeta_0{}^2 + \right.$$
$$\left. -24\,\omega_0{}^2 t_f{}^2 - 96\,\omega_0{}^2 t_f t_0 \zeta_0{}^2 + 48\,\omega_0{}^2 t_f t_0 + 48\,\omega_0{}^2 t_0{}^2 \zeta_0{}^2 - 24\,\omega_0{}^2 t_0{}^2 + 504\right) \tag{B.3}$$

$$Q_{22} = \frac{(t_f - t_0)^5}{6930}\left(\omega_0{}^4 t_f{}^4 - 4\,\omega_0{}^4 t_f{}^3 t_0 + 6\,\omega_0{}^4 t_f{}^2 t_0{}^2 - 4\,\omega_0{}^4 t_f\, t_0{}^3 + \omega_0{}^4 t_0{}^4 + 176\,\omega_0{}^2 t_f{}^2 \zeta_0{}^2 + \right.$$
$$\left. -88\,\omega_0{}^2 t_f{}^2 - 352\,\omega_0{}^2 t_f\, t_0\, \zeta_0{}^2 + 176\,\omega_0{}^2 t_f\, t_0 + 176\,\omega_0{}^2 t_0{}^2\, \zeta_0{}^2 - 88\,\omega_0{}^2 t_0{}^2 + 3960\right) \tag{B.4}$$

Next, for simplicity and without loss of generality, setting $t_0 = 0$ in Eq. (B.2) yields

$$\mathbf{Q} = \begin{bmatrix} \frac{t_f{}^5\left(\omega_0{}^4 t_f{}^4 + 48\,\omega_0{}^2 t_f{}^2\,\zeta_0{}^2 - 24\,\omega_0{}^2 t_f{}^2 + 504\right)}{630} & 0 \\ 0 & \frac{t_f{}^5\left(\omega_0{}^4 t_f{}^4 + 176\,\omega_0{}^2 t_f{}^2\,\zeta_0{}^2 - 88\,\omega_0{}^2 t_f{}^2 + 3960\right)}{6930} \end{bmatrix} \tag{B.5}$$

Since $\mathbf{Q}$ is diagonal, its eigenvalues $\boldsymbol{\lambda}$ are readily determined as

$$\boldsymbol{\lambda} = \begin{bmatrix} \left(\frac{\omega_0{}^4 t_f{}^9}{630} + \frac{8\,\omega_0{}^2 t_f{}^7\,\zeta_0{}^2}{105} - \frac{4\,\omega_0{}^2 t_f{}^7}{105} + \frac{4\,t_f{}^5}{5}\right) \\ \left(\frac{\omega_0{}^4 t_f{}^9}{6930} + \frac{8\,\omega_0{}^2 t_f{}^7\,\zeta_0{}^2}{315} - \frac{4\,\omega_0{}^2 t_f{}^7}{315} + \frac{4\,t_f{}^5}{7}\right) \end{bmatrix} \tag{B.6}$$

Next, setting $y = \omega_0^2$ and considering the most critical case (i.e., $\zeta_0 = 0$) for showing that the eigenvalues $\boldsymbol{\lambda}$ are positive, Eq. (B.6) becomes

$$\boldsymbol{\lambda} = \begin{bmatrix} \left(\frac{y^2\, t_f{}^9}{630} - \frac{4\,y\, t_f{}^7}{105} + \frac{4\,t_f{}^5}{5}\right) \\ \left(\frac{y^2\, t_f{}^9}{6930} - \frac{4\,y\, t_f{}^7}{315} + \frac{4\,t_f{}^5}{7}\right) \end{bmatrix} \tag{B.7}$$

Differentiating Eq. (B.7) with respect to y yields

$$\frac{\mathrm{d}\boldsymbol{\lambda}}{\mathrm{d}y} = \begin{bmatrix} \left(\frac{2y\, t_f{}^9}{630} - \frac{4\,t_f{}^7}{105}\right) \\ \left(\frac{2y\, t_f{}^9}{6930} - \frac{4\,t_f{}^7}{315}\right) \end{bmatrix} \tag{B.8}$$

Setting Eq. (B.8) equal to zero and solving for y leads to

$$y^* = \begin{bmatrix} 12\ \ t_f{}^{-2} \\ 44\ \ t_f{}^{-2} \end{bmatrix}, \tag{B.9}$$

whereas the eigenvalues evaluated at y^* yield

$$\boldsymbol{\lambda}(y^*) = \begin{bmatrix} 4\ {t_f}^5/7 \\ 92\ {t_f}^5/315 \end{bmatrix} \tag{B.10}$$

Further, the second derivative of $\boldsymbol{\lambda}$ becomes

$$\frac{\mathrm{d}^2\boldsymbol{\lambda}}{\mathrm{d}y^2} = \begin{bmatrix} {t_f}^9/315 \\ {t_f}^9/3465 \end{bmatrix} \tag{B.11}$$

Clearly, since $\mathrm{d}^2\boldsymbol{\lambda}/\mathrm{d}y^2 > 0$, the expression for the eigenvalues $\boldsymbol{\lambda}$ as a function of y is convex, and thus, the points in Eq. (B.9) correspond to minima for $\boldsymbol{\lambda}$. Further, since $\boldsymbol{\lambda}$ is positive at y^*, $\boldsymbol{\lambda}$ is positive for any arbitrary values $\omega_0 > 0$ and $0 < \zeta_0 < 1$. In conclusion, all eigenvalues of matrix $\mathbf{Q}$ are positive, and thus, $\mathbf{Q}$ is positive definite.

Appendix C: Gröbner basis for NNMs determination of the linear oscillator example

$$
G = \begin{bmatrix}
b_2^3 + 1.91b_2^2 - 4.09b_2 + 3.0a_1 - 2.7a_2 - 0.3b_1 - 1.91 \\
a_1^2 + 0.18a_1 - 1.0b_2^2 + 0.6a_2 + 0.3b_1 - 0.09 \\
-0.15b_2^2 - 0.91a_2 - 0.5b_1 + 0.5a_1a_2 + 0.15 \\
a_2^2 - 0.9a_2 - 0.09b_2^2 - 1.09b_2 + a_1 - 0.3b_1 + 0.09 \\
0.1a_1b_1 - 0.3a_2 - 0.2b_1 - 0.06a_1 + 0.03 \\
0.05b_2^2 - 0.03a_2 + 0.05a_2b_1 - 0.05 \\
0.1b_1^2 + 0.03b_1 + 0.3a_1 - 0.3b_2 \\
0.2a_1 - 0.09a_2 - 0.2b_2 + 0.1a_1b_2 - 0.1 \\
0.2a_2 + 0.1b_1 + 0.03b_2 + 0.1a_2b_2 + 0.03b_2^2 - 0.03 \\
0.03a_2 + 0.02b_1 + 0.01b_1b_2 \\
0.01a_3 \\
0.01a_4 \\
0.01a_5 \\
0.01a_6 \\
0.01a_7 \\
0.01a_8 \\
0.01a_9 \\
0.01b_3 \\
0.01b_4 \\
0.01b_5 \\
0.01b_6 \\
0.01b_7 \\
0.01b_8 \\
0.01b_9
\end{bmatrix} \tag{C.1}
$$